Master's thesis

NTNU
Norwegian University of Science and Technology
Faculty of Information Technology and Electrical Engineering
Department of Electric Power Engineering

Eivind Dalane

Magnetic Measurements of the Higher-Order Corrector Magnets for the High-Luminosity Upgrade of the Large Hadron Collider at CERN

Master's thesis in Energy and Environmental Engineering
Supervisor: Prof. Arne Nysveen
Co-supervisor: Dr. Ing. Carlo Petrone
September 2022

NTNU
Norwegian University of
Science and Technology

Eivind Dalane

Magnetic Measurements of the Higher-Order Corrector Magnets for the High-Luminosity Upgrade of the Large Hadron Collider at CERN

Master's thesis in Energy and Environmental Engineering
Supervisor: Prof. Arne Nysveen
Co-supervisor: Dr. Ing. Carlo Petrone
September 2022

Norwegian University of Science and Technology
Faculty of Information Technology and Electrical Engineering
Department of Electric Power Engineering

NTNU
Norwegian University of
Science and Technology

Abstract

This report describes the development of two measurement systems for the room temperature magnetic measurements of the corrector package for the High-Luminosity upgrade of the Large Hadron Collider at the European Laboratory for Particle Physics, CERN. Both the physical setup and the post-processing procedures of the systems are described, together with measurements used for determining the optimal set of measurement parameters. The rotating single-stretched wire measurement system was developed for the measurements of the magnets' magnetic axis and azimuthal orientation. It comprises a taut conductive wire that is moved on a circular trajectory, measuring the magnetic flux density of the AC-powered magnet. The harmonic content of the flux density is used to find the axis and orientation of the magnet. A translating coil fluxmeter was developed for the measurements of the longitudinal center and magnetic length of the corrector magnets. It comprises a set of induction coils, tangentially positioned onto a measurement head. It is manually moved through the magnetic field, giving the longitudinal field profiles of the magnets, which is used to locate longitudinal centers and magnetic lengths. The developed systems were tested to characterize their measurement uncertainty, which is requested to be within pre-defined limits for the measurement campaign. To this end, a single, ten-pole corrector magnet was measured with both systems. To fully characterize the rotating single-stretched wire method, a more powerful magnet was also tested, and the results compared to measurements with a well-known measurement system. Lastly, the systems were used to measure the present assembly of the corrector package, to provide feedback to the assembly and fabrication processes, and for further validation of the measurement systems.

The validation measurements showed the ability of the systems to determine the measurands, and gave their spread from several measurements. The rotating single-stretched wire proved to yield the magnetic axis with an uncertainty of ±20 μm, which when referred to the physical magnet is increased to ±170 μm. The system was able to measure the roll angle with an uncertainty of ±0.06 mrad. This is well beneath the measurement requirements. The measurements with the translating coil fluxmeter proved the system to have a spread of less than ±1 mm for the measurements of both the longitudinal center and the magnetic length. This is ten times lower than the required uncertainty. As such, both systems were deemed suitable for further measurements. The present assembly of the corrector package was measured with both systems. The measurements with the rotating single-stretched wire method showed offsets of the magnetic axis within the expected deviations for all the magnets, even though they were rather large. The measured roll angles were found to exceed the expectations by a factor eight. The latter points are most likely the results of misalignment of the magnets during the assembly phase, as this is not yet complete. For the measurements using the translating coil fluxmeter, it was proven to have an uncertainty of less than the requirements with the entire corrector package powered in series, even at lower field values. The deviations were within the expectations for both the longitudinal center and the magnetic length for nearly all the magnets. However, the magnetic length of the quadrupole corrector was found to be higher than expected. This could be explained by low precision in the design phase, and the uncertainty introduced by the mechanical movement of the measurement head.

The measurement systems both showed great promise for future measurement campaigns. The rotating single-stretched wire performed better than what could be expected, and will be used in the future measurements of the corrector packages. The translating coil fluxmeter was deemed sufficiently precise and accurate for these measurements, and as such could be used in its current state for further measurements. However, reducing the mechanical noise from the movement of the measurement head is advised for the future development.

Sammendrag

Denne rapporten beskriver utviklingen av to systemer for magnetiske målinger av en samling korreksjonsmagneter som skal benyttes i High-Luminosity-oppgraderingen av the Large Hadron Collider ved Den Europeiske Organisasjonen for Kjernefysisk Forskning, CERN. Rapporten presenterer utviklingen av både det fysiske måleinstrumentet og post-prosesseringen av måledata, samt et sett med optimale parametre, funnet gjennom ulike forsøk. Et måleinstrument bestående av en strukket, elektrisk ledende tråd ble utviklet for å måle magnetisk akse og asimut rotasjon. Tråden beveges i en sirkulær bane, og måler tidsvarierende magnetisk flukstetthet. Magnetisk akse og rotasjon beregnes fra det målte magnetfeltets harmoniske innhold. Det andre måleinstrumentet består av induksjonsviklinger plassert tangentielt på et sylindrisk målehode. Magnetfeltet måles ved å bevege målehodet manuelt gjennom et konstant magnetfelt, noe som gir magnetisk flukstetthet som funksjon av posisjon i lengderetning. Fra dette bestemmes magnetisk senter og magnetisk lengde. Et sett med målinger ble gjennomført for å karakterisere målesystemenes usikkerhet. En enslig, ti-polet korreksjonsmagnet ble benyttet til dette formålet. En kraftigere magnet ble så brukt for å bestemme usikkerheten til målingene av magnetisk akse og rotasjon, hvor akse og rotasjon funnet ved det nyutviklede systemet ble sammenliknet med resultater funnet ved bruk av et mer standardisert målesystem, med allerede kjent usikkerhet. Til sist ble systemene brukt til å måle hele rekken av korreksjonsmagneter. Resultatene av disse målingene brukes som tilbakemelding på produksjon og montering av samlingen av korreksjonsmagneter.

Valideringen av målesystemene viste at usikkerheten ved systemene er lavere enn kravene for de magnetiske målingene av korreksjonsmagnetene. Usikkerheten knyttet til målingene av magnetisk akse var mindre enn ± 20 μm, men denne økes til ± 170 μm når resultatet refereres til magnetens eksterne målepunkter. Tilsvarende usikkerhet for målingene av rotasjon var mindre enn ± 0.06 mrad. Dette er mye lavere enn kravene til målingene. Spredningen av målt magnetisk lengde og senter ble bestemt til ± 1 mm, ti ganger så lavt som kravene til måleusikkerheten. På bakgrunn av dette ble begge målemetodene funnet gode nok til å fortsette målingene av de installerte korreksjonsmagnetene. Av hele samlingen av magneter, lå alle målte magnetiske akser innenfor forvented avvik fra nominell posisjon. Samtidig var avviket relativt stort, og med maksimalt avvik for asimut vinkel målt til å overstige nominell verdi med en faktor åtte, viste målingene at sammenstillingen av magnetene ikke er godt nok gjennomført. Dette kan forklares med at denne prosessen enda ikke er helt fullført. Målingene av senter og magnetisk lengde viste seg å ha en usikkerhet lavere enn kravene også med målinger av alle magnetene koblet i serie, selv om dette fører til lavere verdier av flukstettheten. For både senter og lengde, ble avviket beregnet til å være innenfor forventningene for alle magnetene bortsett fra den fire-polte magneten, hvor magnetisk lengde var for lang. Den sannsynlige forklaringen på dette er todelt, med lav presisjon i designfasen, samt mekanisk støy fra den manuelle bevegelsen av induksjonsviklingene.

Begge målemetodene viste stort potensiale for videre målinger av korreksjonsmagnetene. Spesielt metoden for å måle magnetisk akse og orientering viste seg å overgå forventningene, og vil bli brukt i videre målinger. Også for måleinstrumentet med tangentielt posisjonerte induksjonsviklinger ble det konkludert at usikkerheten er lav nok til at det kan brukes som det er i fremtiden. Samtidig er man rådet til å fortsette utviklingen av måleinstrumentet for å redusere påvirkningen av støy fra den manuelle bevegelsen av målehodet.

Preface and Acknowledgements

This thesis concludes the five year master program Energy and Environmental Engineering at the Norwegian University of Science and Technology. The first four years were spent in Trondheim, and I would like to thank my fellow students for an including and friendly environment. I would especially like to thank Sondre A. Kaldheim for his friendship, teamwork, support and for all the laughs we shared during our long days of study.
I spent the fifth and final year of the study program in Geneva, as part of the technical student program in the Testing and Measurements section at CERN. I am grateful for the opportunity to spend time at such an inspiring and interesting environment, and would like to express my gratitude to section leader Dr. Ing. Habil Stephan Russenschuck and Dr. Ing. Carlo Petrone for accepting me to the program. I would also like to thank everyone in the section for their help and guidance during this year; the technicians and staff in the laboratories for their patience and tirelessness in answering questions, and to the remaining staff, fellows and student members of the section for guidance and fruitful discussions, and for creating such a welcoming and friendly environment. Lastly, I would like to thank Dr. Ing. Carlo Petrone, for his invaluable guidance, discussions and coffee breaks. I could not have asked for a better supervisor and mentor at CERN.

A large thank you is owed to my supervisors for this task, Prof. Arne Nysveen at NTNU and Dr. Ing. Carlo Petrone at CERN. Thank you for all your guidance throughout this process; to Carlo for giving me such an inspiring task, and for the help with measurements, questions occurring from day to day and for guidance in the writing process, and to Arne for helping me with the structure of my thesis, for fruitful theoretical discussions, for shortening the distance from Trondheim to Geneva, and for showing such enthusiasm for my work.

Then, I would like to thank my family, for their support and encouragement through life and my studies. Finally, I am forever grateful to my partner Live, for being there for me through nearly five years of studies, and in life in general. I am so lucky to have you in my life.

Eivind Dalane, 2022

Nomenclature

Throughout this thesis, the following nomenclature has been adopted. It is presented with units given in brackets [ ]:

- $\mathbf{B}$: Magnetic Flux Density - [T]
- $\mathbf{H}$: Magnetic Field Intensity - $[\frac{\mathrm{A}}{\mathrm{m}}]$
- $\mathbf{A}$: Magnetic Vector Potential - $[\frac{\mathrm{Vs}}{\mathrm{m}}]$
- Φ: Magnetic Flux - $[\frac{\mathrm{T}}{\mathrm{m}^2}]$
- ϕ_{m}: Magnetic Scalar Potential - [A]
- $\mathbf{E}$: Electric Field Intensity - $[\frac{\mathrm{V}}{\mathrm{m}}]$
- $\mathbf{D}$: Electric Flux Density - $[\frac{\mathrm{C}}{\mathrm{m}^2}]$
- μ_0: Permeability in Vacuum - $4\pi \cdot 10^{-7}[\frac{\mathrm{Ns}^2}{\mathrm{C}^2}]$
- ϵ_0: Permittivity in Vacuum - $\approx 8.85 \cdot 10^{-12}[\frac{\mathrm{C}^2}{\mathrm{Nm}^2}]$
- $\mathbf{J}$: Electric Current Area Density - $[\frac{\mathrm{A}}{\mathrm{m}^2}]$
- ρ: Electric Charge Volume Density - $[\frac{\mathrm{C}}{\mathrm{m}^3}]$
- e: Elementary Electron Charge - $1.60217662 \cdot 10^{-9}$ [C]
- $\mathbf{v}$: Linear Velocity - $[\frac{\mathrm{m}}{\mathrm{s}}]$
- m: Mass - [kg]
- γ: Lorentz factor - [-]
- r: Distance from Origin to a Point in Polar Coordinates - [m]
- R: Distance from Origin to a Point in Spherical Coordinates - [m]
- r_0: Reference Radius of a Magnetic Measurement - [m]
- r_c: Shortest Distance to the Iron Boundary or Current Density of a Domain - [m]
- s_{c}: The Magnetic Center of an Accelerator Magnet - [m]
- L_{m}: The Magnetic Length of an Accelerator Magnet - [m]
- θ: Mechanical Angle of an Accelerator Magnet - [rad]
- B_n/A_n: Normal/Skew Magnetic Multipole Component of Order n- [T]
- α_{roll}: Roll Angle of an Accelerator Magnet - [rad]
- β^*: Transverse Beam Size in the Interaction Point - $[\mathrm{m}^2]$
- S_n^{tan}: Coil Sensitivity Function of Order n, for a Tangential Rotating Coil Assembly - $[\mathrm{m}^2]$
- S_n^{rad}: Coil Sensitivity Function of Order n, for a Radial Rotating Coil Assembly - $[\mathrm{m}^2]$
- S_n^c: Coil Sensitivity Function of Order n, for a Translating Coil Assembly - $[\mathrm{m}^2]$

Contents

Figures

Tables

Chapter 1

Introduction

Close to Geneva, on the border between France and Switzerland, lies the European Laboratory for Particle Physics. After the Second World War, scientists from Europe and America saw the need for a European atomic physics laboratory, in order to stop the migration of scientists across the pond, and to reunite a torn Europe after the war. Therefore, in 1953, the twelve first member states signed the convention establishing the *Conseil Européen pour la Recherche Nucléaire*[I], CERN [1]. Today, CERN is one of the World's larges research facilities, with 23 member states, and scientists from all over the world pushing the frontiers of science and technology. This has resulted in, amongst other, the discovery of the Higgs boson and the making of antimatter to study the building-blocks of the Universe in the World's largest particle accelerator, the Large Hadron Collider. Operating these experimental areas requires the collective effort from not only theoretical physicists, but also technicians and engineers from a wide range of disciplines, pushing the boundaries within their own fields of expertise. This has lead to breakthroughs in various fields, such as medicine, cryogenics, material technology, and data management, to mention some. One example is the invention of the World Wide Web at CERN in 1989.

Magnetic fields are used in circular particle accelerators to guide and focus the bunches of particles, as they move close to the speed of light. Thorough knowledge of the magnetic field is therefore of key importance to the design, assembly and operation of the accelerator complex. The *Testing and Measurements* section, under the *Technology* department and *Magnets, Superconductors and Cryogenics* group, TE-MSC-TM, is responsible for delivering reliable magnetic measurements during all phases of the magnets' lives at CERN. The section has equipment and facilities for performing magnetic measurements of both normal- and superconductive magnets. Since measurement systems are rarely off-the-shelf equipment, the section has a lot of experience and expertise in the design and development of measurement equipment, and a large portion of the work undertaken in the section categorizes as research and development.

This thesis falls into the latter category. It is written as part of a one-year technical studentship in the TM-section. The first six months of the stay, I familiarized myself with the field of magnetic measurements, acquired necessary skills and knowledge. It was concluded with a project report concerning magnetic measurements of solenoidal magnetic fields, also presented in [2]. The last six months were spent working on this thesis. It involves the development of a complete measurement system to measure the magnetic axis, roll angle, magnetic length and longitudinal center of a series of superferric corrector magnets for the next upgrade of the Large Hadron Collider. The High-Luminosity upgrade aims at ten-folding the number of collisions. This involves upgrading the existing corrector package of the Large Hadron Collider with a nested dipole corrector magnet, and

[1] In English, this reads *The European Council for Nuclear Research*.

a set of nine superferric higher-order corrector magnets. The magnets are to be operated in a superconductive state, cooled to 1.9 K, allowing for magnetic flux densities of up to 1.75 T at a reference radius of 50 mm. The magnetic measurements, however, are to be performed at room temperature. This complicates the measurements significantly, as the strength of the flux density, and its variation about the magnetic axis are reduced to approximately a thousandth of their design values. This prohibits the use of already available measurement techniques, and therefore calls for the development of new equipment, approaches and post-processing algorithms. The work presented in this thesis, can be formulated in the following problem description:

> *The higher-order corrector package comprises a set of nine superferric correction magnets with the purpose of correcting for magnetic imperfections and misalignments in the High-Luminosity upgrade of the Large Hadron Collider. The knowledge of the magnetic axis, roll angle, magnetic length and longitudinal center of the individual corrector magnets is of key importance to the assembly, installation, and operation of the accelerator complex. These qualities of the magnetic fields are to be determined through room temperature measurements, with the added complexity of low field values and gradients due to the low excitation currents in this state, ruling out already available measurement methods. This calls for the development of measurement systems able to acquire these qualities within predefined limitations of the measurement uncertainty. The development is concluded with the measurement of the first corrector package assembly.*

The main objective of this thesis is therefore to develop measurement systems able to measure the required qualities of the magnetic flux density of the corrector magnets, while installed in the corrector package. The work involved with the development can be divided into the following tasks:

- To design and develop one or more measurement systems for the measurements of the magnetic axis, roll angle, magnetic length and longitudinal center. This can be achieved using already existing measurement systems, or through the development of new systems.

- To establish measurement approaches, and through testing determine a set of optimal parameters for the measurement system. This includes the development of post-processing algorithms for the treatment of measurement data to acquire the required magnetic properties.

- Through a set of magnetic measurements, validate and determine the precision, accuracy and uncertainty of the measurement system. The outcome of this metrological characterization will be compared to the measurement requirements, to determine the system's suitability to measure the required magnetic qualities.

- To measure the first corrector package assembly with the goal of providing initial results and feedback to the fabrication and assembly process of the corrector package.

- Present suggestions for the future steps of the measurement methods for further development and measurements at CERN.

The work in this thesis is limited to the development and testing of the chosen measurement methods, in addition to presenting the theory required to understand the working principles of electromagnets used in particle accelerators, the measurement principles and the post-processing of the measurements. The post-processing of the measurement data is performed using various functionalities in MATLAB. No analytic calculations or simulation tools have been utilized in the work with

this thesis. This would definitely be of interest, especially in the optimal design of the measurement systems. It was opted away for the work in this thesis, due to time restrictions both of the work with the thesis, and for the measurements themselves.

The rest of the thesis is structured in the following way:

Chapter 2 presents relevant theory for the development of the measurement systems in this thesis. The chapter gives a description of the working principles of charged particle accelerators, and the importance of magnetic fields for the circular accelerators. The multipolar magnetic field theory is developed from Maxwell's equations, as this is of key importance to the correction strategy adopted for the Large Hadron Collider, and also for the High-Luminosity upgrade. The magnetic field theory is then presented in light of the physical accelerator magnets used at CERN, and the need for corrector magnets are discussed. Magnetic measurement theory is presented, with an emphasis on induction-coil methods, as the measurement techniques are largely based on this.

Chapter 3 presents the developed measurement methods. First, the measurement requirements and expected results are presented. Then, the challenges of measuring superconducting accelerator magnets at room temperature are presented, together with an explanation of how this rules out using established measurement techniques for the measurements. Then, the measurement techniques are presented, with a step-by-step explanation of the method and post-processing phase. The parameters used, and the tests determining these, are presented.

Chapter 4 describes the metrological characterization and validation of the measurement, through a set of measurement campaigns. The results of these measurements are then presented, and their impact on the measurement technique is discussed. The conclusion of these measurements presents whether the system is suitable for measuring the initial corrector package assembly.

Chapter 5 deals with the measurements of the present corrector package assembly. It explains the challenges encountered with these measurements that were not present in the validation measurements, and how these effects are mitigated. Then, the measurement results are given, together with a discussion of the results compared to the expectations, and additional sources of uncertainty.

Chapter 6 summarizes the discussions from the previous chapters, and points towards future steps in the development and use of the measurement systems.

Chapter 7 concludes the thesis; both the measurement systems and the measurement results.

Appendix A presents important aspects regarding digital signal processing, and the adopted treatment of the data prior to the Fourier analysis used in these measurements. **Appendix B** shows the effect of inserting a conductive tube, such as the cold bore of the corrector package, into an alternating magnetic field, and how this affects the measured magnetic flux density.

Chapter 2

Theory

This chapter describes the theory needed for the development of the measurement systems and techniques presented in the following chapters. It starts by giving a short introduction to the working principle of charged particle accelerators at CERN, with emphasis on the importance of magnetic fields in circular accelerators. Secondly, the representation of magnetic fields through its Fourier coefficients, the so-called multipole theory, is developed from Maxwell's equations, as this is used to describe the working principles of corrector magnets in accelerators. Magnetic measurements in rotated and displaced magnetic fields are also presented. Then, ideal magnetic fields are discussed in light of the restrictions introduced in real magnets used in accelerator complexes, and how this results in erroneous field components. Techniques for how these effects can be mitigated are presented. This part also presents the High-Luminosity upgrade of the Large Hadron Collider, with an emphasis on the need for the corrector package that is the magnet assembly under consideration in this thesis. The chapter is concluded with an introduction to magnetic measurements; the most important properties of magnetic fields, and different measurement techniques for obtaining these. The main focus is on induction-coil measurements, as the measurement methods developed in this thesis to a large extent is based on these principles.

2.1 Charged Particle Accelerators

2.1.1 The CERN accelerator complex and the Large Hadron Collider

Particle accelerators are used to investigate the building blocks of the universe. The basic principle of charged particle accelerators is to accelerate charged particles to velocities approximately equal to the speed of light. The particle beams collide, and the debris is investigated in large experimental areas. There are different types of particle accelerators, but they all need three main components; a source of elementary particles or ions, a tube to accelerate the particles in a high vacuum, and apparatus to accelerate, confine and focus the particle beams, such as generators of electric fields and magnets. There are different types of charged particle accelerators. In linear accelerators, LINACs, the charged particles are accelerated by oscillating electric potentials along a linear path. In circular accelerators, the particles are accelerated by passing oscillating electric potentials several times. Circular accelerators can be of several types, namely *cyclotrons*, *synchrotrons* and *storage rings*. In cyclotrons, particles are accelerated in high-frequency electromagnetic fields in two electrodes and spiral outwards as the energy increases. Synchrotrons were a breakthrough when they were first built, as they were the first large-scale accelerators. This was enabled by using separate components in their construction. They can accelerate particles very close to the speed of light and reach much higher energies than cyclotrons. Storage rings are technically synchrotrons but with two counter-rotating particle beams. They require a much better vacuum than the synchrotron but offer many more collisions than any other accelerator. Furthermore, the particles can be rotated for several hours at a time, enabling a lot of collisions [1].

The accelerator complex at CERN is depicted in Figure 2.1. It shows the collection of accelerators and experiments currently at CERN, and it also shows the development of the complex throughout time.

The Large Hadron Collider, or the LHC, is shown in the top part of the figure. With its circumference of approximately 27 km, it is the largest and most powerful accelerator in the World and the most prominent scientific instrument ever built. In the rest of this section, a brief description of the working principle of the LHC will be given to act as a basis for the theoretical developments in the rest of this thesis.

The particles used in the LHC are supplied from a bottle of research-grade hydrogen gas. Electric fields are used to strip the electron from the hydrogen atom, leaving a proton and a positron, *hadrons*. The hadrons are then accelerated through LINAC4 by radio-frequency cavities, where radio frequency power is fed to cavities made of copper. This results in an oscillating electric field within the cavities, accelerating the passing particles. The particles are collected in bunches spaced by 25 ns. When a bunch has reached its destined energy in the LINAC, it is passed on to the circular accelerators. Each accelerator increases the beam's energy until the maximum is reached, and the beam is passed on to the next accelerator. When the particles reach the LHC, they have an energy of 450 GeV[I]. In the LHC, as for the LINAC 4, superconductive radio-frequency cavities made of copper are used to generate an alternating electric field. The oscillating field is designed to make the velocity of the particles in each bunch as similar as possible by kicking the "slower" particles whilst slowing down the "faster" particles. Superconductive electromagnets are used to guide (dipoles) and focus (quadrupoles) the particle bunches along the circumference of the accelerator. Whilst in the LHC, for roughly 20 minutes, the bunches reach a velocity exceeding 99.999% the speed of light, and an energy level of 7 TeV, by the time the collisions start. At this stage, the particles make 11245 circuits per second, resulting in above 600 million collisions per second, of which 200 million are usable.

[1] eV is a unit of energy equal to the work needed to move a single particle through a potential difference of 1 V.

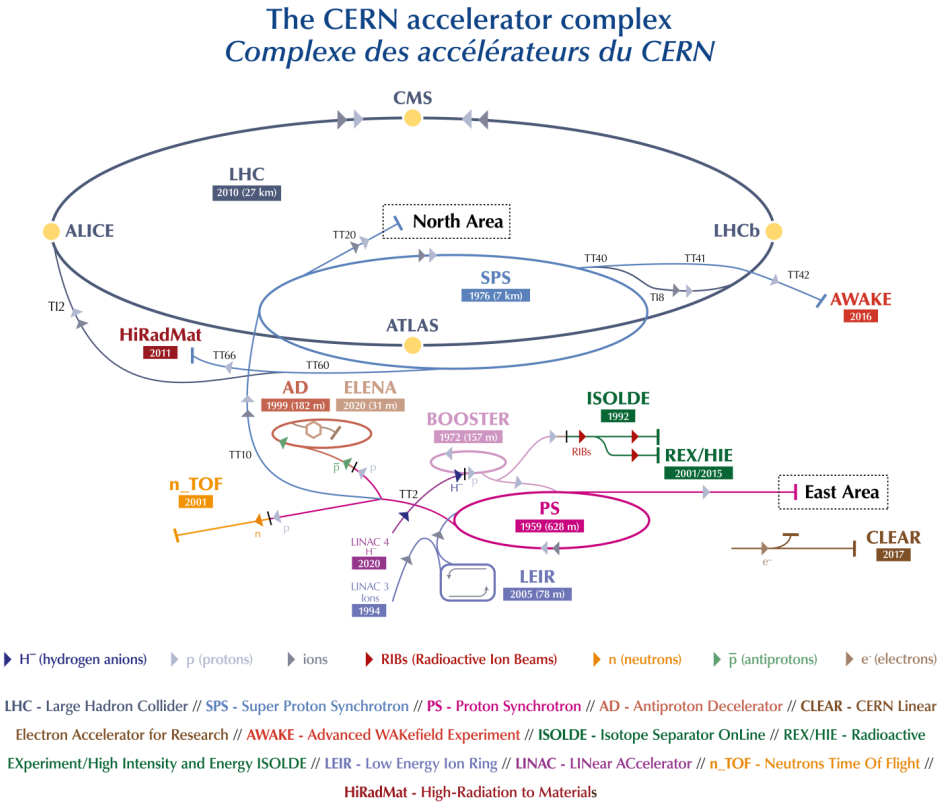

Figure 2.1: The accelerator complex at CERN, complete with injection chains, accelerators, and experiments. The figure is taken from [3].

When the particles collide, the debris is bent using strong solenoidal fields. The resulting particle's mass is calculated from their trajectories' observable curvature, giving knowledge about the proton's building blocks [1][4][5].

2.1.2 Magnetic fields for charged particle accelerators

Lorentz's force is the governing equation describing the force on a particle with charge q moving with a velocity $\mathbf{v}$ through electric and magnetic fields, $\mathbf{E}$ and $\mathbf{B}$:

$$\mathbf{F} = q \cdot (\mathbf{E} + \mathbf{v} \times \mathbf{B}). \tag{2.1}$$

It can be seen that the force given by the magnetic field is perpendicular to the particle's movement. Consequently, the magnetic field does not perform any work on the particle. However, magnetic fields guide and focus the particles on their trajectory within the accelerator. At relativistic speed, the effect of the electric and magnetic field on the charged particle is equal if $|\mathbf{E}| = c|\mathbf{B}|$, where c is the speed of light. The guiding force on the charged particle corresponding to a field of 1 T, which is easily achievable in the magnets used for charged particle accelerators, would require an electric field of approximately $3 \cdot 10^8$ Vm^{-1}. As a consequence of this, even though electric fields could also have been used for steering and focusing the charged particles, according to eq. (2.1), required field levels in the range of GVm^{-1} make magnets the only feasible solution [6].

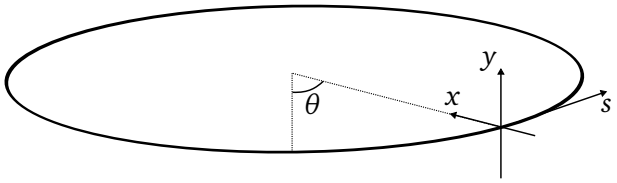

Figure 2.2: Coordinate system used for charged particle movement in circular particle accelerators.

A basic description of the magnetic fields in charged particle accelerators is given in the following. The coordinate system adopted for explaining the forces acting on particles moving along the circular accelerators is presented in Figure 2.2, where x and y describe the transverse plane, and the s-axis gives the tangential component of the ideal particle trajectory at a given moment. In the following of this thesis, the s-axis is used as the longitudinal axis, fixed at each point under the assumption that the curvature of the accelerator is negligible. This is justified by the fact that we are mainly concerned with magnets of a few meters. In the following discussion, we assume no particle acceleration, only transversal field components, and ideal magnetic components perfectly positioned.

In circular particle accelerators, dipole magnets guide the charged particles. The magnetic flux density distribution of a dipole magnet and force field exerted on a positively charged particle moving out of the paper is presented in the following Figure 2.3. From the force field to the right in Figure 2.3,

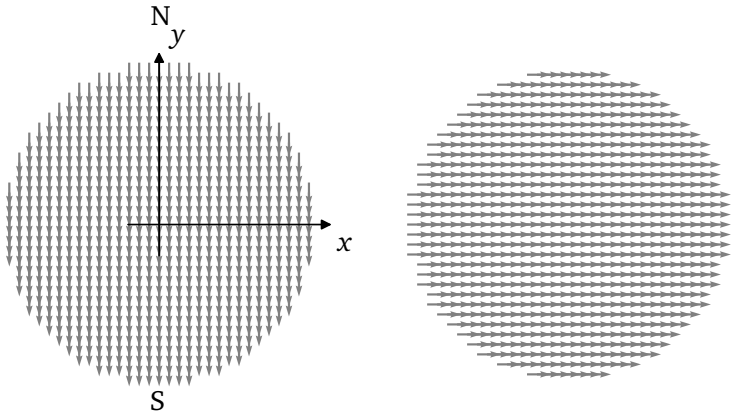

Figure 2.3: The magnetic field from a dipole (left), and the corresponding force experienced by a positively charged particle moving out of the plane (right). The grey arrows show the direction and magnitude of the fields.

it is clear that it is theoretically possible to create a perfect circular trajectory for a single particle using only dipole magnetic fields with a constant bending force. This is called the *reference orbit*. For a single particle, the reference orbit is achievable. However, when there are more particles, which is the case in the particle beam, the initial velocity and angle of the individual particles to the reference orbit are never perfect. Consequently, the axes of rotation for the particles are different, resulting in orbits not corresponding to the reference orbit [7]. If the difference between the particle orbit in one plane and the reference orbit is plotted, it gives a harmonically oscillating function called a *betatron oscillation*. The number of these oscillations around the machine is called the *tune*. Furthermore, assuming a vertical component in the particle's initial velocity, the resulting trajectory would be diverging spirals. This way, the particles would be lost, and no collisions would occur.

The solution is to add forces that control the movement of the particles by pushing and *focusing*[II] them closer to the reference orbit. This means that particles with a position further away from the reference are pushed with a greater force than particles located closer to the reference orbit. Such forces are obtained using quadrupole magnets, that is, magnets with four poles. An example of a normal quadrupole magnet field and the corresponding force fields in the vertical and horizontal direction is presented in Figure 2.4. The term normal refers to the orientation of the transverse magnetic field about the axis. In contrast, a skew magnetic field is rotated by 90 electrical degrees, for the quadrupole magnet meaning 45°mechanical rotation.

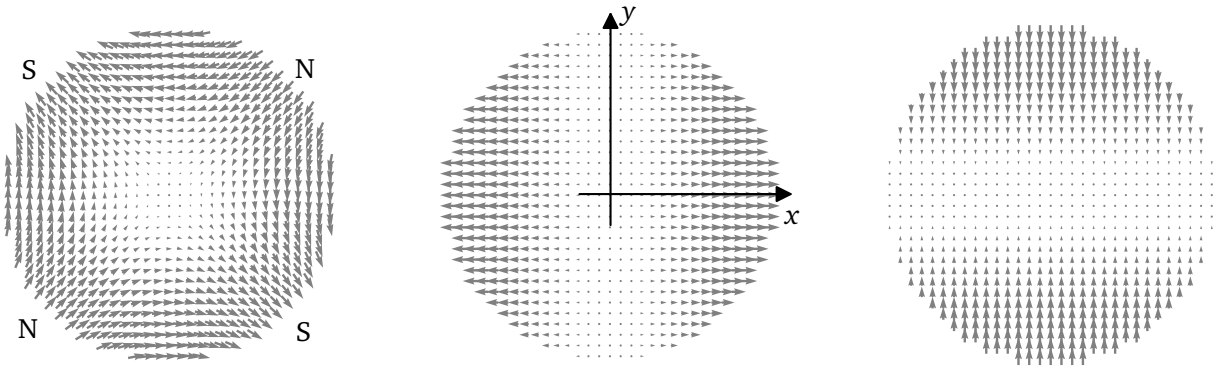

Figure 2.4: The magnetic field from a quadrupole magnet (left) and the corresponding force experienced by a positively charged particle moving out of the plane in the horizontal plane (center) and the vertical plane (right). All the field plots use the transversal coordinate system displayed in the central plot.

The rightmost force field in Figure 2.4 shows that the normal quadrupole exerts a force that focuses the particle towards the reference orbit in the vertical plane. It can also be shown that the field increases linearly from the axis, making the force stronger for particles further away from the reference orbit (assuming this corresponds to the axis, which by design it should). At the same time, as is seen in the central plot, the normal quadrupole defocuses particles in the horizontal plane. If, however, the quadrupole magnet is mechanically rotated by 90°, or simply with inverted polarity, the force fields are opposite:

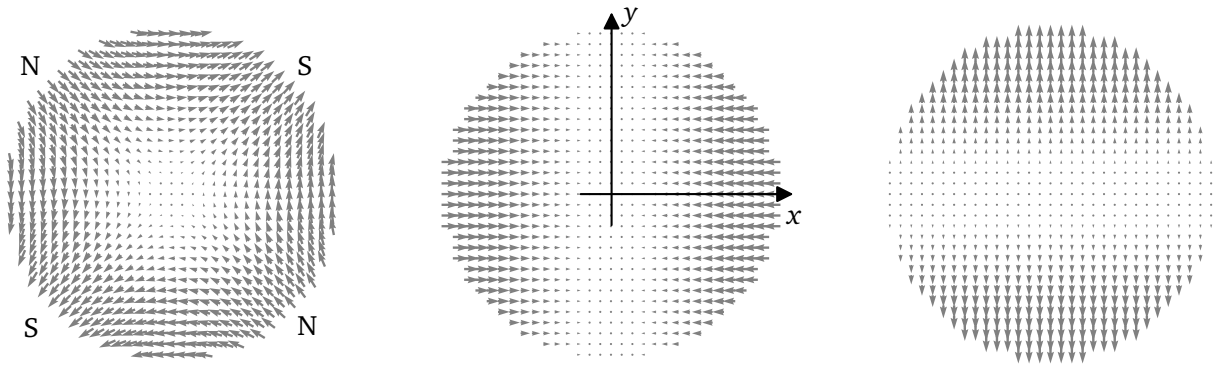

Figure 2.5: The magnetic field from a quadrupole magnet (left) and the corresponding force experienced by a positively charged particle moving out of the plane in the horizontal plane (center) and the vertical plane (right).

[II]The term focusing/defocusing refers to converging/diverging particle trajectories.

By convention, quadrupoles that focus the charged particles in the horizontal plane are called focusing quadrupoles, while those focusing in the vertical plane are referred to as defocusing quadrupoles. It is, therefore, impossible to achieve focusing in both planes with a single quadrupole. In circular charged particle accelerators, quadrupoles with alternating polarity are used in so-called Focusing-Defocusing-cells or *FODO-cells*. They consist of a focusing quadrupole and a defocusing quadrupole, with open spaces between them. The open spaces may contain drift spaces, bending dipoles or radio-frequency accelerator structures, as long as they do not affect the focusing of the particles. It can be shown that a FODO-cell has an overall focusing effect in both planes, given equally strong focusing and defocusing quadrupoles [6].

The general equation for the transverse motion of a particle moving through the circular accelerator can be described by the second order differential equation for the horizontal component:

$$x'' + k_{\mathrm{n}}(s)x = 0, \tag{2.2}$$

where $k_{\mathrm{n}}(s)$ is the normalized gradient of the magnet, expressing the normalized bending force of the magnet, depending on the position along the trajectory [6]. Assuming a harmonic oscillatory behavior, the resulting equations describing the horizontal position, $x(s)$, and angle, $x'(s)$, of the particle are given as

$$x(s) = \sqrt{\epsilon\beta(s)}\cos(\psi(s) - \phi), \tag{2.3}$$

$$x'(s) = \sqrt{\frac{\epsilon}{\beta(s)}}\sin(\psi(s) - \phi). \tag{2.4}$$

A similar expression is given for the position and angle in the vertical plane. In eqs. (2.3)-(2.4), the parameters ϵ and ϕ are constants dependent on the initial conditions, $\beta(s)$ is called the *beta function*, and $\psi(s)$ is the phase advance [6][7]. The two latter parameters are dependent on the focusing strength. Of the above-mentioned parameters, the beta function is of interest to our discussion about particle motion within the accelerator. When the particle moves through the FODO-cell, the angle and position of the amplitude can be described as an ellipsis in the phase-space plane, $x - x'$. When the beam moves through the FODO-cell, the cell can be approximated as a thin lens, where the deviation from the reference orbit oscillates with eqs. (2.3)-(2.4). This oscillation is shifted by 90° for the vertical plane, and from the equations, it is shown that the deviation is bound by the envelope given by $\mathrm{E}(s) = \sqrt{\epsilon\beta(s)}$ [6]. The working principle of the FODO-cell, along with the envelope for transverse particle movement in both planes, is shown in the figure below.

The discussion in this section assumes a rather ideal case, as discussed above. The field of beam optics includes several effects a lot more complicated than the ones discussed in this section. One such effect is found when there are longitudinal field components, for example the ones found in solenoids, or when there are skew quadrupoles in the machine. This causes so-called linear coupling, where a velocity along one axis causes an acceleration of the particle along the other axis. The effect of having skew quadrupole magnets in the machine is shown in the figure below. It is observed that a motion in the vertical direction causes a force to accelerate the particle in the horizontal direction and vice versa. It can be shown that this causes the betatron oscillations to oscillate back and forth between the transverse axes [7]. In the worst case, particles escape the vacuum chambers as the oscillatory behavior pushes the particles out. This reduces the number of particles in the accelerator, resulting in fewer collisions in the experimental areas. This is an unwanted effect, and it has to be corrected.

To conclude this section, dipole magnets guide the charged particles along the circular trajectory, giving a centripetal force. To contain the particles as closely as possible to the reference orbit, FODO-cells containing focusing and defocusing quadrupoles are used, resulting in an overall focusing in

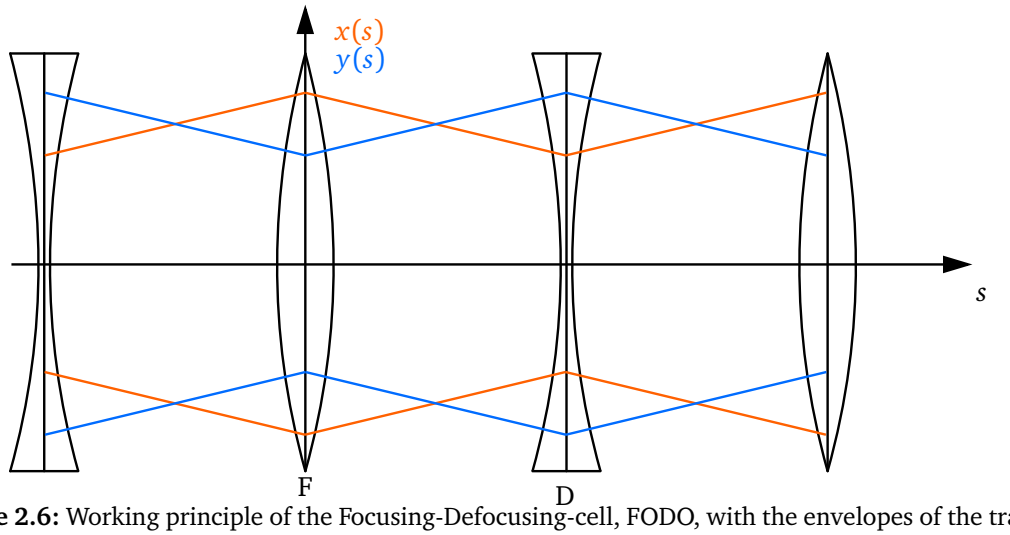

Figure 2.6: Working principle of the Focusing-Defocusing-cell, FODO, with the envelopes of the transverse oscillations of the particles about the reference orbit shown as orange and blue curves. The figure is taken from [6].

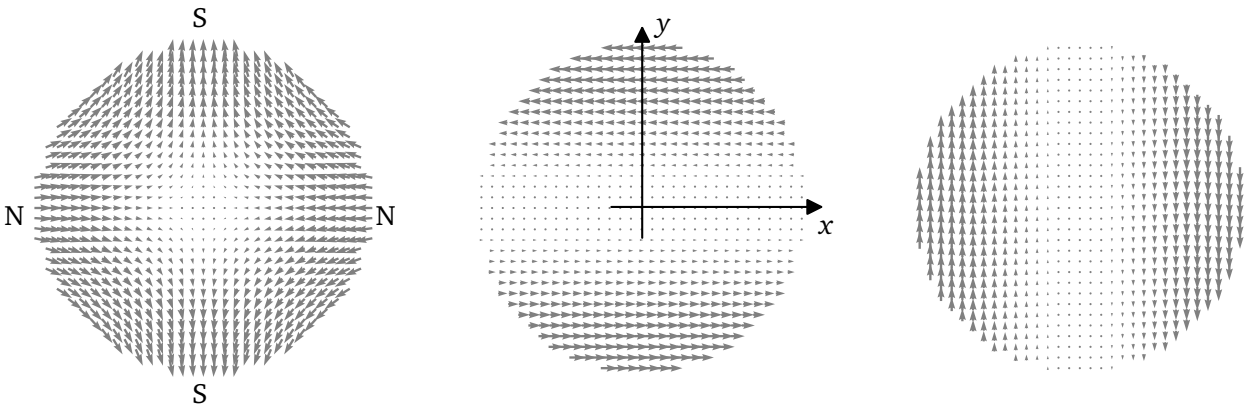

Figure 2.7: The magnetic field from a skew quadrupole magnet (left), and the corresponding force experienced by a positively charged particle moving out of the plane in the horizontal plane (center), and in the vertical plane (right).

both transverse directions. The beta function gives the deviation of the particles from the reference orbit along the accelerator. The beam oscillates and moves with betatron oscillations about the reference orbit but in a controlled manner. The section explains the use of magnets in charged particle accelerators, and it shows the importance of knowing the behavior of the magnetic field in the design and during the production, assembly, and operation of the accelerator.

2.2 Multipolar Description of the Transverse Magnetic Field

This section presents the multipolar description of the transverse magnetic field. It is included in this thesis, as accelerator magnets are usually characterized through their harmonic content, known as multipole components. The main correction strategy adopted for the High-Luminosity upgrade of the LHC is also based on cancelling certain multipole components, therefore knowing the underlying theory is of great importance. Furthermore, the theory presented in this section is used extensively in the development of the post-processing algorithms for the measurement systems, where the multipole components measured in displaced and rotated reference systems includes the necessary information to determine angular and transverse offsets.

2.2.1 Development of the multipolar expansion

This section shows how the magnetic flux density **B** under certain conditions can be described by a set of Fourier coefficients, known as *multipoles*. The derivation is based on the book *'Field Computation for Accelerator Magnets'* by S. Russenschuck [6] and the paper *'Basic Course on Accelerator Optics'* by J. Rossbach and P. Schmüser [8].

First, we consider smooth[III] scalar and vector fields, a prerequisite for the following treatment of Maxwell's equations. This description validates magnet areas where the longitudinal field component does not change. In practice, in central areas of the *aperture* of the magnet[IV]. The aperture is the opening going through the magnet along its longitudinal axis, surrounded by the magnetic poles, allowing the particles to pass through the magnetic field. The field can therefore be described in two dimensions by its transverse components. Furthermore, the area must be free of any charged particles or magnetic material. These conditions are generally met in accelerator magnets, as their length is usually longer than the diameter of the aperture and as long as one considers a disk in the cross-section of the aperture with a radius less than the shortest distance to any windings or iron. The domains considered, named Ω_i for the internal domain of the magnetic aperture, is presented in Figure 2.8 below. In the figure, the magnetic north pole is shown in the top right corner. Ω_i is free

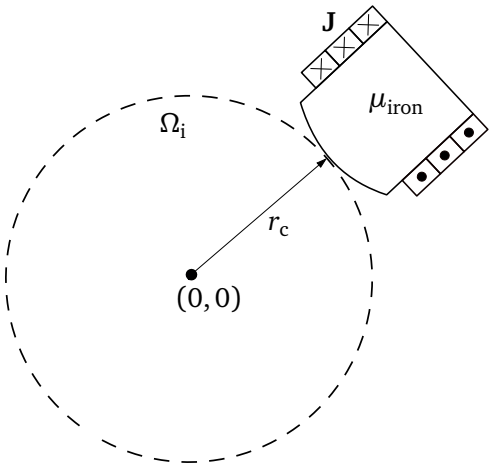

Figure 2.8: Valid domain for the development of the multipolar field description.

of any magnetic material and charged particles, as the iron and current density in the windings of the magnet are outside of the domain.

[III] The first and second derivatives of a function exist and are continuous [9].

[IV] In the end-regions of the magnet, so-called pseudo multipoles can be utilized to describe the magnetic flux density [10].

We start by looking at Ampère's and Gauss' laws in differential form

$$\text{curl}\,\mathbf{H} = \mathbf{J} + \frac{\partial \mathbf{D}}{\partial t}, \tag{2.5}$$

$$\text{div}\,\mathbf{B} = 0. \tag{2.6}$$

As we are dealing with high-conductivity material and relatively low frequencies, the displacement current can be neglected, $\partial\mathbf{D}/\partial t = 0$. This reduces eq. (2.5) to curl $\mathbf{H} = \mathbf{J}$. Furthermore, since we are looking at areas with no currents or magnetized material, the following holds for the curl and divergence of the magnetic flux density:

$$\text{curl}\,\mathbf{H} = 0, \tag{2.7}$$

$$\text{div}\,\mathbf{B} = 0. \tag{2.8}$$

From eq. (2.8) we can define a magnetic vector potential $\mathbf{A}$, where $\mathbf{B} = \text{curl}\,\mathbf{A}$, since the divergence of the curl of a vector always equals zero. From eq. (2.7) we define the magnetic vector potential ϕ_m, where $\mu\mathbf{H} = \nabla\phi_\text{m}$, or $\mathbf{B} = \nabla\phi_\text{m}$, since the curl of the gradient is also zero. The multipoles can be calculated through the Laplace equations from either of these expressions. However, in this thesis, we will use both the vector and scalar potential in the complex form to develop the equations through a Taylor expansion. For this reason, the longitudinal component, usually referred to as the z-component, will in this section be referred to as the s-component, since $z = x + iy$ refers to complex positions in the x-y-plane. This notation is in accordance with Figure 2.2. Since the complex form of multipole expansion is developed to ease the calculation of forces exerted on particles, adopting this reference system is convenient. This is also the most convenient way to work with the multipoles regarding magnetic measurements, where the reference system used for measurements does not necessarily correspond to the magnetic reference system when it comes to axes and rotation, as will be explained in subsection 2.2.2.

The coordinate system adopted for deriving the multipolar expansion is shown in Figure 2.9.

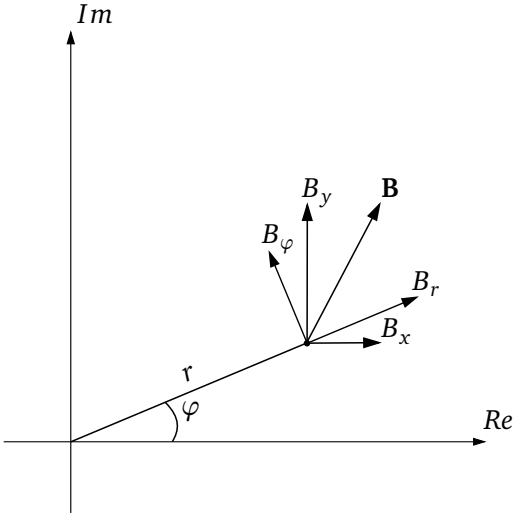

Figure 2.9: The coordinate system adopted for developing the two-dimensional multipolar description of the transversal magnetic field, fixed at the cartesian coordinate system. The cartesian and the polar transverse components are shown at a given point given by r and φ.

Expanding the expressions for $\mathbf{B}$ in $\mathbf{A}$ and ϕ_m yields:

$$\mathbf{B} = \text{curl } \mathbf{A} = \left(\frac{\partial A_\mathrm{s}}{\partial y} - \frac{\partial A_\mathrm{y}}{\partial s}\right)\mathbf{e}_\mathrm{x} + \left(\frac{\partial A_\mathrm{x}}{\partial s} - \frac{\partial A_\mathrm{s}}{\partial x}\right)\mathbf{e}_\mathrm{y} + \left(\frac{\partial A_\mathrm{y}}{\partial x} - \frac{\partial A_\mathrm{x}}{\partial y}\right)\mathbf{e}_\mathrm{s}, \tag{2.9}$$

$$\mathbf{B} = \nabla\phi_\mathrm{m} = \frac{\partial \phi_\mathrm{m}}{\partial x}\mathbf{e}_\mathrm{x} + \frac{\partial \phi_\mathrm{m}}{\partial y}\mathbf{e}_\mathrm{y} + \frac{\partial \phi_\mathrm{m}}{\partial s}\mathbf{e}_\mathrm{s}. \tag{2.10}$$

The expression for the curl of the magnetic vector potential is simplified by the fact that the vector potential only has a non-zero component in the longitudinal direction of the magnet. This can be shown by first inserting $\mu\mathbf{H} = \text{curl } \mathbf{A}$ into eq. (2.5), omitting the assumed constant μ in the notation

$$\text{curl } (\text{curl } \mathbf{A}) = \nabla(\text{div } \mathbf{A}) - \nabla^2\mathbf{A} = \mu\mathbf{J}. \tag{2.11}$$

Until this point, the divergence of $\mathbf{A}$ has not yet been defined. As long as the vector potential $\mathbf{A}$ fulfills curl $\mathbf{A} = \mathbf{B}$, it can be transformed in any way since it is the actual fields that decide the dynamics of the system[11]. Therefore, choosing $\mathbf{A}$ so that its divergence equals zero, the so-called *Coulomb gauge* simplifies eq. (2.11): Defining $\mathbf{A} = \mathbf{A}' + \nabla\gamma$, where curl $\mathbf{A}' = \mathbf{B}$ and $\nabla^2\gamma = -\text{div } \mathbf{A}'$ results in the following properties for $\mathbf{A}$:

$$\text{curl } \mathbf{A} = \text{curl } \mathbf{A}' + \text{curl } (\nabla\gamma) = \text{curl } \mathbf{A}' = \mathbf{B}, \tag{2.12}$$

$$\text{div } \mathbf{A} = \text{div } \mathbf{A}' + \text{div } \nabla\gamma = -\nabla^2\gamma + \nabla^2\gamma = 0, \tag{2.13}$$

fulfilling the requirements for the curl and the divergence of $\mathbf{A}$. Returning to eq. (2.11) it is now reduced to the Poisson equation, with the solution

$$\mathbf{A}(\mathbf{r}) = \frac{\mu}{4\pi}\int_{\mathscr{V}} \frac{\mathbf{J}(\mathbf{r}')}{|\mathbf{r}-\mathbf{r}'|}\mathrm{d}V', \tag{2.14}$$

where $\mathbf{r}$ is the position in space where we are investigating the vector potential, $\mathbf{r}'$ is the position vector of the current density, and $\mathscr{V}$ is the volume confining the current density [6]. Considering areas in the aperture of the magnet far from the end regions, it is clear that the current density only has an s-component. Thus, following eq. (2.14), so has the vector potential, that is $\mathbf{J} = J_s \Rightarrow \mathbf{A} = A_s$.

From this derivation, it is clear that the x- and y-component of the magnetic vector potential is zero, which in turn reduces eq. (2.9) to

$$\mathbf{B} = \text{curl } \mathbf{A} = \frac{\partial A_s}{\partial y}\mathbf{e}_\mathrm{x} - \frac{\partial A_s}{\partial x}\mathbf{e}_\mathrm{y}, \tag{2.15}$$

which, when compared to eq. (2.10) yields

$$\frac{\partial A_s}{\partial y} = \frac{\partial \phi_\mathrm{m}}{\partial x}, \tag{2.16}$$

$$-\frac{\partial A_s}{\partial x} = \frac{\partial \phi_\mathrm{m}}{\partial y}. \tag{2.17}$$

Eqs. (2.16) and (2.17) are the Cauchy-Riemann equations for a complex function $w(z)$ given as

$$w(z) = A_s(x,y) + i\phi_\mathrm{m}(x,y), \tag{2.18}$$

where $z = x + iy$ is the complex number. In complex analysis a complex function $f(z) = u(x,y) + iv(x,y)$ is said to be complex analytic, or *holomorphic*, if its four partial derivatives, u_x, u_y, v_x, v_y

exist and are continuous throughout a domain $\mathscr{D}$, and if there exist a unique limit of $\mathrm{d}f/\mathrm{d}z|_{z_0}$ that is independent of the direction of Δz approaching a given point z_0 [6] [9]. This means that to analyze the complex function by its derivatives, the partial derivatives must exist in all directions. Furthermore, the derivative must be equal for the same point in space when approached from any direction. If the former holds, then the latter expression, equivalent to the Cauchy-Riemann equations, is sufficient to show that a function is holomorphic. As we only consider smooth vector fields and scalar potentials, the complex potential $w(z)$ in eq. (2.18) consists of smooth scalar functions A_s and ϕ_m, fulfilling the requirements above. Furthermore, we know that $w(z)$ gives the Cauchy-Riemann equations. Thus, the complex potential is a holomorphic function. With this established, complex analysis tells us that the complex potential can be expressed by its Taylor expansion around the origin of our domain:

$$w(z) = \sum_{n=0}^{\infty} \mathscr{C}_n \cdot z^n = \sum_{n=0}^{\infty} (\mathscr{B}_n + i\mathscr{A}_n) \cdot z^n, \tag{2.19}$$

with $A_\mathrm{s} = \mathrm{Re}(w(z))$ and $\phi_\mathrm{m} = \mathrm{Im}(w(z))$. From the complex analysis, we know that this expression converges for all z inside a circle, where $|z| < r_c$, and r_c is the smallest distance to the iron boundary of the domain, seen in Figure 2.8.

For the further development of the multipoles, it is convenient to change from complex to cylindrical notation, using $x = r\cos\varphi$, $y = r\sin\varphi$, where r and φ are shown in Figure 2.9. This gives:

$$z^n = (x+iy)^n = r^n(\cos\varphi + i\sin\varphi)^n = r^n(\cos n\varphi + i\sin n\varphi) = (re^{i\varphi})^n, \tag{2.20}$$

where the third step uses De Moivre's theorem. Inserting this into eq. (2.19), gives

$$w(r,\varphi) = \sum_{n=0}^{\infty} r^n(\mathscr{B}_n + i\mathscr{A}_n)(\cos n\varphi + i\sin n\varphi) = \sum_{n=0}^{\infty} r^n[(\mathscr{B}_n\cos n\varphi - \mathscr{A}_n\sin n\varphi) + i(\mathscr{B}_n\sin n\varphi + \mathscr{A}_n\cos n\varphi)], \tag{2.21}$$

yielding:

$$A_s(r,\varphi) = \mathrm{Re}(w(r,\varphi)) = \sum_{n=0}^{\infty} r^n(\mathscr{B}_n\cos n\varphi - \mathscr{A}_n\sin n\varphi), \tag{2.22}$$

$$\phi_\mathrm{m}(r,\varphi) = \mathrm{Im}(w(r,\varphi)) = \sum_{n=0}^{\infty} r^n(\mathscr{A}_n\cos n\varphi + \mathscr{B}_n\sin n\varphi). \tag{2.23}$$

The magnetic flux density can now be expressed as the curl of the magnetic vector potential

$$B_r(r,\varphi) = \frac{1}{r}\frac{\partial A_s}{\partial \varphi} = \sum_{n=1}^{\infty} r^{n-1}n(-\mathscr{B}_n\sin n\varphi - \mathscr{A}_n\cos n\varphi), \tag{2.24}$$

$$B_\varphi(r,\varphi) = -\frac{\partial A_s}{\partial r} = -\sum_{n=1}^{\infty} r^{n-1}n(\mathscr{B}_n\cos n\varphi - \mathscr{A}_n\sin n\varphi). \tag{2.25}$$

To simplify the expressions for the Fourier coefficients in the next stage, we define the new constants $\mathcal{D}_n = -\mathscr{A}_n$ and $\mathcal{E}_n = -\mathscr{B}_n$. This changes the expressions for the radial and azimuthal components of

the flux density to

$$B_r(r,\varphi) = \sum_{n=1}^{\infty} r^{n-1} n(\mathcal{D}_n \cos n\varphi + \mathcal{E}_n \sin n\varphi), \tag{2.26}$$

$$B_\varphi(r,\varphi) = -\sum_{n=1}^{\infty} r^{n-1} n(\mathcal{D}_n \sin n\varphi - \mathcal{E}_n \cos n\varphi). \tag{2.27}$$

In Eqs. (2.26) and (2.27) each integer value of n corresponds to the specific flux density components created by ideal magnetic geometries, where $n = 1, 2, 3$ correspond to ideal dipole, quadrupole and sextupole flux density distribution.

The field harmonics $\mathcal{D}_n$ and $\mathcal{E}_n$ in Eqs. (2.26) and (2.27) can now be determined in several ways. The most common is to compare the coefficients in Eqs. (2.26) and (2.27) to the coefficients in the Fourier series expansion of either simulated or measured radial field component B_r along a circular trajectory around the circumference of the magnet's aperture with a radius r_0. The Fourier expansion is expressed as

$$B_r(r_0,\varphi) = \sum_{n=1}^{\infty} (B_n \sin n\varphi + A_n \cos n\varphi), \tag{2.28}$$

$$B_\varphi(r_0,\varphi) = \sum_{n=1}^{\infty} (B_n \cos n\varphi - A_n \sin n\varphi), \tag{2.29}$$

where the Fourier coefficients are calculated as follows

$$A_n = \frac{1}{\pi} \int_0^{2\pi} B_r(r_0,\varphi) \cos n\varphi \mathrm{d}\varphi, \tag{2.30}$$

$$B_n = \frac{1}{\pi} \int_0^{2\pi} B_r(r_0,\varphi) \sin n\varphi \mathrm{d}\varphi, \tag{2.31}$$

where $A_0(r_0) = 1/\pi \int_0^{2\pi} B_r(r_0,\varphi)\mathrm{d}\varphi = 0$ since B_r is divergence-free.

When measuring the magnetic field, for instance with a rotating coil, the signal is not continuous, but instead sampled at N discrete points on the interval $[0, 2\pi)$, where $\varphi_k = 2\pi k/N$ for k = 0,1,2,...,$N-1$. It can be shown that the Fourier coefficients can be calculated by the Discrete Fourier Transform (DFT) [6][12]:

$$A_n(r_0) \approx \frac{2}{N} \sum_{k=0}^{N-1} B_r(r_0,\varphi_k) \cos n\varphi_k, \tag{2.32}$$

$$B_n(r_0) \approx \frac{2}{N} \sum_{k=0}^{N-1} B_r(r_0,\varphi_k) \sin n\varphi_k. \tag{2.33}$$

Comparing Eqs. (2.26) and (2.27) to Eqs. (2.28) and (2.29) we get the expressions for the field harmonics as

$$A_n = n r_0^{n-1} \mathcal{D}_n, \tag{2.34}$$

$$B_n = n r_0^{n-1} \mathcal{E}_n. \tag{2.35}$$

$B_n(r_0)$ and $A_n(r_0)$ are called the *normal* and *skew multipole coefficients*, and they are given in units of tesla at the reference radius r_0. For a real, non-ideal, $2N$-pole magnet, the main component will be

that of order N. However, there will also be components of higher and lower magnetic orders $n \neq N$, usual orders of magnitude lower. For this reason, it is common to express the multipole coefficients relative to the main normal component, which is achieved by dividing all B_n, A_n by B_N. Furthermore, the multipole coefficients can be scaled to any $r < r_c$ by multiplying the expressions in Eqs. (2.28) and (2.29) by $(r/r_0)^{n-1}$. The resulting expressions for the flux density components are given in the equations below:

$$\begin{aligned} B_r(r,\varphi) &= \sum_{n=1}^{\infty} \left(\frac{r}{r_0}\right)^{n-1} (B_n(r_0)\sin n\varphi + A_n(r_0)\cos n\varphi) \\ &= B_N \sum_{n=1}^{\infty} \left(\frac{r}{r_0}\right)^{n-N} (b_n(r_0)\sin n\varphi + a_n(r_0)\cos n\varphi), \end{aligned} \tag{2.36}$$

$$\begin{aligned} B_\varphi(r,\varphi) &= \sum_{n=1}^{\infty} \left(\frac{r}{r_0}\right)^{n-1} (B_n(r_0)\cos n\varphi - A_n(r_0)\sin n\varphi) \\ &= B_N \sum_{n=1}^{\infty} \left(\frac{r}{r_0}\right)^{n-N} (b_n(r_0)\cos n\varphi - a_n(r_0)\sin n\varphi). \end{aligned} \tag{2.37}$$

To finalize the derivation of the multipoles, we transform the equations back to a complex form. It can be seen from Figure 2.9 that the transformation from polar to complex cartesian coordinates is obtained in the following manner: $B_x = B_r\cos\varphi - B_\varphi\sin\varphi$, $B_y = B_r\sin\varphi + B_\varphi\cos\varphi$, or in complex form as $B_y + iB_x = (B_\varphi + iB_r)e^{-i\varphi}$ [V]. Writing out these equations, we get

$$\begin{aligned} B(z) := B_y + iB_x &= \sum_{n=1}^{\infty} (B_n(r_0) + iA_n(r_0)) \left(\frac{r}{r_0}\right)^{n-1} e^{i(n-1)\varphi} \\ &= \sum_{n=1}^{\infty} (B_n(r_0) + iA_n(r_0)) \left(\frac{re^{i\varphi}}{r_0}\right)^{n-1} \\ &= \sum_{n=1}^{\infty} C_n(r_0) \left(\frac{z}{r_0}\right)^{n-1}, \end{aligned} \tag{2.38}$$

where the identity in the last step is found using eq. (2.20), and the complex multipole coefficient $C_n = B_n + iA_n$ is introduced. It is worth noting that even though writing $B_y + iB_x$ instead of $B_x + iB_y$ might be counter-intuitive in the way we are used to defining a complex number, with its real and imaginary part as the cartesian x and y, respectively, inserting the opposite would result in $C_n = A_n + iB_n$, which is not in correspondence with the convention of normal and skew components as the real and imaginary part of the complex coefficients.

The magnetic flux density in an ideal decapole, $B_y + iB_x = C_5(z/r_0)^4$, is shown in Figure 2.10 below.

2.2.2 Flux measurements in rotated and displaced coordinate systems

With the theory of the multipolar expansion of the magnetic flux density, it is possible to calculate the **B**-field in coordinate systems displaced, both translated and rotated, with respect to the "true" magnetic reference system. This is of interest to us since it is rarely the case that the measurements are conducted on an axis perfectly corresponding to the magnetic axis and with the same azimuthal

[V] $B_y + iB_x = B_r(\sin\varphi + i\cos\varphi) + B_\varphi(\cos\varphi - i\sin\varphi) = (B_r e^{i\pi/2} + B_\varphi)e^{-i\varphi} = (B_\varphi + iB_r)e^{-i\varphi}$

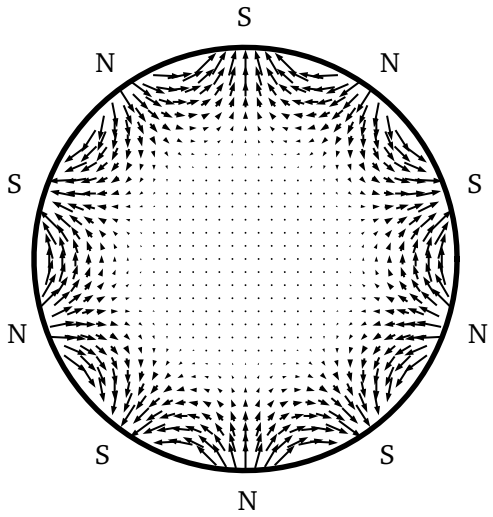

Figure 2.10: Flux density of an ideal normal decapole magnet, with S and N indicating the magnetic south and north poles.

angle. This can be the caused by less precise mechanical measurements of the magnet and the measurement system, saggita effects of the measurement system, and imperfections in the magnet itself. This section provides the theoretical basis for understanding the observable effects of such a misalignment when measuring the flux density and how these effects are treated to find the correct field components in the magnetic reference frame.

Furthermore, these effects are utilized to calculate the displacement and rotation of the mechanical reference system of the magnet with respect to the magnetic reference system, which is of key importance for the construction, installation, and operation of the magnets, as will be discussed in section 2.3. Lastly, the equations and theory developed in this section will be used extensively in the development of the measurement campaign and treatment of measurement data in this thesis.

Definitions

In the following, a few definitions used extensively throughout this thesis are given.
Magnetic axis:
The magnetic axis can be defined in the following manner: "*For all 2n-pole magnets except dipoles, the magnetic axis is defined as the locus of points along which the 2(n–1) pole terms are zero*" [13]. This comes from the fact that the gradient of the magnetic flux density, that is $\mathrm{d}B_y/\mathrm{d}x$ and $\mathrm{d}B_x/\mathrm{d}y$, of a $2n$-pole magnet, is an *(n-1)*-degree term, and at the center of the magnet, this is zero. It is not the same as saying the magnetic flux density is zero in the center of the magnet, as there can be other error terms of a lower order, for instance, a dipole error in a sextupole magnet, but the gradient of the primary term is zero in the magnetic axis.

Furthermore, following the definition, the center of the magnet does not have to be uniform along the s-axis of the magnet due to imperfections and errors introduced in the production of the magnet. However, as we are primarily interested in the integral values of the magnet, we regard the magnet as having a single axis following a straight line.

Roll, yaw, and pitch angles:
The so-called *Tait-Bryan angles* is a set of angles frequently used in literature to describe a body's

orientation in space, stemming from aeronautics [6]. They describe the *roll, yaw*, and *pitch* angles, which are the angles used to describe the different kinds of rotation essential to the alignment of electromagnets in the accelerator complex. They are also essential parameters to the magnetic measurements presented in this thesis, not only in the rotation of the measured magnets but also in the alignment of the measurement equipment.

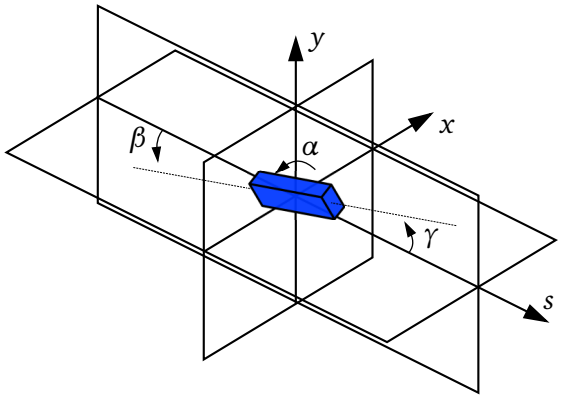

Figure 2.11: Definitions of the angles roll, α, yaw, β, and pitch, γ, used throughout this thesis, as described in [6].

The angles are shown in Figure 2.11, and in this thesis, the angles are named in the following manner; α is the roll angle, β is the yaw angle, and γ is the pitch angle. The roll angle represents a rotation about the central axis of the body. For a magnet, this means rotation about its longitudinal axis, and the result is an observed phase shift of the magnetic flux density as a function of azimuthal angle. The yaw angle represents a rotation of the body about the y-axis, a rotation in the x-s-plane in Figure 2.11. For a magnet, this is the angle between the s-axis of the accelerator in any given point to the x-component of the longitudinal axis of the magnet, or more easily as the "sideways" orientation of the magnet to the s-axis. Lastly, the pitch angle is the rotation of a body to the x-axis shown in Figure 2.11. For an accelerator magnet, this is the angle between the s-axis and the y-component of the longitudinal axis of the magnet, or the tilt it makes to the s-axis.

It is mainly the roll angle that is of interest in this thesis, as the roll angle of the corrector magnets is to be measured. Therefore, a few notes on the calculation of the roll angle are given in the following:

The roll angle of a magnet is found through the main field phase of the signal, calculated directly from the main normal and skew multipole component. The main field phase, defined on the interval $[-\pi/2, \pi/2]$, is given by the relation

$$e^{i\varphi_N} = \frac{B_N - iA_N}{|C_N|}, \tag{2.39}$$

and it is calculated as

$$\cos\varphi_N = \frac{B_N}{|C_N|}, \tag{2.40}$$

$$\sin\varphi_N = -\frac{A_N}{|C_N|}, \tag{2.41}$$

and it is then bound to the interval $[-\pi/2, \pi/2]$ to give a unique definition [14]. This is done by either adding or subtracting π from the angle if it is either less than $-\pi/2$ or greater than $\pi/2$. From

φ_N, the roll angle is found as

$$\alpha = \frac{\varphi_N}{N}, \tag{2.42}$$

where N is the main multipole component. The last step is important to refer the angle from the magnetic reference system to the mechanical reference system, since an n-pole magnet contains n magnetic poles periods per mechanical revolution. The roll angle is defined so that a physical rotation of the magnet by $-\alpha$ makes the field purely normal.

When the field phase is bound to the interval $[-\pi/2, \pi/2]$, it is referred to as the closest pole of the magnet. Therefore, the magnet's polarity could be affected, and a check of this would be required. For example, if a quadrupole magnet is rotated by 45°±1°, the roll angles measured would be ∓44°. In the rest of the thesis, a subscript will be added, α_{roll}, to highlight that the roll angle is meant.

Magnetic length:
The bending angle of the dipoles guiding the particles is slight compared to the magnets' length, and the magnets' length is usually a lot shorter than the period of the betatron oscillations. Consequently, to the particles, the magnets can be regarded as a constant value multiplied by the magnetic length of the magnet and zero elsewhere. This is called the *hard-edge model* and is an approximation often used in the fields of accelerator magnets. Therefore, magnetic measurements are mainly concerned with measuring the integrals of the magnetic field and its derivatives [15] [16].

The magnetic length, or effective length as it is also called, is defined as

$$L_m = \frac{1}{B_0}\int_{s=-\infty}^{\infty} B\mathrm{d}s, \tag{2.43}$$

where B_0 is the field in the longitudinal center of the magnet.

Measured multipoles in a displaced reference system

Assuming the displacement parallel to the magnetic axis, we can derive the relation between the measured multipole components and the actual components as seen from the magnetic axis. This will also enable us to calculate the offset from the axis from our measured harmonic components. The derivation of these equations is based on the material presented in reference [6] and [17].

The coordinate systems used for the derivation are shown in Fig. 2.12, displaying the coordinate system with the magnetic axis in origin, x'-y', and the coordinate measurement system, x-y, off-centered from the magnetic axis by $z_d = x_d + iy_d$. The displacement results in the following $x = x' + x_d$ and $y = y' + y_d$. As shown in the figure, the measured magnetic flux density in the point of the x'-y' coordinate system is the same flux density given in the x-y coordinate system for the same point. Using the complex form of the multipole magnetic flux density developed in Section 2.2.1, we get the following expression

$$B_{y'} + iB_{x'} = \sum_{n=1}^{\infty} C_n'\left(\frac{z'}{r_0}\right)^{n-1} = \sum_{n=1}^{\infty} C_n\left(\frac{z'+z_d}{r_0}\right)^{n-1} = B_y + iB_x. \tag{2.44}$$

The third term of eq. 2.44 can be expressed using the binomial expansion

$$\left(\frac{z'+z_d}{r_0}\right)^{n-1} = \sum_{k=1}^{n}\binom{n-1}{k-1}\left(\frac{z'}{r_0}\right)^{k-1}\left(\frac{z_d}{r_0}\right)^{n-k}, \tag{2.45}$$

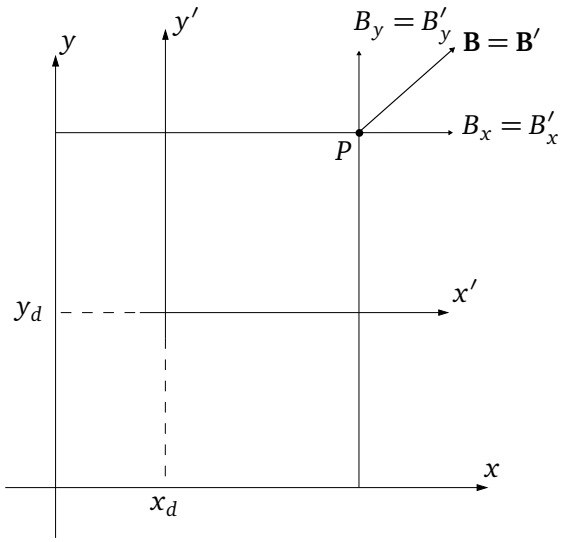

Figure 2.12: Coordinate system fixed at the magnetic axis, x'-y', with the displaced coordinate system with the measurement center in origin, x-y. The displacement of the magnetic axis with respect to the measurement axis is given as $z_d = x_d + iy_d$. The magnetic flux density at point P is also displaced.

where the binomial coefficient can be expressed as

$$\binom{n-1}{k-1} = \frac{(n-1)!}{(k-1)!(n-k)!}. \tag{2.46}$$

Inserting eqs. (2.46) and (2.45) into eq.(2.44), the following expression for the flux density is obtained

$$\sum_{n=1}^{\infty} C_n \left(\frac{z' + z_d}{r_0}\right)^{n-1} = \sum_{n=1}^{\infty} C_n \sum_{k=1}^{n} \frac{(n-1)!}{(k-1)!(n-k)!} \left(\frac{z'}{r_0}\right)^{k-1} \left(\frac{z_d}{r_0}\right)^{n-k}. \tag{2.47}$$

Rearranging the terms[VI] yields

$$B_{y'} + iB_{x'} = \sum_{k=1}^{\infty} \sum_{n=k}^{\infty} C_n \frac{(n-1)!}{(k-1)!(n-k)!} \left(\frac{z_d}{r_0}\right)^{n-k} \left(\frac{z'}{r_0}\right)^{k-1}, \tag{2.48}$$

which, when compared to eq. 2.44, finally gives the influence of the displacement on the measured multipole coefficients

$$C'_k = \sum_{n=k}^{\infty} C_n \frac{(n-1)!}{(k-1)!(n-k)!} \left(\frac{z_d}{r_0}\right)^{n-k}. \tag{2.49}$$

Feed-down

Expanding the first few terms of eq. (2.49) gives

$$C'_k = C_k + C_{k+1}\, k \left(\frac{z_d}{r_0}\right) + C_{k+2}\, \frac{k(k+1)}{2} \left(\frac{z_d}{r_0}\right)^2 + \ldots \tag{2.50}$$

We observe that a displacement of the measurement axis from the magnetic axis gives measured multipole coefficients containing lower-order components. This means that all higher-order components in the magnet reference frame contribute to all harmonics of equal or lower order in the

[VI] $\sum_{n=1}^{\infty} \sum_{k=1}^{n} t_{nk} = \sum_{k=1}^{\infty} \sum_{n=k}^{\infty} t_{nk}$

displaced reference system, a phenomenon referred to as *feed-down*. This is utilized for localization of the magnetic axis, as will be discussed in the following section.

Calculation of displacement

Assuming both that the displacement of the axis is much smaller than the reference radius within the aperture of the magnet, $z_d/r_0 << 1$, and that the higher order terms are small, we truncate eq. (2.49) after the linear term in z_d. The development of the equations for calculating the displacement of the measured axis is based on the fact that in the center of the magnet, the gradient of the main field component is zero. Using eq. (2.49) for the $(k-1)^{\text{th.}}$ multipole coefficient, gives

$$C'_{k-1} = 0 \approx C_{k-1} + (k-1)C_k\left(\frac{z_d}{r_0}\right), \tag{2.51}$$

which, when rearranging the terms, yield the following expression for the displacement of the magnetic axis

$$z_d = -\frac{r_0}{k-1}\frac{C_{k-1}}{C_k}. \tag{2.52}$$

Measured multipoles in a rotated reference system

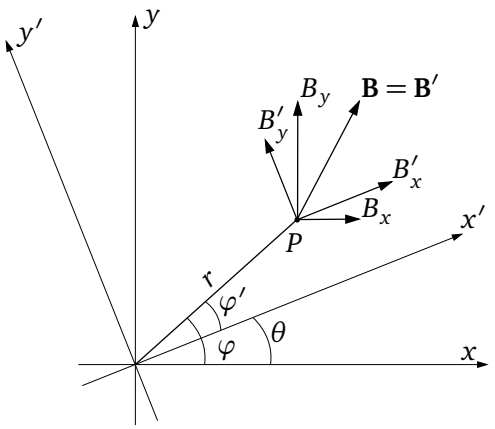

Figure 2.13: Concentric coordinate systems x-y and x'-y' used to develop flux density components in rotated coordinate systems. The system of x'-y' is rotated by an angle θ with respect to x-y-system. This gives a rotation of the components of the B-field at a point P.

The **B**-field at a point P in concentric coordinate systems x-y and x'-y', where the latter is rotated by an angle θ with respect to the former, is shown in Figure 2.13. Following the same procedure for rotation of coordinates as was shown in the conversion between the complex and the cylindrical representation of the multipoles in subsection 2.2.1, however, with a rotation in the counter-clockwise direction instead of a clockwise rotation[VII], we have the following identities for the coordinates:

$$z = re^{i\varphi},$$
$$z' = re^{i\varphi'} = re^{i(\varphi-\theta)} = re^{i\varphi}e^{-i\theta} = ze^{-i\theta},$$

[VII] The difference gives the opposite sign of angle.

and for the field components, we have

$$\left.\begin{aligned} B_{x'} &= B_x \cos\theta + B_y \sin\theta \\ B_{y'} &= -B_x \sin\theta + B_y \cos\theta \end{aligned}\right\} \mathbf{B}(z') = B_{y'} + iB_{x'} = \big(B_y + iB_x\big)e^{i\theta} = \sum_{n=1}^{\infty} C_n(r_0)\left(\frac{z}{r_0}\right)^{n-1} e^{i\theta}. \quad (2.53)$$

With this, the multipolar expansion of the **B**-field in the rotated coordinate system is written as

$$\mathbf{B}(z') = \sum_{n=1}^{\infty} C'_n(r_0)\left(\frac{z'}{r_0}\right)^{n-1} = \sum_{n=1}^{\infty} C'_n(r_0)\left(\frac{ze^{-i\theta}}{r_0}\right)^{n-1} = \sum_{n=1}^{\infty} C'_n(r_0)\left(\frac{z}{r_0}\right)^{n-1} e^{i\theta}e^{-in\theta}, \quad (2.54)$$

which, when compared to eq. (2.53) gives the transformation of the multipole coefficients following a rotation of the reference system:

$$C'_n(r_0) = C_n(r_0)e^{in\theta}. \quad (2.55)$$

From derivation, it is clear that a mechanical rotation by θ degrees of the magnet results in a rotation of the magnetic multipoles of $n\theta$.

2.3 Magnets in Particle Accelerators

2.3.1 Multipole field theory in accelerator magnets

Up until this point, the magnetic fields discussed have been purely theoretical and ideal. In this section, the generation of magnetic fields are discussed briefly, both theoretical and in practice. This will show the necessity of corrector magnets in charged particle accelerators, and more specifically the corrector magnets used in the High-Luminosity upgrade of the LHC.

There are several ways of creating the magnetic fields used in charged particle accelerators. In this thesis, the focus will be on electromagnets, where current distributions are used to set up magnetic fields, according to Ampère's law, eq. (2.5).

To this end, there are two main ways of creating the desired magnetic field; there are magnets where the iron yoke determines the field shape, so-called *iron-dominated magnets*, and there are magnets where the geometry of the windings create the desired flux density, so-called *coil-dominated magnets*. The distinction between the two is the ratio of the field set up by the current to the reduced field from the magnetization of the iron.

In the iron-dominated magnets, the field shape is mainly determined by the geometry of the iron core between the coils. When the current flows in copper or aluminum wires, the magnets are named *normal conductive* magnets, operated at room temperature and usually cooled by flowing water. If superconductive technology is used, the magnets are called *superferric*. In this case, even though the iron yoke might be slightly saturated the field shape is determined by the iron geometry, whilst the field strength is given by a high current density made possible by superconductive technology.

Similarly, coil-dominated magnets can be of both normal conductive and superconductive types. The superconductive coil-dominated magnets are simply calles *superconductive* magnets.

The maximum achievable momentum for the particles in a particle accelerator is, for a given radius of the accelerator, proportional to the bending force given from the dipoles. For the Large Hadron Collider at CERN, LHC, superconductive dipoles are used with nominal magnetic fields of 8.33 T, allowing for energies up to 7 TeV. If normal conductive magnets were used, the required circumference of the accelerator to achieve the same energy as above would be 100 km, as opposed to the 27 km by the use of superconductive bending dipoles [6].

From the flux density created from a long, straight wire it can be shown , by the principle of superposition, that an ideal multipole component can be created by a current distribution given by

$$I(\theta_0) = I_0 \cos(n\theta_0 - \phi), \tag{2.56}$$

on a section of a cylindrical surface, with azimuthal position θ_0. In the equation, ϕ is the angle of the current distribution on the surface and I_0 is the amplitude of the current. By integrating eq. (2.56) over θ, that is along the circumference of the cylinder, it can be shown that the ideal magnetic multipole component of order n is created. If the angle of the current along the cylinder is either 0°of 180°, a normal multipole component is achieved, whilst with an angle of 90°, a skew component is induced [11].

Similarly, it can be shown that an ideal multipole can be created by shaping a material with infinitely high permeability such that the surface follows the parametric curve given by

$$r^n \sin(n\theta - \phi_n) = r_0^n. \tag{2.57}$$

In the equation, θ is the azimuthal angle in the cross-section of the magnet, ϕ_n is the roll angle of the magnetic multipole, n is the ideal multipole component, and r_0 is the minimum distance between the origin of the magnet aperture and the highly permeability material [11].

Of the presented equations above, it is clear that it is theoretically possible to create an ideal multipole field of order n using either an optimally shaped iron yoke, or by creating an ideal current distribution on the surface of a thin conductive cylinder. However, in practice, this is not achievable, as it requires infinite extent of the magnet in the longitudinal direction, infinite permeability and current distributions purely on the surface of a cylinder. Real accelerator magnets therefore consist of a superposition of an infinite number of multipole fields.

Then, there is a distinction between the designed and produced magnet. In the design phase of the magnet, one still has to consider the practical restraints presented above. Even so, the magnetic field at this stage can still be considered ideal, all the time the higher-order multipole components can be simulated, and their effects mitigated through optimal design. The resiudals from the higher-order field components are so-called *systematic* multipole errors. In the fabricated magnets, there will be additional errors stemming from imperfections in the construction and assembly of the magnets. This means that even though two magnets have the same design, thus the same systematic error, they will differ slightly. These errors are called *random* multipole errors, and are impossible to predict in the design phase. Therefore, the design, production and assembly of the magnets for the accelerator complex are conducted in parallel, to adjust and account for errors in the different phases.

The systematic errors in the design phase of the accelerator magnets can, if designed properly, only be composed of certain multipole components. This stems from the fact that for an ideal multipole of order n, rotation of the magnet by π/n results in a change of polarity of the magnet. In the design of the magnets, where the geometry is usually symmetrical, all higher-order multipole components must follow the same rotational anti-symmetry as the main component. The higher-order multipoles obeying this relation are named *allowed* multipoles. It can therefore be shown that the allowed multipoles of order m in a magnet of designed order n are given by the relation $m/n = 3, 5, 7, ...$, when considering $m \neq n$. The *forbidden* multipole components are usually generated by imperfections in the fabrication phase, and are usually dominated by the allowed multipoles [11].

Magnetic field correction

From the theory presented in section 2.1, it is clear that the fields of the accelerator magnets play a crucial role in the movement of the charged particles along the accelerator complex. Furthermore, any errors to the magnetic field is clearly a problem to the operation of the accelerators. For example, a slight misalignment of a quadrupole focusing magnet from its nominal position, will result in too high a focusing force in one plane, and too large a defocusing force in the other plane. These effects are accumulated as the particles undertake more laps of the accelerator, and could result in an unstable operation of the particle beam, and at least reduce the amount of collisions. Other unwanted effects could be deviations in the roll angles of the magnets and higher-order multipoles added due to imperfections in the production phase. This would cause linear coupling in the case of a skew quadrupole, as discussed in section 2.1 and shown in Figure 2.7. Unwanted multipole components change the gradient of the field, affecting the particle's motion, given by eqs. (2.3) and (2.4).

From the discussion about accelerator magnets in the previous section, it is clear that additional higher-order multipole components are inevitable when designing and producing accelerator magnets, both allowed and forbidden. Furthermore, the installation of the magnets also cause imperfections in the magnetic field following the design orbit, as misalignment and mechanical stress occur [15] [11]. Therefore, actions are taken to mitigate these effects. One way to reduce such errors, is to optimize the design of each magnet. This reduces the magnitude of the allowed multipoles, hence reducing their effect. However, random errors are still introduced by production and install-

ation of the magnets. Furthermore, the cost might exceed the gained field quality. If the field of the individual magnets are known, properly sorting the magnets along the azimuth of the accelerator is shown to significantly reduce the error. The use of shims, very thin strips of metal placed in the aperture and between the coils, are also proven to reduce measured imperfections in the fields of accelerator magnets [18].

In addition to the above-mentioned measures, sets of corrector magnets are used to counteract the effects of field errors. They are also used to fine-tune the local beam orbit or the focusing, which is impossible using the main quadrupole magnets, as they are powered in large families of magnets. As the design of magnets perfectly correcting each error in the main magnets is not feasible, the corrector magnets consist of arrays of magnets with higher order. In an integral manner, this accounts for imperfections in field experienced by the particles. Dipole correctors are usually applied for adjusting the necessary bending force, while higher-order magnets are used for field corrections [19]. Other magnetic configurations are also used, where for instance both quadrupoles and solenoids are used to reduce the effects of linear coupling, as discussed in section 2.1. Lastly, there are many configurations of the corrector magnets, as there are approximately 6500 corrector magnets in the LHC; some are attached to the magnets of which they are correcting field errors, and some are collected in assemblies, or corrector packages. For the next upgrade of the LHC, the corrector packages at the intersection point will be upgraded, as discussed in the following section.

2.3.2 The High-Luminosity upgrade for the LHC

The luminosity of a collider is, for a Gaussian distribution of the beam, given by

$$L = \frac{N_b^2 n_b f \gamma}{4\pi\epsilon_n \beta^*} F, \tag{2.58}$$

where N_b is the number of particles per bunch, n_b is the number of bunches per beam, and f is the frequency with which the beam rotates. γ is the relativistic gamma factor, ϵ_n is the normalized transverse beam emittance, and β^* is the beta function at the collision point. The factor F accounts for the reduction of luminosity due to the varying crossing angle at the interaction points, where zero crossing angle causes head-on collisions [6]. It is defined as the number of potential collisions per unit area per second. Together with the availability of the accelerator, it gives the integral luminosity, the total number of recorded collisions per unit area, and as such is the ultimate measure of the performance of the accelerator [20].

The peak luminosity of the LHC at present is limited to approximately $2 \cdot 10^{34}$ cm^{-2}s^{-1}. The limiting factors are the aperture and cooling system of the so-called *inner triplet magnets*, series of three quadrupoles performing the final focusing of the particle beam before the collisions at the interaction points. The LHC has been a great success, and has reconfirmed CERN as the center for high-energy particle physics, both in Europe and globally. To reach a further potential for discoveries, and to extend operation by another decade, it was decided to launch the High-Luminosity upgrade of the LHC, HL-LHC. The upgrade will push the peak luminosity of the machine to approximately $5 \cdot 10^{34}$ cm^{-2}s^{-1}, and ultimately $7.5 \cdot 10^{34}$ cm^{-2}s^{-1}. The upgrade will amongst other parts, focus on reducing the transverse size of the beam in the interaction points, β^*, from 55 cm to 15 cm. This will mainly be achieved by replacing the inner triplets on both sides of the interaction points by stronger quadrupole magnets. Furthermore, decreasing β^*, means that the transverse extent of the beam is increased on both sides of the intersection point, as the focusing results in greater defocusing after the collisions. Therefore, the apertures of the inner triplet quadrupoles are also increased to a diameter of 150 mm [20] [21].

The upgrade is scheduled to be finalized, with the accelerator reaching the nominal luminosity, by the start of 2030. Consequently, the production and testing of the new magnets are well under way.

The layout of the magnets on one side of the intersection point is shown in Figure 2.14 below. This layout is the mirrored image about $s = 0$, meaning all the magnets are repeated in the opposite order for $s < 0$.

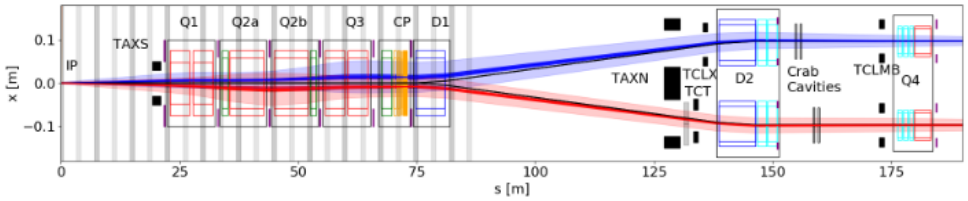

Figure 2.14: Machine layout of one side of an intersection point for the HL LHC. The dark blue and dark red areas highlight the 2σ beam envelope for $\beta^* = 15\,\text{cm}$, with the two colors highlighting the beams rotating in different direction. The shaded areas show the areas corresponding to the 11.9σ beam envelope, including effects of possible unwanted effects. Q1 to Q3 are the new quadrupole magnets in the inner triplet, with dipole correctors marked in green. The yellow boxes are the higher-order correctors of the corrector package, CP, and D1/D2 are the separation-recombination dipoles. The figure is taken from [21].

The HL LHC corrector package

The upgraded inner triplet quadrupoles and separation-recombination dipoles, Q1-Q3 and D1-D2 in Figure 2.14, require an upgraded set of corrector magnets. The corrector magnets used on each side of the interaction point can be split into dipole correctors and higher-order corrector magnets. There are several dipole correctors in and around the quadrupole triplet. A set of double-aperture corrector dipoles are used to correct for any errors to the beam orbit caused by misaligned triplet quadrupoles, and to open the crossing angle in the interaction point. Attached to each side of the Q2-magnets, and on the interaction point-side of the corrector package, CP, nested dipole correctors are installed. They comprise coils wound to control both a normal and skew dipole field, and are also used to correct for orbit errors due to the quadrupole misalignments, and to open the crossing angle. They are single-aperture magnets, and are designed to operate in any powering combination of the nested coils. The dipole corrector attached to the corrector package is twice as long as the other nested dipole correctors, with its magnetic length of 2.2 m. With the same strength, this corresponds to twice the integral field [22].

Then, a set of higher-order corrector magnets are assembled in the corrector package. This correction scheme is based on the scheme developed for the LHC. This means that a dedicated corrector coil is installed for each multipole component which is found to be critical for the containment of the beam within the cold bore. In addition to the corrected multipoles in the LHC, the corrector package comprise skew and normal decapoles and a skew dodecapole; a_5, b_5 and a_6. For each multipole imperfection, the correction is based on cancelling one or more resonance driving terms for both the clockwise and counter-clockwise rotating beams, as they share the aperture on each side of the interaction point [19]. The magnets are powered individually, and can therefore provide an ad hoc correction of the given resonance driving terms.

The higher-order corrector magnets are made with a superferric design, meaning the main field strength is achieved using superconducting coils made of Nb-Ti (Niobium-Titanium), and with iron

poles creating the desired field shape. This was opted for, as the peak field is low enough to avoid saturation in the pole ends, and it allows for a simpler and cheaper design and production [23].

The corrector magnets are the magnets under study in this thesis, and as such, relevant specifications are presented in Tables 2.1 and 2.2. These values will be referred to in the following of the thesis, and they are selected from [21] [24]. The cross-sections of the skew quadrupole corrector magnet, and the normal magnets of order three, four, five and six, are shown in Figure 2.15 below.

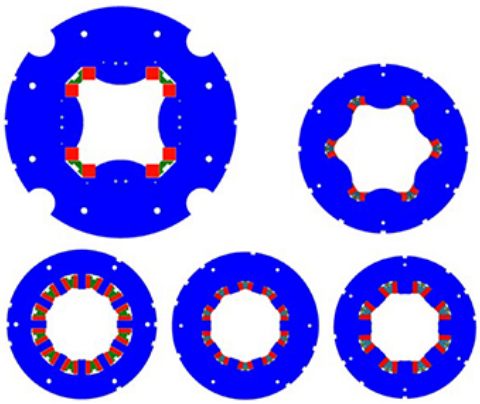

Figure 2.15: The design of the higher-order corrector magnets, where the blue shows the iron yoke of the magnets, the red parts are the Nb-Ti coils, and the green components are supporting structures for the coils. The magnets read clockwise, from the upper left corner: skew quadrupole, sextupole, octupole, decapole and dodecapole corrector magnets. The picture is taken from [22].

In Table 2.1, the magnetic properties of the corrector magnets are presented. In the rest of the thesis, the multipole component, b_n/a_n, will be used as a short-hand notation for the corrector magnets.

Table 2.1: Magnetic properties of the higher order corrector magnets in the HL-LHC corrector package. The values are taken from [21] [24].

Corrector magnet	MCXSF	MCSXF/MCSSXF	MCOXF/MCSOXF	MCDXF/MCDSXF	MCTXF	MCTSXF
Multipole order, n	2	3	4	5	6	6
Multipole component	a_2	b_3/a_3	b_4/a_4	b_5/a_5	b_6	a_6
Integrated strength in Tm	0.700	0.095	0.069	0.037	0.086	0.017
Gradient in T/m^{n-1}	34.8	224	3680	40480	585600	550400
Differential inductance in mH	1530	213	220	120	805	177
Magnetic length in mm	401	168	145	145	469	99
Current in A	174	99	102	92	85	84

The resistances of the copper in the superconductive coils are calculated by

$$R = \rho_{\mathrm{Cu}} \frac{N_{\mathrm{p}} l_{\mathrm{p}}}{A_{\mathrm{Cu}}}, \tag{2.59}$$

where $\rho_{\mathrm{Cu}} = 1.7 \times 10^{-8}$ is the resistivity of copper, N_{p} and l_{p} is the number of poles and conductor length per pole, and A_{Cu} is the cross-section surface area of copper in the coils. These values are presented in Table 2.2 below.

Table 2.2: Calculated values for resistances in the higher order corrector magnets for the HL-LHC corrector package. Values taken from [24].

Corrector magnet	MCXSF	MCSXF/MCSSXF	MCOXF/MCSOXF	MCDXF/MCDSXF	MCTXF	MCTSXF
Copper area in mm^2	0.808	0.133	0.133	0.133	0.133	0.133
Coil length per pole in m	1230	104	105	59	112	439
Copper resistance in mΩ	102.30	78.82	106.11	74.53	169.77	665.43

2.4 Magnetic Measurements - State of The Art

This section presents the theory of magnetic measurements, emphasizing the state of the art of commonly used measurement techniques. The need for magnetic measurements is presented, along with the magnetic field's qualities measured during an accelerator magnet's lifetime. Some basic theory of the alternative measurement techniques to the ones developed in this thesis for the room-temperature measurements of the corrector package is presented. Since the measurement techniques developed in this thesis are mainly based on methods using induction coils, this section emphasizes induction coil-based measurement techniques: It begins with the development of Faraday's law of induction, which is the basis of all these measurements. A presentation of the rotating coil measurement system is given. This is one of the most common measurement techniques applied for the magnetic measurements of accelerator magnets. It is included in this section, since the post-processing of the stretched-wire measurement procedure developed in this thesis uses theory from the rotating coil measurements. Then, theory presenting both the stretched-wire measurement system and translating coil fluxmeters are presented. These techniques are the basis for the development of the measurement procedure for the corrector package. As such, a presentation of the state of the art of these measurements and principles is given. Lastly, some basic theory on magnetic measurements based on magnetic resonance and Hall generators is given to conclude the section about the state of the art within magnetic measurement techniques.

2.4.1 The need for magnetic measurements

From sections 2.1 and 2.3, the importance of accelerator magnets in guiding and focusing the particle beam is obvious. The magnetic field, and therefore the positioning of the magnets, require very high tolerances. Therefore, the knowledge of the field attributes is key to the design, construction, installation, and operation of accelerator magnets [15]. The design of accelerator magnets, to a large extent, is developed using simulation software, such as ROXIE [25]. Even so, the only way to guarantee sufficient accuracy in the magnetic field is through magnetic measurements [26].

The magnetic field properties are characterized as *field strength*, *quality*, and *geometry* in reference [15]. According to the hard-edge model, in the field of magnetic measurements, we are mainly interested in the integral values of the field and their derivatives. By field strength, the maximum field strength and the hysteresis curve of the magnet is meant. This is mainly of interest to low-field, iron-dominated magnets. However, the corrector package comprises super-ferric magnets, so the hysteresis is also of interest to the measurement campaign of these. The field quality is the magnetic field distribution in time and space and comprises the magnetic multipoles, the longitudinal profile, and any imperfections introduced by the production of the magnets. What is meant by field geometry is mainly the (integrated) transverse magnetic axis, the roll angle of the magnet to the horizontal plane, and the longitudinal center of the magnet. Knowing the field geometry allows for the correct positioning of the magnets through a process called *fiducialization*, where the geometry is referred to external mechanical reference positions. During the design phase of the magnets, measurements of the field quality test whether the design meets the requirements and whether the production procedures are able to meet the design.

For series production of magnets, the field strength and geometry is measured to monitor dispersion in the field and to keep track of the fiducialization process for the assembly phase. The magnets are also tested both at room temperature and at cryogenic temperatures. Since the superconductive magnets are used at these temperatures, knowing the so-called *warm-to-cold transfer function*, namely how the mechanical and magnetic properties of the magnets are affected by cooling them to approximately 1.9 K is important. This gives valuable insight and knowledge into the behavior of

these magnets and how the magnetic measurements conducted at room temperature can be adjusted for when the magnets are cooled.

During assembly, the magnetic measurements of in particular field geometry are crucial to ensure the accelerator's design trajectory is met. For dipole magnets, the main focus is on installing the magnets with the correct roll angle, while for the higher-order magnets, the position of the actual magnetic axis is the key point to consider [15]. This is clear when considering the effects of misaligned multipole magnets, where an offset will produce feed-down terms, as shown in subsection 2.2.2. It is also seen from the theory presented in section 2.3, where an offset of quadrupole magnets will give transverse kicks on the beam [27]. When differences in the geometry and strength of the magnetic field are known, magnets can be combined along the accelerator so that the integral effect is minimized, as discussed in subsection 2.3.1.

During operation, the magnetic field is monitored by B-train systems. By doing so, the field can be fine-tuned to fully meet the integral field's requirements to optimize the particle beam's stability. Knowledge about the transfer function of the magnets is used for correct ramping of the individual magnets or group of magnets.

The characteristics of interest to magnetic measurement are usually assumed to have a normal distribution, i.e. with a bell shape about the mean of the measurand, determined by its standard deviation. Therefore, the presented quantities of the measurands in the following of this thesis are given as the mean, with the confidence levels given as the standard deviation of the measurements. The bell shape is determined by the mean and the standard deviation of an infinitely many measurements. In practice, a total of 30 measurements are usually sufficient to determine the correct shape of the distribution of the measurand.

2.4.2 Induction coil-based measurement systems

Faraday's law of induction

Induction-based measurement methods are all based on Faraday's law of induction, in this case, often referred to as the *flux rule*. It states that a changing magnetic flux through a nearly closed conductive loop induces a voltage difference between the terminals of the loop proportional to the rate of change of the flux linkage:

$$U = -\frac{\mathrm{d}\Phi}{\mathrm{d}t}. \tag{2.60}$$

In this section, I will show that the flux rule applies to any change of flux through a loop of wire; 1) due to a time-varying flux linkage, 2) due to a moving wire in a stationary magnetic field, or 3) due to a time-variation in both the **B**-field and in the wire surface. The magnetic flux through a surface $\mathscr{A}$ is given as

$$\Phi = \int_{\mathscr{A}} \mathbf{B} \cdot \mathrm{d}\mathbf{a}. \tag{2.61}$$

Inserting this into eq. (2.60), we get the following:

$$\left.\frac{\mathrm{d}\Phi}{\mathrm{d}t}\right|_{t_0} = \frac{\mathrm{d}}{\mathrm{d}t}\left(\int_{\mathscr{A}} \mathbf{B} \cdot \mathrm{d}\mathbf{a}\right) = \underbrace{\left[\int_{\mathscr{A}(t_0)} \left.\frac{\partial \mathbf{B}}{\partial t}\right|_{t_0} \cdot \mathrm{d}\mathbf{a}\right]}_{a} + \underbrace{\left[\frac{\mathrm{d}}{\mathrm{d}t}\int_{\mathscr{A}(t)} \mathbf{B}(t_0) \cdot \mathrm{d}\mathbf{a}\right]}_{b}, \tag{2.62}$$

where the flux through the surface $\mathscr{A}$ can change for different reasons [28]; by a change in the magnetic flux density evaluated at time t_0 and with a fixed area $\mathscr{A}(t_0)$, term (a), by a change in the area of the coil picking up the flux evaluated at time t_0 and with a fixed flux density $\mathbf{B}(t_0)$, term (b),

or by a combination of the two , which by the principle of superposition is shown in eq. (2.62). From this point on, the time dependence is omitted in notation.

Term a is just the Faraday-Maxwell law of induction on the integral form

$$\int_{\mathscr{A}} \frac{\partial \mathbf{B}}{\partial t} \cdot \mathrm{d}\mathbf{a} = -\oint_{\partial \mathscr{A}} \mathbf{E} \cdot \mathrm{d}\mathbf{r}. \tag{2.63}$$

In the case of a fixed surface, the $\partial/\partial t$-term can be placed outside of the integral, yielding

$$U = \oint_{\partial \mathscr{A}} \mathbf{E} \cdot \mathrm{d}\mathbf{r} = -\frac{\mathrm{d}}{\mathrm{d}t} \int_{\mathscr{A}} \mathbf{B} \cdot \mathrm{d}\mathbf{a} = -\frac{\mathrm{d}\Phi}{\mathrm{d}t},$$

proving the flux rule for the case of varying **B**-field through a stationary wire.

Term b is solved by realizing that the term $\mathrm{d}\mathbf{a}$ is the infinitesimal area traced by the line segment $\mathrm{d}\mathbf{r}$ and the displacement of the segment caused by the velocity of the wire at this point $\mathbf{v}\mathrm{d}t$, $\mathrm{d}\mathbf{a} = \mathbf{v} \times \mathrm{d}\mathbf{r} \cdot \mathrm{d}t$ shown in the Figure 2.16 [27].

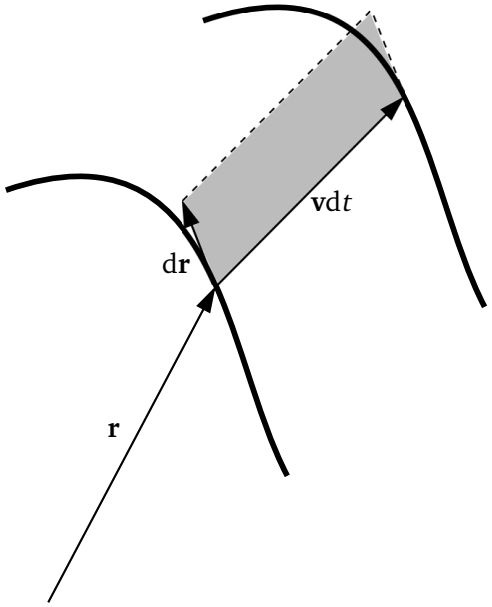

Figure 2.16: Movement of wire with a velocity **v** from time instant t to $t+\mathrm{d}t$, tracing an area given by the cross product of the line segment $\mathrm{d}\mathbf{r}$ and the displacement vector of the wire $\mathbf{v}\mathrm{d}t$: $\mathrm{d}\mathbf{a} = \mathrm{d}\mathbf{r} \times \mathbf{v}\mathrm{d}t$.

By replacing $\mathrm{d}\mathbf{a}/\mathrm{d}t$ by $\mathbf{v} \times \mathrm{d}\mathbf{r}$, term b is given by

$$U = \int_{\mathscr{A}} \mathbf{B} \cdot (\mathbf{v} \times \mathrm{d}\mathbf{r}) = -\oint_{\partial \mathscr{A}} (\mathbf{v} \times \mathbf{B}) \cdot \mathrm{d}\mathbf{r}. \tag{2.64}$$

In the last identity, the rule of the scalar triple product is used. The cross product $\mathbf{v} \times \mathbf{B}$ is known as the *motional* electromotive force[29], and when this is integrated along the moving wire, it too gives the voltage difference between the terminals of the wire. This proves Faraday's law for the case of a stationary magnetic field.

For the case of both a moving wire and a time-varying magnetic field, the principle of superposition applies. Therefore, I have shown that any magnetic flux change through an open-circuited loop of wire induces a voltage between the loop terminals given by eq. (2.60). In the further sections, I will present how this is utilized in different forms of induction-based magnetic measurements.

It is worth noting that in the case of a stationary magnetic field, no induced electric field contributes to the emf. Thus, the only induced voltage measured at the terminals of the loop is given by the change in the area picking up the flux. In the same way, when the coil is stationary, the velocity in eq. (2.64) is zero, and the emf is only given by the **E**-field, which is induced by the changing **B**-field. However, the effects are equal; we can measure the magnetic flux density of a magnet by either pulsing or alternating the magnetic field while measuring with stationary pickup coils, or we can move the coils, either by rotation or translation, through the aperture of the magnet while keeping a stationary magnetic flux density.

Rotating coil

The rotating coil is a measurement device used to measure the integrated multipoles of magnets and is one of the primary measurement devices used at CERN to measure the field quality of the magnets that are to be used in the accelerator complex. It offers relative accuracies of 10^{-4} on the main field and 10^{-6} on multipoles, and it locates the magnetic axis to an accuracy of less than 0.1 mm [30]. It comprises a set of induction coils mounted on a cylindrical shaft, which is positioned within the aperture of the magnet. The shaft is rotated with a constant angular velocity whilst the magnet is powered in DC mode, and the changing area spanned by the pick-up coils induces a voltage at the terminal of the coils. An angular encoder is also attached to the shaft, giving trigger pulses at predefined angular positions. The pulses are used to sample the induced voltage acquired and integrated by the integrators at these specific angular positions. This transforms the time-dependent flux change into a spatial value, resulting in the flux variation along the circumference traced by the rotating coils. Since the encoder triggers the signal at a very small angular increment, the magnetic field components can be approximated from the flux through the area spanned by the coils.

Since the entire length of the rotating induction coil measures a changing flux, the induced voltage obtained is the integrated value over the length of the induction coil along the longitudinal axis of the magnet. It, therefore, only gives a two-dimensional magnetic field description, following the hard-edge model described above. For the measurements to be in line with the two-dimensional multipolar description of the magnetic field, the ends of the coils must be well outside the fringe field region of the magnet. This means that the measured multipoles are valid if the coil shaft is longer than the magnet, so that both ends are outside of the fringe field of the magnet, if both ends are within the central regions of the magnet using relatively short coils, or by having one end in the central region and one well outside the fringe field region. When this is the case, the flux from the longitudinal field components through the area spanned by the induction coils will equal zero. If the coil end is within the fringe-field region, the flux picked up by the coils will also contain longitudinal components, and the two-dimensional multipolar description will no longer be valid. The length of the shaft varies from 0.1 m to 1 m [30], and measurements can be performed by measuring at several longitudinal positions along the length of the aperture in a scan.

The magnetic flux linked with the coil within the aperture of the magnet is given by eq. (2.61). This can be expanded into

$$\Phi = \int_{\mathscr{A}} \mathbf{B} \cdot \mathrm{d}\mathbf{a} = \int_0^L \int_{P_0}^{P_1} \mathbf{B} \cdot \mathrm{d}\mathbf{n}\mathrm{d}l, \tag{2.65}$$

when considering $P_{0,1}$ to be the transverse position of the two ends of the induction coil and L to be the length of the coil. In [16], the author shows through a change of coordinates how this expression changes going from vectorial to complex notation:

$$\Phi = -N_t L \mathrm{Re}\left\{ \int_{z_1}^{z_2} B(z)\mathrm{d}z \right\}. \tag{2.66}$$

In the equation above, N_t is the number of layers of the wound coil, and $z_{1,2}$ is the complex positions corresponding to $P_{1,2}$. The figures below show the positions of the ends of the wire, and the grey lines highlight the areas spanned by the wires with the corresponding normal vectors. Inserting eq. (2.38) for $B(z)$ into eq. (2.66), and integrating, yields the following expression:

$$\Phi = -N_t L \mathrm{Re}\left\{ \sum_{n=1}^{\infty} \frac{C_n}{n r_0^{n-1}} (z_2^n - z_1^n) \right\} = -\mathrm{Re}\left\{ \sum_{n=1}^{\infty} \frac{C_n}{r_0^{n-1}} S_n e^{in\theta} \right\}. \tag{2.67}$$

In the equation above, S_n is known as the *coil sensitivity factor* [6]. The sensitivity factors are calculated as follows [16]:

$$S_n := \frac{N_t L}{n} (z_2^n - z_1^n) e^{-in\theta}, \tag{2.68}$$

and they are determined purely by the geometry of the coil, with θ being the starting angle of the coil to the horizontal axis. The sensitivity factors are quantities explaining how sensitive the induction coils are to measure the specific magnetic multipoles, and multiple geometries can be combined in a process called *bucking* to obtain coils that are sensitive to certain multipoles of a magnet even though their amplitude is less prominent than other components [6]. As each coil is wound slightly differently, the coils are calibrated in reference magnets, dipoles, and quadrupoles, to get the correct sensitivity factors. Sensitivity factors also apply to measurements of longitudinal field components, as will be explained later.

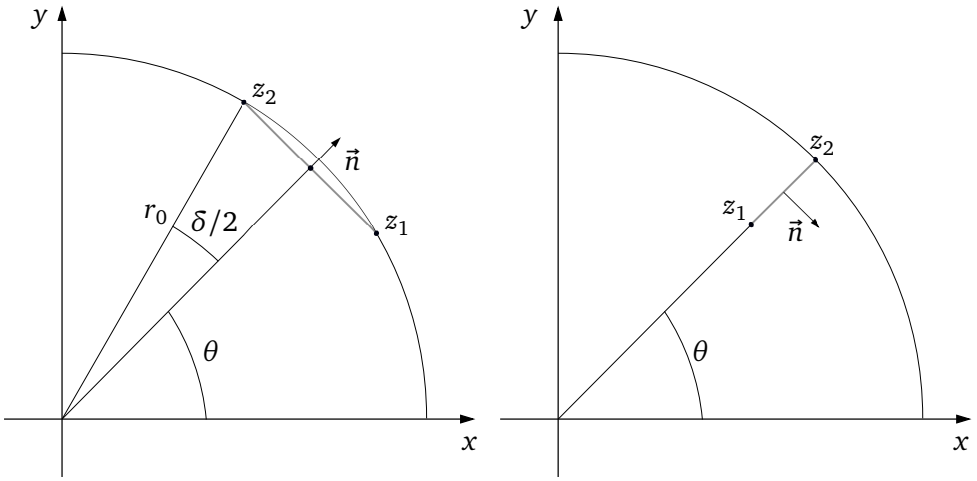

Figure 2.17: Illustration of the tangential (left) and radial (right) coil design used in rotating coil magnetic measurements. The figure is taken from [16], with a few alterations.

Rotating coils can be wound using different methods, such as manually wound coils and printed circuit boards (PCB), and in different configurations. The most used configurations are the tangential and radial coil designs, shown in the leftmost and rightmost parts of Figure 2.17. The tangential coil comprises a set of coils tangential to the shaft's rotation, measuring the flux density's radial component. The radial position of z_1 and z_2 are the same, whilst their angles are different and given as $\theta \pm \delta/2$, as shown in Figure 2.17. It can be shown that the sensitivity factor of the tangential coil is given as [6] [16]:

$$S_n^{tan} = \frac{2iN_t L}{n} r_0^n \sin\left(\frac{n\delta}{2}\right), \tag{2.69}$$

where δ is called the *opening angle* of the coil and shows the angle between the go- and return sides of the induction coil. From eq. (2.69) it is clear that the coil's sensitivity to the specific multipoles are given by the opening angle of the coil. For example, induction coils with opening angles $k \cdot 72^0$, $k = 0, 1, 2...$, cannot detect the main multipole component in a decapole magnet, the fifth-harmonic. This is so since these opening angles correspond to an integer number of periods for a sine wave with an angular frequency of five revolutions per mechanical revolution. Therefore, as the coil rotates, the change in flux through the coil is constantly zero, as the flux "gained" by one coil end is "lost" in the other. However, induction coils with opening angles $k \cdot 36^0$ have maximum sensitivity to the decapole component.

The radial coil design used in rotating coil measurements is constructed using arrays of coils mounted perpendicularly to the direction of rotation, hence measuring the azimuthal components of the magnetic flux density. In this configuration, the two positions $z_1 = r_1 e^{i\theta}$ and $z_2 = r_2 e^{i\theta}$ have the same angle, but the radii differ. From the expression of $z_{1,2}$ it is easily shown that the sensitivity factors of the radial coils are given as

$$S_n^{rad} = \frac{N_t L}{n}(r_2^n - r_1^n). \tag{2.70}$$

From eq. (2.70), it is clear that the sensitivity of all multipole components increase as the factor r_1/r_2 decrease, which is highly logical given the amount of flux through the wires increase by the area spanned. However, one loses the opportunity to perform bucking to enhance specific multipole components that might be weak compared to the main components in a signal.

The AC mole

Another way of using induction coils mounted on cylindrical shafts is to keep the coils stationary whilst powering the magnet with an AC excitation current. This technique is utilized in the so-called *AC mole*, a device used to measure the magnetic and mechanical axis of superconductive magnets during the assembly of the LHC [31]. The AC mole comprises a set of induction coils mounted tangentially onto a cylindrical measurement head, moved along the longitudinal axis of the magnet. At discrete positions, measured precisely with a laser tracker system, the magnet is powered, and the coils measure the flux according to eq. (2.63) whilst stationary. The magnetic axis is located either by comparing the signals of induction coils mounted opposite of each other on the support, using the symmetry of the magnet to locate the axis, or performing a rotational scan in each position. The rotational scan is performed the same way as the longitudinal scan; the measurement head is rotated a given angle, and the magnet is powered in AC to acquire the fluxes. After a given amount of angular displacements, the measured flux density at several angular positions is investigated through a Fourier analysis to find the roll angle and the axis through the feed-down of the multipoles [31]. Using this system, the magnetic axis can be measured locally with an accuracy of less than 0.1 mm [30], performing just as well as the rotating coil.

Magnetic measurements based on wires

Wire-based magnetic measurements have been applied in magnetic measurements for several decades. With improvements of the technology, this is today considered the standard measurement device for obtaining the magnetic axis, roll angle, and field integral due to its high accuracy [30]. There are several different measurement methods using wires. However, they all comprise a set of two linear stages supporting a taut conductive string with a diameter of less than 1 mm. The stages move in x- and y-direction with accuracy within 1 μm, and together with the size of the wire, this

allows for versatility in the measurement procedure; the wire can be traced in different patterns according to which measurand[VIII] is investigated, and it is adaptable to small aperture sizes [27]. The conductive wire is connected to a return wire in one end, which is led back either outside or inside the magnet to the unconnected wire stage, creating a nearly closed wire loop. As with the rotating coil, the wire has to be stretched far enough to be outside the magnet's fringe field region. The stretched- and return wires are connected to either a voltmeter or a current source, depending on the use case of the measurement wire.

There are two main measurement techniques applying a stretched conductive wire. The first technique is the *single-stretched wire* (SSW) measurement technique. It is based on measuring induced voltage as the stretched wire is moved within a constant magnetic field. As the wire is moved within the aperture of the magnet, the change in wire position traces out an area, shown in Figure 2.16, and a voltage is induced according to eq. (2.64). The stretched- and return wires are connected to a voltmeter, and the induced voltage is digitally integrated and sampled by an external trigger source. The flux density component normal to the traced surface is calculated from this. Several wire trajectories can be applied, depending on the desired outcome of the measurement. The following figure shows three trajectories for obtaining the multipole components of a quadrupole magnet's magnetic field.

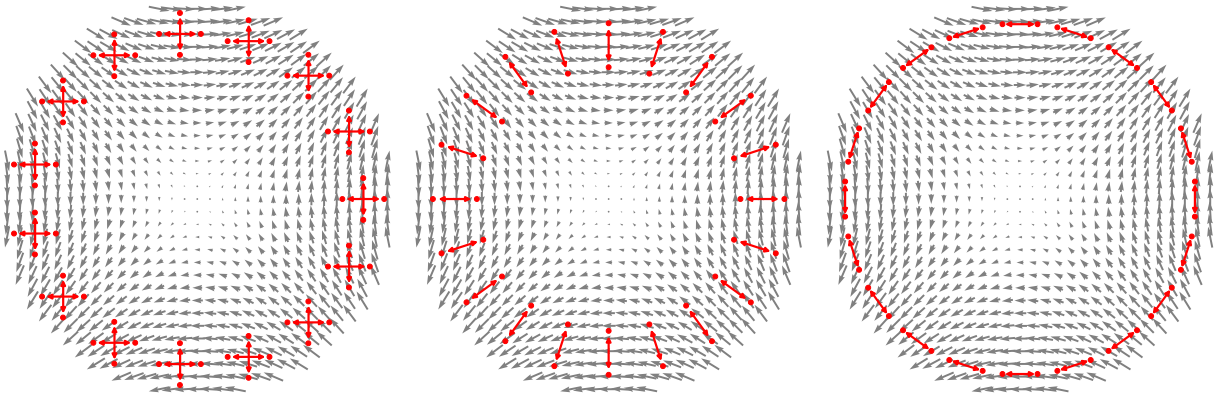

(a) $B_x - B_y$ wire trajectory. **(b)** B_φ wire trajectory. **(c)** B_r wire trajectory.

Figure 2.18: Wire trajectories for measuring multipole components in a quadrupole field.

In **(a)** of Figure 2.18 the complex multipole coefficients are measured and calculated, and in **(b)** and **(c)** the azimuthal and radial components are measured, respectively. The latter two resemble measurements with rotating coils. Fourier analysis is applied to yield the multipole components, and from the field phase and feed-down terms, the roll angle and integrated magnetic axis can be found. In addition to performing Fourier analyses on circular trajectories, arbitrary wire positions can be utilized. The multipoles can be approximated through a power series evaluated at these positions, using eq. (2.19) [32].

The single-stretched wire method can also locate the longitudinal center of magnets and the magnet's pitch and yaw angles using non-parallel wire movements [27].

The single-stretched wire is the reference measurement technique for determining the integral magnetic axis and roll angle. The multipoles can be used for this, but the standard measurement method uses the symmetries of the field gradient about the axis to determine the axis and roll angle. The process is shown in the following figures.

[VIII] The object under investigation.

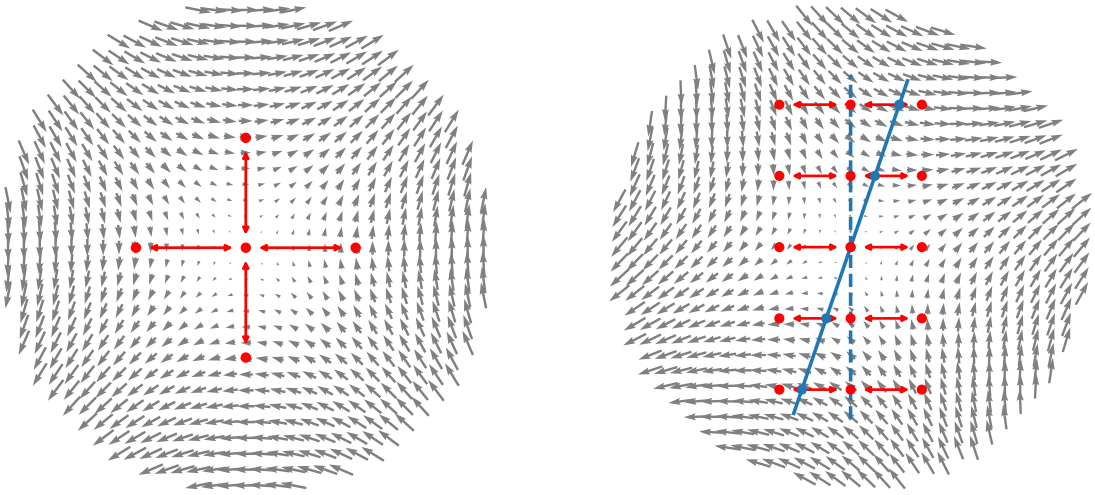

(a) Field symmetry measurement for locating the integrated magnetic axis.

(b) Field symmetry measurement for locating the roll angle.

Figure 2.19: Wire trajectories for measuring the integrated magnetic axis and roll angle based on the symmetry of the field gradients. The red dots are measurement points, and the arrows highlight the wire movement. The stippled line shows the mechanical y-axis, the blue dots show the magnetic axis at different heights, and the solid blue line gives the interpolated magnetic y-axis. The roll angle is found between the solid and the stippled blue lines.

The method of measuring the integral magnetic axis is shown in subfigure **(a)** of Figure 2.19. As the field's gradient in amplitude is symmetrical about the magnetic axis, equidistant wire movements with the initial wire position in the field axis will yield an equal amplitude in the measured signal. If the initial wire position is not in the magnetic axis, these wire movements will not yield the same amplitude, and the axis offset can be calculated from this. The wire moves in equidistant steps in both the horizontal and vertical directions. In a set of iterations, where the wire is moved to the measured axis offset, the wire position after the final iteration gives the magnetic axis. The roll angle is found using a similar approach: the magnetic axis is measured at several vertical positions given by the mechanical reference system (aligned to gravity). If there is zero roll of the magnet, the found axis in the horizontal plane will lie on a vertical line. Any roll angle, however, will yield measured axes lying away from the vertical axis when moved away from the vertical magnetic axis. The roll angle is then found as the angle between the interpolated line of the measurements and the vertical axis of the mechanical system, as shown in subfigure **(b)** of Figure 2.19. Other wire trajectories exploiting the symmetries can also be used [27], but the ones presented above are the most common way of measuring the magnetic axis and roll angles of accelerator magnets.

The single-stretched wire method are also used to measure alternating magnetic field. In this case, the wire is moved to a given position, and then the alternating field is acquired and integrated. This yields a flux measurement between the stretched wire and the return wire. Different field qualities can be retrieved by performing several measurements within the aperture of the magnet and combining them. This gives similar results to the AC mole, and with many possible trajectories, it can be used to determine the magnet's magnetic axis, roll angle, and polarity. This technique has been used previously, but never for higher-order multipoles. This is the basis of the *rotating single-stretched wire* measurement technique presented in this thesis.

The other technique employing the conductive wire is the *vibrating wire method*. In this technique,

the wire is powered by an alternating current and stretched through the stationary magnetic field. According to Lorentz's force, eq. (2.1), the force on the wire will oscillate with the same frequency as the current. Exciting the wire with its natural frequency results in oscillations measurable by optical sensors in both the vertical and horizontal planes. The magnetic axis is found where the first harmonic takes its minimum, and the pitch and yaw angles can be found by investigating the second harmonics. Using the vibrating wire method, the integral axis can be found at the micrometer level, and the pitch and yaw angles can be found at the sub-milliradian level [27].

Translating coil fluxmeters

The working principle of translating coil fluxmeters is very similar to that of rotating coils, where a flux linked with a changing area of search coils induces a voltage between the coil terminals. The difference between the methods is mainly the direction of movement, where the translating coil fluxmeters are moved along the axial direction of the magnet, in contrast to the azimuthal movement of the rotating coils. Therefore, the main idea of the translating coil fluxmeter is to measure the flux density as a function of axial position within the aperture. This is conducted by moving the fluxmeter parallel to the magnet's axis, integrating the time-based induced voltage, and triggering the integrators to assign a $\Delta\Phi$-value to the longitudinal position. The same can be accomplished with rotating coil magnetometers if a longitudinal scan is performed, but with a more significant time penalty than with a translating magnetometer, and with difficulties obtaining the same longitudinal resolution.

Translating coil fluxmeters can be designed specifically to the magnetic configuration to measure, and different technology can be used to produce the induction coils. An example of a solenoidal translating coil configuration where a PCB comprises a set of the induction coil is presented in reference [2], and manually wound coils are used for the same purpose.

In the following, the equations describing the measurements with translating coil fluxmeters are presented, based on unpublished work by Liebsch, Russenschuck, and Kaeske [33]. For the measurements of the corrector magnets, a set of tangentially positioned PCBs are proposed. Therefore, the equations used are based on translating coil fluxmeters measuring transversal field components. The main goal of this development is to show how the flux linkage measured by an induction coil with a non-negligible longitudinal extent is a function of both the local flux density and the windings' sensitivity to measure the spatial frequency components of the signal.

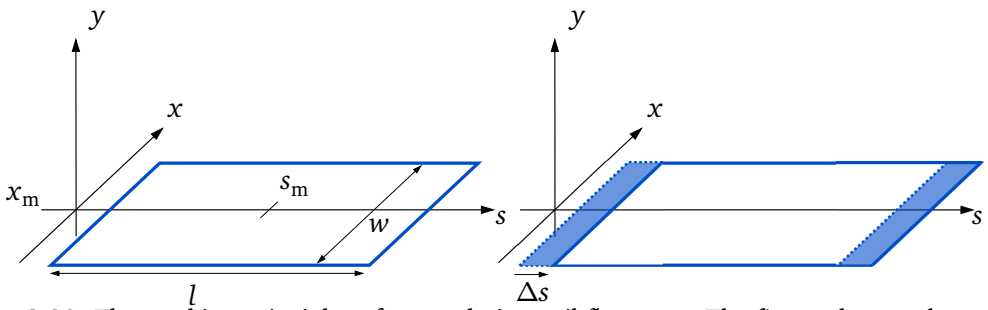

Figure 2.20: The working principles of a translating coil fluxmeter. The figure shows relevant parameters and resulting areas of a single induction coil.

Figure 2.20 shows the working principle of a single, rectangular search coil moved in the horizontal plane. The center of the coil is located in (x_m, s_m), the width of the coil is w and its length is l. The coil moves strictly in the s-direction with velocity $\dot{s}(t)\mathbf{e}_s$, where $\mathbf{e}_s$ is the unit vector in the longitudinal direction. According to Faraday's law of induction, eq. (2.64), the amplitude of the voltage

induced in the leading and lagging edges of the coil is given as

$$|U_{ind}| = \oint_{\partial \mathscr{A}} (\mathbf{v} \times \mathbf{B}) \cdot \mathrm{d}\mathbf{r} = \oint_{\partial \mathscr{A}} (\dot{s}(t)\mathbf{e}_s \times B_y) \cdot \mathrm{d}\mathbf{r}, \tag{2.71}$$

where $\partial \mathscr{A}$ is the four sides of the coil tracing the active area of the induction coil, and the flux linked with the coil stems from the vertical field components. Since the vector product of the coil's velocity and the magnetic field is perpendicular to the s-axis, the integrand along the length of the coil is zero. Therefore, omitting the norm of the vector, eq. (2.71) reduces to

$$U_{ind} = \int_{x=x_m-w/2}^{x_m+w/2} \big(\dot{s}(t)B_y(x, s(t)+l/2)\mathrm{d}x\big) - \int_{x=x_m-w/2}^{x_m+w/2} \big(\dot{s}(t)B_y(x, s(t)-l/2)\mathrm{d}x\big). \tag{2.72}$$

Introducing

$$\overline{B}_y(s) = \int_{x=x_m-w/2}^{x_m+w/2} B_y(x,s)\mathrm{d}x,$$

gives the short-hand notation of eq. (2.72):

$$U_{ind} = \dot{s}(t)\big[\overline{B}_y(s(t)+l/2) - \overline{B}_y(s(t)-l/2)\big]. \tag{2.73}$$

The induced voltage is integrated over some time ΔT, yielding the increment in flux from eq. (2.60) as

$$\Delta\Phi(t) = \int_{\tau=t}^{t+\Delta T} U_{ind}\mathrm{d}\tau = \int_{\tau=t}^{t+\Delta T} \dot{s}(\tau)\big[\overline{B}_y(s(\tau)+l/2) - \overline{B}_y(s(\tau)-l/2)\big]\mathrm{d}\tau. \tag{2.74}$$

From a change in variables, the expression can be transformed to longitudinal positions as

$$\Delta\Phi(s(t)) = \int_{s(t)}^{s(t+\Delta T)} [\overline{B}_y(s+l/2) - \overline{B}_y(s-l/2)]\mathrm{d}s. \tag{2.75}$$

The induced voltage is integrated, and the integrators are triggered by encoders measuring the longitudinal position of the induction coil. For simplicity, and without loss of generality, it is assumed that an encoder triggers the signal at M equidistant points, where $s_m = S_0 + m\Delta s$ for $m = 1, .., M$. This way, the time-dependent position can be expressed as a sampled point $s(t) = s_m$, $s(t+\Delta T) = s_m + \Delta s = s_{m+1}$. Eq. (2.75) can now be expressed as

$$\Delta\Phi(s_m) = \int_{s_m}^{s_{m+1}} \overline{B}_y(s+l/2) - \overline{B}_y(s-l/2)\mathrm{d}s. \tag{2.76}$$

We now regard the **B**-field through its inverse Fourier transform along the axis of the magnet,

$$\overline{B}_y(s) = \frac{1}{\sqrt{2\pi}} \int_{\omega=-\infty}^{\infty} \mathcal{F}\{\overline{B}_y\}(\omega) \cdot \mathrm{e}^{js\omega}\mathrm{d}\omega, \tag{2.77}$$

where ω is found using the spatial frequencies of the signal, given in 1/m. Inserting this into eq. (2.76), and working out the different terms, yields the following expression for the flux increments measured by the induction coil:

$$\Delta\Phi(s_m) = \sqrt{\frac{2}{\pi}} \int_{\omega=-\infty}^{\infty} \mathcal{F}\{\overline{B}_y\}(\omega) \sin(\omega l/2) \frac{\mathrm{e}^{j\omega\Delta s} - 1}{\omega} \mathrm{e}^{j\omega s_m}\mathrm{d}\omega. \tag{2.78}$$

From eq. (2.78), we see that the flux increments measured by the induction coil are dependent on several factors in addition to the **B**-field, namely the geometry of the coil and the length of the step size. These effects are given by the sensitivity function of the measurement:

$$S^c = \sqrt{\frac{2}{\pi}} \cdot \sin(\omega l/2) \cdot \frac{e^{j\omega\Delta s} - 1}{\omega}, \tag{2.79}$$

and they show that there are two restrictions on the design of the coil and the measurement in order to retrieve the full information of the **B**-field:

$$(1) : l \neq \frac{2\pi k}{\omega}, (2) : \Delta s \neq \frac{2\pi k}{\omega}, \tag{2.80}$$

for integer values of k. The first term, (1), shows that the frequency components with a period equal to the length of the induction coil, the so-called *blind-eyes* of the induction coils, will not be picked up by the coil, in the same way as for rotating coils and opening angles. The second term shows that the frequency components with a period equal to the step size of the measurement will also not be sensed by the coil. On the other hand, the sensitivity for specific frequencies can be increased by increasing the step size. Since the encoders used for these measurements have a resolution in the micrometer range, the blind-eye frequencies of the term (2) are very high. As can be seen from measurements, the errors introduced by truncating the spectrum frequencies at well beneath the kHz range, which will usually be well beneath the blind-eye frequencies due to low increments [33].

The theoretical development above is based on a single measurement coil, but the same applies to real-life measurement equipment as well, where sets of several coils, usually distributed over multiple layers, by the principle of superposition. Low sensitivity values for specific frequencies result in a less accurate recreation of the flux density if no signal treatment is conducted. As an example, simply dividing the flux by the complete area of the coils to obtain the flux density will give a less steep **B**-field in the fringe field regions than what is physically correct. This is caused by the fact that the high-frequency components in this region are smoothed out by low sensitivity. Another straightforward approach is to divide the measured flux by the sensitivity factors to obtain the **B**-field. This usually gives terrible results, as the frequency components in the blind eyes of the measurement signal are strongly amplified when divided by a factor approaching zero, creating large oscillations with the blind-eye frequencies. There are, however, solutions to this problem. One is to design the system, and in particular, the layout of the coils, to avoid blind-eyes below the cut-off frequency applied to the signal. If this is not an option, filtering of the signal can be applied. *Deconvolution* of the measured signal, that is a de-coupling of the signal from the sensitivity factors, using, for instance, a Wiener filter, have been shown to give very good results [10]. This involves filtering out noise components using the expected noise-to-signal ratio, damping the frequency we expect to be noise rather than correct signal frequencies. The downside to this approach is that it requires prior knowledge of the signal to calculate the inverse of the expected signal-to-noise ratio. This can be calculated, for instance, if the simulated field profiles are given.

Another way of recreating a more physically correct field profile is to approximate it using *spline interpolation*. Spline interpolation is a piecewise polynomial interpolation, where polynomials of a given order are used to approximate a function in-between specified nodes [34]. This can be used to approximate the measured **B**-field in an iterative way, initially using just a few nodes, so-called *knots*. The spatial integral of the spline is calculated, and it is evaluated over the area of the induction coil to obtain the flux intercepted by the coil at each longitudinal position from the approximated flux density. This result is then compared to the measured flux, and the error made by the spline approximation is found. Then, in the next iteration, more knots are added in the positions where the

error is the largest, making the apprioximation more refined. The iterations are continued until an acceptable level of error is reached.

2.4.3 Other measurement techniques

Hall generator

Magnetic measurements using a hall generator is based on the Lorentz force on a current in a perpendicular magnetic field:

$$\mathbf{F} = I\mathbf{l} \times \mathbf{B}, \tag{2.81}$$

where we assume no electric field present, $\mathbf{l}$ is the vector with magnitude equalling the length of the current path, and I is the magnitude of the current. The hall probe comprises a small strip of semiconductor material, where an electric current is applied from one side to the opposite. Eq. (2.81) states that the charged particles moving perpendicular to a magnetic field will experience a force normal to the plane of the current and the **B**-field. The trajectories of the charged particles are curved by this force, making one side of the hall probe electrically charged. The electric force used to balance the Lorentz force is measured as a voltage between terminals perpendicular to the direction of the current. In the ideal case, the magnitude of the Hall voltage, V_H, is given by

$$V_H = GR_H IB\cos(\theta), \tag{2.82}$$

where $B\cos(\theta)$ is the component of the **B**-field normal to the surface of the Hall generator, I is the amplitude of the current, G is a geometrical factor depending on the shape and size of the generator itself, and R_H is the Hall coefficient characterizing the material in the Hall probe [26].

Even though the theoretical basis of the Hall generator is simple, there are several factors complicating their use. Relative large connections compared to the small volume, ranging from $0.01\,\mathrm{mm}^3$ to $0.1\,\mathrm{mm}^3$, result in complications in the current flow of the Hall generators. This gives a non-linear response to the magnetic field, which together with additional non-linearities given by the material properties, result in an overall non-linearity that must be addressed through proper choice of material and geometry of the probes. Furthermore, the Hall generator carries the disadvantage of a large temperature dependency, in the order of 100 to 1000 ppm/C° [26]. These effects are kept to a minimum by a proper calibration and knowledge of the field-to-voltage relation of the generator. This is achieved through measurements in known fields at given temperatures, and by making sure this temperature is kept as constant as possible during the measurement. There are also sources of offset voltages to consider when measuring with Hall generators. First of all, there is a temperature dependent voltage offset at zero applied field, due to geometric and material properties, such as stress, connections and gradients in the material properties. An additional voltage offset is given by the so-called *planar* Hall effect, where a field component in the plane of the Hall generator but with an angle to the current, due to anisotropy in the generator leads to an additional voltage measured at the terminals [26] [35]. This offset is periodic with a 2φ-dependence, where φ is the angle between the current and **B**-field component in the Hall generator plane, and as such it is sensitive to misalignments of the Hall probe. The voltage offsets are countered by calibrating the constant offset voltage in a zero-field chamber, a chamber of ideal volume, zero field and known temperature. Correct alignment of the Hall generators is of great importance, especially if the direction of the field is known. This reduces the planar Hall effects by keeping the Hall generator as perpendicular to the main field direction, and it increases the signal-to-noise ratio, as the Hall probe mainly measures the perpendicular field component. Due to their small volumes, Hall generators offer the advantage of giving nearly point-like measurements of the magnetic field. Hall generators are therefore often used

in scans of accelerator magnets, giving a three-dimensional grid of the magnetic field. They are also used in measurements of magnetic field in hydro-power generators, where the size and simplicity of use and installation are key points [36]. The size also makes Hall generators applicable to a large range of aperture sizes, and the development of semiconductor material have made Hall generators an affordable measurement device. Furthermore, using stable power supplies and precise voltmeters, field levels in the micro tesla range can be measured, achieving a measurement accuracy of down to 100 ppm [26].

Nuclear Magnetic Resonance

Magnetic measurements using Nuclear Magnetic Resonance, *NMR*, is considered the most reliable measurement technique in measuring constant field levels, achieving accuracy up to 0.1 ppm, and is today the primary standard for calibration of other measurement instruments [26]. An example is in calibration of induction coils; an NMR probe is used to determine the constant field that is compared to the induced voltage signal of the coil, which when compared gives the calibrated surface area of the induction coil. In addition to calibration measurements, NMR measurements are used in scans to measure the field in near-constant areas of magnets.

When a particle with a magnetic and an angular momentum is placed within a magnetic field, the particle will spin around the axis of the external field density. The frequency of this precession, called the *Larmour-frequency*, is proportional to the field strength by the relation

$$f = \gamma B, \tag{2.83}$$

Where the constant γ is a standard property of the specific particle, with values given in tables [26].

The NMR probe comprise a sample of water, and the individual magnetization vectors are rotated, using radio-frequency pulses, to achieve coherence within the sample. Then, the Larmour frequency is measured either by coupling of the rotating magnetic momenta by an induction coil, or as resonance absorption.

The upsides of this technique is its linearity, precision, accuracy and ability to measure fields down to fractional milli tesla. The main disadvantage is the field requirements, limiting the gradient of the measured field, as well as the variation in time. The gradient can be counteracted using shimming coils that induce an opposite field gradient [26][15].

Chapter 3

Proposed Measurement Methods

In this chapter, the proposed measurement methods are presented, along with the parameters used for each method. First, the uncertainty requirements for the measurements and the expected deviations of the measurands are given. Then, the challenges encountered with measuring the corrector magnets at room temperature and their consequences on the chosen measurement methods are discussed. The proposed measurement methods are then presented together with measurements to establish the optimal parameters.

3.1 Measurement Requirements

As explained in section 2.3, the corrector package will be used as an ad hoc correction to cancel out resonance driving terms in the error components of the triplet quadrupoles and separation/recombination dipoles in the insertion regions. We have also seen in section 2.3 that the magnetic axis and roll angle knowledge is essential in predicting the force exerted on the particles. Therefore, knowing the internal positioning of the corrector magnets, especially their *functional axis*, the magnetic axis, in the assembled corrector package is a crucial part of the measurement campaign, and will be used to validate the methods.

The measurements of the field quality, the multipole components, the transfer functions, and gradients of the corrector magnets have been conducted at cold, with the magnets cooled to a superconducting state. The positioning measurements conducted at warm, meaning room temperature, are performed for quality control of the final assembly. It is proven that measurements at room temperature yield magnetic axis, roll angle, and harmonic content that relate well to the magnetic characteristics at nominal current at a superconductive state [37].

As the development of the different aspects of the High-Luminosity upgrade is still ongoing, the requirements used as a benchmark for the room temperature measurement of the corrector packages, and presented in this thesis, are based on the demands presented in reference [38].

The measurement uncertainties expressed in 3σ-values are limited to the values presented in the table below for the warm measurements [38]. It is worth noting that the requirements capture the total uncertainty ranging from the magnetic measurements of the given measurand to the mechanical measurements of the fiducialization process. In our case, this means referring the magnetic measurement results from the internal measurement reference frame to reference positions on the external surface of the magnet, called fiducials. In the case of the corrector packages, there are three points on each end of the assembly. This means that the uncertainty of measuring the external fiducials using, for example, a laser tracker system is also included.

Table 3.1: Measurement requirements for the transverse center, roll angle, longitudinal center, and magnetic length for room temperature measurements of the HL-LHC corrector package [38].

Transverse center in mm	Roll angle in mrad	Long. center in mm	Mag. length in mm
0.4	0.3	10	10

As the corrector magnets are to be powered to finely tune the trajectories of the counter-rotating particle beams in these areas, the positioning requirements of the corrector magnets are stringent. This is especially the case for the transverse center and roll angle, as misalignments of these are critical for the force on the passing particles, particularly in the insertion regions, as the two rotational beams share the same aperture. The relatively high tolerance for measurement uncertainty of the longitudinal magnetic center and the magnetic length is based on the experiences from LHC. Still, the new measurements are expected to obtain better accuracy [38].

The expected deviations for the magnetic axis, horizontally and vertically, longitudinal center, magnetic length, and roll angle for the different corrector magnets are given in Table 3.2 below. The magnets are internally positioned using precise stoppers, giving high internal position accuracy. However, the high expected deviations for the longitudinal location of the magnetic center and the magnetic length stem from the lamination used between the iron sheets in the cores of the magnets, with a thickness of 3 mm, yielding an integer number of 3 mm wide magnets. There is also an uncertainty in the contraction of the material when the magnets are cooled to a superconduct-

Table 3.2: Expected deviation of the roll angle and magnetic center with respect to the aperture axis of the HL-LHC corrector package expressed as 3σ-values [38]. H, V and S are the horizontal, vertical and longitudinal deviation, respectively.

H in mm	V in mm	S in mm	Mag. length in mm	Roll angle in mrad
1	1.58	10	10	0.1

ing state. The corrector magnets have the same expected deviations of the transverse measurands, axis and roll angle, as the other magnets. Since the magnets are relatively short, and the field shape largely determined by the iron yoke, the expected deviations of the longitudinal measurands, magnetic center and length, are given as the uncertainty of the measurements [38]. The reason why the expected deviation is larger than the measurement uncertainty in the transverse direction, is because a misalignment can be corrected for, when known with a given uncertainty.

3.2 Challenges of Measuring the Corrector Magnets in Room Temperature

This section discusses the most critical challenges encountered with the room temperature measurements of corrector magnets ranging from order two to six, and how they limit the use of the already available measurement methods discussed in section 2.4 .

Low field values

The main challenge with the magnetic measurements of the higher-order corrector magnets in room temperature, is the low field values. As the magnets are meant to be powered in superconductive state, the copper areas of the wires are only sufficiently large to protect the strands during a quench[I], and to keep the necessary mechanical stability. When the strands are cooled to 1.9 K, the Nb-Ti strands are in a superconductive state, and are able to support a current of up to 174 A for the skew quadrupole magnet. However, at room temperature, the resistivity of Nb-Ti is increased, and the current is led through the copper of the strands. Therefore, the current is limited to the copper cross section. At room temperature, the magnets can be powered at a maximum of 200 mA, and it was chosen to stay well below this at 105 mA.

From Ampère's law, it is clear that the flux density in the magnet is significantly reduced when the current is reduced by a factor thousand. Assuming linear behavior of the iron in the magnets, a rough estimation of the expected field values at a measurement radius of 68 mm can be carried out in the following manner:

$$|\mathbf{B}_{\mathrm{nom},\mathrm{r_m},\mathbf{n}}| = G \cdot r_{\mathrm{m}}^{n-1}, \tag{3.1}$$

$$|\mathbf{B}_{\mathrm{m},\mathrm{r_m},\mathbf{n}}| = |\mathbf{B}_{\mathrm{nom},\mathrm{r_m},\mathbf{n}}| \cdot \frac{I_{298\,\mathrm{K}}}{I_{1.9\,\mathrm{K}}}, \tag{3.2}$$

where $\mathbf{B}_{\mathrm{op},\mathrm{r_m},\mathbf{n}}$ and $\mathbf{B}_{\mathrm{m},\mathrm{r_m},\mathbf{n}}$ are the field strengths during nominal operation and during room temperature magnetic measurement, respectively, measured at a radius $\mathrm{r_m}$. G is the gradient, given in $\mathrm{T/m}^{n-1}$, n is the order of the magnet, and $I_{298\,\mathrm{K}}$ and $I_{1.9\,\mathrm{K}}$ are the currents used in the case of room temperature measurements and superconductive operation, respectively. Calculations using the equations above, inserting the parameters given in Table 2.1, yield the following expected field values for the different corrector magnets:

Table 3.3: Expected flux density amplitude of the room temperature magnetic measurements of the higher-order corrector magnets.

Corrector magnet	a_2	b_3/a_3	b_4/a_4	b_5/a_5	b_6	a_6
Expected field strength in mT	1.4	1.1	1.2	1.0	1.1	1.0

The low field values is a challenge for all the measurement methods, even though some methods are still feasible. Especially using the stretched-wire method in DC to measure the multipole components on a circular trajectory is difficult, as the induced voltage is proportional to the wire movement and the field strength, both of which are small in this case. Furthermore, remanence field from magnetic measurements at cold will be present in all the magnets of the corrector package. Since the stretched-wire measurements only measure the integral field along the wire, the relative

[I]The transition from the superconductive to the normal state of the material [6].

strength of the remanence field in the remaining magnets to the imposed field in the one measured will be high. Therefore, measuring the actual multipoles in the powered magnet is too difficult to use the DC stretched-wire multipole measurements to obtain the axis and roll angle.

Flat gradient around the axis

The main challenge of measuring DC powered higher-order magnets with the stretched- and vibrating wire techniques, is the flat gradient around the magnetic axis. For instance, an octupole magnet has a cubic magnetic gradient, which displays a rather flat region in the proximity to the magnetic axis. Even with nominal field levels, the stretched-wire techniques are rarely applied for the measurements of magnetic axis and roll angle for magnets of order three and more. Therefore, measuring this using the stretched- and vibrating wire techniques is challenging, all the time they are dependent on field symmetries and the amplitude of the gradient to determine the axis. This is further complicated by the above-mentioned low field values, scaling the gradients accordingly. Another aspect is the remanence field in the remaining corrector package, which will add to the gradient of the powered magnet, as discussed above. Together, this rules out the use of the single-stretched wire methods in DC for the measurements of the magnetic axis.

Similarly, for the measurement of the roll angles, as this is also based on measuring the magnetic axis at vertical positions, the low field strength and relatively high remanence field rules this method out for measuring the roll angles as well.

Therefore, another system must be utilized for the measurements of the magnetic axis and roll angle.

Difficulties with measuring the internal position

Rotating coil magnetometers are the most used measurement method to acquire the harmonic content of accelerator magnets. From this, the magnetic axis can be calculated, as presented in subsection 2.2.2, and the roll angle can be found from the field phase of the measured flux density. The system is in fact used for the measurement of the field quality of the corrector magnets, at cryogenic temperatures. It would therefore be natural to use this system for the roll angle and magnetic axis measurements also at warm. However, there are difficulties in precisely measuring the internal position of the coils with respect to the external fiducials, and the measurement method is therefore ruled out [38].

The AC Mole is another option, where powering the magnets in AC would result in higher induced voltage. The system was already used to measure the magnetic axis and roll angle of the decapole corrector magnet, see [39]. However, using this system, the spread of the roll angle is reported to be nearly a factor ten above the required uncertainty. Furthermore, it was proved difficult to position the AC Mole within the magnet, and as such it is deemed infeasible to position it with sufficient accuracy to measure the axis and roll angle of the full corrector package assembly.

Lastly, both rotating coil magnetometers and AC Moles could be utilized in scans to measure the longitudinal field profiles, hence obtaining both the longitudinal centers and magnetic lengths of the individual magnets. However, as the corrector magnets are short, the length of the measurement head would have to be very short to obtain the required resolution along the s-axis. Therefore, another system was opted for.

Similarly, scanning the longitudinal field profiles using Hall probe mappers could also be used. The obvious downside to this is the lengthiness of such measurements, which by itself rules out the measurements. Furthermore, the mechanical structures would have to be very large, as the corrector package is more than five meters long. This would also impose difficulties with vibrations of

the Hall probe support. Lastly, the non-linearity of the Hall probes complicates the measurements, and induction-coils are generally easier and more robust to use. In total, performing scans using Hall probes was deemed infeasible for this kind of measurements, and other choices were further investigated.

3.3 Proposed Method for Measuring the Magnetic Axis and Roll Angle: "The Rotating Single-Stretched Wire"

This section presents the measurement method for locating the magnetic axis and the roll angle. It uses induction coils and combines the mechanical advantages of the single-stretched wire and the theory of roll angle determination and feed-down from measurements with rotating coils, as presented in subsection 2.2.2. The novelty of this measurement method lies in the combination of measuring magnets of high multipole orders, the single-stretched wire measurements performed in AC, and the connection to the multipole theory for calculating the magnetic axis and roll angle. Stretched-wire measurements using magnets powered in AC mode have been performed in the past. However, to the knowledge of the author, not for magnets of orders above two or three, and at least not in an assembly with orders ranging from one to six. The added value of this system, if it proves to deliver results with an accuracy and precision within the requirements, is a system able to measure magnets in a range of orders, with low field values and difficult assembly configurations. First of all, it will benefit the measurement phase of the HL-LHC, with several measurement requests expected in the years to come. Secondly, it will be an addition to the "toolbox" of available measurement methods for future encounters with challenging measurement campaigns.

In the first part of this section, the general idea of the measurement method is presented. Then a thorough description of the acquisition- and data post-processing phases of the measurement method is given. For both parts, results from measurements conducted to determine the optimal choice of parameters are used to explain the choice of parameters and methods.

3.3.1 General measurement principle

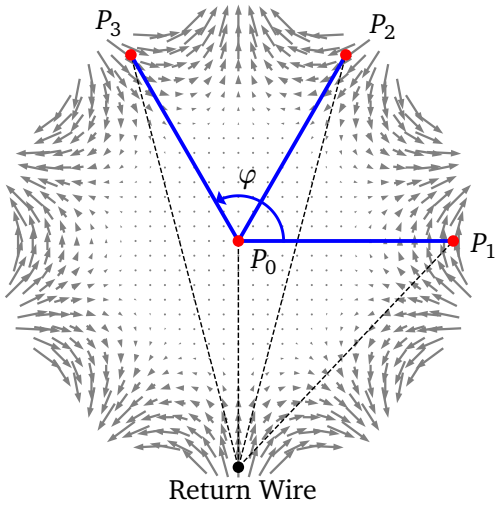

Figure 3.1: Illustration of the general principle of the rotating single-stretched wire measurement method. P_0 is the initial measurement point, P_1-P_3 are the circumferential measurement points, and the return wire is the black dot at the bottom. The stippled lines show the area spanned by the stretched and return wires. The blue lines show the resulting areas spanned by the circumferential measurements and the central measurement, resulting in a rotating single-stretched wire counter-clockwise following φ.

For a single corrector magnet, the general principle of the measurement method is the following: The magnet is powered with an alternating current of a given frequency, causing an alternating flux

density within the aperture of the magnet. We use the SSW-bench to stretch the conductive wire parallel to the magnetic axis through the aperture, which together with the return wire constitutes a nearly closed surface. To mimic a rotating coil, the wire is moved in a circular trajectory of N points within the aperture, with an additional point in the mechanical center. The induced voltage caused by the alternating flux through the surface spanned by the wire bench is acquired and integrated for a given time at each point. In the post-processing phase, a Fourier analysis is conducted to find the amplitude and phase of the flux evaluated at each point. So far, the measured flux amplitudes are the flux linked with the surface bound by the stretched wire and the return wire, seen as the stippled lines in Figure 3.1. However, by subtracting the central measurement value from all the circumferential ones, $\Phi|_{P_{ret.}}^{P_i} - \Phi|_{P_{ret.}}^{P_0}, i \in [1, N]$, the values obtained are given as the flux intercepted by an area spanned by the stretched wire in the center and in the circumferential position, $\Phi|_{P_0}^{P_i}, i \in [1, N]$, shown as the blue lines in Figure 3.1. This is valid since the magnetic flux density is divergence-free within the aperture.

The set of measurements now consists of $[\Phi|_{P_0}^{P_1}, .., \Phi|_{P_0}^{P_N}]$, assigned to spatial positions within the aperture, and can be regarded as a measurement conducted with a single rotating induction coil. Due to the circular trajectory, we can use Fourier analysis on the spatially distributed flux density to obtain the multipole coefficients and the offset of the measurement axis from the actual magnetic axis and the roll angle.

3.3.2 Measurement setup, approach, and choice of parameters

Measurement setup

The setup used for the validation measurements of the rotating single-stretched wire measurement technique is shown in Figure 3.2 below. The setup is also valid for the measurements of the complete corrector package. Still, it was chosen to use the setup for the validation measurement to illustrate the system, since it shows the whole setup in one single picture.

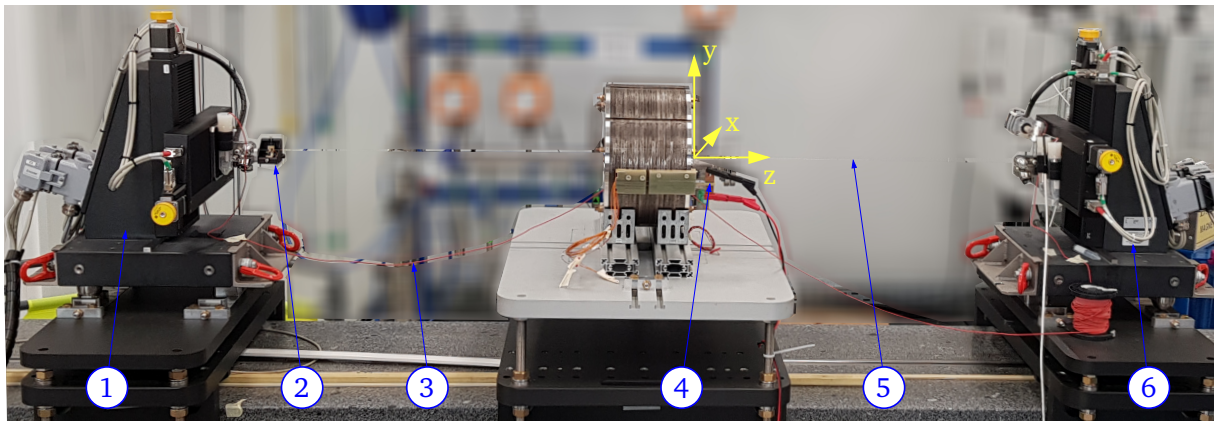

Figure 3.2: Measurement setup and reference system used for the validation measurements of the Rotating Stretched Wire measurement technique. The magnet is in the center of the picture, with the yellow coordinate system attached at its side. The The picture shows wire precision linear stages A/B (6)/(1), the optical sensor (2), the return wire (3), power connections (4), and barely visible; the stretched CuBe-wire (5).

The magnet used for these measurements is a single decapole corrector magnet, not installed in the corrector package. It can be seen in the center of the figure, with the coordinate system attached

at the terminal side. The magnet is connected at the copper terminals to a 6221 Keithley® AC and DC Current Source, which can power the magnet to create an alternating and constant field. A Copper Beryllium wire with a diameter of 125 μm is stretched through the aperture of the magnet, barely visible in the figure. At the B-stage, it is connected to the return wire, which is also led through the magnet aperture, taped to the bottom to keep it still during the measurement. The wire is supported at each side of the magnet by a set of wire stages, which keep the wire taut. Each stage comprises a set of Pi miCos® HPS-170 linear precision stages, enabling wire movement in the horizontal and vertical planes measured by linear encoders. Marble plates support the stages for better stability. Even so, there is an angular offset in the movement of the precision stages, given by positioning the stages onto the marble plate and the rest of the support. This offset is regularly calibrated in a reference quadrupole magnet and can therefore be adjusted for in the roll angle calculation.

As the magnetic flux through the area spanned by the stretched- and return wire changes, the induced voltage is acquired and digitally integrated by a *Fast Digital Integrator*, *FDI*, with a frequency of 500 kHz. The trapezoidal rule is used to integrate the signal[40], and then it is sampled at 1024 Hz before it is stored. The Flexible Framework for Magnetic Measurements, *FFMM*, a C++-based measurement software developed in the Testing and Measurement section at CERN[41], controls the entire measurement procedure.

A summary of the equipment used for the validation measurements, along with their specifications and the parameters used, is presented in Table 3.4.

Table 3.4: Equipment, parameters, and specifications used for the validation measurements for the rotating single-stretched wire measurement method. The specifications for the power supply are dependent on the parameters used.

Equipment	Type/Model	Parameters and Specifications
Power Supply	6221 Keithley® AC and DC Current Source	$\hat{I} = 105 \pm 0.001$ mA, ± 0.4 mA offset, $f_{PS} = 23 \pm 0.0023$ Hz [42]
Precision Wire Stages	Pi miCos® HPS-170	$\pm 0.2\,\mu$m repeatability, 1 μm absolute precision, 50 nm encoder resolution [43][27]
Optical Sensor	Sharp® GP1S094HCZ0F phototransistor	-
Stretched Wire	CuBe-Wire	$\varnothing$ 125 μm
Integrator	FDI	$f_{sampl.} = 1024$ Hz, $f_{int.} = 500$ kHz

Approach and choice of parameters

In this part, the measurement technique approach is presented in detail. The presentation is based on the figure below, showing roughly every step in the process from measurement to resulting roll angle and axis offset of one of the decapole corrector magnets. The parameters chosen for the validation measurements of the measurement method are also presented, based on a set of tests to determine the optimal parameters considering measurement time and signal quality. This section uses terminology and principles from digital signal acquisition and processing. The key terms are discussed in Appendix A.

Excitation current:
An alternating current is used to power the magnet. There are two main reasons for doing so. First, the only possibility to measure more than just noise is to power them in AC. The induced signal increases linearly with the frequency of the flux density, which can be seen from Faraday's law of induction. The higher the frequency, the higher the $\mathrm{d}/\mathrm{d}t$-term is. As explained in section 3.2, the corrector magnets can at maximum be powered at 200 mA when they are at room temperature due to the low copper surface in the conductors. It was decided to power them way below this to avoid destroying them, at 105 mA. Measuring the field change with an alternating current gives a higher

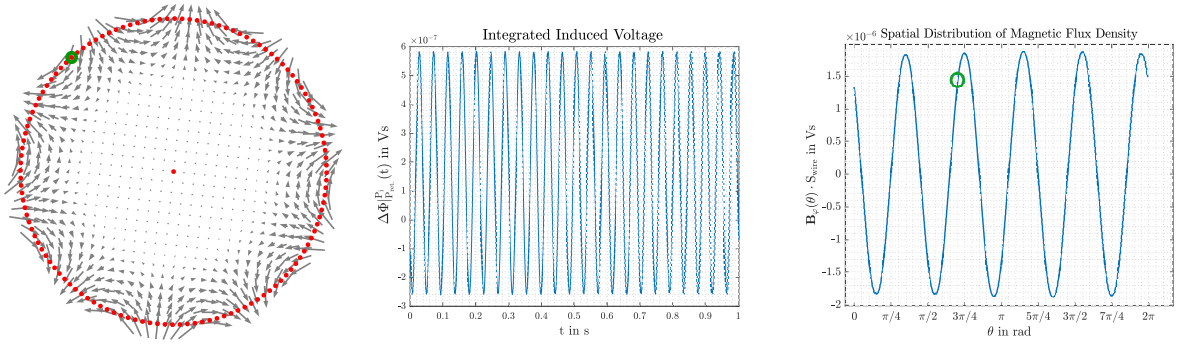

Figure 3.3: Visualization of the measurement- and post-processing procedure followed in each measurement point for the Rotating Single-Stretched Wire measurement method, resulting in the spatial distribution of the azimuthal flux density. The leftmost figure shows the 129 measurement positions within the magnet aperture, with the stretched wire located in the position highlighted with the green circle. The figure in the middle displays one second of the measured and step-wise digitally integrated induced voltage between the stretched wire in the given position and the return wire. The rightmost figure shows the spatial distribution of the flux density after subtracting the measured value in the magnet's center. The green circle highlights the amplitude obtained by a digital Fourier analysis of the measured signal in the central figure.

induced signal, enabling measurement of the actual field value and not only noise, given that the frequency of the current exceeds the rate of change of flux picked up by moving the coil in a stationary field.
Secondly, when powering the magnets in AC, we avoid any bias due to the remanence field of the magnets. In ferromagnetic materials, such as different iron alloys used in the yoke and bearings of the ferromagnetic corrector magnets, the characteristic curve showing the relationship **B**(**H**) follows a so-called hysteresis curve, where after increasing the **H**-field above an initial limit, the behavior of **B** follows that of **H**, but lagging. This follows from the fact that within the material, the magnetic momenta of internal domains, which in an unmagnetized piece of iron are either randomly directed or ordered in a way that the total field is zero, are directed according to an externally applied field. When the field saturates the material, meaning all the internal momenta are directed uniformly, decreasing the external field to zero will not decrease the internal field to zero but will give a *remanence* magnetic field density, and a negative field must be applied to reduce the internal field to zero [6]. Since the corrector magnets have already been tested in a superconductive state, the remanence field might be higher than what we can achieve by exciting the magnets with 105 mA, making it impossible to counteract it before measuring. However, when we power the magnet in AC, the remanence field will be measured as a constant offset, which is then filtered out by the Fourier analysis, as this finds only the amplitude of the frequency component of the flux corresponding to the frequency of the excitation current. It is worth noting that the approach assumes that the remanence field is symmetrically distributed. However, as the magnets by design should have such a distributed remanence field, and there are no available data suggesting otherwise, this is a weak assumption.

The choice of parameters for the excitation current was based on the limitations of the available power supply and an optimization measurement campaign. The current amplitude is limited to 200 mA, and it was chosen to power the magnets by a Keithley AC and DC source, with the specifications listed in Table 3.4. It has a maximum output of 105 mA, which was then set to the amplitude of the excitation current. The frequency of the excitation current is of great importance, as it decides the magnitude of the induced signal. When measuring with alternating currents, one crucial

aspect is to avoid any harmonic components of the primary power supply frequency to separate any electromagnetic noise generated by appliances connected to the mains from the magnetic field. In Switzerland, the power supply frequency is 50 Hz, and so, the frequency chosen for the powering of the magnets should not have 50 Hz as a multiple. Apart from this, the frequency was chosen based on measurements investigating the amplitudes of the main signal and noise levels for different frequencies. The induced voltage was measured at a few wire positions within the magnet for a set of different frequencies fulfilling the requirements mentioned above. The measurements were repeated in the same setup ten times to give the measured quantity's spread, the standard deviation. In each position and for each frequency, the frequency spectrum and main harmonic amplitude were investigated. The spectra of the frequencies at a single wire position are shown in Figure 3.4.

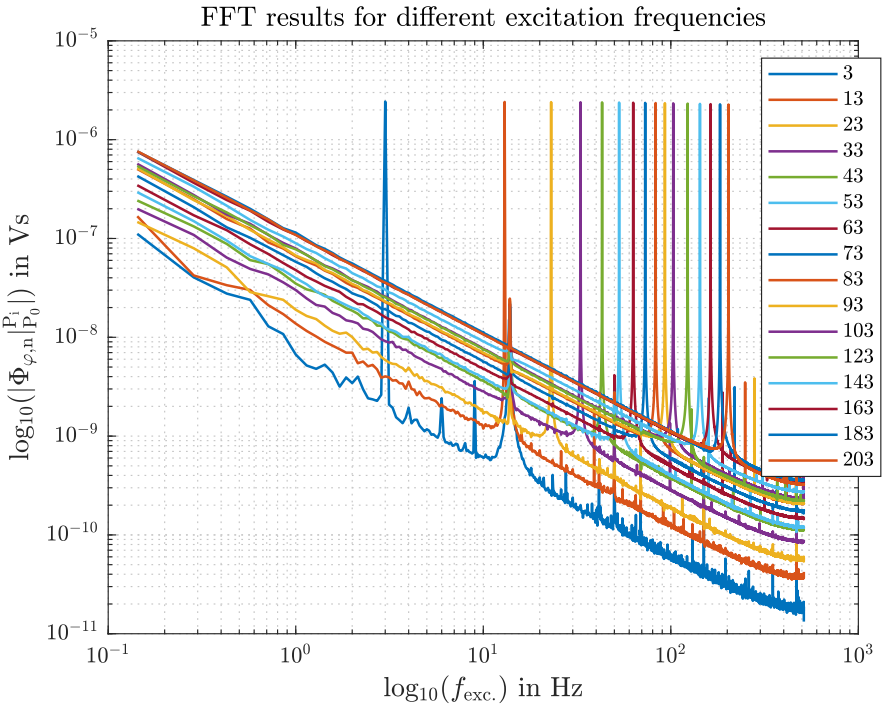

Figure 3.4: Logarithmic plot of the spectra measured at a single position within the aperture, averaged over ten repetitions, for each of the excitation frequencies tested.

The measured amplitudes' corresponding spread is calculated as the relative standard deviation presented in units of 10^{-4}. It is calculated as the standard deviation of the measured main harmonic amplitude of the ten repetitions divided by the measured amplitude. The standard deviation is calculated using the *std*-implemented function in MATLAB, presented in [44], and it captures the variations in the measured amplitudes over the ten consecutive repetitions for the same wire position.

Table 3.5: The relative spread of the measured main-harmonic amplitudes over ten consecutive measurements is presented in units of 10^{-4} of the measured amplitude.

Frequency in Hz	3	13	23	33	43	53	63	73	83	93	103	123	143	163	183	203
Relative spread in units of 10^{-4}	3.1	3.0	0.4	0.7	0.4	0.6	0.8	0.9	0.6	1.2	0.8	1.25	2.0	1.5	1.7	2.5

The results of these measurements, shown in Figure 3.4 and Table 3.5, together with similar results from the other wire positions, give the basis for the choice of the excitation frequency. The

spectra in Figure 3.4 show a slight decay in the measured fundamental frequency signal for increased frequency. The amplitudes are not increasing since the signal is integrated before the DFT is applied, so the higher amplitude of the induced signal is counteracted by the lower signal period. Furthermore, increasing the frequency might result in iron saturation in the magnet, explaining the slightly reduced amplitude. This results in a lower signal-to-noise ratio, as seen in the figure, where all other signal components are more prominent, as shown by the difference between the parallel lines in the figure. When the main-harmonic amplitudes are lower for increasing excitation frequencies, while the noise increases with frequency, the ratio between signal and noise decreases.

From the spread of the signal, it is clear that using frequencies below 15 Hz gives a higher spread of the measured values and an optimum between the signal-to-noise ratio, given by the amplitude of the main-harmonic signal, and as low a spread as possible is found above this limit, and below the higher frequencies, roughly below 53 Hz.

Another interesting result from these measurements was that there seems to be a source of noise at a frequency of approximately 14.75 Hz. This can be seen just to the right of the 13 Hz-spectrum in Figure 3.4, where a peak is visible for all measurements, independent of the excitation frequency. This effect is also visible in the measurements in the laboratory where the complete corrector package is measured, see subsection 5.1.1, and it was observed that it is independent of the mechanical movement and vibrations of the wire. Furthermore, after discussions with the author of [37], this noise component seems to be caused by some equipment in the environment at CERN, as the same noise component can be seen with measurements of a bare pick-up coil in Fig. 3.18 in [37]. Therefore, it was chosen to avoid integer frequencies of 14-15 Hz for the excitation current.

Based on the measurements described above, it was chosen to power the magnets with a frequency of 23 Hz and with an amplitude of 105 mA.

Acquisition time:
With the magnet powered, the wire is used to measure the varying flux in each measurement position. Before the acquisition and integration of the induced voltage starts, the system is programmed to wait for a given time to have sufficient damping of the mechanical vibration of the wire for it to be ultimately still when it is measuring. When we measure only one magnet, a waiting time of 2.5 s is sufficient, but this will be prolonged for measurements of the complete corrector package.

When the timer has finished, meaning the wire is still, the induced voltage is acquired and integrated for a set amount of time before the wire moves on. The acquisition time is of key importance to the post-processing phase of the measurements, as this directly determines the resolution of the frequency bins in the Fourier analysis, as discussed in [36]. This aspect will be discussed in the following section on the measurement data post-processing. The acquisition time is chosen as an optimum between the quality of the Fourier analysis and the measurement time. The effect on the calculated offset from the magnetic axis and the roll angle of changing the acquisition time was also investigated. This was measured by truncating the induced voltages at given positions at the correct acquisition time. Hence the same set of initial measurement data was used. Each measurement was repeated five times to give the spread of the measured axes and roll angles, shown as σ in the table below.

The results of these measurements are given in Figure 3.5 and Table 3.6, where the spectra measured at one wire position and the effect of using different acquisition times on the measured axis and roll angle are presented, respectively. From the spectra in Figure 3.5, it is clear that when shortening the acquisition time, the resolution of the frequency bins is too low to capture the correct frequency component completely, as seen from the curves of measuring with less than 1 s. However, its effect on the measured axis offset and roll angle shows that the measurands change very little, in the order

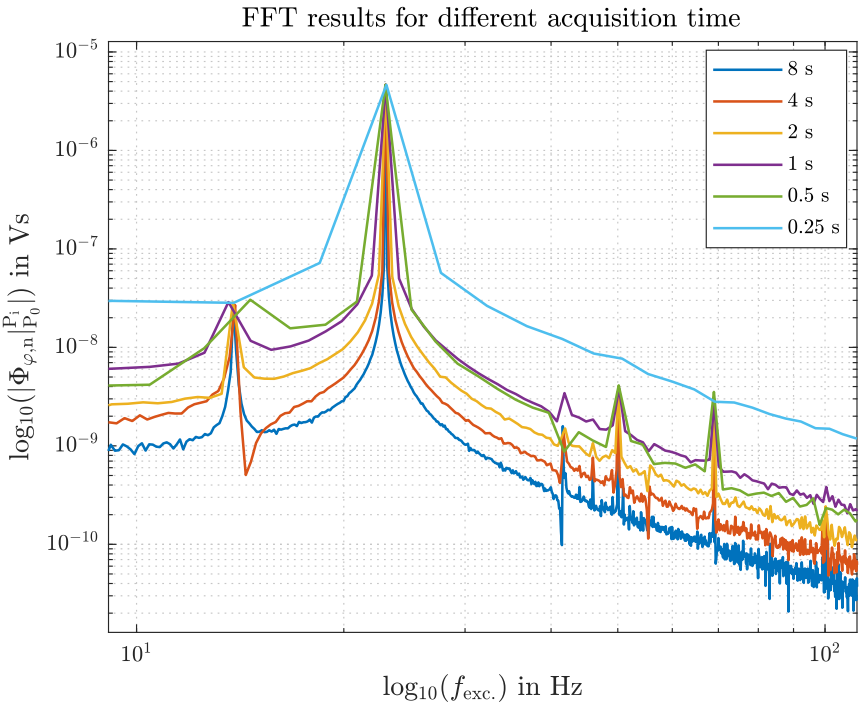

Figure 3.5: The resulting spectra from a single measurement point from reducing the acquisition time.

Table 3.6: Resulting axis offset and roll angle with varying acquisition time, given with 1σ standard deviation.

Acquisition time in s	0.25	0.5	1	2	4	8
$\Delta x \pm \sigma$ in μm	120.3±2.0	119.0±1.1	119.7±0.4	119.5±0.3	119.4±0.3	119.7±0.6
$\Delta y \pm \sigma$ in μm	148.5±2.8	149.4±0.8	149.4±0.8	149.4±0.2	149.2±0.3	149.2±0.3
$\alpha_{\text{roll}} \pm \sigma$ in mrad	153.96±0.05	153.96±0.01	153.96±0.01	153.96±0.00	153.96±0.00	153.96± 0.00

of sub-micrometer for the axis offsets and less than 10 μrad for the roll angle. The only noticeable difference is in the spread of the measurand, where it is increased when succeeding 1 s of acquisition time. The small changes of measured axis and roll angle is mainly due to the filtering effect given by the Fourier analysis when using as many as 256 circumferential points, and it shows the robustness of the measurement approach. It was seen that acquiring for as little as 2 s was sufficient to obtain a precise and repeatable result. Even so, to be on the safe side, and to reduce the probability of random effects such as vibrations and electromagnetic noise in less controllable environments, increasing it to 4 s is even better. Therefore, an acquisition time of 4 s is chosen as an optimum between the quality of the spectral analysis and the measurement time. However, as this analysis was conducted in parallel to the measurements, the acquisition time used for the validation measurements was 8 s, as using the full signal once measured only increases the quality of the measurements.

Measurement points:
The wire positions within the aperture of the magnet are shown in the leftmost subfigure of Figure 3.3, with the initial position in the center of the magnet and the remaining points equally spaced around the circumference of the aperture. The number of points also plays an essential role in the time consumption of the measurement procedure.

From the Shannon sampling theorem, it is known that the maximum frequency component that can be recreated from discretely sampled measurement points is given as less than half the sampling frequency. Therefore, measuring the decapole corrector magnet, with a frequency of five pole pairs over one mechanical rotation, having more than ten circumferential measurement points would be theoretically sufficient for these measurements. However, this would not be sufficient in practice, as the Fourier analysis is based on entirely circular measurements, and therefore the number of measurement points increases drastically. For measurements with rotating coils, approximately 60 measurement points in one revolution are required for sufficient accuracy [6]. For our purposes, more points are required since the wire trajectory traced by all the measurement points needs to be circular. Even though the wire stages move very accurately, there is still some uncertainty about the exact position of the wire in each position, resulting in uncertainties about the circularity of the trajectory. However, the more measurement points used, the more filtering is applied to the wire trajectory, as imperfections cancel out. Therefore a circular trajectory can still be assumed if enough points are used.

Again, an optimal solution involving enough points to thoroughly over-sample the measurements whilst still keeping the measurement time as low as possible is needed. To find this optimum, the measurement was down-sampled to investigate how many points are needed to find the correct axis offset and roll angle. To this end, measurements with as high a number of points, for as long as possible acquisition time are considered to yield the best results, and we want to see how much the measurands are affected by down-sampling. The effect of changing both the number of points and the acquisition time was investigated, with acquisition for 4 s and 8 s. The results are shown in the figure below, where the error bars show the spread of the measurement.

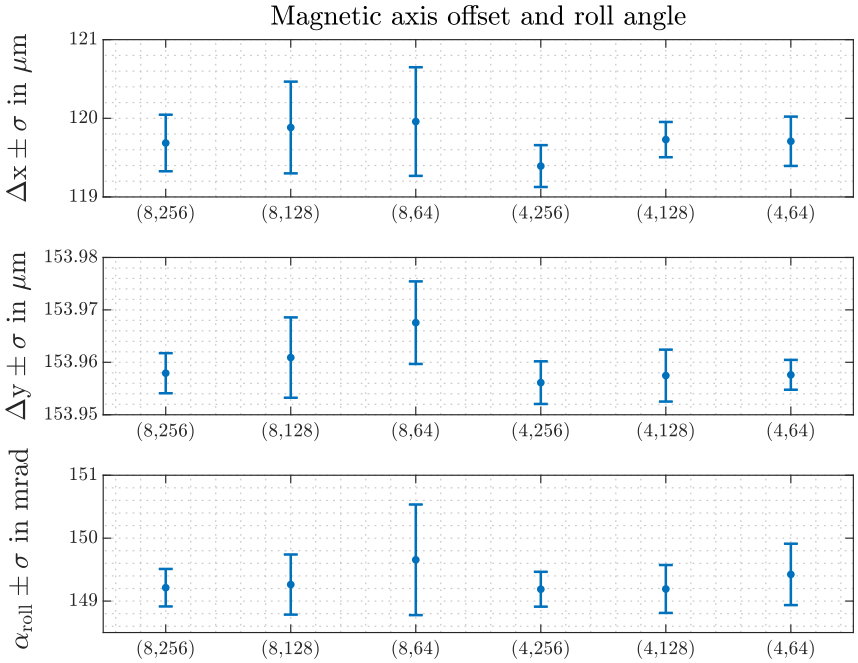

Figure 3.6: The effect of reducing the number of measurement points, together with the acquisition time, on the measured axis offsets in the horizontal (top), vertical (middle) direction, and the roll angle (bottom). The error bars show the spread expressed in 1σ.

What can be concluded from these measurements is that the number of measurement points plays a more significant role in the measured axis and roll angle than the acquisition time. The differences are not very big regarding the measured axes, but the effects are more prominent for the roll angles. Especially the spread of the measurement increases with fewer measurement points. This follows the findings above, that many points smooth the signal to reduce errors introduced in the acquisition. The optimum was chosen to be 128 measurement points, but since this processing was carried out parallel to the validation measurements, 256 circumferential points were used. For future measurement campaigns, it is also seen that increasing the number of points might be the solution if the measurement environment proves difficult. Since the requirements are more stringent for the measured roll angle, it varies more than the offset.

Measurements with different radii showed that the larger the radius, the better the signal quality. This is an effect of the higher-order gradients, which increase rapidly towards the outermost part of the aperture. Therefore, using as large a radius as possible gives a higher signal-to-noise ratio, improving the quality of the Fourier analysis. The largest radius chosen was 68 mm, a bit less than half of the aperture diameter, to have some margin not to touch the inside of the magnet with the wire. For future measurements, the largest radius possible should be chosen.

Several repetitions are carried out with the same parameters to get the repeatability, or spread, of the measurement. FFMM automatically handles this, so the correct amount of repeating revolutions containing the correct amount of spatial points are measured without the need for an operator to interact in between, reducing the sources of error.

The complete set of parameters used in the measurement part of the validation measurement campaign is presented in Table 3.7, where both the values used for the validation measurements and the optimal values found through different measurements that will be used for future measurements are presented.

Table 3.7: Measurement parameters used for the validation measurements, together with optimal calculated parameters applicable for future measurements.

Parameter	Used value	Optimal value
Excitation current amplitude	105 mA	-
Excitation current frequency	23 Hz	23 Hz
Acquisition time	8 s	4 s
Circumferential measurement points	256	128
Measurement radius	68 mm	68 mm

Post-processing algorithm

After the induced voltages are measured in the post-processing, the data is treated, and the axis offset and roll angle is calculated. In this section, the full post-processing algorithm is presented in chronological order.

Reading and treatment of data:
In each of the above-mentioned measurement points, P_i, the induced voltage is acquired for a given time. The voltage signal, as well as the current used to power the magnet, is acquired at a frequency of 500 kHz where it is digitally integrated in an FDI. The integrated induced voltage, or $\Delta\Phi|_{P_{ret.}}^{P_i}$-signal, is stored at the sampling frequency, resulting in an array of $\Delta\Phi|_{P_{ret.}}^{P_i}$-values in each position, together with the measured excitation current. This can be seen in the middle figure of Figure 3.3. The signal

is truncated to ensure that it contains an integer number of periods. This is important to avoid spectral leakage in the signal spectrum, as discussed in Appendix A. The digital integrators suffer from several factors causing low-frequency drift of the integrated signal [45]. If the integrated induced voltage is cumulatively summed to yield the flux linked with the area spanned by the stretched wire and return wire, the slowly varying drift would add up as a linear term. To counteract most of this effect, we subtract the average of the integrated signal, as the signal oscillates about zero, before it is cumulatively summed. This yields an array of values representing $\Phi|_{P_{ret.}}^{P_i}(t)$, digitally sampled, in each wire position.

Extracting the amplitude in the measurement position:
After the data is collected, trimmed, and cumulatively summed, it is treated to find the amplitude of the flux acquired between the stretched- and return wire. This is where the Fast Fourier Transform implementation in MATLAB, *fft* as presented in [46], comes into play. The Fast Fourier Transform is applied to $\Phi|_{P_{ret.}}^{P_i}(t)$, and to the current readings, with the two-sided complex spectral density as the output. This means that it includes both positive and negative frequency bins, with the energy found through the FFT, is divided equally between the positive and corresponding negative bin. Therefore, a so-called *folding* about the DC signal (0 Hz frequency) is required; the signal is stripped for the negative frequency bins, and the energy in the positive bins (except for the DC one) is doubled to account for the energy in the newly removed negative frequency bins. Then, the amplitude and phase of the signal with a frequency corresponding to the excitation current frequency are found. It is worth noting that the power supply frequency is not necessarily the frequency we intended, as it can vary with ±0.0023 Hz, see Table 3.4. Therefore, it is essential that all the frequency bins in an interval around the frequency we expect to find are investigated and that the maximum amplitude is chosen. Lastly, the sign of the amplitude is determined from the phase difference between the current going into the magnet, and the resulting flux picked up by the wire, $\vartheta_{res.} = \vartheta_I - \vartheta_\Phi$. From this, we find the sign from the sign of $\cos\vartheta_{res.}$.

To sum it up, applying the FFT algorithm on the raw $\Phi|_{P_{ret.}}^{P_i}$-signal gives the amplitude of the spatially distributed flux density averaged over the surface spanned by the stretched- and return wire in one position, shown as the green circle in the rightmost figure of Figure 3.3. Therefore, this process lies between the central and rightmost figure.

Assigning the spatial distribution of the flux density:
The process described above is then applied to the measured data from all the measurement points, resulting in a distribution of the flux measured from the return wire to all the measurement points along the circular trajectory and within the center of the magnet. Then, to mimic a radial pick-up coil, the central measurement is subtracted from all the circumferential measurement points, as explained in subsection 3.3.1 and shown in Figure 3.1. This gives the spatial flux density distribution as a function of mechanical angle as if it was measured with a radial rotating coil, that is $B_\varphi(\theta) \cdot S_{\text{wire}}$. From this point on, well-known measurement procedures from rotating coil analysis can be applied based on the DFT of the now spatially distributed flux measurement.

Fourier analysis of spatially distributed flux density:
As explained in subsection 2.2.1, the multipole coefficients can be found through a DFT of the measured flux. This procedure is similar to the one performed on the time-dependent signals above; the output of the *fft*-algorithm is the two-sided spectrum, and the signal is therefore folded. Then, since the magnet is powered in AC, there is no need for the DC signal, which is removed. As was discussed in section 2.4.2, the flux linked with a radial rotating coil, if the starting angle is assumed to be zero,

is given by

$$\Phi(\vartheta) = Nl \int_{r_1}^{r_2} B_\varphi(r,\vartheta)\mathrm{d}r = \sum_{n=1}^{\infty} S_n^{rad} \cdot [B_n(r_0)\cos(n\vartheta) - A_n(r_0)\sin(n\vartheta)],$$

where r_1 and r_2 are the coils' inner and outer radii, and l is the length of the wire. The coil sensitivity factors are given as

$$S_n^{rad} := \frac{2N_t L r_0}{n}\left[\left(\frac{r_2}{r_0}\right)^n - \left(\frac{r_1}{r_0}\right)^n\right],$$

and shows how sensitive the search coil is to signals from multipole n. As the rotating single-stretched wire method measures with the initial position in the center of the coordinate measurement system, $r_1 = 0$, and the expression for the sensitivity factors reduces to

$$S_n^{rad} := \frac{2N_t L r_0}{n}\left(\frac{r_2}{r_0}\right)^n. \tag{3.3}$$

As the measured signal is the product of the sensitivity factor of the wire and the actual azimuthal flux density, the resulting complex Fourier coefficients from the *fft*-algorithm are divided by the corresponding sensitivity factors to yield the correct coefficients.

Calculation of roll angle and displacement vector:
Once the correct multipole coefficients are in place, the roll angle and the displacement vector from the measurement axis to the magnetic axis are found.

The main field phase, φ_N, is the phase angle of the main multipole component, defined on the interval $[-\pi/2, \pi/2]$, and is calculated using a four-quadrant inverse tangent function implemented in MATLAB [47], taking care of the cases when $x < 0$. If it is still outside of the interval, an angle of $\pm\pi$ is added to accunt for this, as defined in subsection 2.2.2. As φ_N is expressed in the magnetic reference system, meaning a full 2π rotation going from one pole-pair to another, it has to be divided by N to be expressed in the mechanical measurement system, which is based on the theoretical developments in section 2.2.2. Therefore, the roll angle is found as

$$\alpha_{\text{roll}} = \frac{\varphi_N}{N}. \tag{3.4}$$

The measurement axis offset displacement from the magnetic axis, or the axis offset, is calculated as in section 2.2.2:

$$z_d = -\frac{R_{ref}}{N-1}\frac{C_{N-1}}{C_N},$$

with $k = N$. In the remainder of this thesis, Δz is used instead of z_d, to highlight that what is measured is an offset from the magnetic axis, and since this is the standard from the magnetic measurements of the LHC magnets [14].

The multipoles could also be investigated and manipulated further from this stage, thoroughly described in [14]; they are usually rotated to make the main multipole purely normal, and it is common to calculate the other multipoles in units relative to the main component. However, since it is only the axis offset and roll angles of the magnets that are of interest in this stage of the magnetic measurements of the corrector package, this has been left out of this work to keep the procedure simple and robust so that other operators can carry it out at CERN in the coming months and years.

Fiducialization process and wire sagitta correction

The remaining part of the measurement process is to relate the measured quantities to the external fiducials, which in the case of the corrector package are three points on each side of the magnet assembly, as seen in the case of a single decapole corrector magnet in the leftmost picture of Figure 3.7. This is important since it is the only step relating the internal measurement coordinate system to the physical magnet. This, in turn, is needed for the correct assembly of the corrector package into the machine, as well as knowledge of where the actual magnetic axis is with respect to this position.

For the fiducialization measurements, all quantities are measured using a *LEICA ABSOLUTE TRACKER 930* laser tracker system, with absolute angular performance of $\pm 15\,\mu\text{m} + 6\,\mu\text{m/m}$ for measurements of spatial points. For scans along one dimension, where only the interferometer of the tracker is used, a precision of $\pm 0.5\,\mu\text{m/m}$ is obtainable[48]. The precision data given above are based on measurements in optimal surroundings. For the actual measurements, worse performance is expected. However, with careful treatment of the system, errors can be kept to a minimum.

The external fiducials and the wire stages are measured with the laser tracker system before the magnetic measurement is conducted. This way, we know where the initial wire position is relative to the magnets we measure, which is sufficient to connect the magnetic measurements to the physical positions. At each wire stage, the tracker system uses two primary holders for the target: One carefully calibrated in the x-direction and one in the y-direction. This can be seen in the central part of Figure 3.7, with fixation points for both the horizontal and vertical measurements shown, together with the actual position of the wire. From the calibration procedure, the distance from the laser targets to the actual position of the wire is known to the micrometer level.

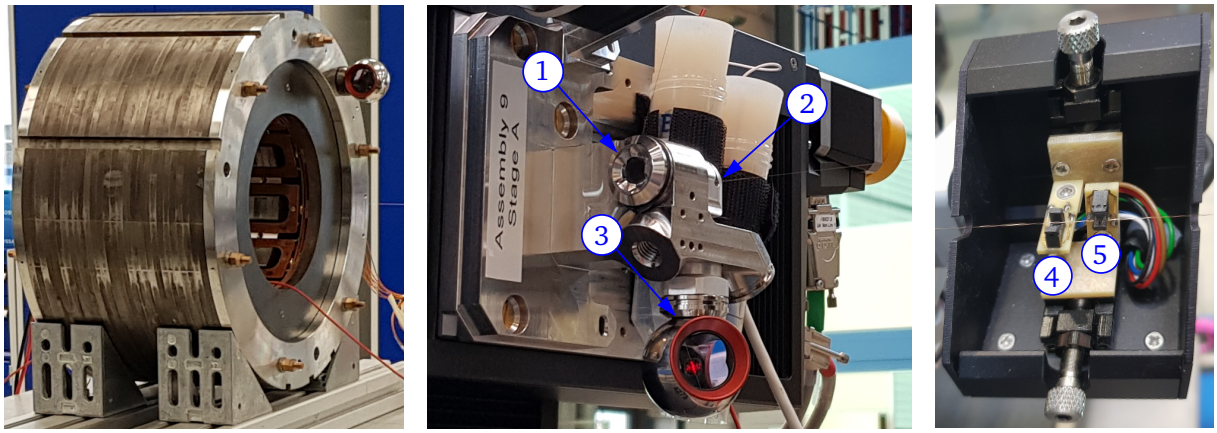

Figure 3.7: Key points in the fiducialization process. The leftmost figure shows the decapole corrector magnet with two external fiducials, the leftmost and lowermost perforations, and the third is occupied by the laser system target. The figure in the middle shows the fixation points for the laser tracker targets (1) and (3), as well as the actual position of the wire (2), together with the laser tracker target attached at fixation point (3). The distances between (2)-(1) and (2)-(3) are calibrated as $\Delta x_{cal.}$ and $\Delta y_{cal.}$ respectively. The third figure shows the phototransistors attached to wire stage B. They measure wire movement in the vertical (4) and horizontal (5) planes.

Once the initial wire position is known, the position of the wire within the magnet aperture is calculated. Due to its weight, even though the wire is stretched taut between the two stages, it will still follow a so-called catenary curve from one stage to the other, with the lowest point known as the *wire sagitta*, or simply *sag*. The wire trajectory at the initial position of the measurement of the skew quadrupole corrector magnet is shown in Figure 3.8, where the blue line shows the wire from its

connections at stages A and B, and the orange line shows the average position of the wire within the aperture. This has to be considered when referring to the found axis offset to the external fiducials, as the wire position within the magnet aperture is lower than the position measured at the stages.

A simple approach to calculating the wire sagitta is found if one assumes equal height of the wire stages and the only force acting on the wire is gravity. Under these circumstances, the wire sagitta can be calculated according to the following formula [49]:

$$\text{sag} = \frac{g}{32 f_1^2}, \tag{3.5}$$

where f_1 is the fundamental frequency of the wire, given in Hz. However, if the stages are not positioned at the same height, which in general is not the case, the position of the wire is calculated from the differential equation of the motion of the wire. Solving for the particular solution in one plane to the equation given by gravity, it can be shown that the following equation is found for the vertical position due to gravity of the wire as a function of the longitudinal position s [49]:

$$y_g = \frac{m_l g}{2T} s^2 + C_1 s + C_2, \tag{3.6}$$

where m_l is the mass per unit length of the wire, g is the acceleration due to gravity, and T is the tension force acting on the wire. $C_{1,2}$ are constants, which are found by inserting the boundary values; assuming zero velocity of the wire, $y_g' = 0$, and that wire stage A is positioned at $s = 0$. Instead of operating with the tension force on the wire, the expression of the fundamental frequency of the wire, $\omega_1 = \pi^2 T / m_l L^2 \Rightarrow m_l / T = (\pi / \omega_1 L)^2$, is inserted to get the final equation for the wire trajectory following from one stage to the other:

$$y_g = \frac{g}{2}\left(\frac{\pi}{\omega_1 L}\right)^2 s^2 + \frac{1}{s_B}\left(y_B - y_A - \frac{g}{2}\left(\frac{\pi}{\omega_1 L}\right)^2 s_B^2\right) s + y_A. \tag{3.7}$$

In the equation, y_g is the vertical position due to gravity along the wire, and $y_{A,B}$ are the vertical positions at stages A and B, respectively. At the same time, s_B is the longitudinal position of stage B, and L is the length of the wire. From the laser tracker measurements, the position of the wire is found at each of the stages, and after the coordinates are transformed into the s-y-plane, with one of the stages at $s = 0$, eq. (3.7) can be applied once the natural frequency of the wire is measured.

The natural frequency of the wire is found by exciting the wire with an AC current, and changing the frequency of the current until the natural frequency of the wire is found. From Lorentz's force, we know that the current in the wire will be affected by external magnetic fields (such as the earth's magnetic field), and by altering the current, there will be a force acting on the electrons in the wire which will make the wire oscillate with the same frequency as the current. The phototransistors measure the oscillations in both the horizontal and vertical plane at wire stage B, seen in the rightmost figure of Figure 3.7, and the natural frequency is found as the frequency that results in the most significant oscillations of the wire. With this in place, eq. (3.7) is applied to find the correct wire trajectory after it is rotated back in space.

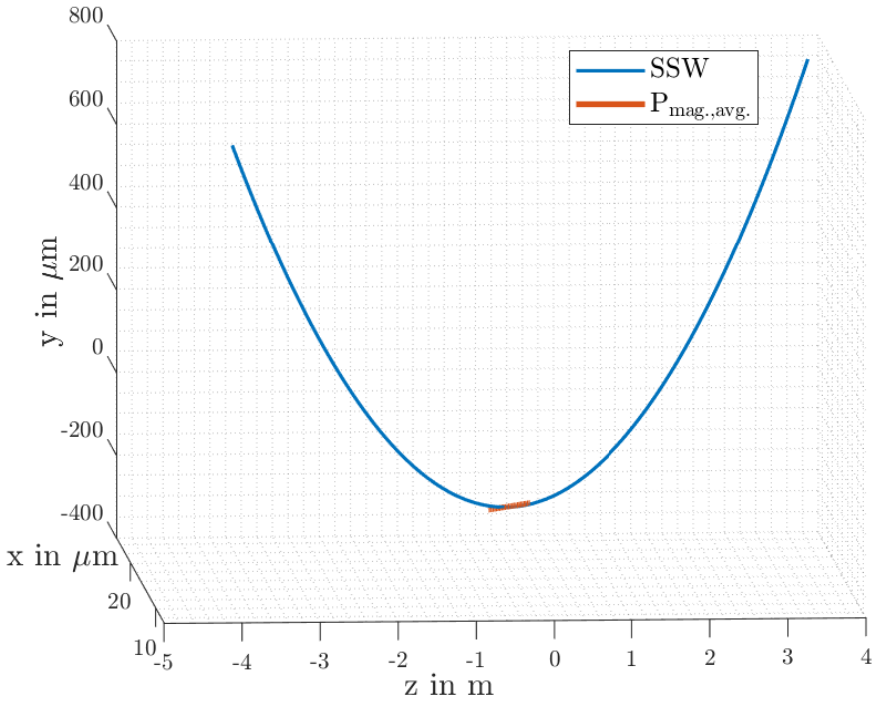

Figure 3.8: Wire trajectory from the SSW measurements of the corrector package. The blue curve shows the trajectory of the wire between the two stages, and the orange line shows the average wire position within the skew quadrupole corrector magnet.

3.4 Proposed Method for Measuring the Longitudinal Magnetic Center and Magnetic Length: "The Translating Coil Fluxmeter"

This section presents the proposed method to measure the longitudinal center of the magnetic field and the magnetic length of the magnet. The system is based on translating induction coils, using Printed Circuit Board technology, PCB, and manual movement to link a changing flux with the coils. It uses the theory presented about translating coil fluxmeters in section 2.4.2 to measure the stationary radial field components of the corrector magnets. The presented method is simple and fast, able to measure the magnetic field of all the magnets in the corrector package in a single measurement, simply set up and moved. Translating coil fluxmeters have been used successfully in previous magnetic measurements, and is a proven measurement method. However, the combination of tangentially positioned induction coils, higher-order magnets, low field values and a simple and easy-to-install setup is to the author's knowledge new to the magnetic measurement society. If proven sufficiently accurate and precise, the measurement system will provide a robust and user-friendly measurement technique for the further measurements of HL-LHC corrector magnets.

The first part of the section presents the general measurement principle, while the next part gives a more detailed explanation of the measurement system; components, measurement principle and post-processing of the measured signal. It also presents the measurements used to determine some key design features of the system, and of the chosen post-processing of the signals.

3.4.1 General measurement principle

A simple layout of the working principle of the measurement head is shown in Figure 3.9 below.

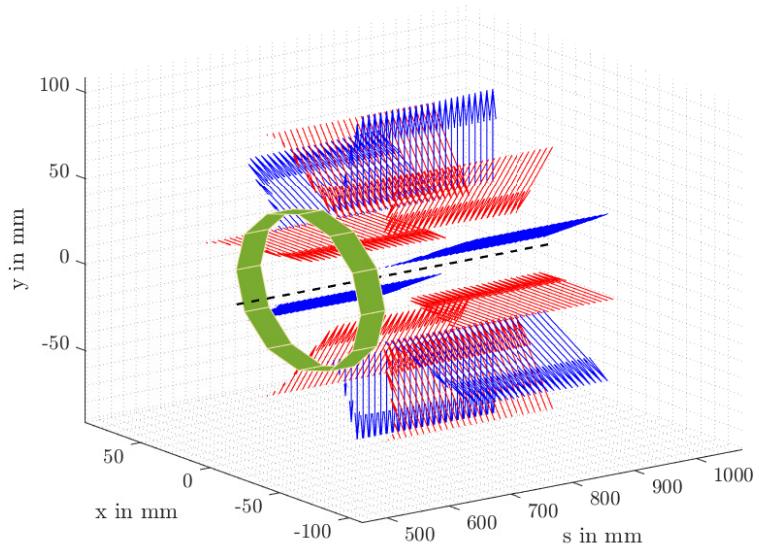

Figure 3.9: Visualization of the translating coil fluxmeter measurement system. The green cylinder shows the principle of the PCBs as they enter the fringe-field region of a dodecapole corrector magnet. The arrows highlight the radial magnetic flux density components flowing to (blue) and from (red) the magnetic poles. The black stippled line shows the integral axis of the magnet, of which the measurement head is moved parallel to.

The magnets are powered in DC mode, giving a stationary magnetic flux density. A set of induction coils, made using PCB technology, are positioned tangentially on a cylindrical measurement head with equidistant spacing. This is visualized as the green cylindrical shape in Figure 3.9. The measurement head is moved manually through the corrector package's aperture by using a guiding rod. As the PCBs are pushed along the magnetic axis, the coils are linked to a changing magnetic flux, and a voltage is induced according to Faraday's law of induction. The voltage is acquired and integrated in time, and as the measurement head moves in the s-direction, the integrated voltage is triggered, giving an array of incremental flux-signals assigned to each longitudinal step, as shown in eq. (2.76), $\Delta\Phi|_{s_\mathrm{m}}^{s_{\mathrm{m}+1}}$. In the post-processing phase of the measurements, these signals are treated to give the longitudinal field profile. The magnetic length is calculated from the field profile using eq. (2.43). The magnetic center is then found where the spatial integral of the flux density on each side is equal, or

$$s_\mathrm{c} \equiv \int_{s_0}^{s_\mathrm{c}} B_r \mathrm{d}s = \frac{1}{2}\int_{s_0}^{s_1} B_r \mathrm{d}s, \tag{3.8}$$

where s_c is the magnetic center of the magnet, and the points s_0 and s_1 are points well outside of the field regions of the magnet.

3.4.2 Measurement setup and approach

The measurement system used for the metrological characterization and validation of the translating coil fluxmeter measurement system is presented below. As this is the first iteration of this translating coil fluxmeter system, each component will be discussed in detail, and the design choices will be explained.

Induction coils

The translating coil fluxmeter measures the radial component of the magnetic flux density through the flux linked with a set of induction coils moved manually through the aperture of the magnet. The induction coils, made with PCB technology, are mounted on the measurement head as shown in Figure 3.10. PCBs consist of alternating conductive and insulating layers. Thin copper windings, in this case with widths less than 35 μm and 17.5 μm for the external and internal layers, respectively, are precisely printed to the surface of the PCB. They can be used to connect components or, in this case, comprise induction coils.

The measurement head consists of a set of 13 PCBs mounted tangentially to the surface of the head. Of these, 12 are mounted equidistantly around the circumference of the measurement head, the centers spaced with 30°. This design was chosen for the first iteration of the measurement system as it dramatically simplifies the design. First of all, due to the flat field gradients for low radii, the radius of the PCBs was chosen to be as high as possible to optimize the signal-to-noise ratio. Secondly, there might be an optimal tangential positioning of the PCBs along the circumference, capturing as much signal as possible for the complete set of corrector magnets. However, as there is no apparent symmetry covering as many magnetic poles with as many PCBs as possible for all the magnets, an equidistant positioning was chosen. An option would be to simulate the induced voltage of different PCB symmetries for the complete corrector package assembly, using optimization algorithms, for instance in COMSOL Multiphysics. This would be a rather time-consuming process, making it infeasible for this project. Furthermore, as the system is moved manually, guaranteeing the correct positioning of the PCBs at all times is very difficult, reducing the effect of optimal coil positioning. Consequently, using equidistant PCBs is an overall good approach for the first iteration of the measurement system. The thirteenth coil is positioned in-between PCB 1 and PCB 12, as shown in Figure 3.10. Since there

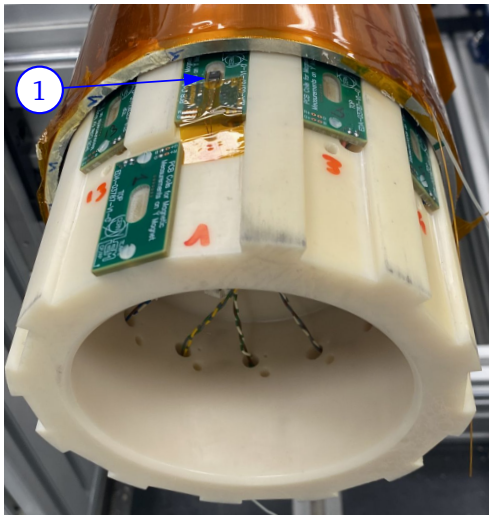

Figure 3.10: The measurement head of the translating coil fluxmeter within the cold bore of the corrector package. Five of the 13 PCBs are shown, and the Hall probe is highlighted by (1).

are only 12 PCBs at approximately the same longitudinal position at any given time, the measured signal of the higher-order multipole magnets might be very low due to symmetries. For example, assuming point-like induction coils, it would be possible to measure zero radial field in a dodecapole magnet. Better signal quality can be achieved by rotating the measurement head between measurements. The thirteenth PCB was added to compare two consecutive measurement runs with a rotation of the measurement head by 15°.

The type of PCB used in the measurement setup is EDA-03787-V1-0, designed and produced at CERN for the Testing and Measurements section. They have 14 layers of copper windings printed on top of each other with thin insulating layers in-between. Each PCB has a calibrated surface of approximately $0.0594\,\mathrm{m}^2$.Each layer has eleven windings, and the layers are connected. The first layer starts at the outer side of the PCB, spiraling eleven times towards the center, with a slightly decreasing radius from turn to turn. At the center, it is connected to the next layer, thus in this layer the coils spiral outwards. The outermost terminals of the first and last layer are connected to the acquisition system to form a closed induction loop. It is important that the connecting wires do not form closed surfaces, as that will pick up changing magnetic flux, giving contributions to the measured signal of unknown quantity. Therefore, the wires leading between the PCBs and the acquisition system are twisted, which can be seen on the inside of the measurement head in Figure 3.10.

The measurement head also includes the option of adding Hall probes in the indentation of the PCBs' centers. One Hall probe was added to the measurement head for the validation measurements of the decapole corrector magnet and can be seen in Figure 3.10, highlighted as (1).

Apart from the measurement head and the PCB assembly, the measurement setup is nearly identical to the one previously used to measure solenoidal field components, as described in [2]. The whole setup of the validation measurements of the translating coil fluxmeter measurements is shown in Figure 3.11. The figure shows the mechanical setup and the measurement rack with all the electronics used in the measurements. It consists of a moving rod, (1), a linear wire draw encoder, (2), the decapole corrector magnet, (3), and a guiding tube, (4). The electronic rack comprises an encoder board (5), terminals for the induction coils (6), a set of digital integrators (7), and the power supply used to excite the magnet (8). Furthermore, the measurements are set up in FFMM, communicating with the user through the built-in computer of the measurement rack.

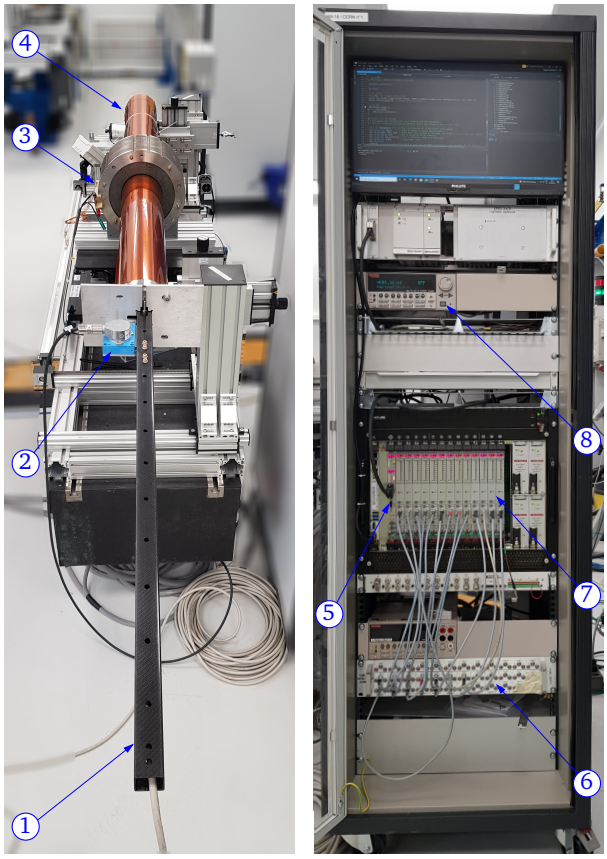

Figure 3.11: Measurement system for the metrological characterization and validation of the translating coil fluxmeter measurement system. In the leftmost figure, the following are shown; carbon moving rod (1), the linear wire-draw encoder (2), decapole corrector magnet and powering connection (3), and the cold bore (4). In the rightmost figure, the electronics are shown; the encoder board (5), the connections to the PCBs (6), the set of FDIs (7), and the magnet power supply (8). The control of the measurement lies with the FFMM-script, controlled by the user of the system through the built-in computer, with the screen shown at the top of the rack.

The magnet is powered using the same power supply as the one used in the rotating single-stretched wire measurement, a 6221 Keithley® AC and DC Current Source. The magnet is powered at maximum output current, 125 mA, with a stability of ±0.001 mA, and a possible current offset of ±0.4 mA.

PCB support, moving rod and guiding tube

The PCB support is the part of the measurement head supporting the induction coils, making the tangential position as constant as possible during measurements. The measurement head is attached to the end of the moving rod, as shown in the figure. It lies within a guiding tube, in this case, a three-meter length of the cold bore[II] that will be used in the corrector package. The circumferential positions of the PCBs need to be as constant as possible. This requires the outer diameter of the support to be as close to the inner diameter of the tube as possible. Still, if it is too tightly assembled, the movement of the measurement head will be too limited. The diameter of the PCB support was therefore chosen to be 136.5 mm, whilst the inner diameter of the tube is 136.7 mm. It was 3D

[II] A continuous tube separating the superfluid helium from the vacuum in which the beams travel[50].

printed using a polymer material, and it is therefore non-magnetic and non-conductive, making it ideal for magnetic measurements. In the end, it was slightly too wide for the cold bore, and to make it fit, we had to sand it down slightly.

The moving rod is made of carbon and consists of two rods joined by polymer bolts. It is used to push the measurement head manually through the cold bore and therefore needs to be sturdy. Carbon is non-magnetic, which is a prerequisite for all the measurement system components. However, all moving parts should also be non-conductive, as moving conductive material through a constant magnetic field induces eddy currents that distort the measured magnetic field. Carbon is slightly conductive, which is a drawback of using it for the moving fluxmeters. However, the radius of the carbon rod is very small compared to the measurement head. Therefore, the field that will induce eddy currents is negligible compared to the magnetic field picked up by the induction coils.

The tube used for guiding the measurement head in these measurements is the cold bore of the corrector package. It is made of the austenitic stainless steel AINSI 316 LN, making it non-magnetic. It is extruded, therefore completely smooth and free from any edges distorting the magnetic flux density. However, it is highly conductive, meaning a changing magnetic field would create eddy currents in the tube. The measurements with the translating coil fluxmeter are conducted with the magnet powered in DC, removing the effect of eddy currents. This is, however, not the case for the rotating single-stretched wire measurements, as discussed in subsection 5.1.1.

The measurement head and moving rod are kept parallel to the tube by the end plate, supporting the wire encoder, as seen in Figure 3.11, (2).

Acquisition system, triggering and spatial assignment of data

As discussed in subsection 2.4.2, the induced voltage of the fluxmeter is acquired in time by the acquisition system and the set of digital integrators. The FDIs read and, by the trapezoidal rule, integrate the voltage at 500 kHz. The integrated voltage signals are triggered to yield incremental delta flux-values $\Delta\Phi|_{t_i}^{t_{i+1}}$. To get the spatial distribution of the flux density, the triggered signal is assigned to a certain distance in space between the point of the previous trigger and the present trigger point. Therefore, as discussed in subsection 2.4.2, the flux measurement is now transformed from a time-based signal to a spatial measurement distribution.

There are a few different methods to trigger the integrators, two of which were applied in the measurements, and compared and discussed in this thesis:

Linear wire draw encoder:

The triggering system shown in Figure 3.11 is a wire draw encoder. It consists of a highly flexible stranded steel wire wound onto an enclosed bobbin. The encoder is incremental, meaning it gives the relative movement from the starting point. The bobbin rotates when the wire is pulled, and electrical trigger signals are sent to the encoder board. The number of trigger signals per revolution of the wire bobbin depends on the wire encoder.

The SICK PFG08-P1AM03PP EcoLine wire draw encoder was used for translating coil fluxmeter measurements, presented in [51]. It comprises a 3.2 m highly flexible stranded steel 1.4401 stainless steel V4A wire, with a measuring range of 3 m. One revolution of the bobbin corresponds to 230 mm, and with $2^{16} = 65536$ trigger signals per revolution, the maximum reachable resolution is approximately 3.5 μm. The encoder signals are sent to the encoder board. In the encoder board, the signals can be down-sampled by a decimation factor n, meaning only the $n^{\text{th.}}$ trigger signal is used to trigger the FDIs. Since the trigger frequency of the wire encoder increases linearly with the velocity at which the measurement head is moved, using too low decimation factor, i.e. higher resolution, results in a saturation of the FDIs. This will give losses in the data sampling, invalidating the correspondence between the flux density measurement and the longitudinal sampling. Therefore, a decimation factor

of 32 or 64 is typically applied, giving resolutions of 112.3 and 224.6 μm, still sufficient to determine the magnetic center and magnetic length within the requirements. Furthermore, since the signal data stems from the acquisition of 500 kHz, the signal can be re-sampled to obtain a higher resolution, if needed. Since the encoder is only incremental, to have the absolute position, the initial position of the measurement head must be measured precisely, preferably with a laser tracker.

The wire encoder has a reproducibility of less than 300 μm, linearity of less than ±2 mm, and a hysteresis of less than 1.2 mm [51]. The linearity describes the encoder's accuracy and gives the maximum deviation for measuring a defined path. The reproducibility is given as the maximum scatter from consecutive positioning measurements to a point from the same direction, and the linearity describes the same as the reproducibility, but with movement from a different direction. The accuracy of the wire measurements is relatively low, considering the maximum uncertainty of the measurements of 10 mm. Furthermore, before the encoder starts triggering, it is armed by at least one full, and at most nearly two, revolutions of the wire bobbin. This makes the absolute positioning of the system rather tricky, as the first trigger point might not be given at the same position from measurement to measurement. One alternative is to measure the last point with the laser tracker instead of measuring the initial point. From this, the absolute positions can be recreated going backward.

Its main advantage is the simple design. Attaching the encoder to the end plate and the wire itself to the measurement head is sufficient to measure the complete corrector package quickly. Furthermore, it mitigates the effect of external noise, which laser tracker systems suffer more from.The nominal velocity of the wire encoder is 4 m/s. This is way above the speed we can pull the moving rod, and a velocity of approximately 0.13 m/s is achieved in the measurements. Therefore, a metrological characterization of the wire encoder itself will be conducted in the next chapter to investigate its ability to yield reproducible and accurate longitudinal triggers.

Time-based laser tracker measurements:

The second system to correlate the magnetic measurements to the spatial domain is a time-based triggering of the Leica AT930. The layout of the system is presented in Figure 3.12 below.

The idea behind this mechanical measurement method is to measure the location of the measurement head in a scan with the laser tracker. According to its specifications, the precision of a scan is given as ±0.5μm/m. In the setup of the measurements of the complete corrector package the maximum distance from the laser tracker to the target is approximately 8 m, resulting in a worst precision of ±4 μm. The target is measured with a given internal frequency of 1000 Hz, with the output triggered by an external system. The wire draw encoder or a time-based triggering can give the external triggers. The laser tracker cannot be triggered by more than 1000 Hz, and it was seen that triggering it by the wire encoder gave less control in the trigger rate. This results in a less reliable measurement system, as pulling or pushing the measurement head too fast could result in lost information. Therefore, time-based triggering was opted for. It uses a programmable National Industry PXI-6289 multifunction I/O module to give an output triggering frequency with an absolute accuracy of ±1% [52]. In this configuration, the encoder board is substituted by the I/O module, which then triggers all the FDIs and the laser tracker in series. This enables us to measure the mechanical position by the laser tracker without exceeding its trigger frequency range, staying well beneath this at 800 Hz.

Another advantage of this system is that it gives the position of the measurement head in more than just the longitudinal direction. The manual movement of the measurement head necessarily gives a slight offsets of the PCBs with respect to their nominal position, both rotations of the measurement head and transverse movement. Even though a single measurement point is not sufficient to determine precisely the nature of the movement, the knowledge about any other movement other than along the s-axis will help determine the magnetic measurement's validity.

Figure 3.12: Leica AT930 laser tracker setup for the validation measurements of the translating coil fluxmeter measurement system. It shows the laser tracker, (1), the fixed target on the inside of the measurement head, (2), and the target on the external fiducial of the magnet, (3).

The drawback of this triggering setup is mainly the resolution of the measurements. As the velocity varies during the measurements, the measured and sampled incremental fluxes will not be equidistantly spaced. Even so, with a measured average velocity of 0.134 m/s, and a triggering frequency of 800 Hz, the average resolution of the measurement is 167.5 μm, similar to the wire draw encoder, even though this could be quite a lot higher for some positions, as the movement is uneven.

Measurement approach

Once the measurement system is set up, with the appropriate device for triggering and assigning the spatial position, the measurement approach is quick and straightforward. The magnet is powered, and through the interface of FFMM, the FDIs and either the encoder board or the I/O module is initialized and started. When the PCBs are moved through the stationary magnetic flux density, it induces a voltage acquired by the FDIs, integrated and output by one form of an external trigger. The movement of the PCBs is at this stage of the system development based on manually moving the measurement head by the moving rod. To avoid mechanical instability, the movement should be as constant as possible and neither too fast nor too slow, to obtain a higher resolution and better signal-to-noise ratio. The data is written to text files, where the data from the internal clock, Hall probe measurement, and acquired and integrated $\Delta\Phi$-signals are stored.

Data refinement

In the post-processing phase, the incremental flux signals are treated to get the flux density distribution along the axis of the magnet. As the output of the FDIs are given as incremental flux signals, $\Delta\Phi|_{s_i}^{s_{i+1}}$, the signal is cumulatively summed to give longitudinal distribution of the flux measurement. Matlab's *cumsum*-function is used for this operation, presented in [53]. When cumulatively summing a signal, any small deviations from the actual flux linkage is increased over the course of the measurement. This is especially an issue with the drift in the integrators, an assumed constant offset, which results in a linear divergence of the signal when summed. This is particularly the case for the room temperature magnetic measurements of the corrector magnets, as their field strength is low, yielding a low signal-to-noise ratio when the integrator drift is added. To mitigate this effect, two measures are taken. Most of the drift can be compensated for by subtracting the average of the signal before the cumulative sum is applied. As the integrated induced voltage will have an average of zero, since the fluxmeter is moved to and from longitudinal positions well outside field regions. Thus, the average of the incremental flux measurements stems from drift and other constant components of noise. However, the noise and integrator drift might not be constant, and a slight linear increase of the measured signal is still observed after the cumulative sum. Therefore, confining the part of the signal that will be cumulatively summed to as small an interval as possible reduces the effect of the noise. The interval should be chosen such that it covers a minimal zero-field region, but it should still cover both fringe field regions. Deciding this interval is usually based on prior knowledge of the field, or from simply assessing the field distribution, and adjusting. The mechanical position of both ends of the magnets can also be used as a first assumption, or other sensors included in the measurement system can be utilized. For the validation measurements, the Hall generator is used to determine the position of the roll-off[III] of the magnetic field. The advantage of the Hall probe is that directly gives the shape of the flux density of the magnet. The Hall probe installed in the measurement head, see (3) in Figure 3.10, is of the type Analog Hall Sensor HE244, from Advanced Sensor Technology, AST. It has a linearity of less than 0.2%, typically 0.1%, a large magnetic field range, and 2 mA nominal supply current [54]. The Hall probe is powered by an Analogic Data Precision 8200 power supply [55]. To smoothen the noisy Hall voltage, it is fed through an integrator. Therefore, we divide by the time increments to obtain the Hall voltage from the integrated signal. Then, the Hall voltage is used to find the limits of the field values, where a limit of 30 μT is used to give the correct positions of summation, with an additional offset added to each side of the interval. This is applied to the signal from both pulling and pushing the moving rod, splitting the signal into two separate runs. The laser tracker data, giving the spatial position of the measurement head, is selected to correspond to the new intervals.

Once the spatial distribution of the flux measurements is given, the data is treated to give the longitudinal center of the magnet and the magnetic length. Firstly, the signals from the 12 induction coils are averaged, to give one signal per measurement. This reduces the effect of mechanical instability of the measurement, and it is based on the assumption that if the transverse movement of the measurement head reduces the induced voltage in an induction coil, the coil displaced by 180°will measure an equally larger signal. Therefore, averaging all the signals makes the system more robust to the likes of vibrations. However, a rotation of the measurement head might increase or decrease the signal in each coil, depending on the symmetry of the field with respect to the positioning of the coils. A pure averaging of the signal would in most cases reduce in nearly zero measured field, again due to the symmetry of the magnetic field. Therefore, half of the signals are inverted before they are averaged.

Then, the signals are resampled to increase the resolution, and in the case of time-based triggering, to transform all measurements to the same spatial basis. The s-axis is recreated from the

[III]The intervals on each side of the magnets with increasing or decreasing field.

first and last spatial point of the chosen window, for the first measured signal, to produce a set of N equidistant points, where N gives the resolution of the new longitudinal axis. This is used as the new spatial basis, and all the other measurements are linearly interpolated to fit this.

At this stage, there are a few different approaches to how the measurement data is treated. The first is to divide the flux values by the calibrated surface area of the coil, to obtain the flux density in the simplest approach. Strictly speaking, this does not yield the correct flux density distribution, as the signal is the convoluted signal of the actual flux density and the sensitivity functions of the PCBs, as discussed in subsection 2.4.2, and shown in eq. (2.78). In another way, it can be explained as a filtering and smoothing of the flux density, where the windings of the PCBs measure the same flux density at different longitudinal positions. This filters the signal, and the resulting distribution has a less sharp roll-off, meaning some higher frequency components of the signal is lost. As a consequence, the rising and falling edges are less steep than in the actual flux density. To account for this, the signal can either be deconvoluted with the sensitivity function of the induction coils, or it can be fit with a basis spline function. Both approaches will be explained in this section, before the two methods will be investigated in the validation measurements of the system.

Solving the equations for the Fourier series along s:
From the theory presented in subsection 2.4.2 for the translating coil fluxmeters, the sensitivity functions of the coil measurement is convoluted with the actual flux density. Deconvoluting this directly using the sensitivity functions can be achieved in several ways. The flux density distribution can be found through the inverse Fourier transform of $\mathcal{F}\{\Delta\Phi\}(\omega)/S^c(\omega)$, where S^c is the sensitivity function in the frequency domain, and $\mathcal{F}\{\Delta\Phi\}(\omega)$ is the Fourier transform of the measured flux increments. Another approach is to use a least squares-estimation of the errors by solving the equation

$$\mathbf{\Phi} = \mathbf{H} \cdot \mathbf{c}, \tag{3.9}$$

where $\mathbf{\Phi} = (\Phi(s_0), ..., \Phi_M)^T$ is the array of measurement points along the s-axis, $\mathbf{H}$ is the measurement matrix including the sensitivity functions of the all the induction coils and step sizes, and $\mathbf{c} = (c_{-K}, ..., c_K)^T$ are the complex Fourier coefficients of the flux density, truncated at positive and negative frequencies K. The latter stems from the truncated Fourier series of the radial flux density component along the s-axis:

$$\overline{B}_r(s) = \sum_{k=-K}^{K} c_k e^{2\pi j k \frac{s}{L}}, \tag{3.10}$$

where K is the truncation frequency, c_k the $k^{\text{th.}}$ expansion coefficient, and L the total length of the measurement, in meter. The sensitivity matrix is found by integrating the flux density over the surface area of all the induction coils, and by assuming a constant flux density in the azimuthal direction. This way, it can be shown that $H_{m,k}$, corresponding to the $m^{\text{th.}}$ measurement position and the $k^{\text{th.}}$ frequency component, is given by

$$H_{m,k} = \sum_{i}^{I} \int_{s'=s_m - l_i/2}^{s_m + l_i/2} w_i e^{(2\pi j k \frac{s'}{L})} \mathrm{d}s' = \frac{L}{\pi k} \sum_{i}^{I} w_i \sin(\pi k \frac{l_i}{L}) e^{2\pi j k \frac{s_m}{L}}. \tag{3.11}$$

In the equation, the element is summed over all I induction coils, with lengths l_i and widths w_i [33]. By expanding the last terms of eq. (3.11), and by remembering that the $k^{\text{th.}}$ frequency of the Fourier series is given as k/L, it can be seen that they are in fact the same sensitivity functions as described in eq. (2.68). Eq. (3.9) is solved for $\mathbf{c}$ by the least squares method, which is solvable since we measure with a high resolution, giving a lot of measurement points, and truncate the signal at $K = 130$, thus the equations are overdetermined.

At this stage, the only unknown parameters are the lengths and widths of the PCB coils. As they are in fact spirals, and at several radial positions, a few simplifications are applied: First of all, it is assumed that the signal strength is equal over the height of the PCB, so the sensitivity factors are the same, and can be achieved by multiplying by the number of layers. As the PCB is 2.5 mm high, this gives a slight error, at maximum approximately 50 μT for the quadrupole[IV], which is tolerable for our purposes. Furthermore, as any error is scaled equally, this will have no effect on the calculation of the magnetic center or the magnetic length, as the center is purely a calculation of the field shape, and the error will cancel in the calculation of the magnetic length, where it is multiplied in the integral, but also in B_0, see eq. (2.43). The next assumption is that the spirals can be approximated by rectangles, which greatly simplifies the calculation of the sensitivity factors. It could be calculated through the curl of the A-field linked with the line segments of the PCB tracks, but for the first iteration of the measurement system, the slightly simpler approach was opted for. The PCB tracks were imported, and from this the rectangles could be estimated. For a spiral, the widths and lengths of a turn is never the same twice, and choosing one side over the other creates a larger or smaller surface area in total. The total surface area of the reconstructed, simplified PCB was compared to the calibrated surface, and the design with the highest correspondence was chosen. Then, in the deconvolution, the relative difference between calibrated and calculated surface area is included, to account for the slight difference. The resulting PCB coils are shown in Figure 3.13 below. In the figure, the PCB tracks dis-

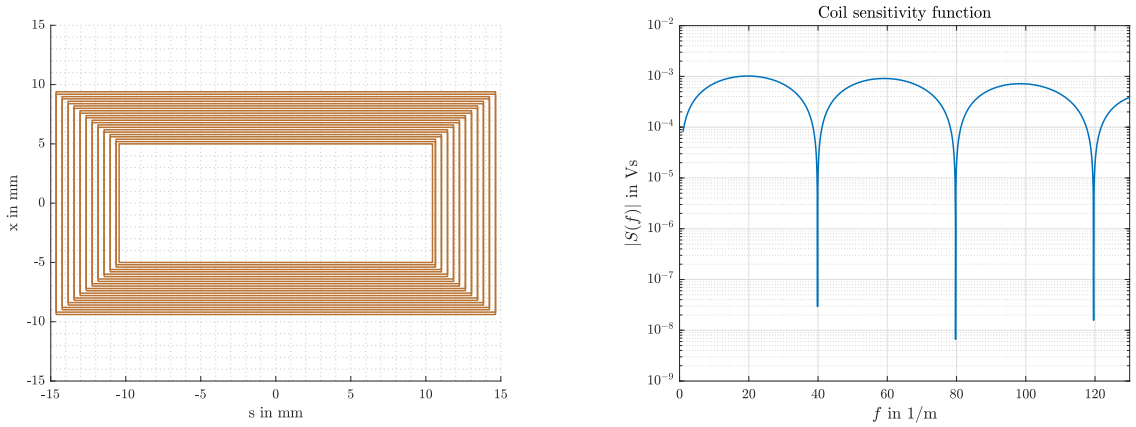

Figure 3.13: The approximated rectangular windings of the PCB (left) with the resulting sensitivity function calculated from eq. (2.68) of the PCB.

plays more than eleven windings. In fact, 23 rectangles can be seen, since it is a combination of two layers. Every second layer is slightly wider than its neighbouring layers, as there is a slight shift in tracks used in the design. Furthermore, the innermost rectangle is always continued in the next layer, giving the additional turn for every second coil. Therefore, in approximating the turns by rectangles, 23 rectangles are used, and only 7 layers. At the right side of Figure 3.13, the sensitivity function of the rectangular coils is shown. It is clear that the PCB suffers from three blind-eye frequencies below the cutoff frequency of 130 Hz, and we would expect this to give large oscillatory behaviour in the deconvoluted signal. This effect will be investigated in the validation measurements of the system. From the rectangles, the widths and lengths are used for defining the measurement matrix elements.

*B-spline approximation of the **B**-field:*

[IV] Calculated in the following manner: $\Delta B_r \approx (I_{298K}/I_{1.9K}) \cdot g_2 \cdot \Delta r = 0.105/174 \cdot 34.9\,\mathrm{T/m} \cdot 0.0025\,\mathrm{m} \approx 0.05\,\mathrm{mT}$, where g_2 is the quadrupole field gradient, and the fraction scales the values to the room-temperature measurements.

The last approach considered in this thesis, is to approximate the **B**-field by a set of basis spline functions. The approximation is based on the same idea as the Fourier series approach; the field can be represented using a set of basis functions, summing them up to acquire the correct field distribution. The b-spline approach is, however, a more adaptable approach, as the splines themselves are defined only on a certain interval [34]. Therefore, the sharp edges in the roll-off of the magnetic field that gives a significant amount of higher-frequency components in the Fourier analysis, causing oscillations due to the sensitivity function of the PCBs, are instead fit only locally with the b-splines without the problems of propagating oscillatory behaviour to flatter parts of the distribution. There is another main difference; where the frequency resolution is fixed for the Fourier series approach, and only the coefficients are determined from the inverse calculation, the solution with b-splines is given in an iterative manner. We start off by splitting the interval into seven equally large parts, and then the intervals are iteratively split into two where it is needed to reduce the error made by the spline approximation.

In the following, the main steps of the deconvolution process using b-splines are explained: The s-axis is split into seven equally long intervals. From this, the knots used in the first iteration is found using the *augknt*-function implemented in MATLAB, see [56], for the chosen order of the spline. In this case it was chosen to operate with fourth-order polynomials. Then, the coils' sensitivity to the different spline functions are calculated, and stored in a similar measurement matrix as discussed above. This is calculated in the same way as the measurement matrix elements in eq. (3.11), but with the integration of the splines along the length of the individual coils. The splines are made using the function *spmak* implemented in MATLAB, presented in [57], with the knots from the previous step. To calculate the sensitivity of all the polynomial in the spline interpolation, the contribution to the magnetic flux density from each of the spline polynomials is evaluated for each of the coils in the PCB. Together, the total sensitivity of the PCB to measure the spline components are stored in a measurement matrix, **D**, similar to **H** in eq. (3.9). With the measurement matrix at hand, the coefficients of the basis spline approximations of the magnetic flux density is given by the vector **a**, which is found by solving the following matrix equation

$$\mathbf{\Phi} = \mathbf{D} \cdot \mathbf{a}, \tag{3.12}$$

for **a**. Even though obtaining the flux density from the flux picked up by the induction coils yield the wrong field distribution, the flux measurements themselves are correct. Therefore, by the least squares solution to eq. (3.12), the technical definition of the measurement matrix and the abstract spline approximation is connected to the physical magnetic measurement, ensuring our approximation is correct. In other words, the flux density obtained is approximated in a way such that the flux linkage with the PCBs would induce the same voltage as the physical measurement did. After **a** is found, the flux density is approximated by the splines made with the knots already created and the coefficients of **a**, evaluated along s. As eq. (3.12) is solved by a least squares approach, there are residuals between the physical flux measurement, and the flux measurement recreated by solving eq. (3.12) with **D** and **a**, yielding $\mathbf{\Phi}_{\text{rec.}}$. The residuals exist on the intervals between the knots. By refining the knots, the residuals are reduced, as we add another interpolation point, where a fourth-order degree polynomial can be fit. Therefore, the interval with the biggest error is split in two, and the full process of designing the measurement matrix, solving for **a**, and calculating the flux density is repeated until the residuals are acceptable. However, by over-refining the splines, oscillatory behaviour is experienced. There is, therefore, an optimal solution to the iterative process.

The elements of the measurement matrix can be seen together with the calculated flux density after five interval refinements in Figure 3.14. It is clear that the refinements have been applied where the magnetic field is measurable, and especially in the field in the central parts of the magnet. This is

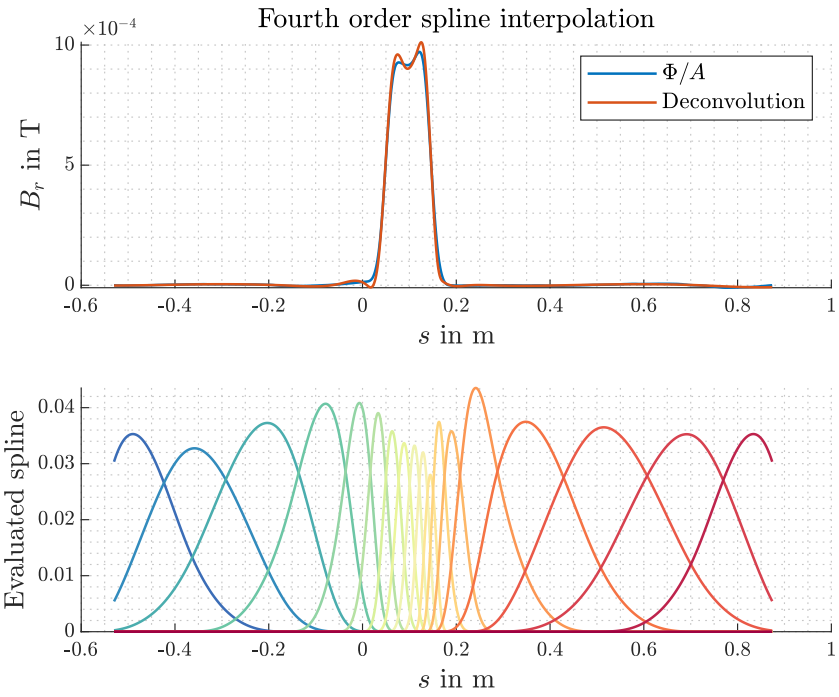

Figure 3.14: Flux density calculated using a simplified Φ/A approach, and deconvoluted by fourth order basis spline functions, together with the b-spline functions after five refinements of the evaluation intervals.

seen from the shorter intervals between knots, compared to the splines far outside of the field region.

In Figure 3.15, the resulting magnetic flux density is shown after one, five and nine iterations. In the lower plot, the residuals are plotted together with the knots at each iteration. It is clear that the first approximation is way too crude. This is also shown from the residuals, which are in the order of 10^{-2} relative to the field level. However, it is seen that after just five iterations, the field matches the expected distribution very well, with residuals a hundred times less than for a single iteration. Finally, with nine iterations, the flux density is exactly how we would expect, with residuals in the order of 10^{-8}.

As we can see from Figure 3.15, the flux density distribution approximated by fourth order basis splines has a sharper roll-off, and a longer interval of constant field. This is what we would expect.

The different methods of obtaining the flux density distribution, magnetic center and length of the corrector magnets will be investigated in the validation measurement campaign of the translating coil fluxmeter.

Calculation of magnet center and magnetic length

With the data processing finalized, the center of the magnet and the magnetic length is calulated. According to eq. (3.8), the magnetic center is found where the integrals of the magnetic flux density looking both sides along the longitudinal axis are equal. Therefore, the magnetic center is found in the post-processing phase by integrating the flux density from both sides, and choosing the position where the two integrals are equal:

$$\int_{s_0}^{s_c} B_r \mathrm{d}s = \int_{s_1}^{s_c} B_r \mathrm{d}s. \tag{3.13}$$

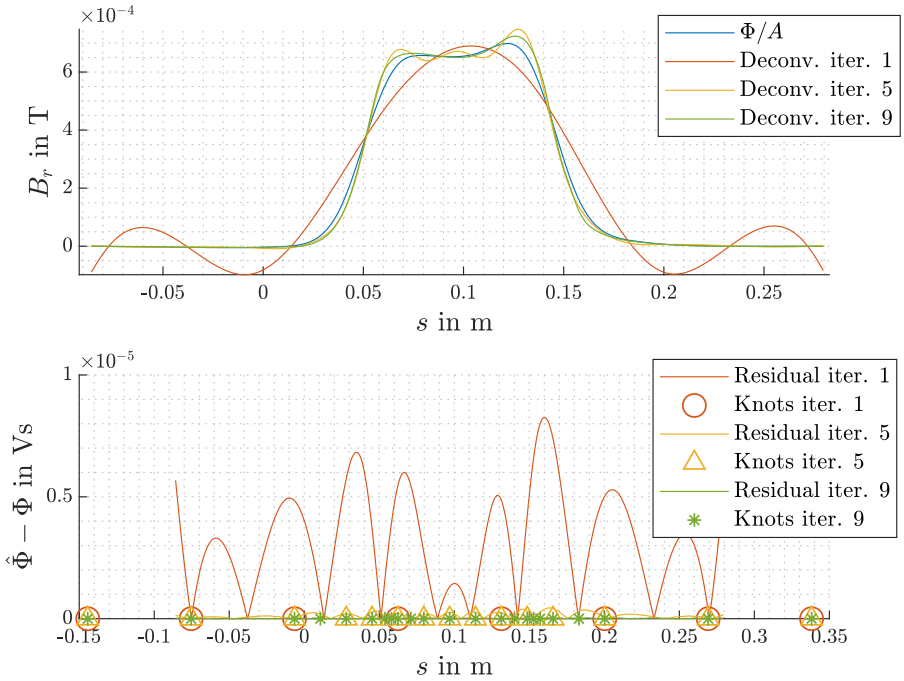

Figure 3.15: Deconvolution process for one, five and nine iterations, showing both the flux density distribution (topmost graphs), and residuals and corresponding knots (bottom). The simplified approach of Φ/A is used for comparison .

The magnetic length is then calculated using eq. (2.43), choosing $B_{r,0} = B_r(s_c)$.

Chapter 4

Metrological Characterization of the Proposed Methods

It is important to validate the measurement techniques before the full corrector package is measured. Therefore, in the first part of this thesis a set of measurements were conducted on the decapole corrector magnet to validate the proposed measurement methods. The aim of these measurements is to investigate whether or not the proposed methods are able to measure signals exceeding the noise floor, that the correct magnetic axis, roll angle, longitudinal centre and magnetic length can be located, and with what certainty the results can be presented. In total, *metrological characterizations* of the measurement techniques are required. This means stating the uncertainties of the measurement systems, found as their precision and accuracy of measuring the measurands.

This chapter presents these measurements with a focus on explaining the tests and what they are designed to investigate, as well as the significance of the results. It is concluded with a discussion of the validity of the measurement methods, as well as draw-backs and key points to consider in the further measurements of the corrector package.

4.1 Metrological Characterization of The Rotating Single-Stretched Wire Method

The single-stretched wire measurement method will be used to locate the integral magnetic axis and the roll angle of the corrector magnets within the corrector package. A metrological characterisation is necessary to validate that the method gives these properties of the magnet, and that they are correct. Showing that the technique works for any given magnet is insufficient. It is also important to know that the method can give the integral axis and roll angle of the *corrector magnets*, measured at *room temperature*, with the challenges presented in section 3.2.

The main challenge with validating the measurement method is that the integral magnetic axis is not yet known for the corrector magnets and, as discussed in section 3.2, the field values are too low to use standard measurement methods for finding it. As mentioned above, we cannot simply use another magnets for the validation measurements, as it is necessary to know that the measurements work as intended on the corrector magnets. The solution to this issue is the following:

1: As a first approach, the rotating single-stretched wire measurement method is used to locate the magnetic axis and the field phase of the decapole corrector magnet. This is continued in a series of measurements, where known offsets, both transverse and rotational, are applied to the measurement coordinate system, with the aim of measuring the same displacement from the magnetic measurements. From the measurement in each position, the mean and the spread, i.e. the standard deviation, of the measurand is obtained from several measurement repetitions. The series of displaced measurements gives the consistency in the averaged results, meaning the ability of the system to determine a precisely imposed offset in the measurand. Together, the spread and consistency gives the precision of the measurement system.
   If the measurement campaign yields a sufficiently good precision, the next measurement campaign will be launched:
2: A more powerful quadrupole magnet is measured using both the rotating single-stretched wire method and the standard measurement of magnetic axis and roll angle, using symmetries in the DC powered magnet. The resulting axes and roll angles are compared, and the integral axis and roll angle found using the standard DC measurement is used as a benchmark for how well the rotating single-stretched wire method performs in locating the axis and roll angle. This approach enables us to determine the accuracy of the measurement method.

Together, the two validation measurements determines both the accuracy and the precision of the rotating single-stretched measurement method. Measuring several times also gives the repeatability of the measurement method, validating whether the method is able to locate the magnetic axis and roll angle of the corrector magnets measured at room temperature.

In the following sections, each of the above-mentioned measurements will be presented. The setup and ideas behind the measurements will be described, and the results will be presented. The validation measurements of the rotating single-stretched wire will be concluded with a discussion of the results.

4.1.1 Characterization measurement 1: Measurements of the decapole corrector magnet

Measurement setup and principle

The measurement setup for the validation measurements on the decapole corrector magnet is the one shown in Figure 3.2, and explained in detail in subsection 3.3.2. The wire bench used has a calibrated

roll angle of -0.008 mrad. For simplicity, a summary of the parameters used is presented in the following table. These measurements are performed in a highly stabilised mechanically and thermally laboratory belonging to the Testing and Measurements section. The environment is therefore to a large extent controlled, and well suited for the measurements of low fields.

Table 4.1: Measurement parameters used for the validation measurements.

Parameter	Used value
Excitation current amplitude	105 mA
Excitation current frequency	23 Hz
Sampling frequency	1024 Hz
Acquisition time	8 s
Circumferential measurement points	256
Calibrated roll angle offset	-0.008 mrad

The measurements are designed to investigate how well the rotating single-stretched wire measurement technique is able to locate an imposed offset, either a transverse offset of the measurement coordinate system, or of the roll angle. As the magnetic axis is unknown for the decapole corrector magnet, this measurement is only valid for measuring the precision of the method, as well as validating that it is able to measure more than just noise.

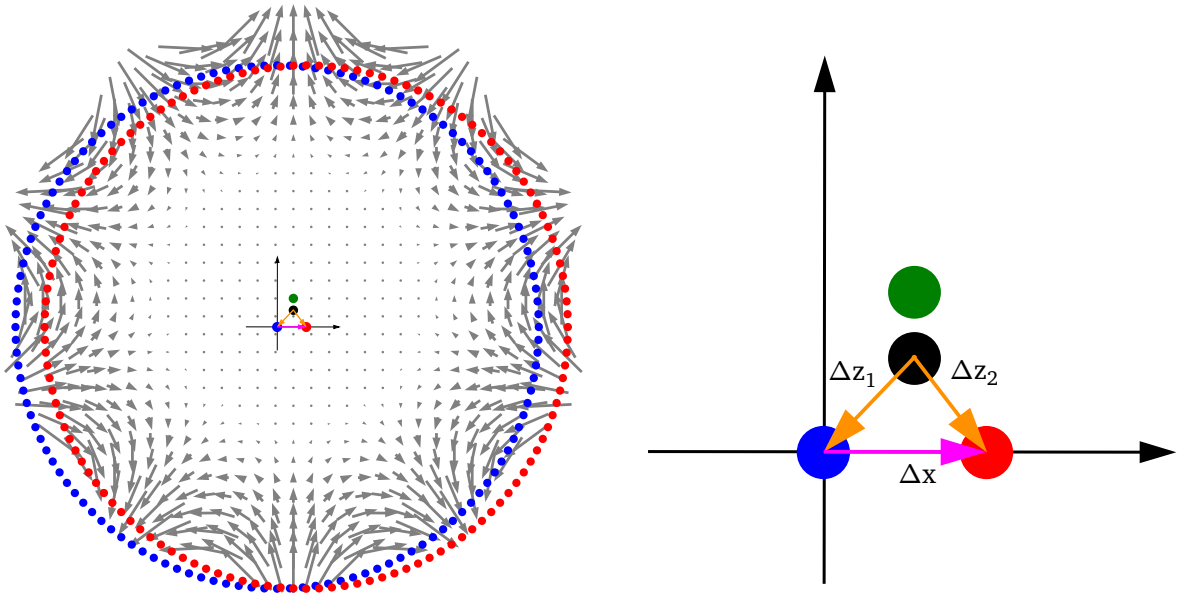

Figure 4.1: Visualization of the measurement process with displaced measurement axis, where the rightmost figure is a zoomed version of the figure to the left. The blue dots show the measurement trajectory of the first measurement, whilst the red dots show the trajectory after the wire stages have been moved in the horizontal plane. The black dot shows the measured magnetic axis in the two cases, and the green dot shows the actual magnetic axis in both cases. The black coordinate system is the coordinate system of the initial measurement. Δz_1 and Δz_2 shows the resulting offset vectors from the two measurements, and their difference gives the vector Δx. The effect of the axis offset is highly exaggerated for visual effects.

A visualization of the measurements is presented in Figure 4.1. The principle of the measure-

ment is that even though the true axis of the decapole is unknown, making it impossible to evaluate the measured magnetic axis, if the measurement technique is able to consistently locate imposed offsets, the precision of the measurement technique is good. The measurements are conducted in the following way: First, the integral magnetic axis is measured with the initial position close to the geometric center of the magnet, and the resulting offset is found to be Δz_1. This measurement is seen as the blue dots in Figure 4.1, with the initial position shown as the blue dot in the centre, and with the measurement coordinate system shown. Then, the wire stages are moved to another initial location in the complex plane, namely the red dot in the center of the red dotted circle. For simplicity, the figure shows a purely horizontal displacement, Δx. The integral axis is measured again, with measurements in each of the positions highlighted by the red dots, and the offset vector Δz_2 is found. Now, if the two measurements found the same magnetic axis, the difference of the two will give the same displacement as was imposed on the measurement system, $\Delta x = \Delta z_2 - \Delta z_1$, down to the precision of the wire stages' movement. This is particularly the case when the displacement is in both the vertical and horizontal plane. The measured magnetic axis is shown as the black dot in the figure, whilst the green dot highlights the true magnetic axis of the magnet. It is important to note that the two axes, measured and true, are not necessarily the same, even though the same magnetic axis is measured in both the measurements, as a constant offset in both measurements would cancel when the two vectors are subtracted. This is the drawback of the measurements with imposed displacements; the accuracy of the measurement method cannot be inferred, as the true magnetic axis remains unknown.Even so, the measured axis with respect to the external fiducials of the magnet is presented, after being aligned to gravity, and the result is compared to results obtained with the AC Mole, in the work presented in [39]. The wire stages are then moved to several initial positions, both horizontally and vertically, and the difference of the found axis offset is calculated with respect to the first measurement.

The same approach is followed for the roll angle. In this case, the initial wire position remains the same throughout the measurements, as the roll angle is independent of the measurement location. As was discussed in subsection 2.2.2, the roll angle is the negative of the rotation needed to make the magnet purely normal. This could mean that when applying an external angle, the resulting roll angle would not at all give the correct difference, as the result is always uniquely determined on the interval $[-\pi/2, \pi/2]$. This naturally depends on the initial roll angle of the measurement setup, and on the externally applied rotation. Therefore, to simplify the measurements in the metrological characterization, instead of the roll angle the field phase is used, as this should give the correct difference in case of a too large imposed angle. The field phase presented is given in the mechanical reference system, namely $\varphi_{roll} = \varphi_N/N$, and will in the following be referred to as the external field phase. First, the external field phase is measured in a standard measurement, where the first circumferential point is located with an angle of $\theta = 0°$ to the horizontal axis, and the found external field phase is given as $\varphi_{roll,1}$. The next measurement comprise an offset angle of θ_{imp}, an angle that is applied to the wire stages by calculating the first circumferential point, so that the vector spanned by $P_1 - P_0$ gives the correct offset angle to the horizontal axis. The found external field phase of this next measurement is given as $\varphi_{roll,2}$, and if the same field phase is found in both measurements, the difference will give the imposed angle: $\varphi_{roll,2} - \varphi_{roll,1} = \theta_{imp}$. As for the axis offset measurements, any constant offset of the angle would also give the same offset angle back, since this effect would be cancelled. Therefore, the angular offset of the wire stages is omitted in these measurements.

Measurement results

The results of the characterisation measurements are presented in this section. All measurements were repeated five times, and the presented results are the averag of the results. The spread of the signal is calculated as the standard deviation of the measurand over the five repeated measurements. It is calculated using the *std*-function in MATLAB [44], and it is reported at 3σ, i.e. three times the standard deviation, to be comparable to the requirements of the corrector package, as presented in section 3.1.

Measured displaced axis

The results of the measured displacements from the magnetic axis are presented below. The measured offsets from the axes are calculated using eq. (2.52), for simplicity repeated below:

$$\Delta \mathrm{z} = \Delta \mathrm{x} + i\Delta \mathrm{y} = -\frac{R_{ref}}{N-1}\frac{C_{N-1}}{C_N},$$

where Δz is the vector pointing from the measurement axis to the magnetic axis, and N is the main multipole component of the magnet, with $N = 5$ in the case of the decapole corrector magnet.

The figure below shows the results from one of the displacement measurement campaigns, where displacements are applied in both vertical and horizontal directions. The red dots highlight the offsets measured with the rotating single-stretched wire method relative to the initial measurement, and the centers of the blue circles show the actual displacement of the wire stages. Note that the blue circles are drawn as empty circles only to better show the relative position of the red dots, and their radii are not supposed to highlight any significant aspect of the measured result. The same results as the ones shown in Figure 4.2 are presented in Table 4.4, and Tables 4.2 and 4.3 gives the results of more displacements measurements, purely in the horizontal and vertical direction, respectively, and with larger step sizes.

The tables show the applied offsets on the wire stages as $\Delta \mathrm{z}_{\mathrm{ws}}$, the absolute offsets in the specific location found through the magnetic measurement as $\Delta \mathrm{x}_{\mathrm{mm}}, \mathrm{y}_{\mathrm{mm}}$ and the relative measured magnetic axis from the initially measured axis as $\Delta \mathrm{x}_{\mathrm{rel}}, \mathrm{y}_{\mathrm{rel}}$. These values are given without accounting for the wire saggita, since this gives a constant offset that will cancel as only the difference between measurements are considered. All the values are given in units of $1\,\mu$m, and with the spread of the measurand at 3σ. When calculating the difference of the measurements, the spread of the result is calculated by the formula for propagated standard deviations, $\sigma_{prop.}$, which when assuming non-correlated measurands A and B with standard deviations σ_A and σ_B is given by

$$\sigma_{prop.} = \sqrt{(\sigma_A^2 + \sigma_B^2}. \tag{4.1}$$

The difference between the measured magnetic axis, and the measured mechanical axis, using Leica AT930 for fiducialization, was calculated as

$$(\Delta x, \Delta y) = (124\,\mu\mathrm{m}, 83\,\mu\mathrm{m}),$$

after being rotated to gravity.

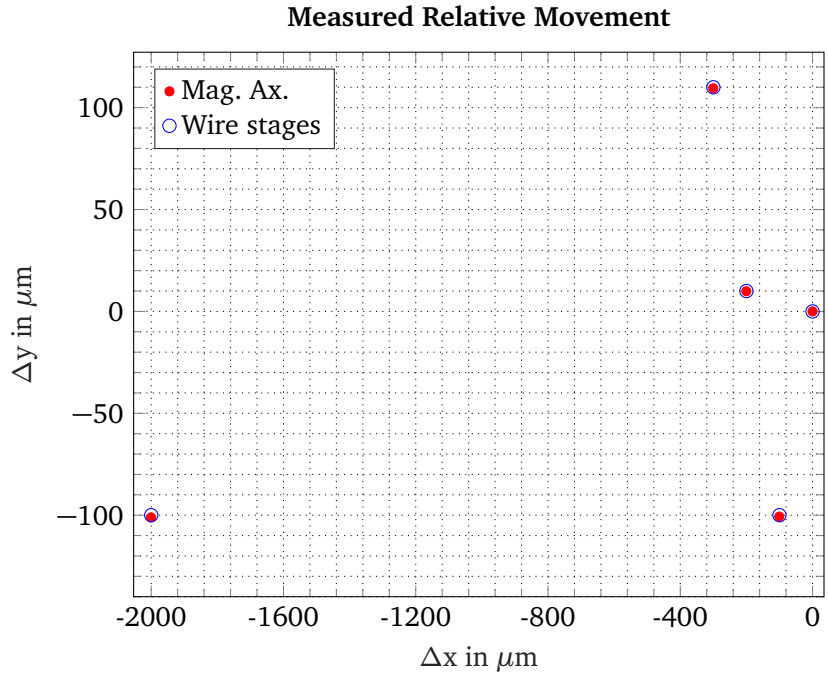

Figure 4.2: The measured relative movement to the initial measurement with the rotating single-stretched wire method. The red dots show the measured offsets from the initial measurement, and the centers of the blue circles shows the applied offset measured by the internal encoders of the wire stages.

Table 4.2: Measured magnetic axis with horizontal displacements of the measurement reference system. The applied displacement is given as Δz_{ws}, the measured axis in each position is given as $\Delta x_{mm}, y_{mm}$ and the displacement relative to the initial measurement is presented as $\Delta x_{rel}, y_{rel}$.

$\Delta z_{ws} \pm 3\sigma$ in μm	$(0,0) \pm 3$	$(1000,0) \pm 3$	$(2000,0) \pm 3$	$(4000,0) \pm 3$
$\Delta x_{mm} \pm 3\sigma$ in μm	-119.69 ± 1.08	880.31 ± 1.05	1880.56 ± 1.74	3881.07 ± 1.40
$\Delta y_{mm} \pm 3\sigma$ in μm	-149.21 ± 0.89	-149.19 ± 1.48	-148.82 ± 1.50	-149.10 ± 1.01
$\Delta x_{rel} \pm 3\sigma$ in μm	-	1000.00 ± 1.51	2000.24 ± 2.05	4000.75 ± 1.77
$\Delta y_{rel} \pm 3\sigma$ in μm	-	0.02 ± 1.73	0.39 ± 1.74	0.11 ± 1.35
$\lvert\Delta x_{ws} - \Delta x_{rel}\rvert$ in μm	-	0.0	0.2	0.8
$\lvert\Delta y_{ws} - \Delta y_{rel}\rvert$ in μm	-	0.0	0.4	0.1

Table 4.3: Measured magnetic axis with vertical displacements of the measurement reference system. The applied displacement is given as Δz_{ws}, the measured axis in each position is given as $\Delta x_{mm}, y_{mm}$ and the displacement relative to the initial measurement is presented as $\Delta x_{rel}, y_{rel}$.

$\Delta z_{ws} \pm 3\sigma$ in μm	$(0,0) \pm 3$	$(0,1000) \pm 3$	$(0,2000) \pm 3$	$(0,4000) \pm 3$
$\Delta x_{mm} \pm 3\sigma$ in μm	−114.03 ± 1.46	−113.85 ± 0.79	−113.75 ± 0.20	−114.41 ± 3.54
$\Delta y_{mm} \pm 3\sigma$ in μm	−140.48 ± 2.58	859.28 ± 1.59	1860.36 ± 1.30	3859.96 ± 0.66
$\Delta x_{rel} \pm 3\sigma$ in μm	-	0.18 ± 1.66	0.28 ± 1.47	−0.38 ± 3.83
$\Delta y_{rel} \pm 3\sigma$ in μm	-	999.77 ± 3.03	2000.84 ± 2.89	4000.45 ± 2.66
$\lvert\Delta x_{ws} - \Delta x_{rel}\rvert$ in μm	-	0.2	0.3	0.4
$\lvert\Delta y_{ws} - \Delta y_{rel}\rvert$ in μm	-	0.2	0.8	0.4

Table 4.4: Measured magnetic axis with transverse displacements of the measurement reference system. The applied displacement is given as Δz_{ws}, the measured axis in each position is given as $\Delta x_{mm}, y_{mm}$ and the displacement relative to the initial measurement is presented as $\Delta x_{rel}, y_{rel}$.

$\Delta z_{ws} \pm 3\sigma$ in μm	$(0,0) \pm 3$	$(-100,-100) \pm 3$	$(-2000,-100) \pm 3$	$(-200,10) \pm 3$	$(-300,110) \pm 3$
$\Delta x_{mm} \pm 3\sigma$ in μm	-106.09 ± 0.69	-206.75 ± 0.84	-2106.48 ± 1.14	-306.51 ± 1.45	-406.37 ± 1.22
$\Delta y_{mm} \pm 3\sigma$ in μm	-132.59 ± 1.37	-233.27 ± 1.13	-233.67 ± 2.17	-122.67 ± 0.60	-23.09 ± 1.01
$\Delta x_{rel} \pm 3\sigma$ in μm	-	-100.66 ± 1.08	-2000.39 ± 1.33	-200.43 ± 1.61	-3000.28 ± 1.40
$\Delta y_{rel} \pm 3\sigma$ in μm	-	-100.68 ± 1.78	-101.08 ± 2.56	9.92 ± 1.49	109.50 ± 1.70
$\lvert\Delta x_{ws} - \Delta x_{rel}\rvert$ in μm	-	0.7	0.4	0.4	0.3
$\lvert\Delta y_{ws} - \Delta y_{rel}\rvert$ in μm	-	0.7	1.1	0.1	0.5

Measured imposed roll angle

The figure below shows the effect of imposing a roll angle to the wire stages, and the magnetic phase shift introduced by this. The resulting external field phases are presented in Table 4.5. The initial measurement without any applied roll angle is given as $\varphi_{roll,0}$, the imposed roll angle is given as θ_{imp} and the measured external field phase with the applied imposed angle is given as $\varphi_{roll,1}$. The difference of the measured external field phases are presented as $\Delta\varphi_{roll}$.

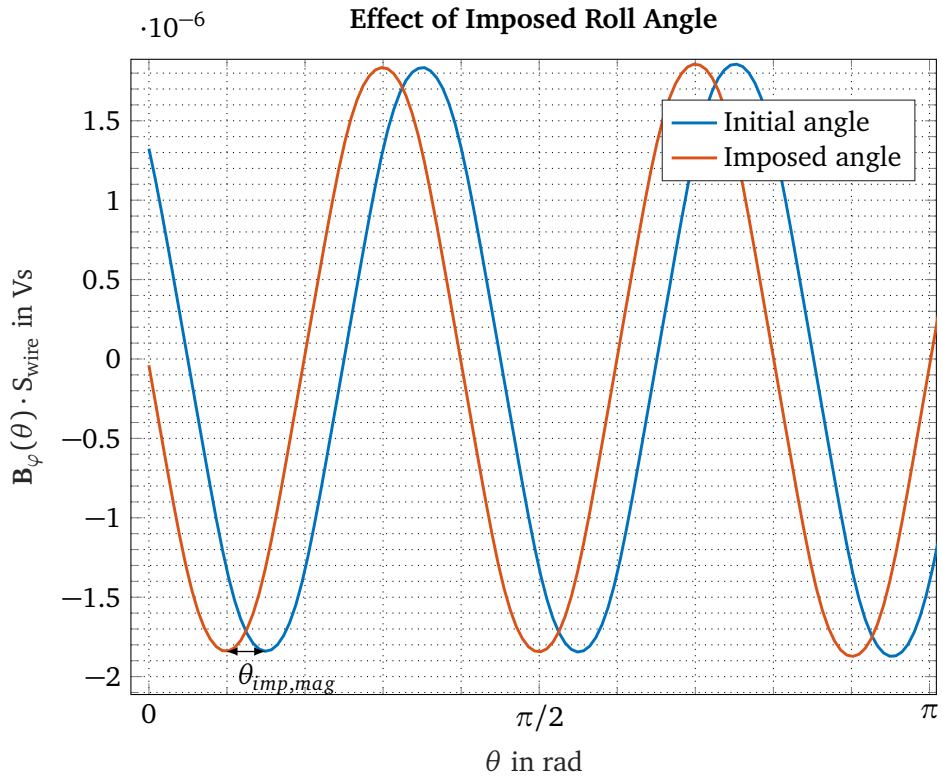

Figure 4.3: The figure shows the effect of imposing a roll angle to the measurement with the rotating single-stretched wire. The blue curve shows the magnetic flux with no imposed angle, and the orange curve shows the same with an imposed angle of $\theta_{imp} = -0.1601$ rad, resulting in a phase shift of the magnetic field measured $\theta_{imp,mag}$.

Table 4.5: The table gives the measured external field phase for the case of no applied roll angle, $\varphi_{roll,0}$, $\theta_{imp} = -0.1601$ mrad imposed angle, and the resulting measured external field phase $\varphi_{roll,1}$. The resulting difference between the measured phase angles is presented as $\Delta\varphi_{roll}$.

$\varphi_{\mathrm{roll},0} \pm 3\sigma$ in mrad	-160.14 ± 0.03
$\theta_{\mathrm{imp}} \pm 3\sigma$ in mrad	-160.1 ± 0.03
$\varphi_{\mathrm{roll},1} \pm 3\sigma$ in mrad	-320.23 ± 0.01
$\Delta\varphi_{\mathrm{roll}} \pm 3\sigma$ in mrad	-160.09 ± 0.03

The roll angles calculated using eq. (2.42) were found as $\alpha_{roll,0} = -160.14 \pm 0.03$ mrad and $\alpha_{roll,1} = 308.09 \pm 0.01$ mrad. When considering the region of the roll angle, $[-\pi/2, \pi/2]$, the latter

angle is found from the corresponding external field phase through the following calculation:

$$\begin{aligned} \varphi_{roll,1} &= -320.23\,\text{mrad} \\ \Rightarrow \varphi_{roll,1,mag} &= -320.23 \cdot 5 = -1601.16\,\text{mrad} > -1570.80\,\text{mrad} = -\frac{\pi}{2}\text{rad} \\ \Rightarrow \alpha_{roll,1} &= \frac{\varphi_{roll,1,mag} + \pi}{5}\text{mrad} = 308.09\,\text{mrad}. \end{aligned}$$

Discussion

The first measurement campaign in the metrological characterization of the rotating single-stretched wire method was carried out with the aim of characterizing the precision of the method, and in a controlled environment investigate the quality of the measurements of very low magnetic fields. In this section the outcome of these measurements are discussed in light of the requirements for the room temperature magnetic measurements of the superferric corrector package, and it is concluded with key points to consider in future measurements.

Measuring the magnetic axis and roll angle

The magnetic measurement campaign of the displaced measurement axis was designed to characterize the precision of the measurement technique through its ability to detect mechanical displacements. The displacements were applied in both the vertical and horizontal plane, and with varying step sizes. It is worth noting that the results of the initial measurements, the ones used as a references, are not necessarily given with the wire stages completely centered in the magnet's reference system, and that the results are presented without adjusting for the sagitta effect on the wire. As they were intended to be used in relative measurements, this was not seen as an important aspect of these particular measurements, and as such, the results with Δz_{ws} as (0,0) are not to be interpreted as the correct magnetic center of the decapole. This is also the reason why the axis seems to vary from the first measurement in each of the tables.

A visual representation of the targeted and measured offsets is given in Figure 4.2. It shows that the method is able to consistently measure relative movement of the magnetic axis to the corresponding movement by the wire stages, with highly varying step sizes and directions. The measured error is visibly well beneath 5 μm. The corresponding results given in Table 4.4, together with the results in Tables 4.2 and 4.3 for the purely horizontal and vertical displacements, show that the spread of the measurand at a 3σ level for all the measurements are less than 4 μm. The consistency in finding the displaced measurement axis is better than 1.1 μm, presented as $|\Delta x, y_{ws} - \Delta x, y_{rel}|$. In total, the precision of the rotating single-stretched wire method in measuring the magnetic axis offset is determined to be approximately 5 μm over relative displacements of up to 4 mm. This is well within the uncertainty requirement of 300 μm, even when adding the uncertainties introduced to the system during the fiducialization process, with the precision of the laser tracker reaching approximately 150 μm at 3σ.

The results are even better when considering the time-scale of the measurements. With the parameters presented in Table 4.1, a single measurement would last for over an hour, which when scaled by the number of repetitions mean that a complete set of displacement measurements were extended over two full working days. This naturally makes the system more prone to error, and it could explain why the difference in applied and measured horizontal displacements shows a jump going from 1000 μm to 2000 μm, presented in Table 4.2, since this was measured at separate days.

To measure the spread and consistency in the roll angle measurements, it was decided to use the external field phase to keep the results easily comparable. From the calculation presented, it is shown

that comparing external field phases is the same as using the correct roll angles. The results show a maximum spread of an individual measurement of 0.03 mrad, and the consistency of the acquired roll angle was found to be better than 0.01 mrad, both at 3σ-levels. Together, this gives a precision of better than 0.04 mrad, which is nearly a tenth of the requirements for the roll angle. The weak point of these measurements is that only a single offset angle was tested. It would have been preferable to use more imposed roll angles, making the consistency results more robust. However, there was insufficient amount of remaining time, so I decided to have the system dismounted to measure the decapole magnet with the translating coil fluxmeter.

To compare the achieved results, the corresponding measurement results from the previous AC mole measurements of the decapole corrector are given in the table below, taken from [39]. In

Table 4.6: Measurement results of the AC Mole measurements of the decapole corrector magnet [39] with the spread of the measurands given at 3σ level. The measurements were conducted with an AC current of 500 mA.

	Centered in mm		Translated in mm	
	x	y	x	y
Leica	0.05	-0.01	1.04	-1.02
AC Mole	-0.25	0.11	1.38	0.94

addition to this, the spread of the axis offset is reported to be 0.03 mm, and field phase measurements 0.9 mrad, both at 3σ-level. This value cannot be used to give a statement of the accuracy of the rotating single-stretched wire method, as also the AC Mole measurements were part of a research project, and as such cannot be used to determine the "correct" magnetic axis and roll angle of the decapole corrector magnet. However, it provides insight into how well the new measurement system performs, and to check that the results are somewhat in the same range.

Since the orientation of the magnet about the longitudinal axis might differ in the two cases, the length of the offset vector is a better measure than its absolute position. For the rotating single-stretched wire measurement, the axis is found to differ from the geometric axis with a radius of approximately 150±4 μm. The consistency of the system, measured as the ability to measure relative displacements was found to be 1.1 μm. The AC Mole measurements show an offset of the magnetic axis from the mechanical axis of approximately 330±30 μm.. The measured relative displacement, with an applied mechanical displacement of (0.99,-1.01) mm, according to the measurements with a Leica laser tracker, see Table 4.6, was measured magnetically to be (1.63,0.83) mm, giving a consistency of approximately 640 μm in horizontal displacements and 1840 μm in vertical displacements. However, this uses the laser tracker as a reference, opposed to the wire stages in the measurements of this report. Therefore, the consistency is not directly comparable. Even so, it can be seen that the rotating single-stretched wire system obtains nearly a factor ten in the spread of the axis localization, and a factor thirty in the spread of the field phase measured. The consistency of the measurements are also significantly better using the rotating single-stretched wire method.

The measured axis offsets in the two cases are also comparable. However, for the AC Mole, the geometric axis is used as the reference for the magnetic axis, since the mechanical structures and assembly of such magnets usually correlates well to the magnetic field. Therefore, the offset measured in [39] is adjusted for, meaning the decapole corrector magnet is used as the reference for calibrating the AC Mole. This is not the approach chosen for this thesis, since the axis, as discussed, is not known at this stage.

To conclude this part, the results from the measurements with imposed transverse and roll angle offsets were sufficiently good to continue the metrological characterization, comparing this measure-

ment method to a proven measurement procedure in more powerful magnets to obtain the accuracy of the measurement system.

Signal quality

The signal measured using this method is naturally very low, in the range of 10^{-6} Vs, and it is therefore prone to error caused by noise. This is counteracted by an optimal choice of excitation current frequency, and through application of Fourier analyses of the induced voltage and flux density, filtering the noisy signals.

Examples of the resulting signals are shown in Figure 4.3, showing the flux density distribution measured in two different intervals in time. It is clear that the signals are corresponding well to the expected azimuthal flux density distribution in a magnet of order five, corresponding to Eq.(2.37) where a set of two and a half magnetic periods are measured over the course of half a mechanical revolution. Furthermore, the signals are smooth, with no visible spikes or dents, and by eye their shapes seem to match. The importance of correct pre-processing treatment of the induced voltages is presented in Appendix A. It is clear that appropriate choice of measurement length reduces the side lobes around the main component. The measurements presented in Figure 4.3 clearly indicate that the method is able to filter out the noisy components, and that the output signal represents the correct flux density within the magnet.

A deterioration of the signal quality was observed where the flux through the induction loop approaches zero. This is naturally the case, since the lower the main signal, the lower the signal-to-noise ratio, when the noise is assumed constant. However, due to the high oversampling of the signal, this effect is to a large extent filtered out. The oversampling of data also reduces the effect of changes in the signals caused by any mechanical vibration in the environment propagating to the wire stages, or changes in the spanned area caused by movements of the return wire.

To conclude, the measurements show that the quality of the induced voltage signal is very good considering the strength of the magnetic field, and due to the great oversampling, the quality is more than sufficient for the purpose of calculating the roll angle and the offset from the magnetic axis. For future measurements, the approach is to start off with the set of parameters presented in subsection 3.3.2. However, if the environment proves to further corrupt the signal with noise, actions should be taken to keep the signal quality high. One such action would be to change the excitation current frequency if noise with similar frequencies are found to affect the signal. Increasing the number of circumferential points to enhance the filtering effect, and also increasing the acquisition time to allow for a finer resolution in the frequency bins of the spectrum, are also ways to mitigate the effects of noise.

Uncertainty in the measured results

Since the decapole was measured in a highly controlled environment, the uncertainty of these measurements is mainly introduced by the movement of the wire stages and vibrations of the wire, the acquisition system and the power supply.

The wire stages were not only used to move the wire, but also as a reference of the displacements of the measurement reference system. The measurement results are therefore only as precise as the wire stages themselves. Initially, a Leica laser tracker system was used to measure the initial positions of the wire stages. The system was reset every morning, with the inclination of the laser tracker, and its position with respect to the external fiducials on the magnet remeasured. However, after a while, the measurements with this system was found to be insufficient with respect to the measured offset. There could be several reasons this. The main reason is likely that during the day, either the laser tracker or the magnet moved slightly. This could be caused by insufficient tightening of the tripod

used to support the tracker causing tilt of the measurement head, vibrations in the laboratory, or caused by thermal drift in the laser tracker. These effects are naturally enhanced by the fact that a single measurement would last for as much as three hours with the parameters used. From these observations we can conclude that for the final measurements of the full corrector package, it will be beneficial to be able to measure any movement of the laser tracker over time. This is achieved using a grid of laser tracker targets fixed at perfectly stationary objects, and by measuring these before and after each wire measurement to adjust for the movement of the laser tracker.

For the metrological characterization, the laser tracker proved to be insufficient, and it was chosen to use the wire stages as reference instead. The precision and repeatability of the wire stages are given as $1\,\mu\text{m} \pm 3\,\mu\text{m}$ at a 3σ level. Since the requirements are to have an uncertainty of less than $400\,\mu\text{m}$ and 0.3 mrad for the transverse centre and roll angle, respectively, an uncertainty of less than $4\,\mu\text{m}$ is clearly good enough for the characterization.

Wire vibration is also a natural source of uncertainty to these measurements. The wire stages are mounted on top of a large block of marble, which naturally reduces the effect of vibration of the stages. The long acquisition time also helps at reducing vibration effects on the signal, especially since the wire used in the metrological characterization was short. This gives a high resonance frequency, the first harmonic was measured and found to be 79.13 Hz, which is high enough for any vibrations to be sufficiently damped by the waiting time of 2.5 s. The last effect counteracting vibrations is the filtering effect of over-sampling. In conclusion, vibration of the stretched wire is assumed negligible to the validation measurements.

The type of power supply used in these measurements were specifically bought for their stability. The values given in the data sheet, presented in Table 3.4, show that it has a relative current ripple of approximately 0.01 ‰, a relative maximum offset of 4 ‰ and a relative variation in output frequency of 0.1 ‰ [42]. When it comes to the variations in and offset of the output peak current, they are considered to be negligible in this setting. A relative ripple of 10 ppm is in itself negligible, and any ripple will be filtered by the integration in the FDIs, as well as by the Fourier analysis of the signal. The constant offset could give differences, but it is assumed to be constant, at least over one full measurement. When this is the case, all frequency components in the spatial Fourier analysis will be scaled equally, therefore not affecting the calculation of measured magnetic axis and roll angle. The only component left to consider is therefore the variation in frequency, and whether this could affect the resulting measurements. The signal is acquired for 8 s, yielding just above 0.005 Hz as the finest achievable resolution of the frequency bins. Therefore, the possible variation of 0.0023 Hz could give spectral leakage that would in fact influence the amplitude found through the Fourier analysis of the induced voltage, as it falls between the resolution of the frequency bins. The oversampling of the signal will once again assist in filtering out this effect. Furthermore, as discussed in Appendix A, the treatment of the induced voltage prior to the Fourier analysis significantly reduces the spectral leakage, and this was found to be sufficient for these measurements.

The acquisition system is considered a boundary condition to the measurements presented in this thesis. It is not within its scope to evaluate or improve this aspect of the measurement procedure. It can be noted that the FDIs and their acquisition system are used for nearly all magnetic measurements performed at CERN, and as so it is assumed to be more than sufficient for the measurements of the corrector package.

To conclude, the uncertainty introduced by the measurement system is well beneath the requirements presented, and as such it is well suited to be used for both measuring the magnetic axis and roll angle, and to act as a mechanical reference to the measured displaced axes.

Conclusion

The precision of the measurement system found during this stage of the metrological characterization

is obtained in a highly controlled area. Since the corrector package is above 7 m long, it is impractical and too risky to move it to this laboratory. The final measurements will therefore be carried out in environments with more noise, adding more uncertainty to the measurements. Even so, the obtained precision from these sets of measurements are well within the requirements of the corrector package measurements, and to such extent that the over-all uncertainty of the measurements will remain within these limits, even with external noise introduced in another environment.

As previously discussed, the precision of the system is not enough to fully determine the uncertainty in the measurement procedure. Still, the precision of the system is clearly sufficient to proceed to the next measurements in the metrological characterization, where the accuracy of the system will be determined.

Even though the resulting precision was found to be very good, there are still improvements to consider in the future measurements. The main improvement is in the alignment of the wire stages. The stages have a constant angular offset stemming from the assembly of the stages onto the marble plates. This offset is known from annual magnetic measurements in reference magnets, calibrating the measurement system. However, the marble plates themselves must be aligned to gravity, meaning the plates must be perfectly perpendicular to the vertical axis. This is a process involving measuring both the roll and the pitch angles of the marble plates, and mechanically adjusting the plates accordingly. This process was not performed at this stage of the measurements, as only relative displacements were considered, cancelling this effect. For the final measurements of the corrector package, however, this needs to be considered. Horizontal and vertical wire movements with tilted wire stages will naturally be non-parallel to the actual planes. Having tilted stages gives errors in the measurements of both the roll angle and the axis offset. The effect on the roll angle is shown by the measurements with an imposed angle. The effect on the axis offset stems from a rotation of the complete measurement coordinate system, with the theory presented in section 2.2.2. Both effects can be countered if the angle is known, however, this angle is likely to remain unknown, as it stems from an error made during the measurement. Therefore, it is important to make sure that the difference between the internal reference system of the wire stages (their horizontal and vertical axes) and the mechanical reference system of the the fiducials of the corrector package is as small as possible. Since the magnets will be aligned to gravity, the stages are required to be aligned to gravity as well.

Another aspect to consider in future measurements, is the proper setup of the laser tracker. Since we have to measure the full corrector package in a less controllable environment, this also imposes new challenges to the fiducialization process, and a larger drift is expected in the laser tracker measurements. This could be caused by more variation in temperature, and movement in the floor and of the air surrounding the tracker. Therefore, it is of great importance to use a grid of targets to measure the drift of the system periodically, and to account for this by "repositioning" the laser tracker within this grid. This way, the laser tracker accounts for any movement we cannot control, making the fiducialization process a lot more robust.

4.1.2 Characterization measurement 2: Measurements of the Ansaldo MEBT quadrupole

To determine the accuracy of the rotating single-stretched wire measurement system, it is tested against the reference system for measuring the magnetic axis and roll angle of lower-order magnets; the single-stretched wire measurement system in DC mode. The principle of the axis and roll angle measurements of the DC SSW system is explained in subsection 2.4.2, in the part of wire-based measurements.

The measurement setup for the two measurement methods are presented, before the results are given, with the subsequent discussion of the obtained values, and how the accuracy of the rotating single-stretched wire method is determined by this.

Measurement setup and principle

The last part of the metrological characterization of the rotating single-stretched wire method is a set of measurements of the magnetic axis and roll angle of the Ansaldo MEBT quadrupole magnet. The magnet is not used in the accelerator complex, and has been stored since it was constructed in 2020. The parameters of the magnet is presented in the table below.

Table 4.7: The design properties of the Ansaldo MEBT quadrupole is given in this table. Values taken from internal documents.

Property	Value
Multipole component	b_2
Cooling system	Water
I_{peak} (cycled)	112.4 A
I_{RMS}	112.4 A
R at 20°C	33.41 mΩ
L	24.04 mH
$g_{2,nom.,peak}$*	8.15 T/m

(*) Quadrupole gradient nominal field at peak current.

The measurement setup of the wire stages, and the coordinate system defined for the measurements, are shown in Figures 4.4 and 4.5.

The wire bench used for these measurements is the same as the one used for the measurements of the decapole corrector magnet, with the parameters presented in Table 3.4, and corresponding to Figure 3.2. The exception is the power supply used to power the magnet, since the Keythley power supply is not powerful enough to power the Ansaldo MEBT quadrupole. Transtechnik, an in-house power converter, excites the magnet in DC mode, with a current of 112 A. The polarity is shown to the left in Figure 4.5, highlighted by (1). At this current level, the magnet is water cooled to avoid damaging the windings, with the pipes highlighted by (2) to the left in the figure. For the measurements with the rotating single-stretched wire method, the powering configuration is presented in the figure to the right of Figure 4.5. The AC signal is generated by a programmable function generator, number (3) in the figure. This signal is fed to a Kepco bipolar operational power supply, highlighted by (5). The current is read by the DCCT shown at point (4) in Figure 4.5. It is connected through the DCCT at the back of the device, and the signal is measured and acquired by the digital acquisition system of the wire-bench. The setup is limited to deliver 20 A at 20 V.

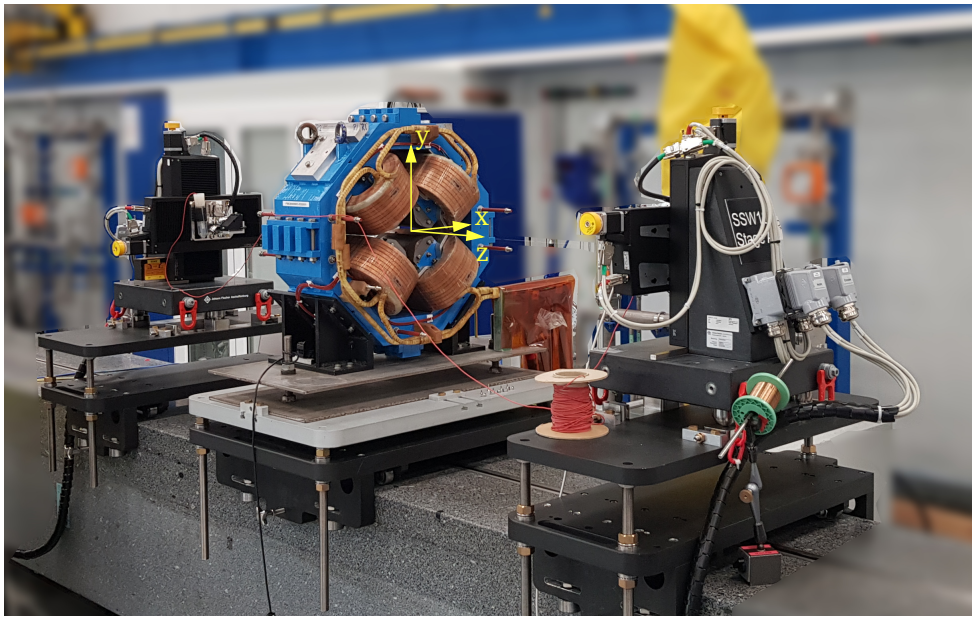

Figure 4.4: The SSW measurement setup for the validation measurements of the Ansaldo MEBT quadrupole. The quadrupole is seen in the center of the figure, the wire stages, stretched-wire and return wire are similarly positioned as in Figure 3.2. The reference system is shown in yellow, attached to ti the aperture of the magnet.

DC measurement

The DC measurements were conducted first. To start as close to the axis as possible, the wire was centered in the magnet before measuring. The centering is performed with the magnet powered in DC, and it uses the standard measurement method for locating the magnetic axis as explained in subsection 2.4.2. If the axis offset measured is bigger than some pre-defined limit, the wire is moved to this location, and the measurements repeated until the found axis is closer than this limit. A limit for the spread of the located axis is also included. To account for other constant field components in the surroundings, mainly the Earth's magnetic field, the measurements were performed with inverted polarity as well. For the centering of the wire, the polarity inversion gives no added value, as the axis found differs, and the wire is moved to the axis found in the last measurement performed.

After the wire was centered, the magnetic axis was measured again, to act as a reference for the following measurements with the rotating single-stretched wire method. Before measuring the axis, we perform a degaussing cycle of the magnet, in order to reduce or mitigate the effect of any remanence field in the quadrupole. This is performed with an oscillating current with decaying amplitude. Then, the magnet is pre-cycled to make sure it is on the rising branch of the hysteresis loop. This is important, since if the magnet is on the decreasing branch, the field at nominal current might differ from the field with using the rising edge of the cycle [58]. Therefore, to keep the magnet consistent, the pre-cycling is performed before all axis measurements with this system.

After the initial steps, the magnetic axis was measured. The measurement is based on the theory presented in subsection 2.4.2, and specifically what is shown in the leftmost part of Figure 2.19. The wire was moved with a step size of 25 mm in both horizontal and vertical direction. The aperture of the magnet would allow for larger step sizes. However, when measuring the axis with the single-stretched wire in DC mode, it is the symmetry of the main multipole gradient that is of interest. Moving too far away from the axis, the higher-order multipoles play a bigger role, and not with

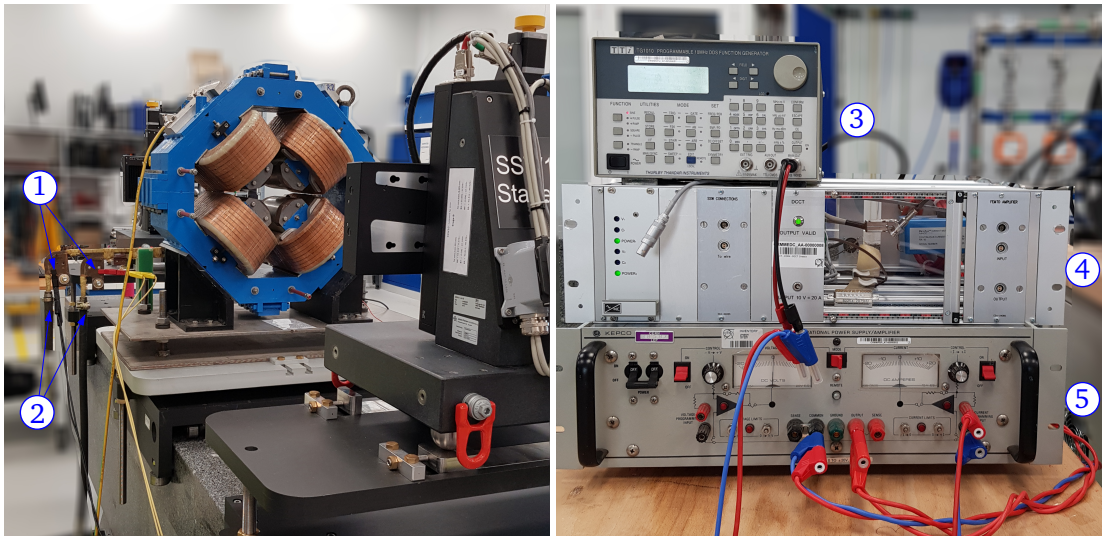

Figure 4.5: Connection scheme and AC powering setup of the Ansaldo MEBT quadrupole. To the left, (1) shows the bus bars of the magnet, where the red and black connectors are connected to the *A*- and *B*-terminals, respectively, together with the connections for the water cooling of the magnet is shown (2). To the right, (3) is the AC signal generator, (4) is the DCCT used for the measurements, and (5) shows the power supply.

the same symmetry or asymmetry about the origin. Since the technique is based on symmetries of the gradients, it is important to stay within the region where the field is less impacted by higher-order multipoles. First, it measured the horizontal offset, and the wire was moved in the following order: (0,0) - (+25,0) - (0,0) - (-25,0) - (0,0), with distances given in millimeter, and relative to the axis of the wire stages. This was repeated five times, and then the same approach was used for measuring the vertical offset, with five repetitions as well. This process was also repeated with inverted polarity of the magnet, with the same step size and number of repetitions. Accounting for external field components is crucial for the DC measurements, as for instance the magnetic field of the Earth is at approximately 75° angle to the ground at CERN, which yields axis offsets in both vertical and horizontal direction. The resulting magnetic axis is presented as the average of the two measurements, and the spread is calculated as the propagated standard deviation.

To measure the roll angle, the procedure shown to the right of Figure 2.19 was followed. It comprises a set of measurements of the horizontal axis of the magnet, at different vertical positions. The roll angle is calculated as the angle between the vertical line and the linear fit of the measured horizontal axes along the vertical displacements. The offset angle of the wire bench was measured in June 2021, and found to be -0.008 mrad. This is subtracted from the measured roll angle. The step size used for in the vertical plane was 25 mm, nine positions were used along the vertical axis: $(0,0)$, $(0,\pm 6.25)$, $(0,\pm 12.5)$, $(0,\pm 18.75)$, $(0,\pm 25)$, in millimeter and relative to the reference system of the wire stages. In each vertical position, ten repetitions were performed to obtain the spread of the measurand. Similar to the axis measurement, the process was repeated with inverted polarity, and the result given as the average, with the spread calculated as the propagated standard deviation.

Rotating single-stretched wire measurement

The theory behind the measurements with the rotating single-stretched wire method, and the setup of the system, is thoroughly explained in section 3.3. Since the magnet is powered in AC, the remanence field and other stationary magnetic components are filtered out, hence there is no need for a pre-

cycling or degaussing of the magnet. There will still be power loss in the magnet, and to be on the safe side, the magnet is cooled in the same way as for the DC measurements. The cooling water is at ambient temperature, therefore it is assumed that the temperature effects of the two measurements are negligible. Furthermore, as discussed in section 3.1, the magnet characteristics relate well across different temperatures.

The magnet is powered with an alternating current. To stay below the limit of the powering setup, the magnet was powered with 18 A and 7 Hz for the measurements with this system. With this frequency, the impedance of the magnet is calculated to be 1.06 Ω, giving a peak voltage of 19 V.

To measure the multipoles, and consequently the magnetic axis and roll angle, a total of 128 circumferential points were used, as the quadrupole requires less measurement points than higher-order multipoles. To optimise the signal-to-noise ratio, a measurement radius of 33 mm was chosen. Since the rotating single-stretched wire method takes advantage of the multipoles, instead of the measured gradient, the contribution from the higher-order multipole components are filtered out, thus choosing as large a reference radius as possible is preferred. The remaining measurement parameters are presented in the table below.

Table 4.8: Measurement parameters used for the validation measurements.

Parameter	Used value
Excitation current amplitude	18 A
Excitation current frequency	7 Hz
Sampling frequency	1024 Hz
Acquisition time	4 s
Circumferential measurement points	128
Calibrated roll angle offset	-0.008 mrad

The difference between these measurements, and the ones presented in the first part of the characterization, is the measurement of the roll angle. As the DC measurement method calculates the roll angle according to the definition, the measured roll angle with the rotating single-stretched wire is also obtained using the procedure explained in subsection 2.2.2. The roll angle offset is subtracted from the measured values in both cases, to give the correct roll angle as measured by the systems.

The measurements of the Ansaldo MEBT quadrupole using the rotating single-stretched wire method was repeated three times, to obtain the spread of the measurands.

Measurement results

The resulting magnetic axis and roll angles from the two measurement methods are presented in Table 4.9. The measured axes are visually represented in Figure 4.6. The presented values are given as the mean over five measurement repetitions for the DC wire axis measurements, ten times for the DC wire roll angle measurements, and over three measurement repetitions with the rotating single-stretched wire. The spread of the measurands are given at 3σ.

Table 4.9: Measurement results with wire initially centered. The spread of the measurands are presented as 3σ.

Measurement	$\Delta x \pm 3\sigma$ in μm	$\Delta y \pm 3\sigma$ in μm	$\alpha_{\text{roll}} \pm 3\sigma$ in mrad
DC at 112 A	-39.6±12.87	-16.14±7.66	0.086±0.079
DC at -112 A	-2.53±27.94	4.69±5.80	-0.133±0.089
DC averaged	-20.84±30.76	-5.72±9.61	-0.109±0.119
AC at 18 A, 7 Hz	-19.65±5.96	8.64±12.39	-0.125±0.289

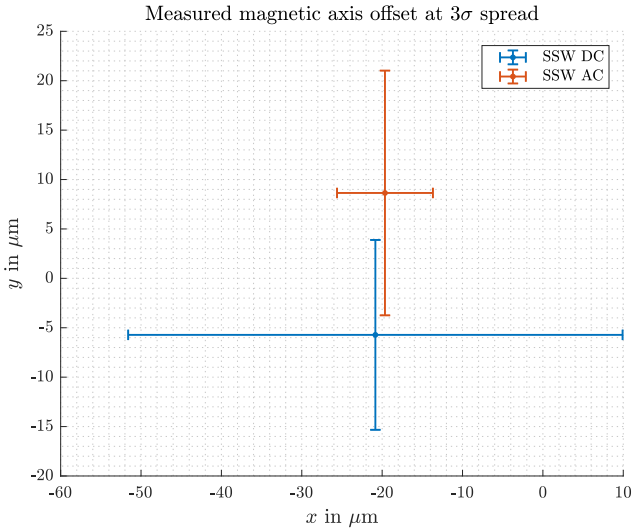

Figure 4.6: Measured magnetic axis using the DC stretched-wire measurement, and using the rotating single-stretched wire method. The dots show the averaged centers, and the error bars display a 99.73% confidence level in the measured axis for both cases.

Discussion

The measured magnetic axis using the two different systems, are presented in Table 4.9, and visually represented in Figure 4.6. With a confidence interval of 99.7%, meaning with a spread of 3σ, we see that the measurements are so-called *compatible*. This means that for the two systems, the measured axis is known to be within the error bars in Figure 4.6 for both the measurements. Since the error bars overlap, there is a chance that the measured values are the same for the two measurement systems, meaning the results are compatible. This is also the case for the roll angle measurements.

It can be seen that the measurements differ slightly in several ways. For the measured axis offset in the x-direction, the measured averages differ with less than 1 μm. For the measurements in the vertical direction, however, the difference between the measured axes is nearly 15 μm. On the other hand, the spread of the measured axis in the x-direction for the DC measurements is quite a lot more than for the corresponding measurements using the rotating single-stretched wire, and for the measurements with both systems for the vertical axis offset. It is important to note, however, that the differences are in the range of a few tens of micrometer, and that any disturbances of the wire movement or power supply could be the source of this difference. Repeating the measurements back to back, and averaging over five and three full measurements, reduces these effects. To investigate further, the wire stages moved the wire 100 μm in both vertical and horizontal direction, and the measurements were repeated. The results show the same behaviour, proving the measurements to be consistent.

Accounting for this, it was chosen to determine the accuracy of the system by the differences between the measured axis offsets in the y-direction. This, because the spread of the measurements showed more consistency between the two systems, and since the differences between the measured axes is larger than what is the case in the horizontal measurements. Using the "least favorable" result, increases the confidence in that the measurement system will in fact deliver more accurate results than the accuracy given by these measurements. Therefore, the accuracy of the rotating single-stretched wire method is found as the difference between the measured offset from the vertical component of the magnetic axis for the two systems, yielding an accuracy of better than 15 μm.

The roll angle was measured using a measurement radius of 33 mm for the rotating single-stretched wire. For the DC measurements, due to some uncertainty to the possible contribution of the higher-order multipoles, the roll angle was measured with a maximum step size of 25 mm. Even with the differences, the roll angle is found to be compatible. The accuracy of the system in measuring the roll angle is found as the difference between the measured averaging, yielding an accuracy of 0.016 mrad for the rotating single-stretched wire.

4.1.3 Metrological characteristics of the rotating single-stretched wire

In this part, the measured metrological characteristics of the rotating single-stretched wire method is presented. The accuracy of the system is found as the differences between the measurands using the well known and trusted DC wire method and the rotating single-stretched wire, measuring the ANSALDO MEBT quadrupole. The precision of the measurement system is found as the sum of the spread and consistency of the measurands from the measurement campaign of the decapole corrector magnet. The uncertainty is calculated as the sum of the accuracy and the precision of the system. All the characteristics of the system; accuracy, precision and uncertainty, are given at 3σ, to be comparable to the requirements of the measurement uncertainty.

From the metrological characterization of the axis measurements using the rotating single-stretched wire, measuring the decapole corrector magnet, the precision of the system was determined to be better than 5 μm. The accuracy of the measurements are found from comparing the system to the

DC wire measurements, and the resulting accuracy was found to be better than 15 μm. Together this gives an uncertainty of less than 20 μm in the axis localization with the rotating single-stretched wire method. However, as the axis measurements are dependent on measurements of the fiducials on the magnet and the wire stages, the uncertainty of Leica Absolute Tracker AT930 must be included. This is found to be approximately 150 μm, see subsection 5.1.3. In total, the uncertainty of the magnetic axis measured by the rotating single-stretched wire and Leica AT930 laser tracker system is given as 170 μm at 3σ, mainly limited by the uncertainty of the laser tracker measurements. This is within the requirements of the measurement uncertainty. Furthermore, since the fiducialization process necessarily uses Leica AT930, the uncertainty cannot be any lower than 150 μm. The measurement system itself offers an uncertainty of less than 20 μm, which is on the limit of what is achievable. Therefore, the uncertainty is sufficiently low for the further measurement campaign of the corrector package.

It was found that the accuracy of the system in measuring the roll angle of the magnets is 0.016 mrad. From the metrological characterization on the decapole corrector magnet, the precision of the system in measuring the roll angle was found to be 0.04 mrad. As the roll angle is independent of the mechanical position, the uncertainty of the laser tracker is not included in this calculation. From this, the uncertainty of the roll angle measurements using the rotating single-stretched wire is 0.06 mrad at 3σ. This is below the required maximum uncertainty of 0.1 mrad at 3σ, presented in Table 3.1, and the measured uncertainty is therefore accepted for the future measurements of the roll angle of the corrector magnets.

4.2 Validation and Metrological characterization of the Translating Coil-Fluxmeter

In this section, the measurements conducted for the validation and metrological characterization of the translating coil fluxmeter are presented. The main purpose of these measurements was to investigate whether the measurement system is able to measure signals sufficiently higher than the noise to acquire the longitudinal center and magnetic length of the decapole corrector magnet. The spread of the measurands are to be investigated, and the system will be metrological characterized by this. However, as the translating coil fluxmeter used in these measurements is only the first iteration of the system development, the term "metrological characterization" might be a slight exaggeration, since testing the main principles of the measurement system is the main goal of these measurements. Furthermore, there are no available magnets with known magnetic length and center where the guiding tube could also be installed. Therefore, to validate the measurement system, the measured magnetic center and length are compared to the mechanical measurements of the external fiducials, measured by the Leica AT930 laser tracker system, which is known to give good results, as the fields follow closely the mechanical structure of the magnet [38].

In the following, the measurement setup is presented briefly, together with the main parameters used. The main parameters investigated are the magnetic length and center. However, tests were carried out to investigate the choice of triggering device and spatial assignment of measurement points, the two main approaches for data refinement presented in section 3.4, and their impact on the measurands. The latter part is presented first, as the resulting field profiles, magnetic center and length are based on the results in this part.

Measurement setup and choice of approach

The validation and metrological characterization measurements of the translating coil fluxmeter were conducted at the magnetic measurements laboratory for normal conductive magnets at CERN. The measurement hall is a highly mechanically and thermally stable room, making for ideal surroundings of the measurements. Leica AT930 laser tracker is used to measure the external fiducials of the decapole corrector magnet. The three points shown in the rightmost figure of Figure 3.7 are used to fit a circle, with the direction of the longitudinal axis given by the circle's normal vector. The origin of the measurement reference system is fixed at the center of the circle, and therefore $s = 0$ shows the end plate of the mechanical structure of the magnet.

The measurement setup for the validation measurements is the one presented in Figure 3.10, Figure 3.11 and Figure 3.12. To benefit from the Hall probe measurement, the wiring for the last PCB was replaced by the wiring for the Hall generator, as the connection wire used only included enough connectors for 12 PCBs and one Hall generator, and since time limitations did not allow for changing the cable. Therefore, the 12 circumferential PCBs were used, with the Hall generator placed in the center of the first one.

For the triggering of the FDIs and spatial measurement, it was chosen to investigate how well the wire draw encoder performs compared to the Leica AT930 laser tracker. With the wire attached to the measurement system, and a laser tracker target glued to the measurement head, the wire was pulled and released several times, with the Leica AT930 laser tracker measuring the positions in each trigger point. The nominal resolution, determined by the decimation factor written to the encoder board, set to 64, is 224.6 μm, and the resulting step sizes should correspond to this. For a scan in one direction, Leica AT930 has a precision of ± 0.5 μm/m, which with the laser tracker positioned at maximum 8 m from the target gives a precision of ± 4 μm. The measurement was repeated eleven

times, and the results are presented in Figure 4.7 and Table 4.10.

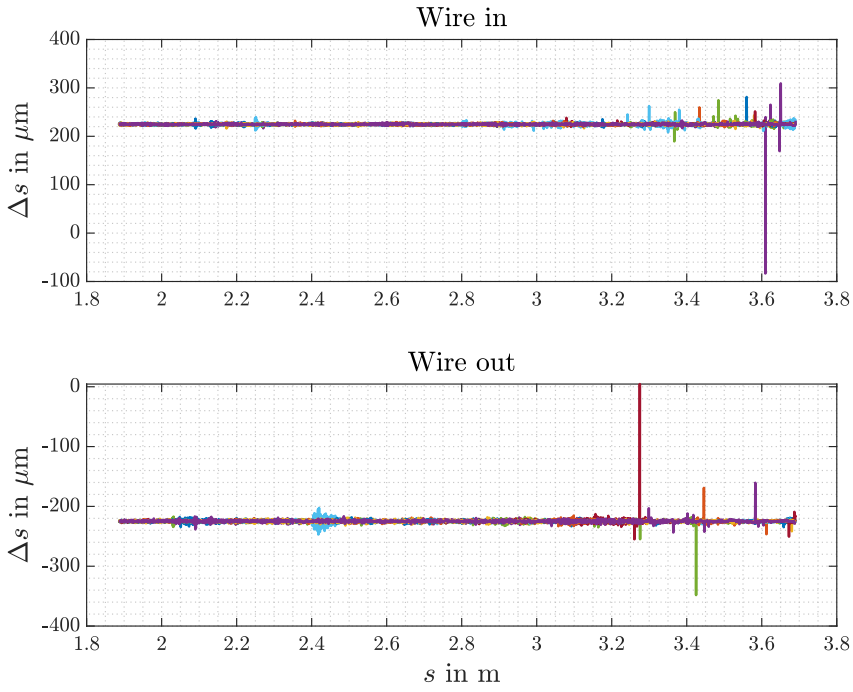

Figure 4.7: Longitudinal step sizes measured by Leica AT930 laser tracker for eleven consecutive runs, both by pulling the moving rod (Wire in) and pushing the rod (Wire out).

Table 4.10: Longitudinal step size measured by Leica AT930 laser tracker, triggered by the wire draw encoder. The wire is both pulled and released, and the results are given with a spread of 3σ. The average of the two directions, along with the average of all runs, are presented.

Run	$\Delta s \pm 3\sigma$ in μm	
	Wire going in	Wire going out
1	224.80 ± 3.97	-224.80 ± 3.32
2	224.78 ± 3.56	-224.78 ± 3.56
3	224.78 ± 3.20	-224.81 ± 3.81
4	224.77 ± 11.24	-224.82 ± 3.75
5	224.80 ± 5.31	-224.79 ± 6.17
6	224.80 ± 7.25	-224.78 ± 5.66
7	224.78 ± 3.70	-224.80 ± 9.04
8	224.77 ± 3.61	-224.77 ± 4.66
9	224.78 ± 3.71	-224.78 ± 4.06
10	224.77 ± 3.84	-224.78 ± 4.04
11	224.79 ± 5.80	-224.79 ± 7.57
Average	224.78 ± 5.52	-224.79 ± 5.36
	224.79 ± 5.05	

From the results presented in Table 4.10, it is clear that the accuracy of the wire measurement, with the inherent uncertainty of the laser tracker, can be achieved to the sub-micrometer level, and with a spread of 5 μm, a total uncertainty of approximately 5 μm is achievable at the given working conditions. We also see that the precision and repeatability of the measurements with the wire going

in and out of the encoder is nearly identical. From Figure 4.7, it is clear that for most part of the measurement, the ripple in the measurements is very low. However, there are some larger spikes at the end of the measurements. These are probably caused by mechanical instabilities in these regions. If the encoder experiences vibrations, this could give artificial triggers, which would corrupt the measurements. During the measurements with this first iteration of the measurement system, quite a lot of vibration and mechanical instabilities were experienced, due to friction between the measurement head and the tube, as will be discussed in later sections. Even so, we see that we are within the reproducibility of 300 μm, showing that the encoder can be used with the same metrological characteristics as is given in the data sheet.

However, the wire is not long enough to measure the full corrector package assembly. Consequently, for the final measurements of this thesis, the laser tracker will have to be used, and therefore it was opted for using this in the validation measurements as well.

For the data refinement in the post-processing phase, a deconvolution using both the sensitivity factors from the Fourier analysis, and the fourth-order spline approximation can be used to yield more physically correct flux density distributions. Both methods have been implemented in the post-processing phase, and an analysis was carried out to investigate which one of the methods gives the most physically correct flux density. The results using the two methods described in section 3.4 are shown in Figure 4.8 below.

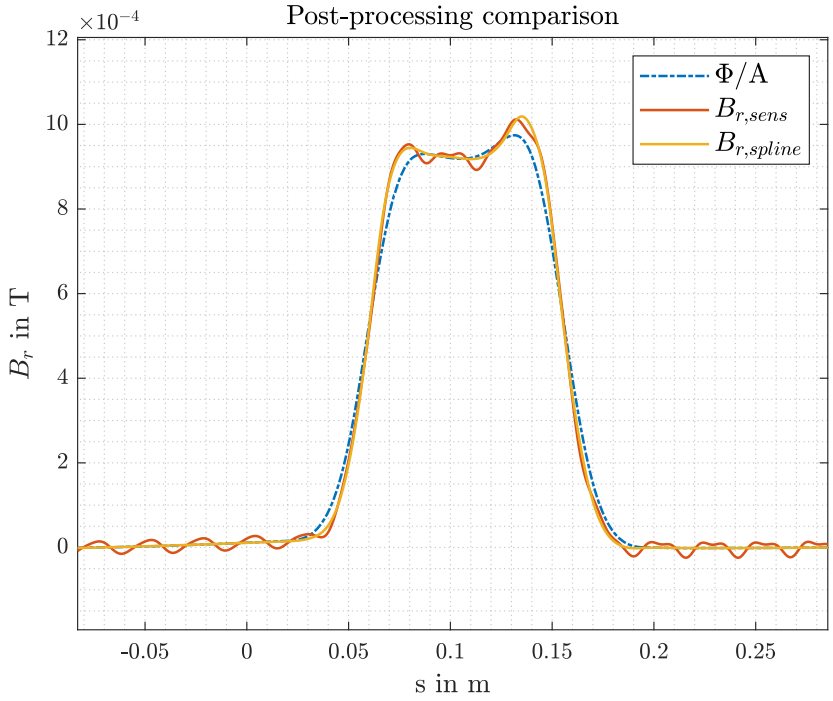

Figure 4.8: Comparison of deconvolution approaches for the magnetic measurements of the decapole corrector magnets.The graphs show the flux density distribution when the flux is deconvoluted by the Fourier sensitivity function (orange), using a spline interpolation (yellow) and simply by dividing by the surface area of the PCBs (blue dashed and dotted)

From the resulting field profiles, a few aspects can be discussed. First of all, both deconvolution methods are able to give sharper edges than by simply dividing by the area of the coils, as was expected. Apart from this, we clearly see that the spline interpolation is superior to the sensitivity

deconvolution. From the deconvolution with the Fourier sensitivity function of the PCBs, $B_{r,sens}$, a clear oscillatory behaviour is observed. By closer inspection, it can be seen that they mainly oscillate with approximately 40 m^{-1} and 120 m^{-1}, corresponding to the blind-eye frequencies of the induction coils. In an attempt to reduce these effects, the flux signal was filtered by a stop-band filter, filtering out the two components. The resulting flux density distribution is shown in Figure 4.9 below. It is

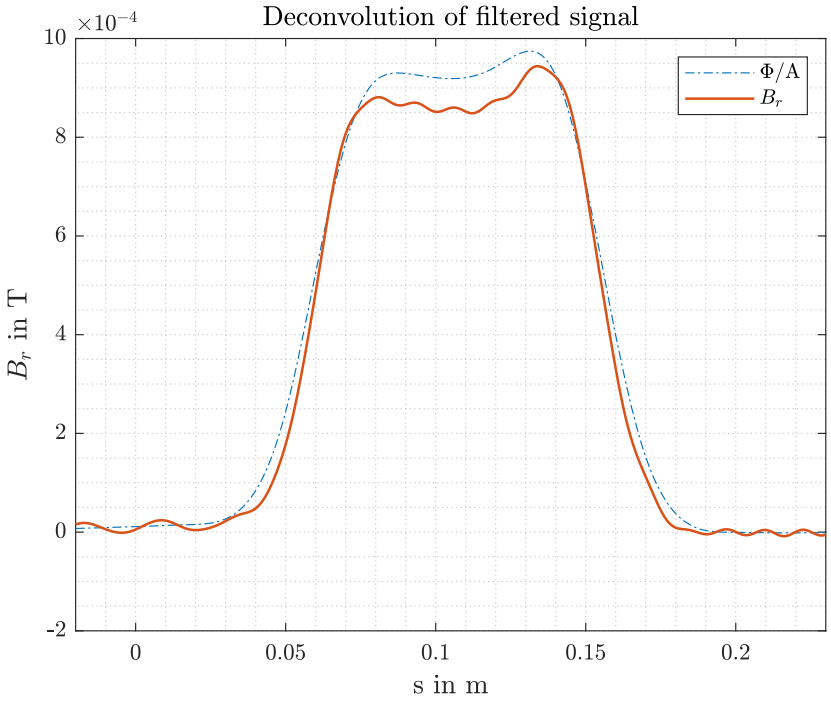

Figure 4.9: Caption

clear from the plots that the oscillations of 40 m^{-1} and 120 m^{-1} are filtered out, and that the remaining noise component oscillates with a frequency of 60 m^{-1}, which is the last blind-eye frequency from Figure 3.13. However, the amplitude of the signal is significantly reduced, even though the edges are sharper. This means that some of the blind-eye frequencies of the PCBs are actually main components in the flux density distribution. Therefore, filtering these components out, the signal cannot be reconstructed. One solution would be to use a so-called Wiener-Kolmogorov deconvolution as in [10], where the reconstructed flux density is given by $\hat{B}_r(f) = g_W(f)\tilde{B}_r(f)$, where the tilde denotes the measured radial flux density component, the hat the reconstructed flux density component, and the filter g_W is given by

$$g_W = \frac{1}{s^c(f)} \frac{|s^c(f)|^2}{|s^c(f)|^2 + \frac{\mathbb{E}[n(f)]^2}{\mathbb{E}[B_r(f)]^2}}. \tag{4.2}$$

The Wiener-Kolmogorov filter, eq. (4.2), includes the sensitivity functions of the measurements, but also includes the inverse of the signal-to-noise ratio in the last expression in the denominator. This means that the frequency components dominated by noise are not divided by only the, possibly very low, sensitivity factor, but also reduced in amplitude, as the signal-to-noise ratio would be lower for this component. This would therefore keep the frequencies needed for the signal to behave correctly, without grossly amplifying the noise. However, this requires a priori knowledge about the

noisy components and the expected distribution, to get the inverse signal-to-noise ratio. The noisy components are easily found through a Fourier analysis, but to get the expected signal one would need the simulated signals, and they were not available during this work. The last solution, and possibly the most robust one, would be to design the PCBs with coils that have the first blind-eye frequencies above the cutoff frequency chosen for the measurement. Then, one could simply divide the measured flux by the sensitivity factors in the frequency domain to obtain the flux density. This is a time consuming process, and would only be applicable to the next iteration of the measurement method. Furthermore, it also requires knowledge of the signal, thus having the simulations of the flux density distribution would be beneficial in the design process.

As the spline deconvolution yield better results, at a much simpler approach, it was decided to continue using this in the measurements.

Then, the impact on the measurands of deconvoluting the signal was investigated. The hypothesis is that the filtering of the field distribution by the windings of the PCB is symmetrical. As a result, the magnetic center and magnetic length should not be affected, as they are determined by the symmetries in the field shape. Therefore, the measured center and magnetic length should be equal for the simplified approach of dividing by the surface area, and when deconvoluting the signal using b-splines. Also the impact of changing the interval of integration was investigated, with the offsets from the intervals found by the Hall probe measurements were changed from -15 mm to 50 mm. The iterations for the spline interpolation was cut off with the maximum residual below $1.5 \cdot 10^{-7}$ Vs, as manually checking each signal is too time consuming. For some of the induction coils' signals, this threshold is too low, and oscillatory behaviour could be observed. They are usually seen in the flat regions of the flux density distribution, and this test is therefore a good indication of how well the approach of signal deconvolution could be automatized in the post-processing, and if this would affect the measurands. Especially by increasing the intervals, this effect would be captured, as longer intervals have larger zero-field areas on both sides of the magnet. The results of the measurements are presented in Table 4.11 and Table 4.12, where Φ/A signifies the simple approach of dividing the flux measured by the area of the coils, while B_r is the flux density approximated by fourth-order b-splines.

Table 4.11: Magnetic center for the two post-processing approaches, with varying integration interval, Δs.

Δs	$s_c \pm 3\sigma$ in mm	
	Φ/A	B_r
50 mm	110.12 ± 2.19	110.13 ± 2.19
25 mm	109.74 ± 1.11	109.75 ± 1.13
15 mm	109.42 ± 0.91	109.41 ± 0.93
5 mm	109.13 ± 0.80	109.16 ± 0.83
0 mm	109.05 ± 0.77	109.07 ± 0.81
-15 mm	109.05 ± 0.77	109.07 ± 0.81

From the results, it is clear that the found magnetic centers and lengths using the two approaches are nearly the same, for all intervals of integration. Especially the magnetic centers found with the two approaches match very well, differing with some tens of micrometer. The spread of the measured centers also behave accordingly. The results vary slightly more for the calculation of the magnetic length. The differences are still less than 1 mm, but the spread for the measurements using the b-spline deconvolution is significantly larger. This can be explained by the oscillatory behavior of the b-spline interpolation. Since the calculation of the magnetic length also include the magnitude of the

Table 4.12: Magnetic length for the two post-processing approaches, with varying integration interval, Δs.

Δs	$L_m \pm 3\sigma$ in mm	
	Φ/A	B_r
50 mm	104.66 ± 8.59	104.92 ± 8.58
25 mm	103.33 ± 0.64	103.51 ± 0.75
15 mm	103.87 ± 0.49	103.53 ± 1.16
5 mm	103.73 ± 0.58	104.68 ± 3.08
0 mm	103.59 ± 0.58	104.30 ± 2.13
-15 mm	103.59 ± 0.58	104.30 ± 2.13

field, and not only the symmetry of the distribution, if there are oscillations in the central regions of the magnet, this might change B_0 in one measurement, resulting in a higher or lower magnetic length. The differences are still quite low, and might therefore also stem from the set cut-off limit of the residuals.

Considering the results, it was chosen to proceed with calculating the magnetic center and length using the simple approach of dividing the flux measurement by the surface area. This is justified by the small differences in measured center and magnetic length, both in the average results and in the spread. Furthermore, the simple approach is a lot less computational intensive, and a lot more time efficient. It also displays less spread in the measurands, and is therefore deemed more stable than the deconvoluted signal, at least in the automatized versions. To give the flux density distribution, the approach using b-spline deconvolution will be used, as this gives the most physically correct field profiles, manually choosing when the residuals are low enough for the particular cases. The differences between the measured values at different integration intervals will be discussed in the following sections. By visual inspection, using an additional offset of 15 mm from the positions given by the Hall probe was found optimal for these measurements.

To conclude this part, the parameters used for the validation measurements are presented in Table 4.13 below.

Table 4.13: Measurement parameters used for the validation measurements of the translating coil fluxmeter.

Parameter	Used value
Excitation current amplitude	105 ± 0.001 mA, ±0.4 mA offset
Sampling frequency	800 ± 8 Hz
PCB	12 × EDA-03787-V1-0
Hall generator	HE244
Position measurement	Leica AT930 laser tracker
External triggering	PXI-6289 multifunction I/O module
Interval offset	15 mm

Results

With the choices of parameters and approach presented above, the resulting flux density profile, averaged over all the induction coils, are presented in the figure below. Both the simple approach of dividing the measured flux by the surface area, and the b-spline deconvolution is shown.

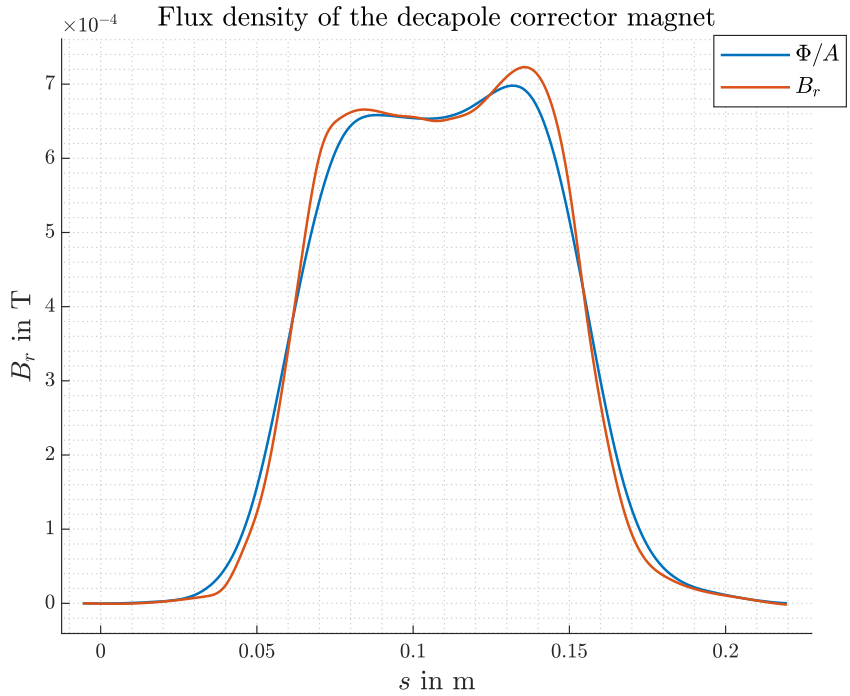

Figure 4.10: Radial flux density component along the longitudinal axis of the magnet. Both the simple approach of scaling the measured flux by the surface area, and the b-spline deconvoluted signal are shown, as the blue and orange curves respectively.

The measured magnetic centers and magnetic lengths for varying summation intervals are shown in Table 4.11 and Table 4.12. The values are given as the average and the spread as the standard deviation of ten measurements, five pulling the moving rod, and five pushing it. The results at the chosen interval are presented below:

$s_c = 109.42 \pm 0.91$ mm at 3σ spread.
$L_m = 103.87 \pm 0.49$ mm at 3σ spread.

Discussion

The decapole corrector magnet was measured in controlled surroundings to validate the measurement principle, characterize the metrological properties of the system and develop the measurement- and post-processing procedure. As this is the first iteration of the measurement system, the term metrological characterization is slightly excessive in this context, as there are several steps to mitigate the uncertainty further that could be implemented in the next iterations. Even so, to use the translating coil fluxmeter in its current state to measure the magnetic centers and lengths of the corrector magnets in the corrector package assembly, the results obtained in the validation measurements need to be sufficiently good. Therefore, the spread is used as a measure for the precision of the system, and it must be within the requirements of the measurement uncertaint for the measurement campaign of the full corrector package to be launched.

Measuring the magnetic center and length

The measured flux density field profile is shown in Figure 4.10. From the profile of B_r, we see that the field rises rapidly when entering the position of the coils, approximately 40 mm within the magnet. Then there is a peak of the field, before the middle parts of the magnet has a more constant field region. Exiting at the near end of the magnet in Figure 3.11, an even higher peak in the field is observed. The two peaks, going in and out of the magnet, does not necessarily have to be symmetric, however the peaks measured for the decapole are quite uneven. As the flux density presented in the figure is the average of the measurements from all the induction coils along the circumference of the measurement head, it is not an effect of a non-parallelism of the measurement tube, as this would give increased signals for some coils but a decrease for the coils displaced by 180°. Furthermore, it could have been an effect of the surroundings of the magnet, for instance the support of the tube. However, all PCBs showed the same behavior of the flux density, irrespectively of the position. This rules out this argument, as the support or surroundings would show an asymmetric effect on the measured flux. Therefore, it is in fact attributes of the magnetic flux density of this particular corrector decapole.

By eye, the measured magnetic center and length correspond well to the profile, with the center positioned approximately at 110 mm, and the equivalent magnetic length of 103 mm also seems correct. With ten repetitions, the measurement method is proved to be robust, with a spread of the measurands of less than 1 mm at 3σ. This is ten times less than the requirements, and it shows that the measurement method is sufficiently precise to measure the centers of all the corrector magnets. Compared to the nominal value, the magnetic center is within the expected limits. Given that the magnet is assembled correctly, the mechanical center should correspond quite well with the magnetic center [38]. From Table 2.1, the magnetic center should be at half the magnet length, when the endplate is taken as $s = 0$. This means, $s_{\mathrm{c,nom.}} = 233/2$ mm $= 116.5$ mm, which makes the measured center approximately 7.1 mm off the expected value. This is below the expected deviation of 10 mm, and as such match well with the expected range and uncertainty of the measurand. When comparing to the nominal values, the resulting magnetic length differ more from the expectations. These values are calculated from simulations, and therefore the uncertainty often exceeds the percentage range. However, the case for the magnetic length deviates too much, with a nominal magnetic length of 145 mm, resulting in an error of more than 40 mm, far exceeding the expected deviation. This could be due to a low accuracy of the measurement system, some sort of systematic error. However, the flux density profiles from all the measurements seem to be centered around 110 mm, and the shape corresponds better to a magnetic length of 103 mm than to 145 mm. Therefore, it seems like the error lies with the magnet itself, and not in the measurement system, as a systematic error shortening the

field profile on both sides is highly unlikely. This could be explained by the field shape observed in the measurements. If there is some field distortion due to a high remanence field in the iron in the magnets, this could explain a higher field value in the center of the magnet, and lower strength in the fringe-field region. A higher central field, and a slimmer field profile could result in a lower magnetic length.

To conclude this part, it is clear that the measured magnetic center corresponds well to the expected center, from mechanical measurements of the magnet. However, the magnetic length does not correspond to the nominal value at all, and is found to be a lot shorter than its nominal length. Even so, as the measurements display a low spread, and since the results by a rough approximation seems to fit very well with the measured flux density, it was chosen to continue the system validation on the corrector package assembly.

Uncertainty in the measurement system

The main cause of uncertainty in these measurements lie in the mechanical movement of the measurement head. The manual pushing and pulling of the movement rod, while the measurement head not quite fills the cold bore, results in uneven movement, which is seen in the raw output data as spikes. In these measurements, pulling the measurement head was a lot more stable than pushing. Including both leads to a higher spread of the measured centers and magnetic length. In the FDIs this effect is smoothed out, but they are not completely mitigated. Furthermore, the fact that the measurement head has room to move transversely within the measurement tube, results in too much movement of the PCBs with respect to the magnetic poles from measurement to measurement. If this movement is purely rotational, the effect would in most cases be smoothed out by the high number of PCBs. However, transverse movement causes some PCBs to come closer to the poles, while their 180°displaced counterpart is not necessarily moved equally away from the pole, especially in the decapole magnet, where the number of pole pairs is antisymmetric to the number of induction coils. Even though the above-mentioned effects are unwanted, they prove the robustness of the measurements to be high, since the precision of the measurements are still well within the requirements.

Another source of uncertainty is any external fields or offsets affecting the measurements, for instance magnetic field components that vary in space. One example is the remanence field of the magnet itself, or any of the other corrector magnets in the final assembly. Any remanence field in the decapole magnet while measuring will add to the field set up by powering the magnet, inducing voltages in the induction coils while moving through. Another is the already discussed FDI drift. These effects can be seen in Table 4.11 and Table 4.12, where the spread of the measured magnetic center and length increases when the measurement interval is increased. This is especially clear when increasing the additional part of the interval from 25 mm to 50 mm, where the spread of the measured axis is nearly doubled, and the spread of the magnetic length is more than ten times as high. These effects are likely due to the integrator drift, and more measures should be taken to mitigate this. For the next step of the measurements, it was therefore decided to measure the magnetic field with the magnets powered with both nominal and inverse polarity. From the set of measurements, the so-called *semi-difference* is calculated. This means averaging the signals, but with a negative sign of the inversely powered measurements,

$$B_{r,\text{semidiff.}} = \frac{B_r^+ - B_r^-}{2}, \tag{4.3}$$

where $B_r^{+,-}$ denotes the measured flux density with nominal and inverse polarity, respectively. From the equation, it is clear that all the unwanted signals, the ones not affected by the polarity of the

magnet, will cancel out. However, the flux density set up by the current in the magnet, and not the remanence field, will be averaged.

Conclusion

The precision of the measurement system to locate the magnetic center and length is defined through the spread of the measurements at 3σ, and was found to be below 1 mm for both measurands. This is well beneath the measurement requirements, and it shows promise for the continued measurement campaign of the translating coil fluxmeter-measurements of the corrector package assembly.

The measured magnetic length was found not to match the nominal value and the expected deviation. However, from the visual inspection of the measured signal, the error seems to be with the magnetic field, and not a systematic error in the measurement system, as the magnetic length hardly can be as long as 145 mm. As the measurement system is easily moved to the location of the corrector package assembly, the validation measurements were ended for further tests and validation of the system on the full assembly.

For the next measurements, it was decided to calculate the semi-difference of the magnetic flux density with opposite polarity, as this is expected to reduce the effects of external sources of measured field. This is expected to be of even greater impact to the measurements of the corrector package assembly, as the remanence field of the other magnets might play a larger role in the measured fields.

Chapter 5

Measurements of the Higher-Order Corrector Magnets Assembly

The first corrector package for the HL-LHC is nearly fully assembled. This process is undertaken in building 180 at CERN, the so-called *Large Magnet Facility*, LMF. As the risk of damaging the magnets by transporting the package to the measurement facilities of the Testing and Measurements section, the magnets are tested at LMF. The present assembly consists of all the higher-order corrector magnets, welded together and aligned to gravity. They are positioned in a cradle, and will be fully enclosed once the nested dipole orbit corrector is installed. At the time being, the magnets are rotated 180°about the longitudinal axis, therefore inverse polarity is expected from some of the magnets, given by the symmetry.

The corrector package assembly is measured with both the developed systems; the rotating single-stretched wire method for obtaining the magnetic axis and roll angle of the individual corrector magnets, and the translating coil fluxmeter for measuring the longitudinal center and magnetic length of the individual magnets. This section presents the measurements with both systems. The first section presents the full setup, measurement approach, results and following discussion of the rotating single-stretched wire. The last part of the section shows the same for the translating coil fluxmeter, however with slightly more emphasis on further developments of the system.

The LMF is not at all designed for magnetic measurements, and several challenges were encountered during the measurement campaigns. These will be presented, with the measures taken to mitigate their effects on the measurements.

5.1 Measurements With The Rotating Single-Stretched Wire Method

The rotating single-stretched wire measurements of the assembled corrector package are presented in this section. It is used to measure the magnetic axis and the roll angle of each of the higher-order corrector magnets in the assembly, in a process where the magnets are powered one by one. Measuring in the LMF adds to the challenges of measuring the axis to within a few hundreds of micrometers, as will be discussed in the further parts of this section.

The results of these measurements are the set of magnetic axes and roll angles for the individual magnets in the array, and we would expect the results to be within the range expressed in Table 3.2. The uncertainties used are the ones determined from the metrological characterization, as time limitations made it impossible to measure the full corrector package several times.

5.1.1 Measurement setup and approach

Measurement setup

The measurement setup for the rotating single-stretched wire measurements of the assembled corrector package is shown in the figure below.

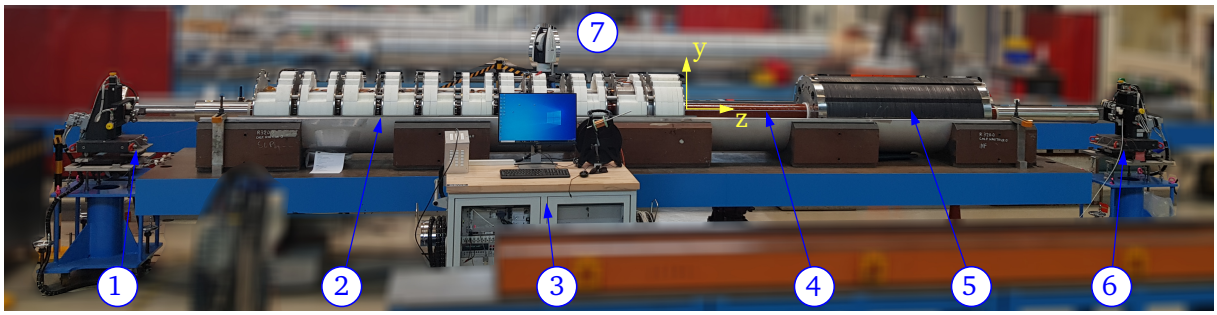

Figure 5.1: The setup for the rotating single-stretched wire measurements of the assembled corrector package. The picture shows wire stage A and B, (6) and (1), the set of higher-order corrector magnets, (2), the measurement bench with the electronics, (3), the cold bore, (4), the MCBXFB-magnet, (5) and LEICA absolute tracker AT930, (7). The reference system used for the measurements is shown in yellow, with the positive x-axis pointing into the paper.

As can be seen from the figure, most of the components are the same as was used for the metrological characterization of the system. The wire bench used this time is a different one, with slightly different setup. The wire stages are mounted on movable supports, since the system is transported to another building. The supports are naturally not as stable as the marble bench, but they are mounted and adjusted to be as stable and levelled as possible. The offset roll angle of the stages were calibrated a month after these measurements, with a resulting offset roll angle of 0,026 mrad. The corrector package is at this stage not complete, as the nested correction dipole has not yet been delivered to CERN. The dipole seen in the picture, (5), is the shorter version, and it is not measured at this stage. Furthermore, the assembled magnets are upside-down in this setup, as the entire package will be rotated and enclosed by another part of the gutter-shaped cradle seen beneath it in the figure, when the dipole corrector is installed. The higher-order correctors are shown in the figure, (2), and reads from left to right; a_3, b_3, a_4, b_4, a_5, b_5, a_6, b_6, a_2. The reference system is shown in the center of the figure, with the positive x-axis pointing into the paper, as defined by the right-hand rule.

LEICA absolute tracker AT930 is used to fiducialize the magnets, and is shown at point (7) in Figure 5.1. It is mounted on a tripod, as seen in Figure 5.2. Due to the length of the corrector package,

Figure 5.2: The setup of the LEICA AT930 laser tracker system used for the fiducialization of the higher-order corrector package. The tracker is mounted on a tripod in the center of the figure, the workstation is shown, and the targets used for re-orienting the tracker is highlighted by red circles.

and since it is placed in a cradle, it is impossible to measure the fiducials on both sides of the package from the same position. They are necessary, as the set gives the correct yaw and pitch angles of the magnet assembly. Therefore, the laser system is placed in three different positions to measure all the points needed; on both sides of the magnet, and in the middle of the magnet to measure the targets on both wire stages at the same time. The last position is shown in the figure. A grid of six targets are placed around the tracker, so that the measured points with the tracker in different positions can be related to each other through this grid. The grid is also used between the wire measurements of each magnet, to measure and correct any drift of the laser tracker. Drift can be caused by mechanical vibrations in the environment, air movement or temperature changes in the surroundings. The target used in these measurement is moved between fixed holders, glued to stable surfaces assumed stationary (such as the floor, the magnet itself and the metallic benches supporting the magnets.) The grid can be seen in Figure 5.2.

With a new set of magnets, and another measurement location, there are a few more challenges to the rotating single-stretched wire measurements of the higher-order corrector magnets. These challenges are discussed in the following, with the measures taken to mitigate their effect.

External sources of noise

An aspect of the change of measurement location, was the introduction of a lot more sources of noise. Where the measurement hall used for the metrological characterization of the method is mechanically and thermally stable, the surroundings in the LMF is quite a lot more challenging. The building is used for the assembly of accelerator magnets, and this involves lifting heavy components and moving them back and forth. Therefore, two huge cranes are attached to the walls. When they move the floor is vibrating, and when heavy components are lifted close to the measurement setup, the vibrations are enhanced. It is therefore of great importance that everything is as stable as possible, to avoid any movement of the stages, the magnets and the laser tracker. Some movement is, however, unavoidable. To mitigate their effects, several measures were put in action. As already mentioned, a grid of laser tracker targets were used to measure any mechanical and thermal movement of the laser tracker. Furthermore, the laser tracker was "relocated" between each magnetic measurement. In this process, the laser tracker measures the reference points, and it moves its own reference system according to the change in measured grid points. The relocation uses all previous measurements of the grid points in the analysis in a fit, minimizing the error between all measurements. Therefore, if

the laser tracker moved, it notices, and adjusts accordingly. This is also the case for the temperature changes in the surroundings. The LMF is a big hall, and during the day, the temperature increases quite substantially. This affects the laser tracker measurements, but apart from measuring the drift, and adjusting for this, there is not much to be done about this effect.

To reduce the errors of the wire measurements during the measurement campaign, the pitch and roll angle of the wire stages were measured every morning, using a WYLER MINILEVEL NT. The resulting angles are given at three decimals of mm/m, that is in the range of microradians, with a maximum error of 1% of the measured value [59]. Between each measurement, the drift of the levelmeter was cancelled out by measuring the angle twice, with the levelmeter rotated 180° inbetween, and calibrating the levelmeter to the average value. Then, the stages were adjusted to have roll and pitch angles in the range of less than $1 \pm 0.01\mu$rad. At the end of the day, the angles were measured again, to see whether the stages had moved. During the measurements, the tension of the wire is measured at each measurement position. In case the wire stages move during the measurement, this will in most cases result in a changing wire tension. This also alters the wire trajectory within the magnet, and in a worst case scenario the measurement cannot be used to locate the axis, as the wire moved too much. Therefore, measuring the tension enables us to check the quality of the measurement.

Excitation frequency

The choice of excitation frequency was discussed thoroughly in subsection 3.3.2. However, with the introduction of the other corrector magnets, it was necessary to adjust this. The reason for this was the inductance of the dodecapole corrector magnet, which is significantly larger than in the decapole corrector, as seen in Table 2.1. Therefore, the power supply was not able to deliver the volage required to power the normal dodcapole magnet with a freqyency of 23 Hz. After some testing, it was found that the highest possible frequency was 21 Hz, and it was chosen to power the magnets by 19 Hz to stay beneath this limit.

In addition to the mechanical and thermal noise of the LMF discussed above, there is more electromagnetic noise in this location. From magnetic measurements, it seems like the source of noise giving rise to the 14.75 Hz-spike discussed in subsection 3.3.2 was enhanced in the LMF. The result of this was a visible *beating* of the induced signal. Beating occurs when two signals with different frequency interfere, and results in the creation of two signals; one signal with the sum of the frequency, and one with the difference of the frequency. Whether it is just the effect of an increased noise component, or if it is an effect of the smaller frequency difference between the induced signal and the noise, this beating was a lot clearer in the measurements of the corrector magnets in the LMF than in the stabilized measurement hall, and a clearly visible component of approximately 4.25 Hz was observed. The effect of frequency beating is filtered out by the application of the DFT, and should not reduce the quality of the measured signal. Still, to ensure better filtering, it was chosen to increase the number of measurement points to 256, and to extend the time between the movement of the wire and the start of the acquisition to 5 s, as this will reduce noise caused by mechanical vibrations of the wire. Since the stretched-wire is now more than 7 m long, this effect is not negligible. The sampling frequency was also increased to 4096 Hz, to reduce effects of aliasing with higher-frequency noise components.

Eddy currents in the cold bore

The measurements of the full corrector package will be conducted with the cold bore installed. The cold bore is an extruded tube made of the austenitic stainless steel AISI 316 LN, meaning that it is made without any welds, thus completely smooth. It is very resistive to corrosion and also non-

magnetic, naturally a very important property for use in an accelerator. The material has an electric resistivity of $0.75\,\mu\Omega\cdot$cm[60], making it a highly conductive material. During the normal operation of the corrector package, this does not give rise to eddy currents, as they will be operated with a constant field in time. However, during the warm measurements of the magnets, they will be powered with a time-varying current, which will give rise to eddy currents in the cold bore. Eddy currents results in a smaller magnetic field and a phase difference measured by the stretched wire, given by the equation below

$$B'_{\varphi} = \frac{B_{\varphi}}{\sqrt{1+(\tau_n\omega)^2}}\sin(\omega t - \tan^{-1}(\tau_n\omega)), \tag{5.1}$$

where $\tau_{\mathrm{n}} = \mu_{\mathrm{r}}\mu_0 a/2n\rho_{\mathrm{V}}$, ρ_{V} is the volume conductivity of the steel, and a is the radius of the tube[61]. A more thorough explanation of the derivation is given in Appendix B.

From this equation we see that when installing a conductive tube, in our case the cold bore, the resulting flux intercepted by the stretched wire lags the induced flux from the coils by an angle $\tan^{-1}(\tau_n\omega)$, and it is a factor $\sqrt{1+(\tau_n\omega)^2}$ less in amplitude. The change in amplitude of the signal has no effect on the spatial Fourier analysis, as it gives an equal scaling of all the multipole components, and is therefore omitted in the calculation. The resulting phase shifts are presented in Table 5.1.

Table 5.1: Phase shifts between the induced flux from the windings of the magnets and the measured flux within the cold bore.

Multipole order n	2	3	4	5	6
Phase shift	-53.8°	-42.3°	-34.4°	-28.7°	-24.5°

There are two ways the eddy currents can have an effect on the measured flux: 1) the phase shift introduced, and 2) by the uneven distribution of the eddy currents given by a possible misalignment of the cold bore with respect to the magnets' apertures. In the following, I will give an explanation of why this does not affect the results of these measurements:

Phase shift

The phase difference between the current and the measured flux is used to determine the sign of the spatial value of the flux distribution within the magnet, as explained in section 3.3.2. Therefore, a change in the phase shift could result in a change in polarity of the spatially distributed signal at a different mechanical angle than in the case with no cold bore. However, since the phase difference between the current and magnetic flux without the tube is ±90°, if the angle difference caused by the eddy currents are less than 90°, the effect of this change would only change the sign of the induced voltage where the polarity would naturally change. This effect would be filtered out through the Fourier analysis, as this mainly considers the peaks of the signal. Due to small phase shifts, the resulting spatial flux distribution has not been affected by adding phase shifts.

Uneven effects due to a misalignment of the bore

A misalignment of the tube with respect to the magnet's aperture would give an asymmetry in the changing flux density in the walls of the bore. This would, in turn, give an asymmetry in the eddy currents, thus in the change of flux density within the tube. However, as the eddy currents are proportional to the field strength at a given point, the effect of the eddy currents distributed along the cold bore will be proportional to its misalignment. Therefore, the flux density distribution as measured will be proportional at all points to measurements without the tube, hence the effect does not

affect the results.

To conclude this part, the parameters used for the rotating single-stretched wire measurements of the corrector package assembly are presented in Table 5.2. The wire frequency was measured after the magnetic measurements, and is significantly lower than for the validation measurements, as the wire stages are positioned more than 7 m apart.

Table 5.2: Measurement parameters used for the rotating single-stretched wire measurements of the corrector package assembly.

Parameter	Used value
Excitation current amplitude	105 mA
Excitation current frequency	19 Hz
Sampling frequency	4096 Hz
Acquisition time	8 s
Circumferential measurement points	256
Calibrated roll angle offset	0.023 mrad
Measured wire frequency	17.75 Hz

Measurement approach

Measuring the correct coordinate system

The measurement of the higher-order correctors in the assembled corrector package is performed similarly to the measurements of the decapole corrector magnet. The only differences are the addition of the Leica AT930 laser tracker, and the scale of the measurements.

The laser tracker system is used for measuring the fiducials of the magnet and the wire stages. This way, the wire measurement can be linked to the physical magnets. To do this, the physical magnet assembly has to be the basis for the reference system of the geometric measurement of the measurement system, and this is achieved in the following manner: All targets are measured by the laser tracker, and the *SpatialAnalyzer*-software is used to store and manipulate the points. The magnets should have been aligned to gravity, but we have no guarantee that this is the case. The main reason for this being, as discussed above, that the corrector dipole has not yet arrived, and the corrector package is not yet in its final assembly. To capture any misalignment of the mechanical axis, assuming the magnets are installed so that the magnets share a common axis, the line between the centers of the magnet on each side of the corrector package are taken as the z-axis of the measurement system. The circles are made by fitting the three fiducial points with a circle. By measuring gravity by the internal inclination sensor of the laser tracker, the y-axis is determined. Then, the right-hand rule gives the x-axis of the measurement. Lastly, the coordinate system is attached to the mechanical center of the skew quadrupole corrector magnet. From this point on, as long as the drift is checked and adjusted for between each measurement, the magnetic coordinates of the wire measurements and the mechanical reference system is connected. The longitudinal position of each magnet was found by attaching targets to the end-plates of the individual magnet. They are used to find the correct vertical and horizontal position of the wire within the magnet in the post-processing.

A screenshot of the SpatialAnalyzer display is shown in Figure 5.3, displaying the position of the measurement head and the targets in space. The fiducials with the fit circles are seen in the center of the figure, and the resulting coordinate system is shown attached to the skew quadrupole corrector

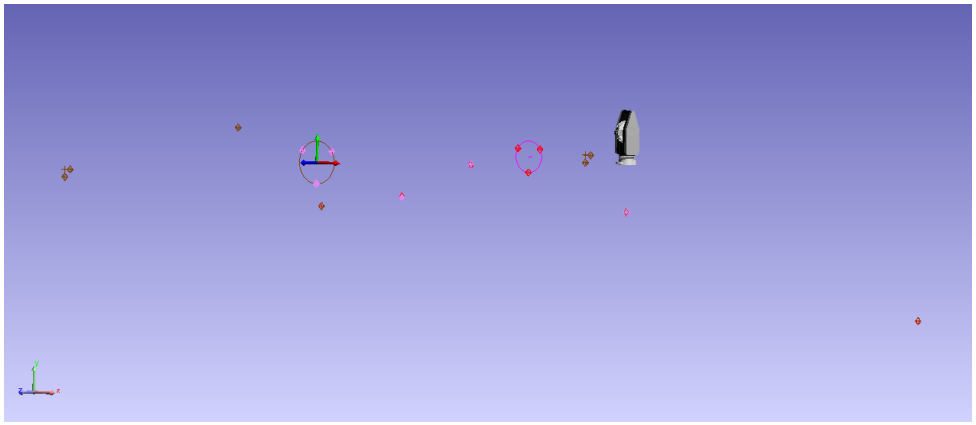

Figure 5.3: SpatialAnalyzer view of the fiducials, reference points and wire stages used in the rotating single-stretched wire measurements of the higher-order corrector magnets.

magnet, and in the bottom left corner. The wire stage targets are shown on each side of the corrector package, and the constructed point where the wire is attached to the stage is shown as a cross. The process of constructing these points are explained in section 3.3.2, and shown in Figure 3.7. The rest of the points in the picture are the reference points used for relocating the laser tracker. They are used for measuring and correcting for the drift of the laser tracker, both before and after each wire measurement, as explained in the previous sections.

Magnetic measurements of the magnets

The magnets are measured consecutively. Since the wire measurement gives the integral field values, to find the magnetic axis and roll angle of each magnet, they are powered one by one. With the increased measurement time due to a longer damping period of the wire vibrations, and to the increased number of points, the full set of measurements last a few days. It was therefore decided not to measure each magnet more than once, and rely upon the accuracy and precision of the metrological characterization to give the uncertainty of the measurements. The additional uncertainty is discussed at a later stage.

Since the measurements of the corrector package is an extensive task, it was decided to first analyse the data using symmetries of the magnet, a slightly simpler approach than the feed-down and roll angle calculation of the full analysis. This would result in a better understanding of the measurements, and to improve the further post-processing, eventually leading up to an increased confidence in the results. This approach can be explained by Figure 5.4 below.

The figure shows the effect of an off-centering of the measurement system with respect to the magnetic axis. When the wire rotates, it will be closer and farther away from the magnetic poles as the axis of the measurement system is closer or farther away from the true magnetic axis. This will be seen as a slightly higher or lower signal, respectively, which is shown in the plot in the bottom of Figure 5.4. The ideal b_6-field is shown as the blue curve, and is found as the main harmonic from the FFT of the measured signal. The orange curve shows the measured signal, displaying a slightly different shape than the ideal field. The envelope is added to show the the decrease of the measured signal in the middle of the measurement. The analysis compares the signal strength of the measured signal at each peak with the peak located 180°mechanically rotated from the peak under investigation. If the mechanical axis corresponds to the magnetic axis, the peaks should be equal, and the difference measured zero. Whenever this is not the case, from the comparison we would know which of the opposite poles the measurement axis is closest to. Comparing half of the peaks with the

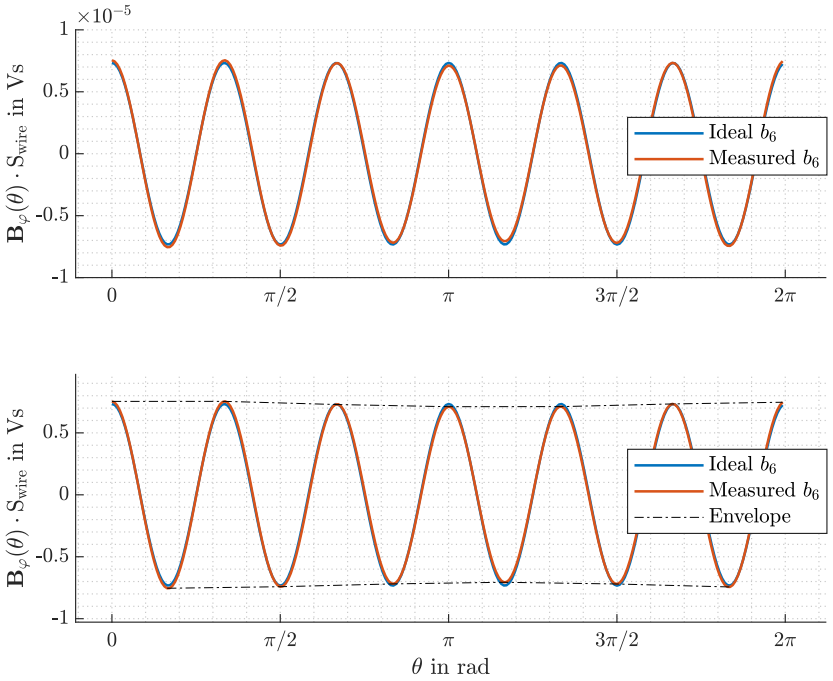

Figure 5.4: Figure showing the simple approach to investigating the displacement vector and difference in field phase of the measured signal compared to the ideal signal for the normal dodecapole corrector magnet.

other half is sufficient to qualitatively know at least in which quadrant we would expect to find the actual magnetic axis from the measurements. Theoretically, the difference in amplitude would also give the exact offset from the axis, not only the direction. However, as the corrector magnets are of higher order, this expression would soon turn very complex, if all other multipolar components were to be accounted for. Therefore it was chosen to use this approach only as a preliminary study of the measurements.

From the DFT of the field distribution, the field phase is obtained. Knowing the field phase, and the designed polarity of the magnets, gives a measure for the roll angle of the magnets, or the external field phase φ_{roll}, as defined in section 4.1.1. Therefore, this is easily obtained from this simpler approach.

After the preliminary study is finished, the post-processing procedure described in section 3.3.2 is applied, and the magnetic axis and roll angle is calculated and referred to the fiducials on the magnet.

5.1.2 Measurement results

This section presents the measurement results of the rotating single-stretched wire measurements of the higher-order corrector magnets in the nearly assembled corrector package.

In Table 5.3, the results of the preliminary analysis of the measurement data is presented. It shows the resulting quadrants in which the displacement vectors of the raw measurement data are located, $\mathrm{Q}_{\mathrm{meas.}}$, and the measured and expected external field phases, $\varphi_{\mathrm{roll,meas.}}$ and $\varphi_{\mathrm{roll,nom.}}$. The difference between the measured and expected external field phase gives the resulting external field, that is the offset angles of the magnets with respect to the design case.

Table 5.3: Results from the preliminary analysis of the measurement data of the corrector magnets using the rotating single-stretched wire method. $Q_{meas.}$ shows the expected quadrant of the measured axis, without correction for position of the wire. $\varphi_{roll,meas.}$ and $\varphi_{roll,nom.}$ are the measured and expected external field phase, respectively. The measured external field phase is adjusted for the angular offset of the wire stages.

Corrector magnet	$Q_{meas.}$	$\varphi_{roll,meas.} \pm 3\sigma$ in mrad	$\varphi_{roll,nom.}$ in mrad	$\varphi_{roll} \pm 3\sigma$ in mrad
a_2	QII	-786.38±0.06	-785.40	-0.98±0.06
b_6	QIII	-1.48±0.06	0.00	-1.48±0.06
a_6	QIII	-263.62±0.06	-261.80	-1.82±0.06
b_5	QIII	626.75±0.06	628.30	-1.55±0.06
a_5	QIII	313.27±0.06	314.20	-0.93±0.06
b_4	QIII	-1.00±0.06	0.00	-1.00±0.06
a_4	QIV	-393.30±0.06	-392.70	-0.60±0.06
b_3	QIV	1046.60±0.06	1047.20	-0.60±0.06
a_3	QIII	523.30±0.06	523.60	-0.30±0.06

The final results of the magnetic measurements with the rotating single-stretched wire system is presented in the following. Table 5.4 gives the measured values of the integrated magnetic axis, both before and after the correction of the wire position within the magnet is accounted for. These results are graphically represented in Figure 5.5, where the uppermost subplot shows the horizontal component of the magnetic axis, and the lowermost shows the vertical component. It is clear that the difference between the measured and corrected axis is greater for the vertical component, as the saggita of the wire plays a big role. The uncertainty values added as the spread of the measurands, is the sum of the accuracy and precision of the system. This was characterized in subsection 4.1.2, and from this an uncertainty of the measured roll angle was found to be ±0.06 mrad, whilst the total uncertainty of the measured axis was calculated as ±170 μm. Both values are presented at 3σ. In the results presented below, the uncertainty added is not the spread of the measurand in these particular measurements, but the total uncertainty from the pure magnetic measurements with an uncertainty of ± 20 μm, through the fiducialization process with the uncertainty of the laser tracker of ±150 μm.

Table 5.4: The resulting magnetic axis measured by the rotating single-stretched wire method. The table gives the raw measured axis, $(\Delta x_m, \Delta y_m)$, and the measured axis corrected for the position of the wire, $(\Delta x_{m,c}, \Delta y_{m,c})$.

Corrector magnet	Measured axis in μm		Corrected Axis in μm	
	$\Delta x_m \pm 3\sigma$	$\Delta y_m \pm 3\sigma$	$\Delta x_{m,c} \pm 3\sigma$	$\Delta y_{m,c} \pm 3\sigma$
a_2	-10.96±170	5.48±170	4.82±170	-218.20±170
b_6	-297.38±170	-154.57±170	-298.90±170	-380.88±170
a_6	-296.56±170	-348.41±170	-301.35±170	-466.04±170
b_5	-322.30±170	-412.93±170	-301.07±170	-519.89±170
a_5	-316.21±170	-510.80±170	-298.89±170	-547.86±170
b_4	-171.29±170	-542.64±170	-153.91±170	-484.44±170
a_4	52.50±170	-501.10±170	79.69±170	-361.01±170
b_3	89.99±170	-284.93±170	98.73±170	-85.67±170
a_3	-15.48±170	-332.19±170	-11.32±170	-14.01±170

The measure roll angles are presented in Table 5.5. It shows the measured roll angle, which for half of the magnets deviate significantly from zero, as they are skew corrector magnets. This effect is adjusted for by this knowledge, shown as $\alpha_{roll,nom.}$, which is the nominal roll angles of the corrector magnets in the current assembly. Then, the final roll angles are presented, along with the internal

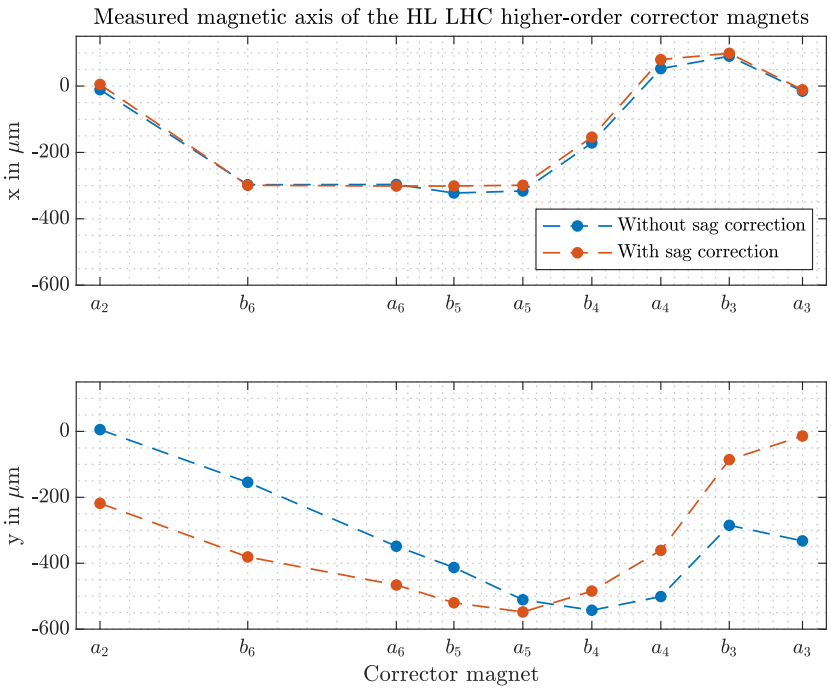

Figure 5.5: The measured magnetic axes of the corrector magnets with respect to the external fiducials of the magnets, before (blue) and after (orange) adjustment of the wire's position within the magnet. The horizontal component of the axis is shown in the uppermost plot, whilst the lowermost figure shows the vertical component.

deviations obtained by rotating the corrector package by the average roll angle, by convention in the clockwise direction [14]. The average roll angle is found to be 1.05 ± 0.06 mrad.

Table 5.5: The resulting roll angles of the higher-order corrector magnets, presented with an uncertainty at 3σ. The table gives the measured roll angles, $\alpha_{\text{roll,meas.}}$, the nominal roll angles by design stemming from the orientation of the magnets, $\alpha_{\text{roll,nom.}}$, the reported roll angle, α_{roll}, and the roll angle subtracted the average value, $(\alpha_{\text{roll}} - \overline{\alpha}_{\text{roll}})$. All values are given as mechanical angles, that is in the external reference system.

Corrector magnet	Roll angle in mrad			
	$\alpha_{\text{roll,meas.}} \pm 3\sigma$	$\alpha_{\text{roll,nom.}}$	$\alpha_{\text{roll}} \pm 3\sigma$	$(\alpha_{\text{roll}} - \overline{\alpha}_{\text{roll}}) \pm 3\sigma$
a_2	-784.41±0.06	-785.40	0.99±0.06	-0.07±0.06
b_6	1.51±0.06	0.00	1.51±0.06	0.45±0.06
a_6	-259.96±0.06	-261.80	1.84±0.06	0.79±0.06
b_5	1.59±0.06	0.00	1.59±0.06	0.54±0.06
a_5	-313.24±0.06	-314.20	0.96±0.06	-0.10±0.06
b_4	1.02±0.06	0.00	1.02±0.06	-0.03±0.06
a_4	-392.07±0.06	-392.70	0.63±0.06	-0.43±0.06
b_3	0.62±0.06	0.00	0.62±0.06	-0.43±0.06
a_3	-523.27±0.06	-523.60	0.33±0.06	-0.73±0.06

5.1.3 Discussion

In this section, the measurements of the higher-order corrector magnets in the corrector package assembly are discussed. The results of the measurements are compared to the requirements and expected deviations of the measurands, which, for simplicity, are added in Tables 5.6 and 5.7. Uncertainties of the measurements are also presented, and the actions made to mitigate them are discussed. The section is concluded with an outlook of the next actions for developing the rotating single-stretched wire method.

Table 5.6: Measurement requirements for the transverse centre, roll angle, longitudinal centre and magnetic length for room temperature measurements of the HL LHC corrector package [38].

Transverse centre in mm	Roll angle in mrad	Long. centre in mm	Mag. length in mm
0.4	0.3	10	10

Table 5.7: Expected deviation of the roll angle and magnetic centre with respect tot the aperture axis HL LHC corrector package expressed as 3σ-values [38]. H, V and S are the horizontal, vertical and longitudinal deviation, respectivelly.

H in mm	V in mm	S in mm	Mag. length in mm	Roll angle in mrad
1	1.58	10	10	0.1

Measurement results

The measured magnetic axes and roll angles match well with the preliminary study of the measurement data, where the measured axes before correction for the sag all lie in the quadrant foreseen by this study, seen in Figure 5.4 and Table 5.4. This is not the case after correcting for the wire location, as this involves moving the results from the magnetic reference system, in which the measured quadrants are expressed, to the mechanical reference. The absolute roll angles match nearly perfectly with the external field phases measured in the preliminary study, and when the average is corrected for in both cases, the differences are in the order of 20 μrad, which is less than the accepted uncertainty of the measurands of 300 μrad. The correspondence between the simplified approach in the preliminary study and the more theoretical method based on feed-down of multipoles therefore validates the connection between the physical measurement signal and the post-processing algorithm.

When it comes to the absolute results, they are given as α_{roll} and $(\Delta x_{\text{m,c}}, \Delta y_{\text{m,c}})$ in Table 5.5 and the Table 5.4. From the measured axes, we see that they are well within the expected deviations, with approximately a factor 3 of margin in both cases. From the plots shown in Figure 5.5, the corrector package seems to be slightly curved in both x- and y-directions, whith an apparently similar sag in both directions. However, in the horizontal plane, correctors b_6 through a_5 seem to be on the same axis. Then, on both sides, the magnets seem to be shifted slightly in the positive x-direction. For the vertical plane, the magnets seem to follow a catenary-like curve after the saggita is adjusted for. One reason for this could be errors in the implementation of the correction for the wire position within the magnets. Therefore, a simpler approach was followed, consisting of comparing the calculated wire trajectory with a linear approach using the simple calculation of the wire saggita, eq. (3.5). The result of this comparison for the skew decapole corrector is shown in the following figure.

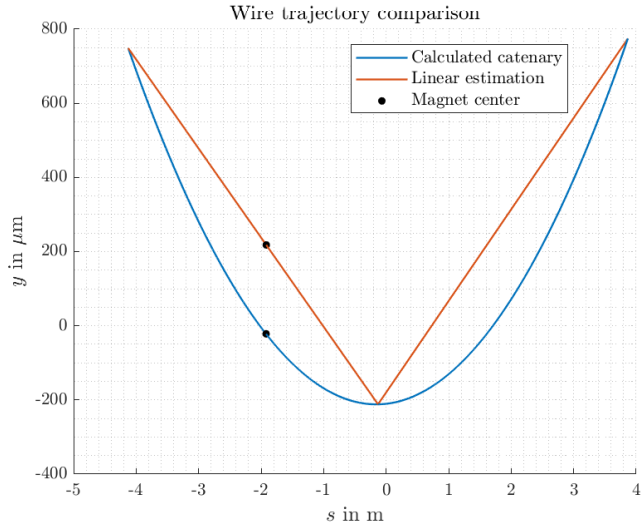

Figure 5.6: Comparison of two calculations of the wire trajectory before the magnetic measurements of the skew decapole corrector magnet. The calculated catenary curve is shown in blue, while a linear estimation using eq. (3.5) is shown in orange. The center of the magnet in the two cases are shown as black dots.

From the comparison, it can be seen that the calculation of the catenary curve matches the simpler approach in the middle of the wire stages. The error made from using the wrong estimate of the wire trajectory is also seen, with a vertical difference between the two curves of more than 200 μm. However, a taut wire follows a catenary curve, as shown in [49], and since the same minimum is found, it is fair to assume the calculations of the wire trajectories are correct.

In section 4.1, the uncertainty of the rotating single-stretched wire system was determined to be ± 20 μm. The measurement uncertainty is therefore mainly determined by the accuracy of the laser tracker measurements of the stages, external fiducials and the measurement grid. For this reason, the uncertainty reported in Table 5.4 uses the full uncertainty of the system, from the measured axis through the fiducialization process, both for the corrected and uncorrected measurements. This is so, since the full reference system is determined by the laser tracker, and as such this determines the uncertainty of all the measurements. However, if the relative axis offset, say from the average, were to be calculated, the uncertainty of the wire system itself, ± 20 μm, would be applied. From the uncertainty analysis implemented in SpatialAnalyzer, over the course of the measurements, a maximum error of 40.5 μm was measured in the fit of the reference points. This means that from the six reference points positioned at different locations in space, the error between any of the measured reference points and the fit of all the points from all the measurements were less than 40.5 μm. This error accounts for all uncertainty introduced by the laser tracker measurement; the uncertainty in each measurement, and changes to the position of the laser tracker itself, or the points, caused by mechanical disturbances, temperature changes or air movement during the laser measurement. As a rule of thumb, the metrological department at CERN operates with a threshold of 80 μm, hence these measurements are well within. The average error between the measurements were 6.4 μm, and can be taken as the spread of the laser tracker measurements. From the data sheet of the laser tracker, the accuracy of the laser tracker measurements is given as $\pm 15\mu\text{m} + 6\mu\text{m/m}$. The distance from the laser tracker to wire stage A is approximately 5.5 m, giving an optimal accuracy of $\pm 144\mu$m at 3σ. Adding the uncertainty of the magnetic measurement of ± 120 μm, the spread of the laser

tracker measurements, and its precision, the total uncertainty of the measured magnetic axes to the external fiducials is approximately ±170 μm. From this, it is seen that both the measured axes and the uncertainty is within the expected deviation and maximum measurement uncertainty.

For the measured roll angle, the case is slightly different. As the roll angle is independent of the initial wire position in the magnet, the uncertainty of the laser tracker measurements are insignificant for these values. Therefore, the uncertainty of the roll angel measurements are the reported uncertainty from the metrological characterization of the rotating singles-stretched wire, ±0.06 mrad. Even though the uncertainty is within the requirements, the measured roll angles exceed the expected deviation with up to a factor 8, from the expected 0.1 mrad to the measured 0.8 mrad of the skew dodecapole corrector. After internal discussions, it has been brought forward that the requirements and expected deviations of the roll angle measurements conducted at room temperature seem too stringent. It was also discussed that the values might be required for the quadrupole triplets, and that it has just been inherited to the corrector package.

Even though the measured axes are within the expected deviations, the differences in measured axes are quite high considering the production methods applied, which usually yield more closely correlation between the geometry of the magnet and the magnetic field. This is also the case for the measured roll angles. One probable reason for these deviations, is the fact that the corrector package is not yet complete, and that it is still lacking the top cradle. This means that there might still be some clearing allowing for misalignment in the corrector assembly. After visually inspecting the corrector package in its current assembly, it was clear that the magnets are not in line, and gaps could be seen in the guiding bars that connect the magnets. The misalignments can be seen in the figure below.

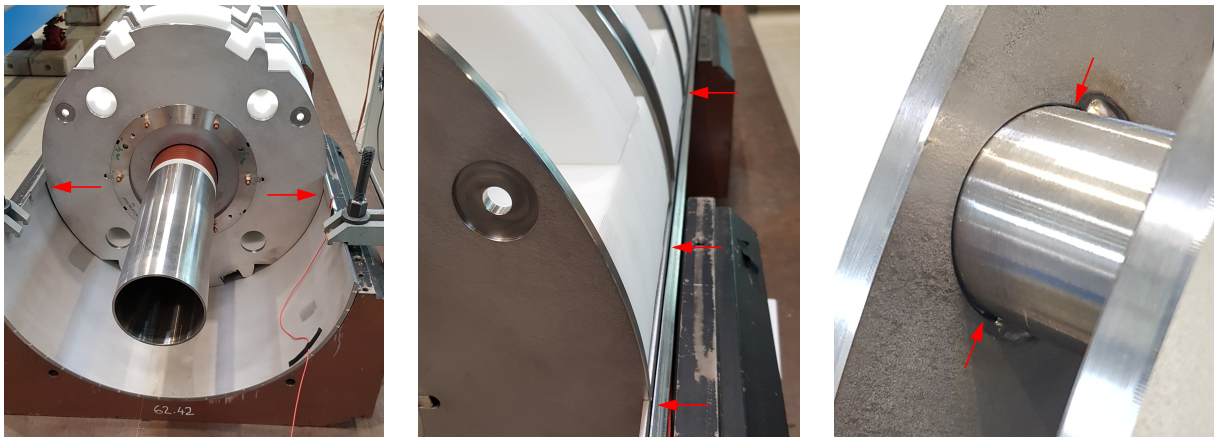

Figure 5.7: Misalignment in the present assembly of the corrector package in the LMF. The visible misalignment is highlighted by red arrows.

From the leftmost figure, it is seen a misalignment of the corrector magnets in the cradle. This misalignment could be equal for all the magnets, as the cradle is not yet attached to the magnet assembly. In the central figure, a change in distance from the cradle to the metallic strip connecting the magnets together can be observed as a slightly decreasing gap. This effect was not evenly distributed along the corrector package, indicating a possible displacement, at least in the vertical plane. In the third figure, there is a clear difference between the gaps of the positioning rod and the guiding perturbation on the two sides. If the rod is not centered in the hole, this would create an unwanted roll angle, which seems to be the case in the assembly. It is naturally not easy to completely state that there are in fact imperfections in the assembly of the magnets from these pictures, but any visible offset help explain the quite large differences in the magnetic axes, and also the roll angles. Fur-

thermore, as the assembly is not yet complete, the addition of a cradle covering the topmost part of the assembly will probably straighten the full corrector package, evening out some of the measured offsets of the magnetic axes. Therefore, the corrector package will have to be remeasured when it is fully assembled, and ready to be installed in the accelerator.

To summarize, the measured magnetic axes are within the expected deviation. However, the deviations are a bit larger than what could be assumed. The roll angles deviate too much according to the requirements, even though these are probably too stringent. The visible misalignment of the corrector magnets on the corrector package assembly would explain the offsets measured.

Other sources of uncertainty

Due to lengthy measurements, and a mechanically and thermally noisy environment, there are a few additional sources of error introduced to the measurements.

As already discussed, mechanical and thermal instabilities add additional errors to the measurements with the Leica AT930 laser tracker. These effects are, however, minimized by actively using the six grid targets installed around the laser tracker. A maximum measured error of 40.5 μm over the course of four measurement days is very good, especially when compared to the limit of 80 μm used as a rule-of-thumb by the metrological characterization team at CERN. However, a few measures could be taken to further reduce the movement of the laser tracker, and the measurement of this. First of all, the tripod used for supporting the laser tracker is less stable than other supports available, due to its many moving parts. They can result in a slight sag of one or more of the three measurement feet, especially with vibrations from the two big cranes in the LMF. One solution would be to use a "tower"-structure with less moving parts. Another slight weakness of the laser tracker measurements in this part, is the use of the grid of targets. In these measurements, most of the grid points were on different positions on the bench supporting the corrector package. To improve, one could have a bit more distance and variations in the target positions, but this was not possible in the environment.

After the system was disassembled, we found that some of the nuts and bolts in the supporting structure of the wire stages were a bit loose. This was most likely caused by a slightly too loose bolt from the assembly of the system, and as time passed, vibrations caused it to loosen more. This have caused the stages to slightly tilt over the days of measuring, which would give an increased sag of the stretched wire. The stages were reset every morning, adjusting for the changing pitch and roll angles. This would reduce the larger effects over time. Furthermore, as the laser tracker was used to measure the stages in between magnetic measurements, the effect is somewhat accounted for. However, the changes during a single magnetic measurement are not so easily measurable, and they could end up polluting the measured signals quite significantly. This is not likely to be the case, however, as several measures are in place to mitigate these effects. The first one being the laser tracker measurements. By looking at the measurements of the wire stages before and after a magnetic measurement, and recreating the wire trajectories, a maximum deviation between the vertical component of the wire within the magnet was found to be in the order of a 50 μm. This might seem a lot, but it is worth noting that this value has an uncertainty determined by the uncertainty of the laser tracker, which is significantly higher than this. The other measure in place, is the continuous measurement of the tension of the stretched wire. It can be shown that the wire sag is inversely proportional to the wire tension [27]. From this, and by knowing the sag of the wire at a given wire tension, the changing wire saggita can be calculated over the course of a full revolution of the wire. This is based on the assumption that the wire stages does not move in the exact same direction, balancing the wire tension. The wire sag is known from the natural frequency measured after the last magnetic measurement, and from this, the differences in wire saggita for all the measurement points, and all the magnets, can be calculated and plotted. The wire saggita for the different measurements

are shown in Figure 5.8 below.

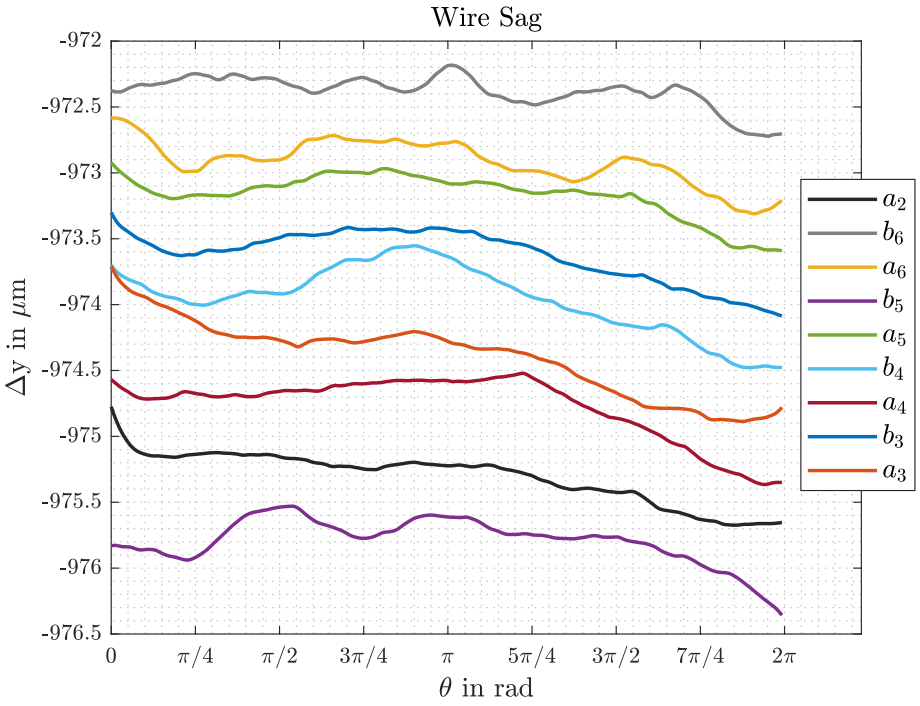

Figure 5.8: The wire saggita recalculated from the wire tension over the course of a full magnetic measurement of the higher-order corrector magnets in the corrector package assembly.

What is seen from these graphs, is that the wire tension, and hence the saggita, has a slight decrease from the beginning to the end of the measurement, which would account for a slight forward tilting of both the wire stages. However, this difference is in the order of 0.5 to 1.5 μm, a change deemed insignificant to the results. It can also be seen that the tension decreases during the course of a day. The magnets were measured in the following order:

Day 1: b_5, a_5, b_4, a_4.
Day 2: b_3, a_3, a_2.
Day 3: b_6, a_6.

A decrease in wire tension is seen in this order from the figure, with a readjustment each morning, seen as a lift of the average in the graph. To reduce this effect, as well as the continuous decrease in wire tension, the tension used to calculate the wire saggita from the laser tracker measurements was adjusted accordingly. The average wire tension of the measurement is compared to the average frequency of the last wire measurement, as the natural frequency of the wire is measured after this. The wire frequency is then adjusted by this factor, and the wire position within the magnet is therefore calculated with a more correct wire frequency than the measured natural frequency.

Another possible effect of the loose bolts and nuts, is the distortion of the signal from sudden skips in the wire tension. This was also investigated, and a plot of the results can be seen in Figure 5.9 below. In all measurements using the stretched-wire technique, the tension of the wire changes over the course of the measurements. This is unavoidable, as a perfect alignment of the wire stages is impossible. In Figure 5.9, the normalized flux density of the normal octupole corrector magnet is plotted, together with the relative deviation of the wire tension. First of all, it can be seen that the

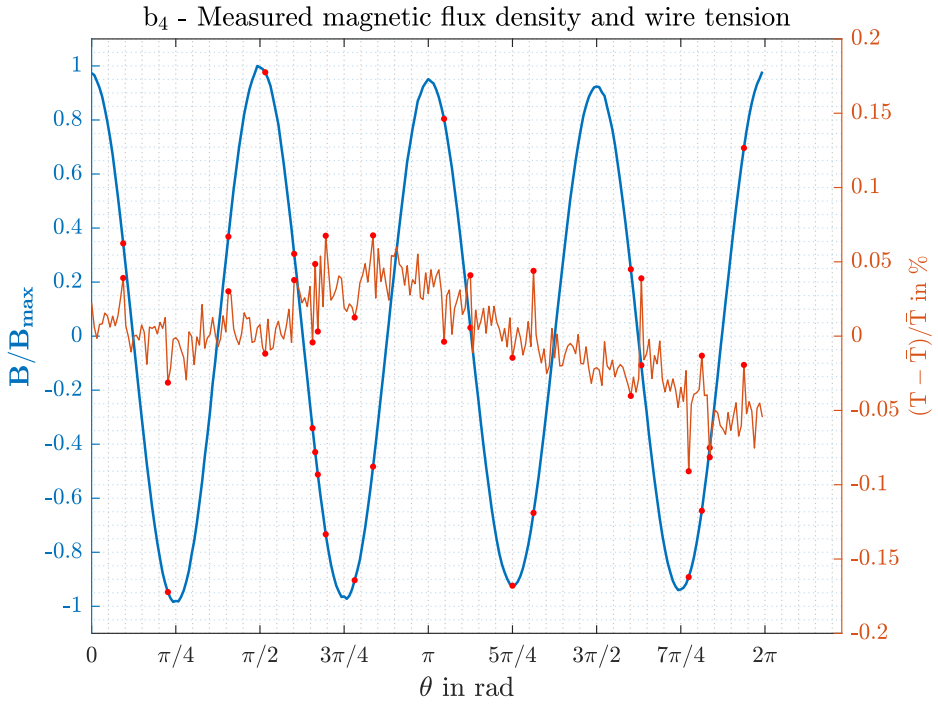

Figure 5.9: The effect of changing wire tension on the measured flux density of the skew octupole corrector magnet. The blue curve shows the normalised flux density, and the orange curve the relative change of wire tension. The red dots highlight the most prominent peaks in the tension, corresponding to the most rapid changes in the tension, and the corresponding flux density measurements.

average deviation is less than 1‰. The peaks of the wire tension deviation is highlighted by red dots, with the corresponding values of the measured flux density. There is no clear effect of the tension spikes on the measured signal, as can be seen in the figure. Furthermore, the amplitude of the flux density at either side of the measurement, $0°\pm\Delta\theta$, matches well, even though the wire tension is lower. In total, it can be concluded that the effect of the changing wire tension is negligible in this case.

To conclude this section, the main sources of uncertainty, in addition to the ones inherent in the system, is the uncertainty connected to the laser tracker measurements, given the mechanical and thermal instabilities of the surroundings, and the movement of the wire stages due to loose bolts and nuts. The laser tracker effects are accounted for, and the setup was found to be sufficiently good for these measurements, all the time the measured errors of the fit grid is way below usual limits. For the movement of the wire stages, the effects are accounted for in the post-processing, by validating that the movement is not too big, and by adjusting for the average wire tension for the given measurements.

5.1.4 Conclusion

The magnetic axis and roll angles of the corrector magnets in the corrector package was measured using the rotating single-stretched wire method. The measured axes were found to be within the expected deviations, even though the offsets from the average were high when considering the usual quality of production. The roll angles were outside the expected deviations. As discussed, the requirements and expectations might be too stringent. The results might be explained by the visible

misalignments of the assembly, both in the transverse direction, and of the roll angles.

With this in mind, the results obtained through these measurements are deemed sufficiently good, and the measurement campaign as a whole is considered a success. Furthermore, the measurement technique proved to be robust to the many external sources of uncertainty, and it will be used for future measurements as well.

After the final assembly of the corrector package, the magnets will be measured again using the rotating single-stretched wire method. Due to a tighter assembly in the final configuration of the corrector package, one would expect a closer correlation of the measured axes and roll angles to the expected deviations. For the future measurements, the setup of the measurement system will have to be more thorough than this, to avoid errors due to mechanical and thermal instabilities in the measurements. It would also be beneficial to measure the magnets in another environment. Preferably, the measurements would be carried out in another laboratory altogether, but as this is less likely, the results would probably be improved by moving the corrector package to one of the smaller rooms used for metrological characterization, as this would reduce the thermal changes, effects of air movement, and to some extent the mechanical instabilities. Furthermore, these rooms are equipped with proper positions for laser tracker grids, improving the quality of the fiducialization.

5.2 Measurements With The Translating Coil Fluxmeter

This section presents the translating coil fluxmeter measurements of the corrector package assembly. As with the rotating single-stretched wire measurements, the magnets were measured in LMF, with the added challenges as explained above. However, the measurements with the translating coil fluxmeter are less time consuming than the wire measurements, thus suffering less from mechanical and thermal instabilities in the surroundings.

In contrast to the measurements of the integral magnetic axes and roll angles of the corrector magnets, the measurements presented in this section are conducted both to locate the magnetic center and length, *and* to investigate and optimize the measurement procedure and measurement system of the translating coil fluxmeter presented in section 3.4. Thus, the measured centers and magnetic lengths are compared to the nominal values and their expected deviations, and the spread of the measurands to the tolerated uncertainty of the measurements. However, the lessons learnt from the measurement campaign about the ability of the system to locate the magnetic center and length, as well as its strengths and weaknesses are equally important as this measurement system will be refined in the following months.

The measurement setup and approach are presented, with emphasis on the differences between the setup in the LMF and in the measurement halls of the Testing and Measurements section, before the results are presented. The section is concluded with a discussion of the measurement system and the results, together with suggestions of improvements for the next iteration.

5.2.1 Measurement setup and approach

Measurement setup

The measurement setup of the translating coil fluxmeter in the LMF is presented in Figure 5.10 below. From the figure, it is clear that the measurement rack, (1), is nearly identical to the one shown in Figure 3.11. The exception is the encoder board, which is replaced by the National Industry PXI-6289 multifunction I/O module, barely visible to the right of the FDIs. The power supply for the Hall probe is seen, (2), however, the Hall probe measurements were redundant in this measurement campaign, due to difficulties positioning the Hall generator with respect to the alterating magnetic poles of the assembly. The mechanical positions of the magnets' end plates were instead used as intervals for the integration. The moving rod and the end plate are shown, (3), with the end plate fixed to the cold bore of the corrector package. By using two joined rods, the measurement head reaches the far end side of the corrector package in this assembly. The corrector package assembly, (4), is the same as for the single-stretched wire, however the dipole was removed before this measurement campaign was launched. As before, the assembly of the corrector package reads; a_3, b_3, a_4, b_4, a_5, b_5, a_6, b_6, a_2, this time going into the picture. The measurement coordinate system is shown in yellow. It is attached to the mechanical axis of the quadrupole corrector magnet, with the origin at the far end of the present assembly. For simplicity, and in accordance with the validation measurements, the longitudinal axis points towards the end plate of the moving rod, thus pulling the measurement head is defined as positive movement. This is the opposite of the longitudinal axis used for the rotating single-stretched wire measurements.

As with the wire measurements of the corrector assembly, Leica Absolute Tracker AT930 was used for the fiducialization of the corrector package. As discussed in section 4.2, the laser tracker was also used for measuring the mechanical position of the measurement head, and therefore two stations are needed at the far end of the corrector package; the tripod station used for measuring the measurement head, (5), together with one of two more stations where the fiducials were measured,

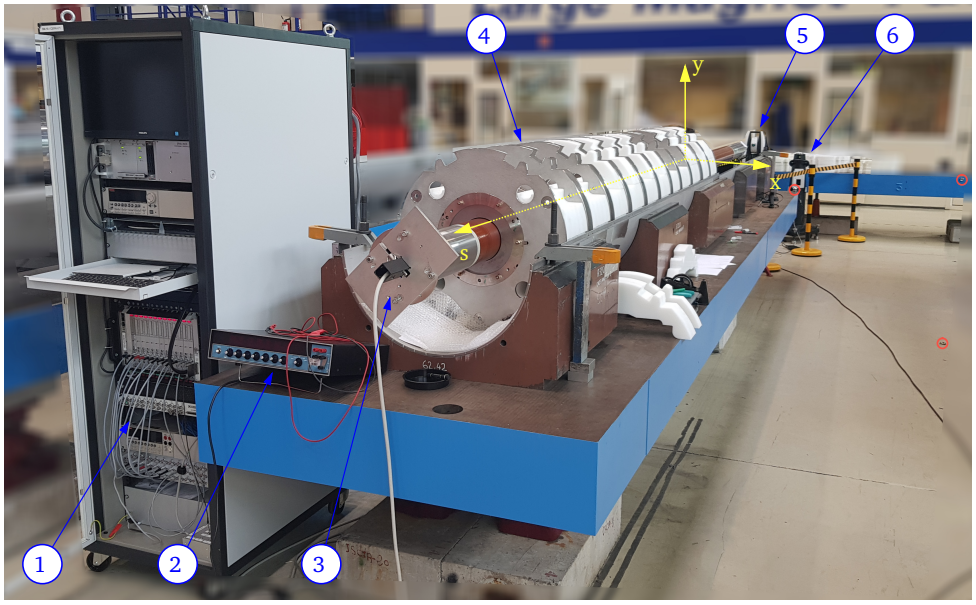

Figure 5.10: Measurement setup for the translating coil fluxmeter measurements of the corrector package assembly. It shows the measurement system, (1)-(3), the magnet assembly (4), and the laser tracker setup, (5) and (6). It also gives the defined coordinate system for the measurements, and shows targets used in the laser tracker localization as red dots.

(6). As the cold bore is long and rather narrow, the laser tracker station (5) was not able to measure the fiducials on the magnet, hence two stations were needed. The last station was positioned approximately where the picture is taken from. As discussed in the "Approach" part of subsection 5.1.1, a grid of eight targets were used to orient the laser tracker in the different positions, of which three are visible in the figure, highlighted by red circles. From this point on, the coordinate system was created in the same way as for the rotating single-stretched wire measurements; the line between the centers of the circles fit to the three fiducials on each side of the assembly constitute the s-axis, the internal inclination sensor determines the vertical axis, and the x-axis follows from the right-hand-rule.

Measurement approach

The magnetic measurements were conducted similarly to the method presented in section 4.2. First, the full corrector package was measured without powering the magnets, to investigate whether the system is sensitive enough to measure the remanence field in the magnets. Then, each of the magnets were measured separately, powered one by one. The measurement campaign per magnet comprised a set of three full measurements per polarity, resulting in six measurements per polarity, as a full measurement includes both pulling and pushing the moving rod.

As these measurements are a lot less time consuming than the measurements with the rotating single-stretched wire, the mechanical instability in the surroundings can be avoided by measuring at times of less work around the measurement system. Therefore, the main source of error for the laser tracker measurements was temperature changes in the environment. Between the measurements of each magnet, the drift of the laser tracker system was checked, and when this exceeded approximately 50 μm, the laser tracker was "re-positioned" to account for the drift. This is an important aspect to reduce the effect of mechanical and thermal instability in the surroundings of the measurement system, as discussed previously. It was achieved by re-measuring the reference points, as explained

for the rotating single-stretched wire measurements in subsection 5.1.1.

After all magnets were measured individually, they were powered in series. This was done to investigate whether there are any *crosstalk* between adjacent magnets, i.e. influence on the magnetic field of a magnet by the magnetic field in its neighbouring magnets. In this configuration, since only a single power supply was available, the magnets could be powered at maximum 60 mA, hence inducing voltage at approximately half the amplitude of the individual measurements. There are several benefits of measuring all the magnets at once; it measures the magnets in their most realistic configuration, it captures any crosstalk, and it is faster and allows for more repetitions. This measurement therefore acts as an investigation to whether a series measurement is feasible using the simple setup, and compares the obtained results with the results of the single measurements. The full magnet setup was measured five full cycles per polarity, yielding a total of ten individual measurements of the flux density after the semi-difference is calculated, when both directions of movement is included.

In the post-processing phase, the optimal solutions found in section 4.2 were applied. The difference is the choice of summation interval, for which the end-plates of the individual magnets were used in these measurements. The importance of the interval is significantly reduced by calculation of the semi-difference of the measurements, as this removes the constant drift of the FDIs, and any other constant sources of error. The intervals are also applied to the series measurements of all the higher-order corrector magnets, reducing drift caused by random noise outside the field region. Then, the signals from the different PCBs are inverted and averaged, to mitigate effects of measurement head rotation, before the signals are resampled. The resampling is of great importance to the calculation of the semi-difference, as we need to ensure the measured flux densities are compared at the same longitudinal position. The signals are resampled at 500 000 positions, yielding a worst-case resolution of less than 0.5 μm, calculated for the length of the normal dodecapole magnet, which is more than sufficient to determine the magnetic center with an uncertainty below the requirements. Then, to represent the flux density field profiles, the signal is deconvoluted using b-splines. Lastly, the magnetic lengths and centers are calculated for the magnets using eqs. (2.43) and (3.8).

Even though the magnets are measured at least six times per polarity, not all measurements are used in the post-processing phase. This is due to mechanical instabilities in the measurements, which will be explained in the following parts.

As there were no available drawings or measurements of the mechanical positioning of the magnets within the assembly, the mechanical position of the end plates were measured by the laser tracker by holding the target to the plates while measuring. The measured centers are then compared to this value. For the magnetic length, the measured values are compared to the nominal values given by simulations of particle trajectories and the corresponding field requirements. These values are presented in Table 2.1.

5.2.2 Measurement results

In this part, the results of the translating coil fluxmeter measurements of the corrector package assembly is presented.

The measured remanence field distribution for the entire corrector package assembly is shown in Figure 5.11 below. The flux density measured in each of the induction coils are shown, and the signals for both the pushing and pulling of the measurement head are shown. The flux signals are divided by the calibrated surface areas. Furthermore, the mechanical reference system was not yet created at this stage, and the positions are therefore given as absolute distances to the measurement head. Therefore, 5.5 m corresponds to approximately 0 m in the correct reference system. The mechanical position of the end plates of the corresponding magnets are shown as black lines, and are

highlighted by the name of the main multipole component.

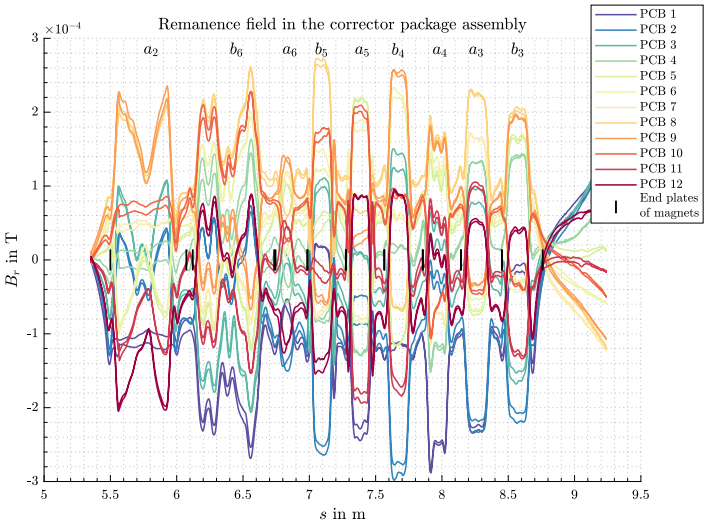

Figure 5.11: The measured remanence field of the corrector package assembly, in each of the induction coils, together with the mechanical measurements of the end-plates of the magnets. The magnets corresponding to the remanence fields are highlighted by their dominant multipole component.

In Figure 5.12, the resulting magnetic flux density profiles are shown for all 12 PCBs of the measurement head. The signals are calculated as the semi-difference of two consecutive runs, with opposite polarity. To reduce computational time, the deconvolution was omitted, and the flux measurements are simply divided by the calibrated surface areas of the PCBs.

The next figure, Figure 5.13, shows the next step of the process, where the signal from all the coils are inverted to have the same polarity, and averaged for all the measurements. The measurements from all runs are then averaged to obtain the final field profiles. The figure includes the field profiles obtained through the simple approach of dividing the measured flux by the calibrated surface area of the PCBs, and the deconvoluted signals, shown as red and black curves, respectively.

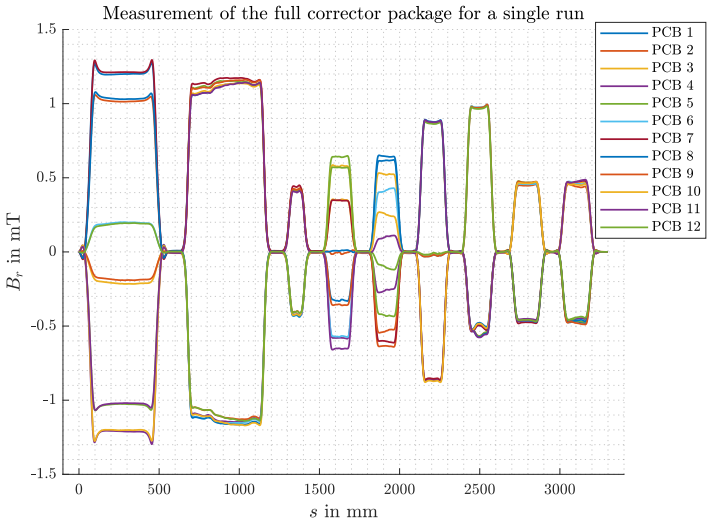

Figure 5.12: Resulting longitudinal profile of the measured flux density for a single run after the semi-difference is calculated.

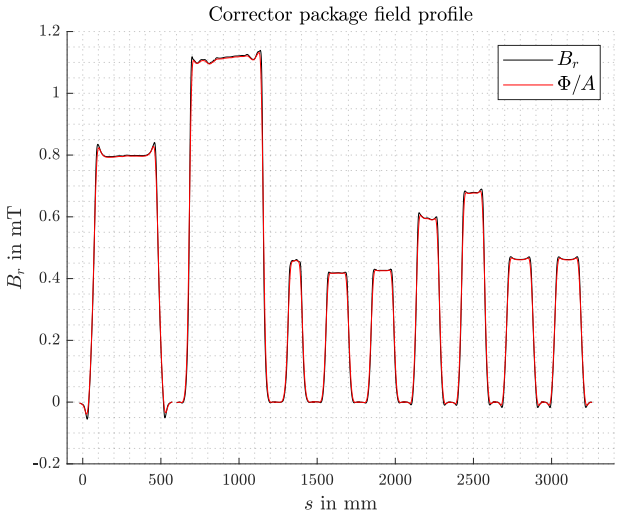

Figure 5.13: Resulting longitudinal profile of the measured flux density, averaged over the 12 PCBs. The signals are shown both for deconvoluted and convoluted signals, namely

The calculated magnetic centers of the measurements with separately powered magnets are given in Table 5.8, and the corresponding magnetic lengths calculated are presented in Table 5.9. The values are given as the average of at least three measurements. The spread of the centers are calculated as the standard deviation of the measured values over the measurements, and given at 3σ level. The deviations from the nominal values are given as absolute and relative differences.

Table 5.8: The magnetic centers of the corrector package assembly, with the magnets powered separately. The spread of the measurands are given at 3σ levels, and the difference to the nominal values are shown both as absolute and relative differences.

Multipole component	$s_c \pm 3\sigma$ in mm	$s_{c,nom.}$ in mm	$s_c - s_{c,nom.}$ in mm	$(s_c - s_{c,nom.})/s_{c,nom.}$ in %
a_2	286.32 ± 1.47	284.30	2.03	0.71
b_6	930.55 ± 2.45	925.17	5.38	0.58
a_6	1366.52 ± 1.59	1363.85	2.67	0.20
b_5	1637.18 ± 0.37	1633.71	3.46	0.21
a_5	1927.17 ± 1.17	1923.44	3.73	0.19
b_4	2216.22 ± 0.89	2213.13	3.08	0.14
a_4	2506.67 ± 1.26	2502.86	3.81	0.15
b_3	2805.66 ± 1.51	2801.59	4.08	0.15
a_3	3113.10 ± 1.11	3109.17	3.94	0.13

Table 5.9: The calculated magnetic length from measurements of separately powered corrector magnets. The spread is given at 3σ level, and the deviations from the nominal values are given in both absolute and relative values.

Multipole component	$L_m \pm 3\sigma$ in mm	$L_{m,nom.}$ in mm	$L_m - L_{m,nom.}$ in mm	$(L_m - L_{m,nom.})/L_{m,nom.}$ in %
a_2	422.05 ± 0.39	401	21.05	5.25
b_6	475.59 ± 3.00	469	6.59	1.41
a_6	97.38 ± 0.66	99	-1.62	-1.64
b_5	151.12 ± 0.57	145	6.12	4.22
a_5	151.06 ± 0.65	145	6.06	4.18
b_4	154.19 ± 0.52	145	9.19	6.34
a_4	153.32 ± 0.06	145	8.32	5.74
b_3	173.16 ± 0.21	168	5.16	3.07
a_3	173.24 ± 0.40	168	5.24	3.12

The same results are presented in Tables 5.10 and 5.11 for the measurements with the magnets powered in series. The results are obtained from the same calculations as presented above.

Table 5.10: The magnetic centers calculated with the corrector magnets powered in series, with the spread of the measurand presented at 3σ level. The deviations from the nominal values are given in both absolute and relative values.

Multipole component	$s_c \pm 3\sigma$ in mm	$s_{c,nom.}$ in mm	$s_c - s_{c,nom.}$ in mm	$(s_c - s_{c,nom.})/s_{c,nom.}$ in %
a_2	285.92 ± 1.20	284.30	1.63	0.57
b_6	928.63 ± 2.98	925.17	3.47	0.37
a_6	1368.44 ± 4.52	1363.85	4.59	0.34
b_5	1637.67 ± 1.05	1633.71	3.96	0.24
a_5	1927.12 ± 1.52	1923.44	3.68	0.19
b_4	2216.16 ± 1.42	2213.13	3.02	0.14
a_4	2506.81 ± 1.73	2502.86	3.95	0.16
b_3	2805.71 ± 1.35	2801.59	4.13	0.15
a_3	3113.21 ± 1.62	3109.17	4.04	0.13

Table 5.11: The calculated magnetic length with the corrector magnets powered in series. The spread of the measurement is given at 3σ levels, and the differences between measured and nominal magnetic lengths are given both in absolute values and in relative values.

Multipole component	$L_m \pm 3\sigma$ in mm	$L_{m,nom.}$ in mm	$L_m - L_{m,nom.}$ in mm	$(L_, - L_{m,nom.})/L_{m,nom.}$ in %
a_2	422.37 ± 1.00	401	21.37	5.33
b_6	472.98 ± 6.88	469	3.98	0.85
a_6	96.92 ± 3.68	99	-2.08	-2.10
b_5	150.53 ± 0.96	145	5.53	3.81
a_5	150.84 ± 1.02	145	5.84	4.03
b_4	153.76 ± 1.79	145	8.76	6.04
a_4	152.89 ± 0.34	145	7.89	5.44
b_3	172.83 ± 0.44	168	4.83	2.88
a_3	172.83 ± 0.52	168	4.83	2.87

5.2.3 Discussion

The translating coil fluxmeter was used to measure the corrector package assembly in the LMF, with the aim of locating the magnetic centers and calculating the magnetic length of the individual corrector magnets. The nominal values of both the magnetic centers and lengths are presented in the tables with the measured values. The nominal magnetic lengths are taken from Table 2.1, whilst the magnetic centers are calculated from the Leica AT930 laser tracker measurements of the end-plates of the individual corrector magnet. It is unknown whether only stoppers are used for the assembly of the corrector package, or if each of the magnets are measured using a laser tracker. Therefore, the somewhat rough values obtained from the end-plate measurements are assumed sufficiently good for the comparison, especially since the uncertainty in the assembly might be as much as 10 mm at 3σ.

The expected deviations and measurement uncertainty requirements are presented in Tables 3.2 and 3.1, respectively. The uncertainty requirements of the measurements are 10 mm for both the longitudinal center and the magnetic length, as well as the expected deviations.

In the following, the measured flux density profiles and the calculated magnetic centers and lengths are discussed, together with comments on the sources of error in the measurements.

Measurement results

Measured field profiles:

The field profiles obtained by the translating coil fluxmeter are shown in Figures 5.11, 5.12 and 5.13. The remanence fields measured in Figure 5.11 show that the measurement system is able to measure field levels of as low as a few tens of microtesla for the skew dodecapole corrector magnet, a_6. This shows that the system is sensitive, even to very low field values, which naturally is of great importance to the room temperature measurements of the corrector magnets. The magnetic field profiles from previous measurements at cold are clearly visible as distinct flat areas for most of the magnets, whilst for the skew quadrupole and normal dodecapole, the field at the entrance and exits of the magnet is the most prominent. With the addition of the mechanical positions of the end-plates of the magnets, seen as black vertical lines, it is clear that the measured flux density actually corresponds to the remanence field of the magnets, instead of being just noise. Furthermore, an increase in flux density is seen at the end of the corrector package assembly. This is found where the measurement head exits the skew sextupole magnet, a_3, and the largest values are obtained when the head exits the cradle in which the magnets are placed. This is most likely the effect of the metallic bench supporting the corrector package assembly. During the measurements with the rotating single-stretched wire, this was found to be slightly magnetic, and the field measured with the translating coil fluxmeter supports this hypothesis. For the wire measurements, this is filtered out in the Fourier analysis of the measured signal. However, when the measurement head of the translating coil fluxmeter exits the corrector package, which is shielding the magnetic field from the bench within the assembly, the PCBs experience a changing magnetic flux, measured as an induced voltage.

The remanence field and the constant field of the supporting bench show the importance of calculating the semi-difference in the post-processing. The effects are clear in Figure 5.12, where the semi-difference of two consecutive runs with the magnet powered in opposite polarity are shown. In this plot, all the magnets are powered in series, and it shows the signals measured by all the PCBs. Comparing to Figure 5.11, it is clear that the remanence fields are removed by the semi-difference calculation. Furthermore, the magnetic flux density of the supporting bench is also removed, with zero field measured at the exit of the skew sextupole magnet. Using this method, the issue of integrator drift is also significantly reduced, seen as the zero field regions in-between the magnets, even though the summation interval spans the entire corrector package.

Another interesting feature of this plot, is that there seems to be no crosstalk between the magnets, since the field profiles display a clear drift space in-between the magnets. It is also clearly seen that even with nearly half the strength of the magnetic field, the measurement system is still able to measure the magnetic flux density of the corrector package assembly. Together, these qualities strengthen the measurement system and approach, as it is clearly seen that the translating coil fluxmeter is able to measure the magnetic field of the full corrector package at once. This significantly reduces the time requirements of the measurements, enabling us to measure the corrector package sufficiently many times to yield a more robust data set for the calculation of the spread and average of the centers and magnetic lengths in the future.

A last comment on the field profiles shown in Figure 5.12 concerns the measured flux density of the skew decapole corrector, a_5, seen as magnet no. five in the figure. Increase and decrease of the measured flux densities are observed, with the low field values experiencing the larges effects. By a closer inspection, it is seen that the PCBs measuring the increasing signal are numbers 1, 5, 6, 7, 11 and 12, reading from the top to the bottom; second dark blue, first green, light blue, burgundy, top purple and bottom green. The remaining experience a more or less decrease in the flux linked with the PCBs. By looking at the field distribution of the decapole, seen in Figure 2.10, considering a symmetrically positioned set of PCBs, this corresponds to a slight rotation of the measurement head. The mechanical movement of the measurement head is the main source of error in these measurements, as will be discussed at a later stage. The reason why the skew decapole corrector seems to be more prone to this effect, is that the position of this magnet corresponds to the length of the first moving rod. The joint is pulled through the end-plate of the measurement system while the measurement head is within the skew decapole magnet. At this position, to avoid collisions of the two ends of the moving rod to the end-plate, the moving rod, thus the measurement head, was sometimes rotated slightly.

The effects of pure rotations of the measurement head is reduced by averaging the signals of all the induction coils. The final longitudinal field profiles of the radial flux density components of the full set of corrector magnets are shown in Figure 5.13. In the figure, both the simple method of dividing the flux measurements by the surface area of the coils, and the deconvoluted signal using b-splines are shown, in red and black respectively. Comparing the measurements of the skew quadrupole in Figures 5.12 and 5.13, we see that the amplitude is greatly reduced, while it is rather constant for the dodecapoles. This is due to the positioning of the PCBs with respect to the positions of the magnetic poles. Whereas all the PCBs will measure nearly the same signal in the measurements of the dodecapoles, the variation in measured field is a lot larger in the skew quadrupole. Averaging reduces the amplitude of the quadrupole, while conserving the amplitude of the dodecapole measurements. Even though the averaging of the measurements within a position is useful, we clearly see that not all imperfections are cancelled out by this. This is especially the case for the normal dodecapole, where the field in the central part of the magnet varies quite a lot. This is most likely an effect of vibrations of the measurement head, which is enhanced when less of the moving rod is available for control of the movement. This affects the last two to three magnets the most, a_2-a_6, as they are farthest away from the end-plate of the moving rod.

The effect of deconvolution can be seen as a sharper increase of the flux density in the end regions of the magnets. It also results in a larger effect of the return field outside of the magnet, seen as dips in the field just before and after entering the magnet. Similarly, a visible over-shoot is seen when entering the central parts of the magnets. This is expected as the coils of the PBCs filter the rapidly varying fields more, such as the field in the end-regions. Therefore, the deconvolution shows a more physically correct signal.

Measured magnetic centers and lengths:
The resulting magnetic centers are presented in Tables 5.8 and 5.10 for the measurements with separately and collectively powered magnets, respectively. The corresponding values for the magnetic lengths are presented in Tables 5.9 and 5.11. The spread of the measurands are presented at a level of 3σ, calculated as three times the standard deviation of at least three measurement repetitions.

The spread of the measurands are below the requirements of the measurement uncertainty for all the measurements, both with the magnets powered one by one, and with the series connection scheme. Considering the spread of the measurands as the only uncertainty component, and by powering the magnets one by one, the uncertainty for all the magnetic centers except from the normal dodecapole, are approximately a factor ten below the requirements. For all the magnets, the uncertainty given by the spread at 3σ is at least a factor three less than the requirements. This is also the case for the magnetic length. When the magnets are powered in series, the uncertainty is increased slightly for the localization of the magnetic center. This shows that even for the first iteration of the measurement system, in more challenging environments, and with field values significantly lower than what is achievable with a more powerful power supply the system has an uncertainty within the requirements. Then, the uncertainty of the laser tracker must also be included, but as this is in the range of a few hundreds of micrometer, it is negligible compared to the uncertainty from the system.

Considering the differences between the expected centers, and their measured counterpart, the deviation is within what is expected for the measurements with both kinds of powering scheme. The differences between the nominal and measured longitudinal centers are slightly less when the magnets are powered in series. This can be explained by the time of measuring the full set of corrector magnets in one go, compared to measuring the magnets one by one. The latter approach will naturally lead to more mechanical and thermal drift of the laser tracker, as the measurements took several hours. This effect was attempted mitigated by regular drift corrections. However, this correction will never capture every effect, and the drift observed between each check differed. Therefore, keeping the measurement time as low as possible will be of great importance to the continued measurements of the corrector package, especially in challenging environments as the LMF. This also allows for more repetitions, reducing the effect of random errors.

The measured magnetic lengths, however, deviate more from the nominal values presented. The measurements of most of the magnets were found to yield results within the expected deviations from the nominal values. For the series connected magnets, the results are even more in correspondence with the expectations. The exception is the skew quadrupole, for which more than 20 mm of difference was found. A possible source of this error, is the position of the quadrupole with respect to the end plate of the measurement system. When measuring the quadrupole, the part of the moving rod outside of the cold bore is very short, reducing the operators control of the movement. This causes significant vibration, polluting the signal. Another source of uncertainty is the calculation of the nominal magnetic length. The nominal values are calculated through simulations of particle movement, precise to the percentage range. Considering the percentage error between the measured and nominal magnetic lengths, the errors are still quite high, even though they are below 10% for all magnets, also for the quadrupole. As the magnetic measurements of field shapes and strength is usually more precise than the calculated centers, this error could be tolerable, also for the case of the quadrupole corrector. Especially since the magnetic centers match very well to the mechanical centers, and there is a close correlation between the two measurands. Even though most measured magnetic lengths are within the requirements, the deviation is rather high compared to the differences found in the calculation of the magnetic centers. A possible cause of these levels of error, is the fact that the nominal magnetic length is calculated for operation at a superconductive state. At

this field range, the iron yoke of the magnet is slightly saturated. Since it is the iron that determines the field shape of the magnets, this might be different when the magnets are measured at room temperature. As long as this difference is symmetrical about the longitudinal center, it will not affect the calculated centers. However, it could play a role in the calculation of the magnetic length, explaining the differences observed between the nominal and measured values.

The final remark of the measured magnetic length and centers, is that there is very little difference between the measurements with the magnets powered in series, and with the magnets powered one by one. Before the measurements, a larger spread of the measurands was expected for the measurements with lower field values, as this would make it more prone to error, due to a lower signal-to-noise ratio. However, the measured spread is rather equal for all the measured magnets. As previously mentioned, being able to measure all the magnets in one go adds to the robustness of the measurements, both when it comes to the drift and uncertainty of the laser tracker system, and since we can perform more measurements of the magnets in the same amount of time. The obtained results give confidence in the measurements of the series-connected corrector package, and as such, the series measurements should be considered the new standard method for the next measurement campaigns.

Measurement uncertainty:
The uncertainty connected to the translating coil fluxmeter measurements of the corrector package assembly, is mainly caused by the manual movement of the measurement head. In Figure 5.14 below, the reconstructed positions of the twelve PCBs during five measurements are shown. The transverse movement of the separate coils are assumed to be purely rotational, therefore the same disturbances are observed in all the coils. This is naturally not the case, as the movement can also be transverse translation of the measurement head. However, seen separately, the movement of PCB 1 is presented correctly. After approximately half the measurement range, a large disturbance is observed for all the separate measurements. This shows the position of the induction coil when the joint of the moving rods are pulled through the end-plate of the cold bore. Apart from this, the changing colors of the curves shows the longitudinal positions where the trajectories of the individual measurement runs intersect. It is therefore a measure of the movement and vibrations each PCB observes, which is in fact in the millimeter range. With this in mind, it is clear that it plays a role in the measured magnetic flux densities. Especially, mechanical noise is observed when the measurement head is in the final third of the corrector package, as seen from the skew sextupole magnet. This is caused by less available moving rod, resulting in less control of the movement. Furthermore, as the measurement setup consists of two moving rods joined together, when only one of the rods is available outside of the cold bore there is also room for movement in the joint, causing the measurement head to tilt slightly within the bore, resulting in more mechanical vibration.

Another source of error is the laser tracker measurements of the longitudinal position of the induction coils. As already discussed, errors caused by drift and mechanical instability would be less significant by shorter measurement campaigns. In this regards, measuring all the corrector magnets at once is beneficial. Furthermore, noise is mitigated by measuring some reference targets in drift checks, and performing a re-positioning of the laser tracker, as discussed for the rotating single-stretched wire measurements. This was performed every time the drift exceeded approximately 50 μm, reducing long time drift effects, such as the gradual heating of the surroundings. However, compared to vibrations and movement of the measurement head in the millimeter range, drift offsets of some tens of micrometer are negligible.

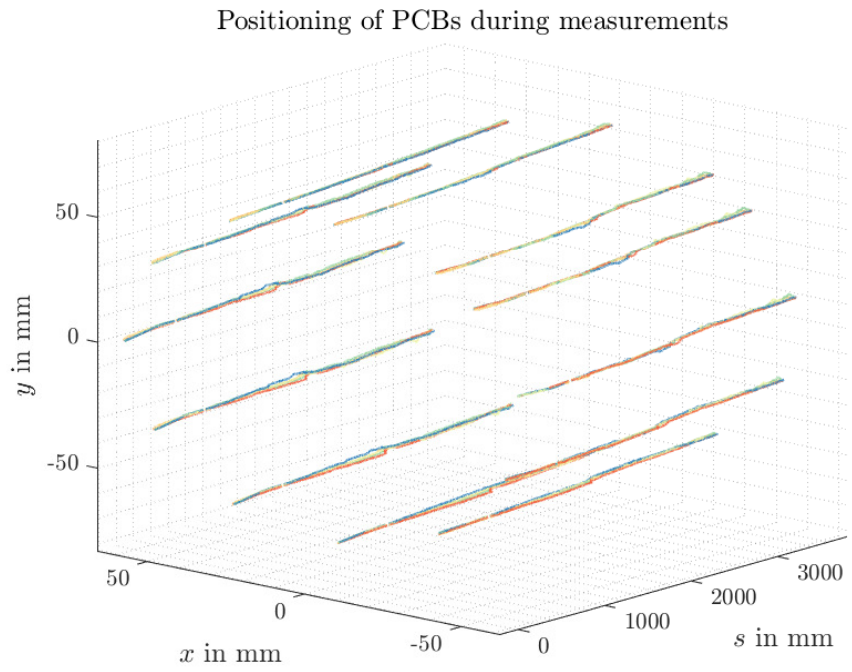

Figure 5.14: Three dimensional position of the induction coil centers during magnetic measurements of the corrector package. Each line corresponds to a single PCB during a single measurement. The measurements are repeated five times, hence each PCB trace five different curves in space.

5.2.4 Conclusion

The translating coil fluxmeter was used to measure the longitudinal centers and the magnetic length of higher order corrector magnets in the corrector package assembly in the LMF. The measured centers were found to match well with the expected values, and are within both the expected deviations and the uncertainty, expressed at 3σ. The measured magnetic length deviated more, but apart from the quadrupole corrector the values are within the expectations. For the quadrupole, the error is below 10%, and since the nominal values are based on simulations with limited precision, the values might be correct. This is supported by the fact that the centers were within the expected values. Furthermore, the errors of the measured magnetic length can be caused by the uncertainty in the behaviour of the iron in operation at room temperature.

Secondly, the measurements act as further investigation and validation of the translating coil fluxmeter measurement system. The main source of error was found to be the mechanical instability of the measurement head during operation. This is caused by the manual movement of the moving rod, with the inherent issues for stable movement. For the next iteration, it is suggested to develop a motorized movement of the measurement head. This would ensure a lot more constant movement, and make the system less prone to mechanical noise. This could be achieved by pushing and pulling the system simultaneously from both sides, with rods fixed at each side of the measurement head. This would also mitigate the effects of tilting of the measurement head, with subsequent vibrations.

Chapter 6

Discussion and Future Work

The methods developed for the magnetic measurements of the HL-LHC corrector package have been tested in several measurement campaigns described throughout this thesis. First, the metrological characterization and validation of the systems were investigated in a highly controlled area, namely the Testing and Measurements section's laboratory for measurements of normal conductive magnets. Then, the the higher-order corrector magnets in the present corrector package assembly were tested in the Large Magnet Facility, where different challenges added to the complexity of the measurement campaign.

The results and sources of uncertainty in the above-mentioned measurement campaigns are already discussed in preceding sections. In this part of the thesis, the key points from these discussions are summarized, with the aim of clarifying the strengths and weaknesses of the methods. Then, future steps in the development of these methods are proposed.

6.1 The Rotating Single-Stretched Wire Measurement Method

The rotating single-stretched wire measurement method was developed for the measurement of the magnetic axis and roll angle of the individual corrector magnets within the final corrector package assembly.

6.1.1 Measurement campaigns

Metrological characterization measurements
A set of two individual measurement campaigns was performed to complete the metrological characterization of the system; the decapole corrector magnet was measured with known offsets to calculate the consistency and spread of the measurands, which together gave the precision of the measurement system. Then, the system was used to measure a stronger quadrupole magnet, which when compared to the measurements performed with the DC single-stretched wire method, the standard method for axis and roll angle measurements, yielded the accuracy of the method. The results of these measurements showed that the system is well suited for measuring the axis and roll angle of the corrector package, with a total precision of ±5 μm and ±0.04 mrad and an accuracy of more than ±15 μm and ±0.02 mrad, for the localization of the magnetic axis and roll angle, respectively. In total, this yield an uncertainty of the measurement system of less than ±20 μm and ±0.06 mrad. In these calculations, the spread of the measurand, i.e. the standard deviation, is given at 3σ, corresponding to a confidence level of 99.7% assuming a normal distribution, since the tolerated uncertainties are expressed accordingly. For the measurements of the magnetic axis, since a laser tracker system is used in the fiducialization process, to capture the full uncertainty, its uncertainty is also included. This gives a total uncertainty for the localization of the magnetic axis of less than ±170 μm. As already discussed, this is within the requirements of ±300 μm and ±0.1 mrad given in [38]. Furthermore, the uncertainty of the axis measurement is largely determined by the uncertainty of the laser tracker, which in the end cannot be omitted. Therefore, the system can hardly perform better.

From the measurements of the decapole magnet, a few aspects of improvement was discovered. The main one was the need for adjusting the wire stages to gravity, as this has a great effect on the measured axis and roll angle. This would prove to be even more important for the measurements of the full corrector package. However, since only the relative axis and roll angle was investigated at this stage of the measurements, not performing the alignment did not corrupt the results. The second improvement was to use a set of grid targets, to mitigate effects of mechanical and thermal instabilities of the laser tracker.

If the measurements were to be repeated, there are a few points to consider that would increase the robustness of the results. They could also be characterized as weaknesses of the chosen approach to the measurements. First of all, the reported precision of the system of the roll angle measurements was determined from five repetitions of two separate measurements; one with zero added angle, and one with a controlled offset angle. As already discussed, a stronger approach would have been to perform these measurements with several offset angles, as was the case for the added offsets in the transverse direction. This way, the consistency of the measured roll angle would be based on a larger set of measurements. However, due to a strict measurement schedule, I chose to proceed with other measurements. Secondly, the amount of measurement repetitions is a little low to thoroughly conclude about the spread of the measurand. This stems from the fact that the measurands are assumed to be normally distributed. As already mentioned, 30 repetitions of a measurement, performed with as identical as possible setups, surroundings, and with the same operator, is usually considered sufficient to determine the correct parameters of the bell shape. However, with the

optimal set of parameters for these measurements, each measurement lasts more than an hour. To be able to perform all the necessary measurements presented in this thesis, and to test the systems in several configurations, it was decided that a total number of five repetitions was sufficient. Even so, looking back, it would have given the metrological characterization more scientific weight if the system was set up to measure the decapole corrector magnet once more, with more than ten repetitions, ideally 30.

Measurements of the corrector package assembly
The rotating single-stretched wire method was also used to measure the present assembly of the corrector package. The results were compared to a simplified approach, showing the connection between the post-processing algorithm and what can be interpreted directly from the physical measurements. It was shown that the two approaches yielded the same results, strengthening the final post-processing of the measurements. The final magnetic axes and roll angles, both before and after correction for the wire position, are presented in Tables 5.4 and 5.5. The resulting integral magnetic axis was found to be within the expected deviation for all the corrector magnets. This was not the case for the roll angles, with a discrepancy between the nominal and measured roll angles exceeding the expected deviation by as much as eight times. The requirements and expected deviations were found to be too stringent. However, for both the roll angle and the axis offset, even though the results are acceptable regarding the measurement uncertainties and the expected deviations, the deviations were larger than expected. An obvious reason for this is the visible misalignment discussed earlier. In the range of below 600 μm and 0.05°, a slight misalignment in the assembly phase would be sufficient to explain the offsets.

The added noise observed during the measurements in a less controllable surrounding was clearly seen from these measurements, as discussed earlier. The main cause of this, and therefore the main weakness of this measurement campaign, was the loose bolt found during the disassembly of the measurement system. As explained, several measures were applied to mitigate its effect, such as re-adjustment of the stages, measurements with the laser tracker in-between magnetic measurements, and finally continuous measurement of the wire tension during operation. Even so, this is still something that must obviously be considered for the next measurement campaign using the stretched-wire system in such noisy environments. Secondly, the laser tracker suffered from using a less stable support during these measurements, enabling the possibility for mechanical movement of the measurement head. This was to a large extent mitigated by the grid of targets surrounding the laser tracker, but it would benefit from a better grid of targets, and from measuring in a smaller, more confined area, as the temperature increase and air-flow in the surroundings was non-negligible during this measurement campaign.

6.1.2 Future work

The rotating single-stretched wire was found to give very good results, with the uncertainty largely determined by the laser tracker uncertainty, considered a boundary condition for these measurements. The results obtained through both the metrological characterization and the measurements of the corrector package assembly show that it is able to give results that correspond well to the nominal values of the magnets, and that it compares well to the benchmark method for measuring the magnetic axis and roll angle; the DC SSW measurement method.

Therefore, this system is planned to be applied for the future measurements of the magnetic axis and roll angle of the HL-LHC corrector package. The first magnet assembly is planned to be finalized this fall, and a new set of measurements is therefore planned before Christmas. This measurement

campaign is expected to yield a more constant offset of the magnetic axes for the different magnets, as the assembly will be a lot tighter. This would further enhance the confidence in the measurement method.

For the future measurement campaigns using the rotating single-stretched wire method, there are a few aspects to consider. The first one is to measure the magnet assembly in more suitable surroundings, as most of the added complexity of the measurements stem from unnecessary sources of noise, such as large temperature changes, air flow and lifting of heavy objects close by. Furthermore, adding more targets to the grid surrounding the laser tracker would reduce the influence of drift in these measurements. In the Large Magnet Facility, there is a room used specifically for metrological measurements, which would help stabilize both the temperature, air flow and the mechanical instability, and in addition comes with a well designed setup for creating a better laser tracker grid. It is advisable to use this space, if available, at least to investigate the achievable improvements of the measurement system.

Furthermore, a thorough metrological characterization of the laser tracker in the surroundings where it is applied will also increase the robustness of the measurement approach. Lastly, the metrological characterization of the rotating single-stretched wire method would benefit from performing a last measurement campaign of the decapole corrector magnet. As mentioned above, this would better determine the correct bell shape of the measurands than with five repetitions, which is probably a bit too few.

6.2 The Translating Coil Fluxmeter Measurement Method

The translating coil fluxmeter measurement method was developed in the work with this thesis for the measurements of the longitudinal centers and magnetic lengths of the individual corrector magnets in the final corrector package assembly. The system was specifically designed to be as sensitive to the low field values achieved by powering the magnetic in DC as possible, and with sufficiently many induction coils to measure all the magnetic poles of the dodecapole corrector magnet.

6.2.1 Measurement campaigns

Metrological characterization and validation measurements
The system presented in this thesis is only the first prototype, and as such the main focus of the initial measurements using the translating coil fluxmeter was to validate the measurement system. The tests were performed on the decapole corrector magnet, which by design shows no symmetry with the positioning of the PCBs, therefore being the ideal magnet for this purpose. The low field values of the DC powered magnet was of concern in these initial tests, and the main focus was on measuring signals of significance with respect to the noise level, and to investigate how well the system performs at consistently measuring the magnetic center and the magnetic length of the decapole. The latter is connected to the metrological characterization of the system, and even though this is merely the initial phase of the system development, it was of interest to see how well these quantities can be measured, and whether the system could be moved to measure the nearly complete set of corrector magnets.

From these first tests, it was shown that the system is in fact sensitive enough to measure the field profile of the decapole corrector magnet. The field profile corresponds well to the expectations, however with a slightly exaggerated peak in one of the extremities of the magnet. The magnetic centers and lengths displayed a spread of below 1 mm, as long as the integration interval was kept sufficiently close to the end-regions of the magnet. This is within the requirements by more than a factor ten, and showed that the system was able to yield consistent values for the measurands. However, the values differed more than expected, with the deviation being approximately 7 mm shorter than the expected longitudinal center of the magnet, and more than 40 mm below the nominal magnetic length. For the case of the magnetic center, this is within the expected deviation, but for the magnetic length the deviation exceeds the expected deviation by a factor four. This does not correspond very well with the repeatability of the system, i.e. the spread of the measurands, and the resulting field profiles. Especially the calculated magnetic length seems to be more correct than the nominal value. Therefore, the results were deemed good enough to continue the measurements on the corrector package assembly.

From the validation measurements, the system was fine-tuned to give the best approach for future measurements. First of all, due to a quite low signal-to-noise ratio, the drift is rather substantial in these initial measurements. This is partly reduced by an optimal choice of interval for the summation of the signal, and by calculating the semi-difference in the future measurements. Secondly, test were performed to investigate whether the simple wire draw encoder is sufficient to trigger the FDIs at longitudinal positions, or whether the laser tracker has to be used for this purpose. From the measurements, the wire draw encoder was found to yield sufficiently good repeatability and accuracy to be utilized for future measurements. However, as the corrector package is more than 3 m long, the wire encoder is too short to be applied for the measurements of the corrector package assembly. Therefore, the laser tracker system will be used also in the continued measurement campaign in the LMF. Another value of using the laser tracker system, is that the transverse position of the measurement head can also be measured, and not only the longitudinal. Lastly, the choice of deconvolution

strategy was to approximate the radial field component by fourth-order b-spline functions. This yield a reconstructed magnetic flux density that suite the expectations of the physical field well, without suffering from the oscillatory behavior as seen in the deconvolution with the induction coils' sensitivity functions. It was shown that using b-splines does not impact the measured magnetic center or length, allowing us to use the simple approach of dividing the flux measurements by the surface area of the coils to obtain the flux density. This requires a lot less computation, hence saving both time and computational power.

Measurements of the corrector package assembly

The system was moved to the LMF to measure the present assembly of the corrector magnets, even though the development of the system was not finalized. Consequently, the measurements of the corrector package was also used in the development phase of the system. Important aspects as the benefit of implementing the semi-difference calculation of the flux densities, the possibility of measuring several magnets powered in series, and the further implementation of the deconvolution process were investigated.

The measurements of the remanence field gave quite impressive results, showing that the system is able to measure distinct peaks of remanence field in the order of a few tens of microtesla. Compared to the mechanical position of the magnets' end plates, the field measured was clearly corresponding to the poles of the magnets. This also shows the importance of calculating the semi-difference of the measured flux density, since the remanence field will contribute to the induced voltage, if this is not accounted for. The resulting field profiles are shown to behave as expected, with zero field observed in the drift areas of the corrector package.

The resulting magnetic centers and lengths of the corrector magnets are presented for both the measurements with the magnets powered one by one, and with the magnets powered in series. The results show very little difference, more likely to be caused by mechanical instability of the measurement head than errors in the field measurements. In fact, the measured magnetic lengths correspond slightly better to the nominal lengths for the series powered magnets than for the individually powered magnets. The added value of measuring with the magnets in series, is the possibility to perform a lot more measurements in shorter time than with the magnets excited one by one. This reduces the effect of external noise, and it allows for more measurements to better determine the mean and spread of the measurands. The spread of the measurands are increased compared to the validation measurements, as these measurements are performed in a more noisy environment. For the magnets powered in series, the spread of the normal and skew dodecapole magnets are a lot higher than for the rest of the magnets. Still, the spread is within the uncertainty requirements of the measurands, and for most magnets the spread is in the order of 1.5 mm, nearly a tenth of the requirements. The measurements with series connected magnets give a larger spread than for the case of measuring a single magnet at a time. This likely stems from the lower signal-to-noise ratio from powering the magnets with less current. One obvious solution is to add one or two more power supplies, and power the magnets in two or three clusters with series connections. Then, the signal-to-noise ratio should be the same as for the individually powered magnets.

For the case of measured magnetic centers, the deviation from the nominal values are well within the expected deviation of 10 mm, for both powering schemes. Considering the magnetic length, the deviations compared to the nominal values are larger than for the centers. For both powering schemes, the deviation from the nominal magnetic lengths exceed the expected deviation for the quadrupole magnet. Apart from this, they are within the expectations, however not by a large margin. Some of the errors could be assigned to the uncertainty of the simulated values, usually in the range of a few percent. Considering this, the deviations are shown to be below 10% for all the mag-

nets. Another source of uncertainty in the calculation of the magnetic length, is the behavior of the iron in the pole. As the expected deviations are given at no specific temperature, it is assumed to correspond to normal operation of the corrector package. This means powering the magnets by the superconducting Nb-Ti strands. This causes the iron to be slightly saturated, which could have an effect on the magnetic length. The mechanical movement of the measurement head is considered an equal source of uncertainty to these measurements, and further investigation is needed to fully understand these deviations. A last noticeable aspect, is that the measured magnetic length of the decapole corrector magnets were determined within the expected deviations. This shows the erroneous behavior of the field distribution of the decapole corrector magnet from the validation measurements presented in section 4.2.

The main source of uncertainty to these measurements, is the mechanical noise experienced by manually pushing and pulling the movement rod. Since the measurement head is a bit too small for the cold bore, slight tilting of the head occurs, giving vibrations and larger skips in position. Also the joint between the two rods cause movement. This comes from both the non-parallelism when only one rod is outside of the cold bore, and from the joint itself exiting the cold bore, where a slight rotation is needed for the joint to fit the hole of the cold bore end plate. Sudden displacements of the PCBs in the order of 1 mm were observed, naturally polluting the magnetic measurements. Furthermore, the measurement method of manually holding the targets to the end plates is not precise enough to decide whether or not the produced magnets differ from their nominal values in the case of their centers. Still, the centers follow the geometry rather well, so as a first approximation, it should be sufficiently precise. Lastly, using a laser tracker for the spatial assignment of the flux measurements also includes uncertainties connected to mechanical and thermal noise. The effects are reduced by drift checks. Errors from the laser system in the order of 150 μm is way below the mechanical instability of the PCB movement, therefore not assumed a focus area for the next iteration of the measurement system.

6.2.2 Future work

From the discussion above, it is clear that the translating coil fluxmeter in its present form is able to locate the magnetic center and length with a spread below the required measurement uncertainty. Since the magnetic center and length closely follows the mechanical shape of the poles of the magnet, the measured values were compared to this. The values obtained for the measurands are also, to a large extent, within the expectations. There are, however, several aspects yet to be understood in the future work, and determining the accuracy of the system to calculate the full uncertainty is one of these. The first point to consider is therefore the actual uncertainty in the nominal magnetic lengths for the magnets, as this is the quantity with the largest difference between the measurements and the simulated value. For the magnetic center, since it is known to follow the mechanical center closely, the approach of measuring the end plates were deemed sufficient for this first iteration of the measurement system. However comparing the measured results to actual plans of the assembly, if this exists, would further determine the accuracy. Then, it would be desirable to measure a magnet with known center and length, similar to the approach for the rotating single-stretched wire measurements of the ANSALDO MEBT quadrupole, to compare the measurands to the known values. This requires the magnet to have an aperture larger than the outer diameter of the cold bore used as guiding tube for the fluxmeter. The simplest improvement for the future measurements is to power the magnets cluster-wise in series, to increase the signal-to-noise ratio of the magnets, as well as reducing the measurement time and complexity significantly.

Also connected to the future work of the translating coil fluxmeter, are further developments of

the system. As already discussed, the main source of uncertainty to this system, is the mechanical instability introduced by the manual movement of the measurement head. One solution would be to implement motorised movement of the coils. This would improve the quality of the movement drastically, and to a large extent mitigate movement in any other direction than the longitudinal. Furthermore, using precise encoders, together with the purely longitudinal movement, would remove the need for laser tracker scans of the measurement head, further reducing the uncertainty of the system. A simpler solution would be to make the measurement head itself more stable. This could be achieved simply by elongating it, reducing effects of tilt angles. One could also imagine a set of wheels mounted on both sides of the measurement head, that could be adjusted radially to reduce the friction of the measurement head to the cold bore.

A drawback of the present design with twelve symmetrically distributed PCBs, is the reduced signal measured for either the normal or the skew dodecapole. Due to difficulties rotating the measurement head precisely, the system was only measured with a constant azimuthal angle. For future developments, the system could be fitted with motors for precise angular movement of the measurement head. This would ensure better signal quality over-all, as several scans with different angular positions of the PCBs could be performed. This would also open for another interesting feature with the tangentially positioned PCBs; using the translating coil fluxmeter for obtaining the magnetic axis and roll angle. As discussed in the parts of the rotating single-stretched wire measurements, this would require a lot of scans to sufficiently oversample the azimuthal positions. A total of 22 scans would have to be performed to obtain 256 circumferential measurement positions. Furthermore, the uncertainty requirements of the measured axis and roll angle makes such a system rather unlikely. However, it would be interesting to compare the measurements from the two systems.

Another improvement would be to develop a new set of PCBs, more suitable for the higher-order corrector magnets. For instance, having more layers would increase the signal-to-noise ratio. The induction coils could also be designed with less width, allowing for more induction coils along the circumference. However, this would rule out the use of FDIs if a single measurement rack is still to be used, as there are only thirteen available slots in the rack. Omitting the FDIs significantly increases the data that needs to be processed, reducing the simplicity of the system. Lastly, as discussed previously, the PCBs could be designed to remove the blind-eye frequencies below a certain frequency. This was done in [33], where each induction coil was wound to have maximum sensitivity for the blind-eye of the previous. This way, deconvoluting the signal with the sensitivity function of the PCB would be a straight forward process of division in the frequency domain. This would simplify the post-processing phase. However, as the magnetic length and center was found to be insensitive to the calculation of the magnetic flux density from the magnetic flux measurements, the simplest approach is still to divide the flux measurements by the calibrated surface area of the PCBs.

Chapter 7

Conclusion

The objective of the work described in this master's thesis, was to develop a measurement system for the room temperature magnetic measurements of the higher-order corrector magnets for the High-Luminosity upgrade of the LHC. The measurands of interest to these measurements are the magnetic axis, roll angle, magnetic length and longitudinal center of each of the corrector magnets in the corrector package assembly. The magnets are superferric, and as such can only be powered with a current approximately a thousandth of the nominal values at room temperature, resulting in too low field values and field gradients to use already available measurement methods. The systems were to be tested, with the aim of determining the uncertainties of the measurements. They were required to fulfill predefined requirements. After this, the present assembly of the corrector package were to be measured, yielding valuable insight into the fabrication and assembly processes, and to the future use and development of the systems. The chosen measurement architecture comprise two different measurement systems:

The rotating single-stretched wire measurement method was developed for measuring the magnetic axis and roll angle of the individual corrector magnets. It is based on the Fourier analysis of the field harmonics, multipoles, as measured by a radial rotating coil on a circular trajectory within the aperture of the magnet. It uses an already available measurement setup in the form of linear stages, capable of moving in both the vertical and horizontal direction, a taut conductive string, and a return wire. With the magnet powered in AC, the wire is moved to circumferential positions, and through the post-processing phase the measurements are interpreted as though the values were obtained by a radial rotating induction coil. The multipole components are found through a Fourier analysis of the measured flux density, and they give the offset of the magnetic axis from the feed-down, and the roll angle from the field phase of the main multipole components. The corrector package is measured by powering the magnets one by one, acquiring the roll angle and magnetic axis of one magnet at a time. Laser tracker measurements are needed to relate the magnetic measurements in the reference system of the wire stages to the fiducials on the magnet.

A metrological characterization of the rotating single-stretched wire method was performed in a highly controllable environment. The system measured the decapole corrector magnet to obtain the precision of the system, and the magnetic axis of a stronger quadrupole, which when compared to the measurements performed with the DC stretched-wire method yielded the accuracy. The uncertainty of the axis measurements by the rotating single-stretched wire measurement method was determined to be $\pm 20\ \mu$m, and when adding the uncertainty of the Leica AT930 laser tracker, the total uncertainty of the measurements were found to be $\pm 170\ \mu$m. The system was proven to measure the roll angle with an uncertainty of less than ± 0.06 mrad. This is well below the maximum allowed uncertainties

of ±300 μm and ±0.1 mrad, and the system is therefore well suited for the measurements of the higher-order corrector magnets.

The full corrector package was measured in a more challenging environment. The measurement campaign proved to be robust in the way the challenging environment was handled, with action made to mitigate the effects of slightly tilting wire stages and drift of the laser tracker. The measured axes were all within the expected deviations, although the magnets in the center of the assembly seemed to sag slightly in both the vertical and horizontal plane. The deviation from the nominal values of the measured roll angles exceeded the expected deviations. Both these effects are likely caused by visible misalignments in the mechanical assembly of the corrector package. This effect is expected to be reduced when the nested dipole is added to the assembly, and the magnets are fully enclosed in the package.

For the future measurements, the system is ready to be applied. However, performing the measurements in a slightly more stable environment is advisable.

A translating coil fluxmeter was designed to measure the longitudinal centers and the magnetic lengths of the individual magnets of the corrector package. The system comprises a set of induction coils, positioned tangentially on a measurement head which is pushed and pulled manually through the apertures of the corrector magnets, within the cold bore. The induction coils are made using PCB technology, and measure the radial flux density as induced voltage from the changing flux linkage. The signals are integrated on the fly, and assigned to longitudinal positions by the use of either a wire draw encoder, or the laser tracker. The latter was applied for the measurements in this thesis, with the added value of showing transverse movement of the measurement head. In the post-processing, the flux is deconvoluted using fourth-order b-splines, to decouple the signal from the sensitivity function of the PCB, and obtain a more physical shape of the flux density. The simple approach of dividing the flux measurement by the surface area of the induction coils was found to yield the same results for the longitudinal center and magnetic length, and is therefore used in the calculation of these quantities to reduce the computational cost of the deconvolution.

The translating coil fluxmeter was validated by a measurement campaign of the decapole corrector magnet. It was found to yield a spread lower than a tenth of the uncertainty requirements, and was therefore deemed suitable for further measurements of the corrector package. It was found that the wire draw encoder is sufficiently accurate for use, simplifying the measurement system significantly. However with a wire of 3 m it is too short to be applied for the measurements of the full corrector package assembly. Furthermore, the validation measurements showed the need for reducing the effects of system drift by the integrators and other constant noise components. This is solved by calculation of the semi-difference of measurements with nominal and inverse polarity. The longitudinal center of the decapole was found to be within the expected deviation from the mechanical center, but the magnetic length was measured to be way too low. This was, however, likely caused by an irregularity in the design of the magnet, rather than a flaw with the measurement system, a point proven by the measurements of the full corrector package assembly.

The further validation of the system, together with the final measurements, were performed on the present assembly of the corrector package. The system proved to be sensitive enough to measure the remanence field of the corrector magnets, and the flux density profiles of the full set of corrector magnets showed expected behavior. Furthermore, it was shown that powering the full set of magnets in series yielded sufficiently good results, even with the limitations of the current supply. This strengthens the approach, and with the addition of another power supply, the signal-to-noise ratio could be further increased. The magnetic centers were all within the expected deviations of the mechanical centers, and the measured spread was well below the measurement requirements.

The magnetic length was measured to be within the nominal values for all the magnets, except the skew quadrupole corrector. This could be caused by low precision in the simulation determining the nominal value, different field shapes when measuring at warm, or it could also be caused by mechanical instability of the mechanical movement of the measurement head.

The translating coil fluxmeter proved to be sufficiently good to measure the magnetic length and longitudinal center of the full corrector package assembly. However, for future measurements, the movement of the measurement head should be made more mechanically stable by motorizing the movement.

The developed measurement systems and methods described in this thesis have proven to meet the requirements of the measurement campaign to a large extent. There are still aspects to improve, but the systems have proven to perform sufficiently well to be used in the future measurements of the HL-LHC corrector package. Especially the rotating single-stretched wire method proved to perform very well, even in difficult environments. The wire-system has never, to the knowledge of the author, been applied in AC measurements of multipoles of such high order, and with such low field values. The development of this system therefore is a valuable addition to the measurement methods of higher-order, low-field magnets. The translating coil fluxmeter presents a simple and easy-to-use measurement system. This design, with tangentially positioned induction coils, has not been applied previously, and with slight modifications it could be extensively applied for measurements of longitudinal field profiles.

Bibliography

[1] 'The history of cern,' in *CERN*, ch. 1, pp. 1–61. DOI: 10.1142/9789814623476_0001. eprint: https://www.worldscientific.com/doi/pdf/10.1142/9789814623476_0001. [Online]. Available: https://www.worldscientific.com/doi/abs/10.1142/9789814623476_0001.

[2] C. Petrone, S. Sorti, E. Dalane, B. Mehl and S. Russenschuck, 'Induction-Coil Measurement System for Normal- and Superconducting Solenoids,' *IEEE Trans. Appl. Supercond.*, vol. 32, 9000605. 5 p, 2022. DOI: 10.1109/TASC.2022.3147142. [Online]. Available: https://cds.cern.ch/record/2806209.

[3] E. Mobs, 'The CERN accelerator complex in 2019. Complexe des accélérateurs du CERN en 2019,' Jul. 2019, General Photo. [Online]. Available: http://cds.cern.ch/record/2684277.

[4] T. Linnecar, 'THE TECHNOLOGY OF THE LHC - Capturing, Accelerating and Holding the Beam,' in *The Large Hadron Collider: a marvel of technology; 2nd ed.* Ch. 4.5, pp. 144–159. DOI: 10.1142/9789814623476_0006. eprint: https://cds.cern.ch/record/2645935. [Online]. Available: https://cds.cern.ch/record/2645935.

[5] 'The Man Who Built the LHC: Lyn Evans,' in *CERN*, ch. 6, pp. 98–107. DOI: 10.1142/9789814623476_0006. eprint: https://www.worldscientific.com/doi/pdf/10.1142/9789814623476_0006. [Online]. Available: https://www.worldscientific.com/doi/abs/10.1142/9789814623476_0006.

[6] S. Russenschuck, *Field computation for accelerator magnets: Analytical and numerical methods for electromagnetic design and optimization*. Weinheim: Wiley VCH Verlag GmbH, Mar. 2010, ISBN: 3527407693.

[7] S. Baird, 'Accelerators for pedestrians; rev. version,' CERN, Geneva, Tech. Rep., Dec. 2007. [Online]. Available: http://cds.cern.ch/record/1017689.

[8] J. Rossbach and P. Schmüser, 'Basic course on accelerator optics,' 72 p, Feb. 1993. DOI: 10.5170/CERN-1994-001.17. [Online]. Available: https://cds.cern.ch/record/247501.

[9] P. K. Kythe, *Complex Analysis: Conformal Inequalities and the Bieberbach Conjecture*, 1st. New York: Chapman and Hall/CRC, Dec. 2015.

[10] S. Russenschuck, G. Caiafa, L. Fiscarelli, M. Liebsch, C. Petrone and P. Rogacki, 'Challenges in Extracting Pseudo-Multipoles From Magnetic Measurements,' in *Proc. 13th International Computational Accelerator Physics Conference (ICAP'18),Key West, FL, USA, 20-24 October 2018*, (Key West, FL, USA), ser. International Computational Accelerator Physics Conference, Geneva, Switzerland: JACoW Publishing, Jan. 2019, pp. 87–92, ISBN: 978-3-95450-200-4. DOI: doi:10.18429/JACoW-ICAP2018-SUPAG03. [Online]. Available: http://jacow.org/icap2018/papers/supag03.pdf.

[11] A. Wolski, 'Maxwell's Equations for Magnets,' 1–38. 38 p, Mar. 2011, Comments: Presented at the CERN Accelerator School CAS 2009: Specialised Course on Magnets, Bruges, 16-25 June 2009. DOI: 10.5170/CERN-2010-004.1. arXiv: 1103.0713. [Online]. Available: https://cds.cern.ch/record/1333874.

[12] E. Stade, 'Special topics and applications,' in *Fourier Analysis*. John Wiley & Sons, Ltd, 2005, ch. 7, pp. 353–420, ISBN: 9781118165508. DOI: https://doi.org/10.1002/9781118165508.ch7. eprint: https://onlinelibrary.wiley.com/doi/pdf/10.1002/9781118165508.ch7. [Online]. Available: https://onlinelibrary.wiley.com/doi/abs/10.1002/9781118165508.ch7.

[13] A. K. Jain, *Determination of Magnetix Axis*, Available: https://lhc-div-mms.web.cern.ch/tests/MAG/docum/References/Schools/USPAS_2006/Jain/Lectures/8_Alignment.pdf.

[14] L. Bottura, 'Engineering Specification
Standard Analysis Procedures for Field Quality Measurement of the LHC Magnets
Part I: Harmonics,' CERN, Geneva, Tech. Rep., 2001. [Online]. Available: https://edms.cern.ch/ui/file/313621/1.0/lhc-m-es-0001-10-00.PDF.

[15] K. N. Henrichsen, 'Classification of magnetic measurement methods,' 1992. DOI: 10.5170/CERN-1992-005.70. [Online]. Available: http://cds.cern.ch/record/245401.

[16] O. Koster, 'Combining rotating-coil measurements of large-aperture accelerator magnets,' Presented 23 Sep 2016, Oct. 2016. [Online]. Available: https://cds.cern.ch/record/2221939.

[17] A. K. Jain, 'Harmonic Coils,' *CERN Yellow Reports: School Proceedings*, pp. 175–213, 1998. DOI: 10.5170/CERN-1998-005. [Online]. Available: https://cds.cern.ch/record/318977/files/CERN-98-05.pdf.

[18] R. Bartolini, P. Fessia, D. Perini, W. Scandale and E. Todesco, 'Magnetic errors of the LHC dipoles and possible cures,' 1999. DOI: 10.5170/CERN-1999-001.127. [Online]. Available: https://cds.cern.ch/record/450375.

[19] A. Ijspeert, M. Karppinen and J. Salminen, 'Design of corrector magnets for the LHC,' 1999. DOI: 10.5170/CERN-1999-001.137. [Online]. Available: https://cds.cern.ch/record/451608.

[20] O. Brüning and L. Rossi, 'Chapter 1: High-Luminosity Large Hadron Collider,' *High-Luminosity Large Hadron Collider (HL-LHC): Technical design report*, 1–16. 16 p, DOI: 10.23731/CYRM-2020-0010.1. [Online]. Available: https://cds.cern.ch/record/2750437.

[21] G. Arduini, R. Bruce, R. De Maria, M. Giovannozzi, G. Iadarola, J. Jowett, E. Métral, Y. Papaphilippou and R. T. Garcia, 'Chapter 2: Machine layout and performance,' *High-Luminosity Large Hadron Collider (HL-LHC): Technical design report*, 17–46. 30 p, 2020. DOI: 10.23731/CYRM-2020-0010.17. [Online]. Available: https://cds.cern.ch/record/2750438.

[22] E. Todesco, H. Bajas, M. Bajko, A. Ballarino, S. I. Bermudez, B. Bordini, L. Bottura, G. D. Rijk, A. Devred, D. D. Ramos, M. Duda, P. Ferracin, P. Fessia, J. Fleiter, L. Fiscarelli, A. Foussat, G. Kirby, F. Mangiarotti, M. Mentink, A. Milanese, A. Musso, V. Parma, J. C. Perez, H. Prin, L. Rossi, S. Russenschuck, G. Willering, S. Enomoto, T. Nakamoto, N. Kimura, T. Ogitsu, M. Sugano, K. Suzuki, S. Wei, L. Gong, J. Wang, Q. Peng, Q. Xu, A. Bersani, B. Caiffi, P. Fabbricatore, S. Farinon, A. Pampaloni, S. Mariotto, M. Prioli, M. Sorbi, M. Statera, J. G. Matos, F. Toral, G. Ambrosio, G. Apollinari, M. Baldini, R. Carcagno, S. Feher, S. Stoynev, G. Chlachidze, V. Marinozzi, V. Lombardo, F. Nobrega, T. Strauss, M. Yu, M. Anerella, K. Amm, P. Joshi, J. Muratore, J. Schmalzle, P. Wanderer, D. Chen, S. Gourlay, I. Pong, S. Prestemon, G. L. Sabbi, L. Cooley and H. Felice, 'The high luminosity LHC interaction region magnets towards series production,' *Superconductor Science and Technology*, vol. 34, no. 5, p. 053 001, Mar. 2021. DOI: 10.1088/1361-6668/abdba4. [Online]. Available: https://doi.org/10.1088/1361-6668/abdba4.

[23] P. Abramian, F. de Aragón, J. Calero, J. de la Gama, L. García-Tabarés, J. L. Gutiérrez, M. Karppinen, T. Martínez, E. Rodríguez, I. Rodríguez, L. Sánchez, F. Toral and C. Vázquez, 'Development of radiation resistant superconducting corrector magnets for lhc upgrade,' *IEEE Transactions on Applied Superconductivity*, vol. 23, no. 3, pp. 4 101 204–4 101 204, 2013. DOI: 10.1109/TASC.2013.2239698.

[24] E. Todesco and P. Ferracin, 'Chapter 3: Insertion Magnets,' *High-Luminosity Large Hadron Collider (HL-LHC): Technical design report*, 47–64. 18 p, 2020. DOI: 10.23731/CYRM-2020-0010.47. [Online]. Available: https://cds.cern.ch/record/2750436.

[25] S. Russenschuck, 'ROXIE: A Computer Code for the Integrated Design of Accelerator Magnets,' 4 p, Feb. 1999. [Online]. Available: https://cds.cern.ch/record/382851.

[26] L. Bottura and K. N. Henrichsen, 'Field Measurements,' 35 p, Dec. 2002. DOI: 10.5170/CERN-2004-008.118. [Online]. Available: http://cds.cern.ch/record/597621.

[27] C. Petrone, 'Wire methods for measuring field harmonics, gradients and magnetic axes in accelerator magnets,' Ph.D. dissertation, Università degli Studi del Sannio, 2013. [Online]. Available: https://cds.cern.ch/record/1601973.

[28] U. Krey and A. Owen, *Basic Theoretical Physics, A Concise Overview*, 1st. Berlin, Heidelberg: Springer-Verlag Berlin Heidelberg, 2007.

[29] D. J. Griffiths, *Introduction to Electrodynamics*, 4th ed. Cambridge University Press, 2017. DOI: 10.1017/9781108333511.

[30] L. Fiscarelli. 'Magnetic measurements @ CERN.' (2016), [Online]. Available: https://indico.cern.ch/event/507584/contributions/2027919/attachments/1290537/1921838/LFiscarelli_workshop_sm18_v2.pdf (visited on 31/07/2022).

[31] M. Buzio, P. Galbraith, J. García-Pérez, E. Laface and S. Pauletta, 'A Device to Measure Magnetic and Mechanical Axis of Superconducting Magnets for the Large Hadron Collider at CERN,' 7 p, 2007. [Online]. Available: https://cds.cern.ch/record/1092675.

[32] G. Le Bec, J. Chavanne and C. Penel, 'Stretched wire measurement of multipole accelerator magnets,' *Phys. Rev. ST Accel. Beams*, vol. 15, p. 022 401, 2 Feb. 2012. DOI: 10.1103/PhysRevSTAB.15.022401. [Online]. Available: https://link.aps.org/doi/10.1103/PhysRevSTAB.15.022401.

[33] M. Liebsch, S. Russenschuck and J. Kaeske, 'An induction-coil magnetometer for mid-plane measurements in spectrometer magnets,' 2022.

[34] E. Kreyzig, 'Spline interpolation,' in *Advanced Engineering Mathematics*. 2011, ch. 19.4, pp. 821–827, ISBN: 978-0-470-45836-5.

[35] S. Sanfilippo, 'Hall probes: physics and application to magnetometry,' 40 p, Mar. 2011, Comments: 40 pages, presented at the CERN Accelerator School CAS 2009: Specialised Course on Magnets, Bruges, 16-25 June 2009. DOI: 10.5170/CERN-2010-004.423. arXiv: 1103.1271. [Online]. Available: http://cds.cern.ch/record/1334470.

[36] H. Ehya, A. Nysveen, I. L. Groth and B. A. Mork, 'Detailed magnetic field monitoring of short circuit defects of excitation winding in hydro-generator,' in *2020 International Conference on Electrical Machines (ICEM)*, vol. 1, 2020, pp. 2603–2609. DOI: 10.1109/ICEM49940.2020.9270942.

[37] P. Rogacki, 'A contribution to the development and characterization of rotating-coil magnetometers,' Deutsche und englische Zusammenfassung. - Druckausgabe: 2022. - Auch veröffentlicht auf dem Publikationsserver der RWTH Aachen University; Dissertation, RWTH Aachen University, 2021, Dissertation, RWTH Aachen University, Düren, 2022, 1 Online–Ressource : Illustrationen, Diagramme, ISBN: 978-3-8440-8493-1. DOI: 10.18154/RWTH-2022-03586. [Online]. Available: https://publications.rwth-aachen.de/record/844012.

[38] R. D. Maria, 'Engineering Specification: Alignment and mechanical tolerances for HL-LHC in Point 1 and 5,' CERN, Geneva, Tech. Rep., Oct. 2021.

[39] Enrico Taglini, 'Design and characterization of devices for the localization of magnetic and mechanical axes in accelerator magnets,' p. 104, 2021. [Online]. Available: https://morethesis.unimore.it/theses/available/etd-01192021-003651/unrestricted/Thesis_Taglini_Enrico_def.pdf.

[40] G. Spiezia, 'A fast digital integrator for magnetic measurements,' Ph.D. dissertation, Università Degli Studi Di Napoli Federico II, 2008. [Online]. Available: https://cds.cern.ch/record/1163375.

[41] P. Arpaia, L. Bottura, M. Buzio, D. D. Ratta, L. Deniau, V. Inglese, G. Spiezia, S. Tiso and L. Walckiers, 'A software framework for flexible magnetic measurements at cern,' in *2007 IEEE Instrumentation & Measurement Technology Conference IMTC 2007*, 2007, pp. 1–4. DOI: 10.1109/IMTC.2007.379293.

[42] *6220 dc current source/6221 ac and dc current source*, 6221 AC and DC Current Source, Source Specification table, p. 5, Keithley. [Online]. Available: https://download.tek.com/datasheet/6220-6221.pdf.

[43] *High-precision linear stage for heavy loads*, HPS-170 626291x10, Specification table, p. 2, PI miCos GmbH, 2020. [Online]. Available: https://static.physikinstrumente.com/fileadmin/user_upload/physik_instrumente/files/datasheets/HPS-170-Datasheet.pdf.

[44] MathWorks, *std - Standard deviation*, Available: https://se.mathworks.com/help/matlab/ref/std.html, Accessed: 20/07/2022.

[45] P. Arpaia, M. Buzio, V. Di Capua, S. Grassini, M. Parvis and M. Pentella, 'Drift-Free Integration in Inductive Magnetic Field Measurements Achieved by Kalman Filtering,' *Sensors*, vol. 22, no. 1, 2022, ISSN: 1424-8220. DOI: 10.3390/s22010182. [Online]. Available: https://www.mdpi.com/1424-8220/22/1/182.

[46] MathWorks, *fft - Fast Fourier transform*, Available: https://se.mathworks.com/help/matlab/ref/fft.html.

[47] MathWorks, *atan2 - Four-quadrant inverse tangent*, Available: https://se.mathworks.com/help/matlab/ref/atan2.html.

[48] *HEXAGON Absolute Tracker solutions*, Technical specifications, HEXAGON Manufacturing Intelligence, 2022. [Online]. Available: https://www.hexagonmi.com/products/laser-tracker-systems/leica-absolute-tracker-at930.

[49] Z. Wolf, 'A vibrating wire system for quadrupole fiducialization,' Dec. 2010. DOI: 10.2172/1000391. [Online]. Available: https://www.osti.gov/biblio/1000391.

[50] V. Baglin, P. Chiggiato, C. Garion and G. Riddone, 'Chapter 12: Vacuum system,' 229–244. 16 p, 2020. DOI: 10.23731/CYRM-2020-0010.229. [Online]. Available: https://cds.cern.ch/record/2750425.

[51] *PFG08-P1AM03PP EcoLine WIRE DRAW ENCODERS*, 1075495, SICK, Jul. 2021. [Online]. Available: https://www.sick.com/no/en/encoders/wire-draw-encoders/ecoline/pfg08-p1am03pp/p/p419845.

[52] *PCI/PXI/USB-6289 Specifications*, External Reference, p. 10, NATIONAL INSTRUMENTS CORP., 2022. [Online]. Available: https://www.ni.com/docs/fr-FR/bundle/pci-pxi-usb-6289-specs/.

[53] MathWorks, *cumsum - Cumulative sum*, Available: https://se.mathworks.com/help/matlab/ref/cumsum.html.

[54] *Linear High Precision Analog Hall Sensor HE244*, Asensor Technology AB. [Online]. Available: https://asensor.eu/onewebmedia/Datasheet-HE244X.pdf.

[55] *Model 8200 DC Voltage/Current Calibration Standard*, ANALOGIC. [Online]. Available: https://testequipment.center/Product_Documents/Data-Precision-8200-Specifications-0E813.pdf.

[56] MathWorks, *augknt - Augment knot sequence*, Available: https://se.mathworks.com/help/curvefit/augknt.html.

[57] MathWorks, *spmak - Put together spline in B-form*, Available: https://se.mathworks.com/help/curvefit/spmak.html.

[58] L. Bottura, M. Lamont, E. Todesco, W. Venturini Delsolaro and R. Wolf, 'Pre-Cycles of the LHC Magnets during Operation,' CERN, Geneva, Tech. Rep., Aug. 2010. [Online]. Available: http://cds.cern.ch/record/1283477.

[59] *MINILEVEL NT*, 011-110-113-001, WYLER AG. [Online]. Available: https://www.wylerag.com/fileadmin/pdf/catalogue/NT_FAMILIE.pdf.

[60] M. W. GmbH, *Material no.: Aisi 316 ln: Physical properties*, https://woite-edelstahl.com/aisi316lnen.html, May 2022.

[61] R. Shafer, 'Eddy Currents, Dispersion Relations, and Transient Effects in Superconducting Magnets,' Sep. 1980. [Online]. Available: https://inspirehep.net/files/6931fb5fb2a3e457cb0f4982abbd

[62] D. Sundararajan, 'Aliasing and other effects,' in *The Discrete Fourier Transform*, ch. 11, pp. 225–248. DOI: 10.1142/9789812810298_0011. eprint: https://www.worldscientific.com/doi/pdf/10.1142/9789812810298_0011. [Online]. Available: https://www.worldscientific.com/doi/abs/10.1142/9789812810298_0011.

[63] Siemens, *Windows and spectral leakage*, Accessed 10.07.2022, 2019. [Online]. Available: https://community.sw.siemens.com/s/article/windows-and-spectral-leakage.

[64] B. Mork, 'Comparison measures for benchmarking time domain simulations,' *Proceedings of the International Conference on Power Systems Transients 1997 (IPST 1997)*, pp. 177–181, 1997, ISSN: 2434-9739. [Online]. Available: https://www.ipstconf.org/papers/Proc_IPST1997/97IPST028.pdf.

[65] S. Kay and S. Marple, 'Spectrum analysis—a modern perspective,' *Proceedings of the IEEE*, vol. 69, no. 11, pp. 1380–1419, 1981. DOI: 10.1109/PROC.1981.12184. [Online]. Available: https://ieeexplore.ieee.org/stamp/stamp.jsp?tp=&arnumber=1456452.

[66] B. Podobedov, L. Ecker, D. Harder and G. Rakowsky, 'Eddy Current Shielding by Electrically Thick Vacuum Chambers,' in *Particle Accelerator Conference (PAC 09)*, 2010, pp. 3398–3400. [Online]. Available: https://accelconf.web.cern.ch/pac2009/papers/th5pfp083.pdf.

Appendix A

Fourier Analysis of Measured Signal

In this appendix the Fourier analysis of the time-depended signal measured with the rotating single-stretched wire measurement system is explained. The main theory of the Discrete Fourier Transform is presented, with emphasis on important factors to consider when using the Fast Fourier Transform-implementation in MATLAB, as well as the implementation of the signal treatment used in the measurement method.

A.1 General Fourier Analysis of Discretely Sampled Data

The Discrete Fourier Transform and The Fast Fourier Transform

The voltage induced in the induction coils due to a changing magnetic flux through the area spanned by the coil is a continuous signal. The measurement and conversion of this signal from voltage to treatable data requires the sampling of this voltage at discrete instances in either time or space. This process therefore converts the continuous signal into a discrete signal, and the continuous-time Fourier Transform can no longer be used to analyse the signal in the frequency domain, hence its discrete counterpart is applied instead.

According to [12], the n-th element of the complex Discrete Fourier Transform, *DFT*, of a function f, represented through a set of N discretely sampled points over the signal length l at equally spaced points in time or space, $f = (f(0), f(l/N), ..., f((N-1)l/N)) \in \mathbb{C}^N$ gives the vector $\tilde{f} = (\tilde{f}_0, \tilde{f}_1, ..., \tilde{f}_{N-1}) \in \mathbb{C}^N$, is given as:

$$\tilde{f}_n = \frac{1}{N} \sum_{k=0}^{N-1} f_k e^{-2\pi i k n/N}. \tag{A.1}$$

The Discrete Fourier Inversion theorem equally gives f_m from $\tilde{f}$:

$$f_m = \sum_{n=0}^{N-1} \tilde{f}_n e^{2\pi i n m/N}. \tag{A.2}$$

In the equations above, the term kn/N is the frequency of the harmonic components making up the signal. The representation of $|\tilde{f}_n|$ as a function of the frequencies is called the *spectrum* of the function f [62].

Solving eq. (A.1) successively for each element n is a time-consuming task. In fact, the complexity of this approach for a vector with N elements is $O(N^2)$[12], which is a far too time- and space-intensive task for measurements with a large set of sampled values. The Fast Fourier Transform,

FFT, is an algorithm that can solve this problem with far less computations. It does this by dividing the problem into J smaller operations, where $N = N_1 N_2 ... N_J$ is factored into prime numbers, and iterating over these operations [12]. Previously the FFT-algorithms required the number of points to be a power of two. It used the "radix 2"-algorithm to reduce the computational time, as the algorithm reaches a complexity of $O(n \log_2 n)$, however with the increase in computational power this is no requirement for the algorithm to still be very fast today. The application of the FFT in this thesis is carried out using the *fft*-function implemented in MATLAB, presented in [46].

The Shannon sampling theorem and aliasing effect

When sampling a continuous signal, the connection between the frequency with which the signal is sampled, the *sampling frequency*, and the frequency of the signal itself, the *signal frequency*, is of great importance when it comes to gathering sufficient information of the signal to uniquely represent it as a spectrum.

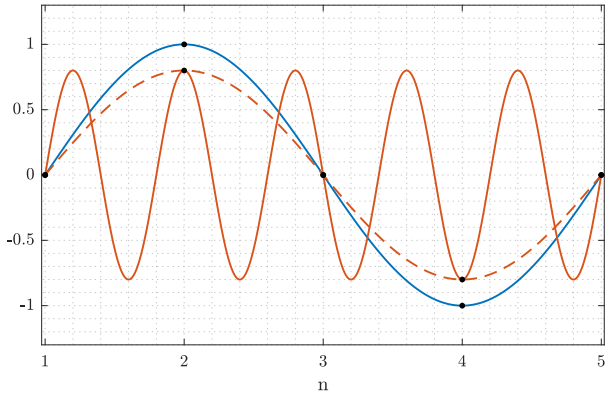

Figure A.1: Aliasing effect of undersampling a sinusoudal signal. The figure shows the sine waves $f_1 = \sin t$ (blue), $f_2 = 0.8 \sin 5t$ (orange) and $f_3 = 0.8 \sin t$ (orange stippled), together with the measurement points n and the corresponding sampled values $f_i(n)$ (black dots).

The effect of using a too low sampling frequency for a given signal is shown in Figure A.1, where two sine waves are plotted together, $f_1(t) = \sin(t)$ and $f_2(t) = 0.8 \sin(5t)$, shown as the blue and orange solid graph respectively. They are both sampled with a frequency of 5 Hz, and the values corresponding to the black dots are collected to represent the signal. What is immediately clear is that from the samples of $f_2(t)$ it looks as though the signal is actually equal to $f_3(t) = 0.8 \sin(t)$, shown as the dotted graph in the figure. This effect is what is referred to as *aliasing*, and it can be summed up as "*the impersonating of high frequency sinusoids as low frequency sinusoids, due to sampling a signal with a sampling interval that is not small enough*" [62].

The effect of aliasing when performing a Fourier analysis is that it corrupts the data, as signal components with too high frequencies appears to be components of lower frequencies to the DFT. Not only do we lose the data from the high-frequency signal, but the aliased signal will give erroneous frequency components for the lower-order signals as well. This is easily seen in Figure A.1, where the 5 Hz-signal will result as an additional 1 Hz-component through the Fourier analysis, distorting the actual component given by the blue curve.

Since we have to measure the magnetic fields discretely, aliasing effects will always be a part of the resulting. There are, however, ways of reducing its effect to allowable limits. One solution is to use so-called *anti-aliasing* filters, where a low-pass filter is applied to clear the signal of frequencies

that will cause aliasing effects. The method used in the measurements for this thesis, is to ensure we sample at a high enough frequency to include all the major frequency components of the signal. According to the *Shannon theorem*, to unambiguously represent a signal with frequency $\frac{N}{2}$, the theoretically required sampling frequency is N[12]. In reality, a higher frequency is required to account for imperfections in the measurement system. In the rotating single-stretched measurement method, a sampling frequency of at least 1024 Hz of the integrated signal is used, ensuring the expected frequency components are well within this limit. There could still be components of measured signal exceeding the maximum frequency we can measure, due to noise, but these are very weak, so the corruption of the measured signal is negligible. Furthermore, as the FFT is performed on signals that are already passed through the FDI, the very high-frequency signal will to some extent be filtered out due to the integration.

The leakage effect

Consider a measured sinusoidal signal, shown in the figure below. The measured data is sampled

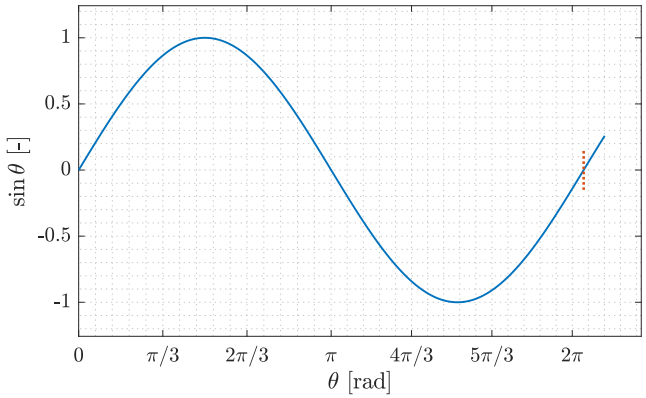

Figure A.2: Measured sinusoidal signal. The signal is captured over just above one full period of the signal, highlighted by the orange dotted line.

to contain just above one full period of the signal, shown as the orange dotted line in the figure. The effect of this "error" is clear when considering the underlying theory of the Fourier analysis; the signal is evaluated over the entire abscissas. Therefore, when the FFT algorithm is fed the signal shown in Figure A.2, the actual interpretation of the signal is shown in the following Figure A.3.

To recreate the sharp peaks of the repeated signal, several sinusoids with high frequencies are needed [62][63]. These frequencies will 'leak' to the neighbouring frequencies, resulting in less sharp peaks in the resulting spectrum and possibly less amplitude of the true measured signal. This effect is called *spectral leakage*.

The best way of avoiding this issue is to carefully choose the length of the measured signal to have an integer number of periods of the measured signal. However, this is not possible for aperiodic signals, and these might require the use of *windows*. A window is a known function starting at zero and ending at zero, the simplest being the rectangular signal, which is one for a specific length in time or space, and zero everywhere else. When the window is multiplied by the measured signal, it is forced to start and end at zero, smoothing out the transient edges and reducing the effect of spectral leakage [63]. The drawback of this method is that it also affects the true signal under investigation, both adding additional spikes in the spectrum and lowering the amplitude of the other spikes. The windows have known frequency responses, and correction factors can therefore be applied.

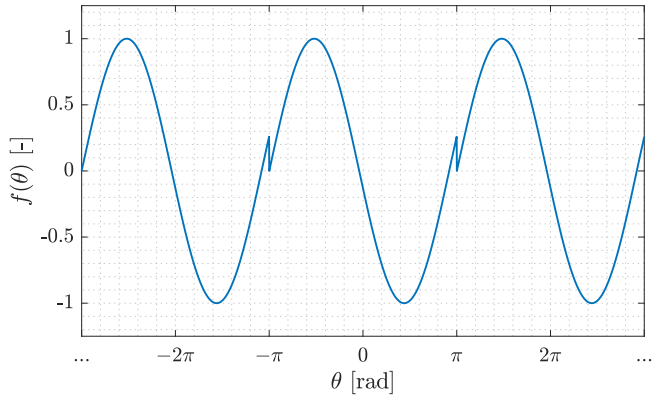

Figure A.3: Extension of the measured sinusoidal signal, as interpreted by the FFT algorithm.

Spectral resolution, spectral density and signal length

The difference in frequency of the sinusoidal components that is found to recreate an input signal given by the DFT is called *spectral resolution*. The finest resolution obtainable is given as the reciprocal of the measurement time. This means the actual number of full periods measured, and not the number of sampling points, as this only gives the upper bound for the measurable frequency as well as the *spectral density*. Therefore, if we are looking for a frequency component of the signal located exactly in the middle of two adjacent frequency bins, the only way of measuring this would be to double the measurement time.

A similar property of the spectrum is the *power spectrum*, as mentioned above. The spectral density gives the spacing between the frequency bins. It is inversely proportional to the length of the measurement signal, but this time it is a matter of measurement points, and not the measured period of the input signal. The spectral density is calculated by the following formula, presented in [64]:

$$\Delta f = \frac{1}{NPTS \cdot \Delta t}, \tag{A.3}$$

where Δf is the spacing between the frequency bins of the DFT, or the spectral density, $NPTS$ is the number of measurement points and Δt is the inverse of the sampling frequency. From the equation, it is clear that by increasing the number of measurement points, the number of frequencies from the DFT increases. This is often done by adding zeros to the end of the signal, so-called *zero-padding*. In this process, the spectrum is interpolated to contain more frequency bins, and it is therefore not a process that increases the spectral density, as it does not contain any new information of the actual input signal [62] [65]. In fact, as is discussed in [64], zero-padding, as well as windowing, gives additional distortions of the spectrum, and in many cases might result in a less accurate outcome of the DFT. The best procedure to increase the number of frequency bins is to increase the spectral resolution, through an increased measurement length.

A.2 Pre-Analysis Signal Processing

Proposed method

From the section above, it is clear that there are many parameters influencing the quality of the spectrum when applying FFT to a signal. The combinations of these parameters might be altered to

enhance different qualities of the spectrum, which also come at different computational costs. Due to this, there are no correct answer to what is the best set of parameters used in an FFT, as this is highly case sensitive.

One such approach is presented in [64], which is shown to give good results for the case where signal frequencies are not fully determined, see [36]. It is based on eq. (A.3), and it uses an iterative approach where the lower bound of Δf is given as the reciprocal of the measurement time, and assuming the number of sampling points to be constant, Δt, given as the inverse of the sampling frequency, is adjusted through a cubic spline interpolation of the measurement points in a re-sampling of the signal [36]. With this approach, one can adjust the frequency spacing to match perfectly with the fundamental frequency of the signal, and it is a powerful approach when the side bands are of great importance.

For the application in the work with the magnetic measurements for the corrector magnets, it is mainly in the treatment of the time-dependent induced voltage in the first phase of the rotating single-stretched wire measurement method the sets of parameters make a noticeable difference. In this case, what we are really interested in is to get the correct amplitude and phase of the fundamental frequency component, as explained in section 3.3.2. The side band harmonics are of less importance. Furthermore, the frequency of the power supply used in the measurements is very stable, as shown in Table 3.4, reducing the need for re-sampling of the signal.

To keep the process simple, it was therefore decided to pursue a simple approach to treat the signal before applying FFT. It is based on consistently choosing an appropriate signal length to get a full set of periods of the signal. The number of peaks of the measured signal is counted, and the true signal frequency is found. Then, the signal is trimmed to contain a full set of signal periods with the correct frequency, before applying FFT on the suitable signal.

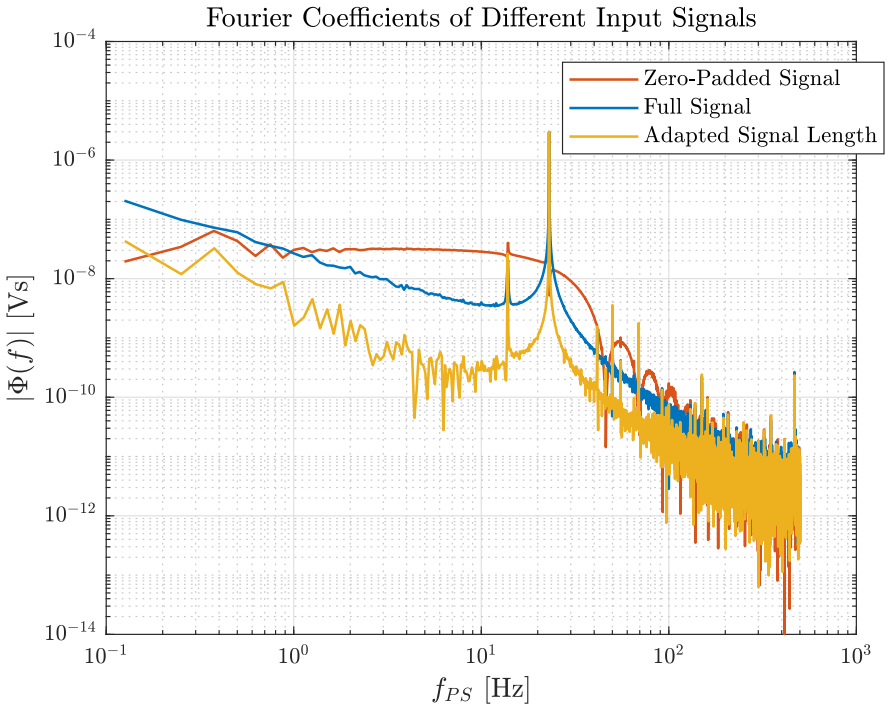

Figure A.4: Fourier Coefficient of Different Input Signal

The effect of this approach is shown in Figure A.4, where the yellow curve shows the spectrum of

the adapted signal, in a logarithmic plot. It is clear that compared to using the full signal (blue curve) and zero-padding the signal (orange curve), the spike at approximately 23 Hz is a lot narrower, and as an effect of this it also has a higher amplitude. The other frequency components, due to noise, are also generally higher for the other signals. Lastly, it is clear from this plot that zero-padding the signal to increase the spectral density clearly increases the side-lobes due to a distortion of the signal.

To conclude, the time-varying induced voltages are treated in order to avoid spectral leakage, resulting in a more defined peak at the fundamental frequency. This is obtained by properly choosing the input signal length in order to get an integer number of periods of the signal. In addition to reducing the spectral leakage, this step guarantees the inclusion of the true signal frequency as a frequency bin in the spectrum, as the new signal length is proportional to the inverse of the actual signal frequency. From Figure A.4 the advantages of this approach compared to 1) no approach and 2) zero-padding is shown.

Appendix B

Eddy Currents in the Cold Bore of the HL LHC Corrector Package

This appendix develops the equation used for the calculation of the phase shifts measured by the rotating single-stretched wire by the eddy currents induced in the cold bore when the magnet is powered in AC. It is based on the developments presented in reference [61].

Consider a magnet comprising a *cosine phi coil*[I], meaning a coil winding which generates a magnetic field with a shape of $\cos(n\varphi)$ for the magnetic multipole of order n, where φ is the azimuthal angle within the aperture of the magnet. With a current density varying sinusoidally in time by an angular frequency ω, it can be shown that the magnetic vector potential within the magnet ($r < b$), where b is the internal radius of the magnet, $\mathrm{A_s}$ is given as

$$\mathrm{A_s} = \mathrm{A_n}\Big(\frac{r}{b}\Big)^n \cos(n\varphi)\sin(\omega t), \tag{B.1}$$

where $\mathrm{A_n} = \mu_0 \mathrm{N_c} \mathrm{I_0}/8n$ is a constant given by the number of turns,$\mathrm{N_c}$, current amplitude, $\mathrm{I_0}$, and the number of pole pairs, n. From this we get the flux density components through $\mathbf{B} = \mathrm{curl}\ \mathbf{A}$:

$$\mathbf{B} = B_r + iB_\varphi = -\frac{nA_n}{B}\Big(\frac{r}{b}\Big)^{n-1}\sin(n\varphi)\sin(\omega t) - i\frac{nA_n}{B}\Big(\frac{r}{b}\Big)^{n-1}\cos(n\varphi)\sin(\omega t). \tag{B.2}$$

We now insert a thin conductive tube with an area resistivity of ρ_s and radius a within the aperture of the magnet. This gives a contribution to the vector potential, and it can be shown that the vector potential within the conductive tube is given as

$$\mathrm{A'_s} = \mathrm{A_n}\Big(\frac{r}{b}\Big)^n \cos(\epsilon_n)\sin(\omega t - \epsilon_n)\cos(n\varphi), \tag{B.3}$$

where $\epsilon_n = \tan^{-1}(\tau_n\omega)\omega$ and $\tau_n = \mu_r\mu_0 a/2n\rho_s$. By again calculating the flux density from the curl of the vector potential, by using the trigonometric identity $\cos(\epsilon_n) = 1/\sqrt{1+tan^2(\epsilon_n)}$ and by inserting $\epsilon_n = \tan^{-1}(\tau_n\omega)$, we get the azimuthal flux density within the conductive tube

$$B'_\varphi = \frac{B_\varphi}{\sqrt{1+(\tau_n\omega)^2}}\sin(\omega t - \tan^{-1}(\tau_n\omega)). \tag{B.4}$$

From this equation we see that when installing a conductive tube, in our case the cold bore, the resulting flux intercepted by the stretched wire lags the induced flux from the coils by an angle

[I]The real name of this type of magnet is *cosine theta*, however, to stay consistent with the already established nomenclature, *phi* is used in this section.

$\tan^{-1}(\tau_n\omega)$, and it is a factor $\sqrt{1+(\tau_n\omega)^2}$ less in amplitude. However, this assumes that the cold bore can be approximated with a very thin tube. In our case, the cold bore is not an infinitesimally thin tube, and we have to replace the area resistivity by the volume resistivity, ρ_V. Furthermore, the tube has to be thin enough for the current to flow somewhat homogeneously over the tube's cross-section for eq. (B.4) to be valid. That is, the thickness of the tubes wall has to be small compared to the skin depth of the material [66]. We can calculate the skin depth as $\delta = \sqrt{2\rho_V/\omega\mu}$ with values for AISI 316 LN [60] get a skin depth of 10 mm, which is 2.5 times the wall thickness of 4 mm. The cold bore can therefore be considered electrically thin.

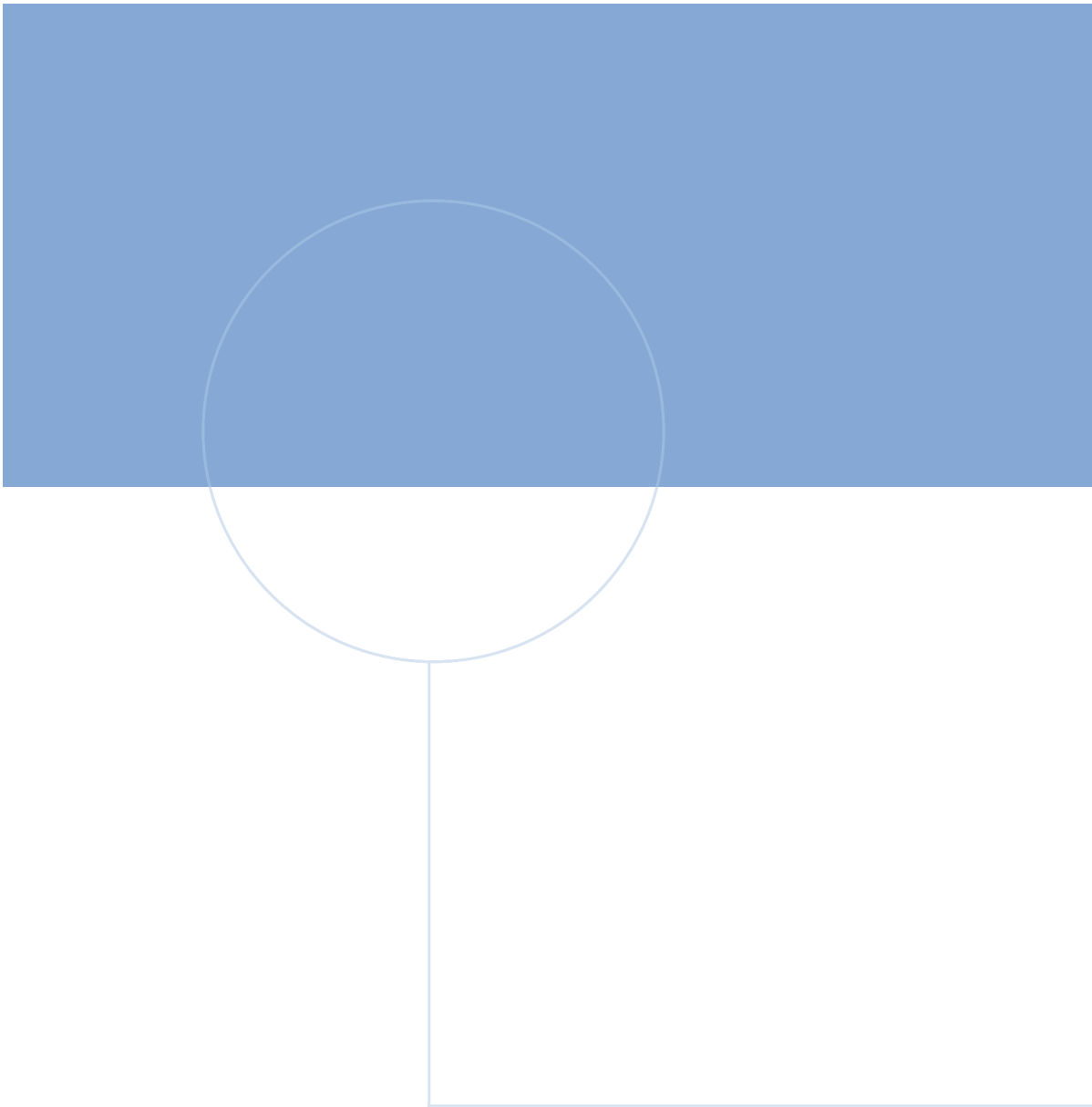

NTNU

Norwegian University of
Science and Technology